Mathematical modeling and data assimilation for biomedical problems.

Annabelle Collin

To cite this version:

Annabelle Collin. Mathematical modeling and data assimilation for biomedical problems.. Mathematics [math]. Université de Bordeaux, 2023. tel-04399487

HAL Id: tel-04399487
https://inria.hal.science/tel-04399487

Submitted on 17 Jan 2024

Thèse présentée en vue d'obtenir le diplôme

Habilitation à Diriger des Recherches

École doctorale de Mathématiques et d'Informatique de l'Université de Bordeaux
Spécialité Mathématiques Appliquées et Calcul Scientifique

par

Annabelle COLLIN

MODÉLISATION MATHÉMATIQUE ET ASSIMILATION DE DONNÉES POUR DES PROBLÈMES BIOMÉDICAUX.

Soutenue publiquement le 7 décembre 2023, après avis favorable de :

Roberto NATALINI	Directeur de recherche, CNR, Rome, Italie	Rapporteur
Mazen SAAD	Professeur des Universités, École Centrale de Nantes	Rapporteur
Marcela SZOPOS	Professeure des Universités, Université de Paris	Rapporteuse

devant le jury suivant :

Fabien CRAUSTE	Directeur de recherche, CNRS, Paris	Examinateur
Astrid DECOENE	Professeure des Universités, Université de Bordeaux	Examinatrice
Florence HUBERT	Professeure des Universités, Aix-Marseille Université	Examinatrice
Magali RIBOT	Professeure des Universités, Université d'Orléans	Examinatrice
Clair POIGNARD	Directeur de recherche, Inria, Bordeaux	Garant
Hugues LOISEAU	Professeur des Universités, PH, CHU de Bordeaux	Invité
Olivier SAUT	Directeur de recherche, CNRS, Bordeaux	Invité

REMERCIEMENTS

Mes premiers remerciements vont à Clair Poignard. Merci de de m'avoir guidée et encouragée ces dernières années. Tes connaissances scientifiques et ton recul remarquable sur de nombreux sujets sont une source d'inspiration pour moi. Les travaux présentés dans ce manuscrit te doivent beaucoup. Je remercie également grandement Olivier Saut. En plus de tes nombreuses qualités scientifiques qui rendent la recherche avec toi enrichissante, je te remercie pour ton accueil chaleureux au sein de l'équipe MONC. Avoir un chef d'équipe aussi bienveillant au début de ma carrière a été très précieux. Je tiens aussi à remercier Thierry Colin – même si nous n'avons pas eu le temps de travailler ensemble très longtemps au sein de l'équipe – pour la confiance que tu m'as accordée lors de mon arrivée sur Bordeaux. Un grand merci également à Dominique Chapelle : chaque jour, je réalise l'importance de ce que tu m'as transmis, en particulier ta curiosité et ta rigueur scientifique.

Un grand merci à Roberto Natalini, Mazen Saad et Marcela Szopos qui ont accepté de rapporter ce manuscrit. Je suis très honorée de l'intérêt que vous avez porté à mon travail. Je remercie également très chaleureusement Fabien Crauste, Astrid Decoene, Florence Hubert, Magali Ribot et Hugues Loiseau d'avoir accepté de siéger dans mon jury. Votre présence me touche beaucoup.

Je tiens également à remercier l'ensemble de mes collaboratrices et collaborateurs qu'elles ou ils soient mathématicien·ne·s, biologistes ou clinicien·ne·s. Ces collaborations sont extrêmement précieuses pour mon travail. Je remercie tout particulièrement Philippe Moireau : c'est à chaque fois un vrai plaisir de travailler avec toi, et je suis enchantée par toutes les pistes que nous avons encore à explorer. Un merci spécial aussi à Mélanie Prague : la question que tu m'as posée il y a quelques années m'a fait découvrir tout un nouveau monde, celui des biostatistiques, et je suis convaincue que cette découverte a beaucoup apporté à ma recherche. Et pour terminer, merci à Christèle Etchegaray. Je prends beaucoup de plaisir dans cette nouvelle collaboration et j'espère qu'elle sera l'occasion que tu m'apprennes plein de choses sur les équations différentielles stochastiques.

L'équipe MONC a la chance de compter de nombreuses personnes brillantes, enrichissantes et pleines de bonne humeur. Je remercie Baudouin, Nicolas, Benjamin, Cédrick, Thibaut, Giorgia, Julien, Emma, Luc, Van Linh, Khaoula, Kylian, Eloïse, Guillaume et Florian pour leur contribution à une ambiance de travail agréable. Je souhaite remercier encore plus chaleureusement celles et ceux qui m'ont fait ou me font l'honneur de vivre l'expérience de la thèse avec moi : Sergio, Pedro, Virginie, Simone, Simon et Audrey. Ce manuscrit vous doit beaucoup, et je considère comme un véritable privilège d'avoir été ou d'être témoin de votre évolution sur ce chemin exigeant mais tellement riche qu'est la thèse.

Je tiens à remercier les collègues de l'Institut de Mathématiques de Bordeaux et d'Inria avec qui j'ai la chance d'interagir régulièrement pour leur contribution à la convivialité de notre cadre de travail. Mes remerciements s'adressent en particulier aux membres de l'équipe Calcul Scientifique et Modélisation pour l'émulation scientifique qu'elles et ils génèrent. Une partie de mon intégration et de mes rencontres s'est réalisée à travers le groupe Femmes & Sciences : je remercie Lisl de m'avoir invitée à le rejoindre. Cette aventure a conduit à la création de la mission parité de l'IMB, dont je suis très satisfaite de l'évolution. Mes remerciements s'adressent aussi à mes collègues de l'ENSEIRB-MATMECA, avec une pensée spéciale pour mes deux collègues de bureau, Héloïse et Natalie, ainsi que pour la super équipe DDRS et les habitué·e·s de la pause midi en salle de détente Matmeca/Informatique. Certains de ces collègues sont même devenus des ami·e·s très proches : un merci tout particulier à Juliette, Mélanie, Mathieu et Nicolas.

Je remercie mes ami·e·s d'ailleurs : Saverio, Hélène, Ludivine, Nicolas, Claire, Aurore, Marion, Dorian, Camille, Max, Caco et Micky. La vie aurait tellement moins de saveur sans vous !

Je remercie ma famille et en particulier mes parents. Leur soutien infaillible est une source de réconfort inestimable. Merci aussi à ma sœur Camille et à mon frère Antoine : je suis très fière de vous, et votre soutien m'est également très précieux. Je remercie également ma belle-famille, avec une pensée particulière pour mes nièces et mon neveu, de m'avoir accueillie au sein de votre famille ainsi que pour l'intérêt que vous portez à mon travail.

Je dédicace ce travail à Lise. Te regarder grandir depuis ces cinq dernières années est la plus belle expérience de ma vie. Mes derniers remerciements sont pour Charles. Je n'ai (toujours !) pas les mots pour exprimer tout ce que tu apportes à ma vie. Les épreuves que nous avons traversées ces dernières années n'ont fait que renforcer le sentiment qu'avec toi, je suis à ma place dans ce monde. Vivement la suite !

À Lise,

Contents

Résumé (en français)

Ce document présente un résumé de mes travaux depuis mon arrivée à Bordeaux en 2015 en tant que maîtresse de conférences (Bordeaux INP, ENSEIRB-MATMECA). Côté recherche, je suis membre de l'équipe MONC (Modélisation en ONCologie) du Centre Inria de l'Université de Bordeaux ainsi que de l'équipe Calcul Scientifique et Modélisation de l'Institut de Mathématiques de Bordeaux.

Mes recherches portent sur les mathématiques appliquées au domaine biomédical. Mon objectif est le développement d'**outils mathématiques innovants** qui ont pour but (1) d'aider les biologistes à comprendre un phénomène et (2) d'aider les cliniciennes et cliniciens à établir un diagnostic ou à améliorer le suivi des patientes et patients.

Le manuscrit – rédigée en anglais à l'exception de ce résumé – est composé d'une longue introduction et de 4 chapitres. Dans l'introduction, je fais une présentation de la stratégie générale que j'utilise dans ma recherche. La première étape de mon approche consiste à définir des problèmes biologiques ou médicaux en consultation avec des expertes et des experts de ces disciplines. Ensuite, si ces problèmes peuvent être résolus ou du moins compris à travers mes domaines d'expertise – que sont la **modélisation mathématique avec des équations différentielles** ordinaires (EDO) ou partielles (EDP), leurs **études théoriques et numériques** et l'**assimilation de données** – une collaboration s'ensuit. Mes collaborations – dont les principales sont listées à la fin de ce résumé – avec des biologistes et des cliniciens sont très précieuses pour mon travail. Enfin et dans le but d'adopter une approche la plus complète possible, je développe des outils mathématiques innovants – principalement basés sur l'étude théorique ou numérique des EDP, l'analyse asymptotique et les observateurs – qui permettent de répondre à la fois à des **questions théoriques** et à des **applications pratiques**. La figure 1 résume cette approche.

Plus précisément, une première partie de mon travail porte sur des aspects théoriques liés à la modélisation ou à l'assimilation de données et une deuxième partie est très orientée vers les applications, notamment lorsqu'il s'agit de travailler avec des données réelles. Une partie de mon travail de recherche s'appuie sur des données médicales qui ont les spécificités (1) de contenir des données difficiles à intégrer dans des modèles mathématiques et (2) qu'une population d'individus (patients/patientes et expériences biologiques) avec la même pathologie est souvent disponible. Ces spécificités sont suffisamment importantes pour avoir des impacts sur ma recherche. En plus de collaborer avec des experts biomédicaux, ma recherche implique également la collaboration avec des mathématiciennes et mathématiciens, dont la liste principale est donnée à la fin de ce résumé. Au sein de ces collaborations, l'une de mes contributions principales réside dans mon expertise à intégrer des données réelles provenant de problèmes biomédicaux dans des systèmes EDO et EDP.

À la suite du chapitre introductif, ma recherche est présentée à travers mes trois plus grands champs d'application : **l'électrophysiologie cardiaque, la croissance tumorale et l'électroporation**. Malgré cette présentation par chapitre, de nombreuses interactions – mises en avant – dans le manuscrit existent.

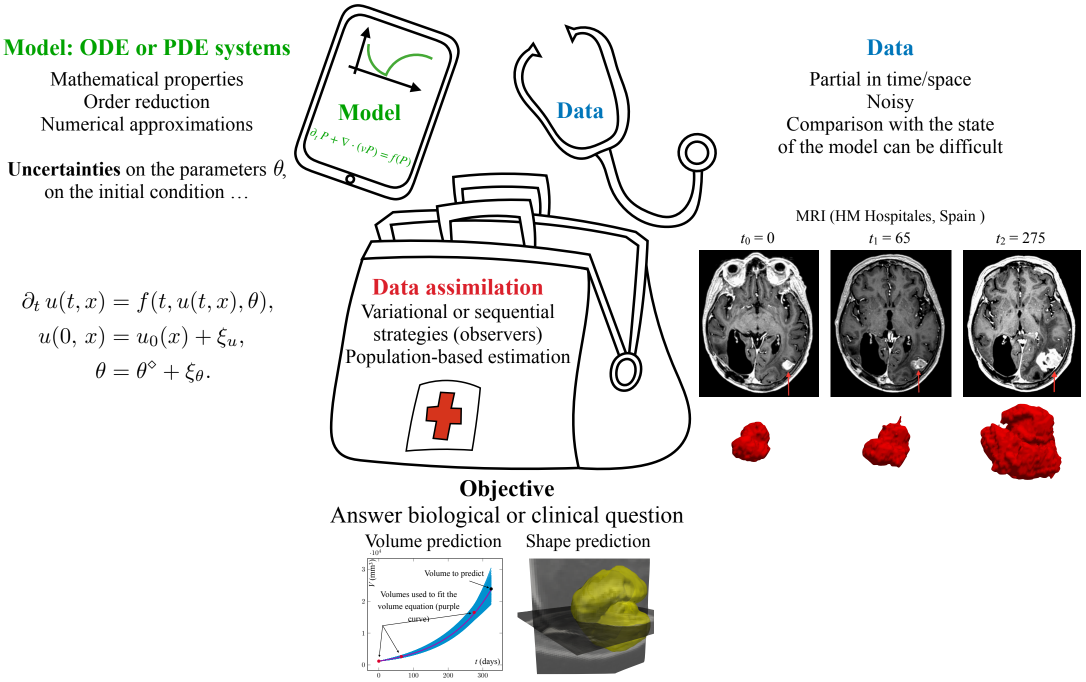

FIGURE 1 – Présentation générale

L'électrophysiologie cardiaque est l'étude de l'onde électrique qui précède la contraction cardiaque. De nombreuses pathologies cardio-vasculaires sont dues à des troubles électro-physiologiques qui perturbent le rythme cardiaque. L'étude de ce phénomène est donc un véritable enjeu de santé publique. Mes principales contributions dans ce domaine d'application – résumées ci-dessous – sont présentées dans le chapitre 1.

(1) Fournir une analyse mathématique de la procédure d'homogénéisation périodique qui conduit au modèle bidomaine macroscopique. Dans ce travail, nous avons comblé une lacune de la littérature en fournissant une analyse mathématique basée sur la *convergence double échelle* de la procédure d'homogénéisation qui conduit au modèle bidomaine macroscopique, le modèle de référence en électrophysiologie cardiaque. Notre analyse est exhaustive dans le sens où nous fournissons des *résultats d'existence et d'unicité*, d'adimensionnement et de *convergence* dans le même cadre mathématique. Ce travail, publié dans [8], est présenté dans la section 1.2.

(2) Étendre le modèle bidomaine microscopique à un modèle bidomaine microscopique prenant en compte les déformations du cœur. Dans ce travail, le couplage complet entre l'électrophysiologie cardiaque et la mécanique cardiaque a été étudié en remontant aux origines du modèle bidomaine afin d'intégrer les effets directement sur les *lois de conservation*. Ce travail est présenté dans la section 1.1.

(3) Déterminer un modèle bidomaine macroscopique intégrant les déformations. Grâce à notre compréhension de l'homogénéisation théorique des équations bidomaines classiques (contribution (1)) et une *homogénéisation formelle*, l'impact des déformations mécaniques sur les équations macroscopiques a été déterminé. Les contributions (2) et (3) sont présentées dans la section 1.3 et ont été publiées dans [11].

(4) Intégrer les données du front de dépolarisation. Les travaux précédents nous ont permis d'obtenir une compréhension précise du modèle direct. Afin que le modèle soit réellement descriptif voire prédictif pour un patient donné, il est fondamental d'estimer ou de contrôler les incertitudes – des conditions initiales et/ou des paramètres du modèle par exemple – à l'aide des données médicales disponibles pour ce patient. Dans cette partie – présentée dans la section 1.4 – nous avons travaillé sur des données de front de dépolarisation à l'aide de *méthodes séquentielles* d'assimilation de données. Une partie des résultats obtenus a été publiée dans [5, 12].

Le chapitre 2 présente mes travaux en croissance tumorale. Le développement de modèles décrivant la croissance tumorale offre la possibilité de suivre l'évolution de la maladie chez un patient spécifique, voire de prédire l'efficacité ou non d'une stratégie thérapeutique. C'est pourquoi la modélisation mathématique de la croissance tumorale suscite l'intérêt de la communauté médicale. Mes contributions principales à ce domaine d'application sont résumées dans les trois points suivants.

(5) Sélectionner des modèles mécanistes pour la croissance tumorale. Contrairement à l'électrophysiologie cardiaque, où un modèle de référence est établi, il n'existe pas de consensus clair pour la modélisation de la croissance tumorale. Une explication possible réside dans les multiples inconnues du système et les incertitudes persistantes concernant les lois de conservation et de comportement régissant la croissance tumorale. Les modèles utilisés par l'équipe MONC se basent sur des *équations d'advection* qui décrivent l'évolution temporelle des densités de cellules saines et tumorales (voir section 2.1).

(6) Développer une stratégie d'estimation des paramètres du modèle qui soit efficace pour les patients atteints de méningiome. Les modèles de croissance tumorale doivent être adaptés à chaque patient afin d'obtenir des simulations prédictives. Dans ce contexte, de nombreuses données médicales (volume, texture, forme des lésions ...) peuvent être utilisées pour estimer les paramètres du modèle. Nous avons développé une stratégie innovante qui combine un *modèle réduit 0D* et une *stratégie d'estimation* basée sur les effets mixtes non linéaires. Cette stratégie – illustrée sur une large cohorte de méningiomes (tumeurs bénignes cérébrales) – permet d'obtenir des prédictions fiables du volume et de la forme des tumeurs. Ce travail – présenté dans la section 2.2 – a été valorisé par deux publications [17, 24].

(7) Adapter notre stratégie d'estimation pour tenir compte de l'évolution des formes tumorales dans le temps. La stratégie précédemment mentionnée se révèle inefficace lorsqu'il s'agit de prendre en compte l'évolution temporelle des formes tumorales. Dans un autre travail, nous avons donc développé et *mathématiquement analysé* un *observateur de type Luenberger* afin de surmonter cette difficulté. Ce travail – présenté dans la section 2.3 – a été publié dans [20].

Le chapitre 3 met en avant mes travaux sur la modélisation de l'électroporation. L'électroporation consiste à appliquer des champs électriques pulsés de forte intensité et de courte durée sur des cellules à l'aide de cathéters. L'objectif est de créer des défauts, appelés pores, dans la membrane cellulaire. L'électroporation réversible permet l'introduction de molécules non perméables dans les cellules vivantes sans les tuer, tandis que l'électroporation irréversible conduit à la mort des cellules de la région ciblée. Mes contributions mathématiques dans ce domaine d'application sont résumées ci-dessous.

(8) Utiliser la modélisation mathématique afin d'améliorer notre compréhension du processus de perméabilisation de la membrane. Notre objectif est de mettre en place des approches mathématiques pour étudier la dynamique des membranes. Dans un premier travail présenté dans la section 3.1.1, nous avons développé une stratégie d'étalonnage robuste pour un montage expérimental à 4 électrodes mesurant l'impédance de myotubes cellulaires soumis à des impulsions électriques. Nous avons également conçu et paramétré un modèle de circuit équivalent pour quantifier le comportement à court terme de la conductance membranaire quelques secondes après l'impulsion. Dans un second travail présenté dans la section 3.1.2, nous avons élaboré un modèle d'électroporation à l'échelle de la membrane qui intègre la teneur en eau de la membrane et le potentiel électrique grâce à un modèle bidomaine microscopique. Une stratégie numérique innovante et efficace nous a ensuite permis d'effectuer des simulations numériques de la formation de pores sur la membrane. Ces travaux ont été publiés dans [25] et [29].

(9) Comparer différents modèles d'électroporation à l'échelle tissulaire à travers une confrontation à des données expérimentales. Dans un premier travail, présenté dans la section 3.2.1, nous avons comparé les solutions de divers modèles d'électroporation provenant de la littérature. Nous avons examiné leur paramétrisation en utilisant des mesures bioélectriques obtenues à partir d'expériences sur des foies de lapin réalisées par Sel et al. [SCB+05]. Dans un deuxième travail présenté dans la section 3.2.2, le choix des conditions aux limites des électrodes passives – très conductrices et minces – a été étudié. En effet contrairement aux électrodes actives qui imposent soit le potentiel, soit le courant (conditions de Dirichlet ou de Neumann), la valeur de l'équipotentielle des électrodes inactives est une inconnue des modèles. Cela conduit à une contrainte non locale du flux le long de l'interface conductrice appelé problème du potentiel flottant. Nous avons développé un modèle pour résoudre ce problème dans le contexte de l'électroporation. Ces deux travaux ont été publiés dans [15, 18].

(10) Étudier les effets de l'électroporation sur la croissance tumorale. Les sphéroïdes sont des modèles de culture cellulaire 3D capables de représenter l'environnement et l'architecture complexes des tumeurs. En utilisant un modèle mathématique avancé, qui s'inscrit dans la modélisation présentée dans le chapitre 2, et en employant des méthodes d'estimation appropriées, nous avons caractérisé la croissance de sphéroïdes après leur exposition à un champ électrique pulsé. Les résultats de cette étude, présentés dans la section 3.3, ont été publiés dans [21].

Un axe de recherche transverse à ces domaines d'application est le développement d'algorithmes pour l'assimilation de données. Plus précisément, nous avons travaillé sur l'utilisation des données d'une population d'individus pour estimer (entre autres) les paramètres d'un système EDO ou EDP. L'exploitation des connaissances et des données que nous avons sur une population suivant une dynamique similaire permet de compenser les incertitudes inhérentes à un individu spécifique. C'est le principe des modèles mixtes qui se sont révélés plus robustes face aux erreurs de mesure et aux minimums locaux dans de nombreux cas d'application. Cependant, cette méthode d'estimation est trop souvent coûteuse en temps de calcul pour être utilisée en pratique sur des systèmes d'EDP. La stratégie que nous avons développé est basée sur une vraisemblance intégrant l'ensemble de la population qui est maximisée à l'aide d'un filtre de Kalman, voir [23]. Nous avons également proposé une version d'ordre réduit de ce filtre adaptée aux systèmes de grande taille. Pour évaluer les performances de l'algorithme (voir Algorithme 6 dans l'introduction), nous l'avons appliqué à un modèle pharmacocinétique. Cette méthode permet de plus d'inclure et d'estimer facilement des erreurs de modélisation. Cette stratégie a été utilisée pour déterminer les associations entre les interventions mises en place par le gouvernement français lors de la pandémie du COVID-19 (confinements, couvre-feux, fermetures d'écoles etc.) et les taux de transmission en se basant uniquement sur les données d'hospitalisation. Le défi était de travailler sans connaissance préalable de la dynamique des taux de transmission. Les résultats obtenus ont été publiés dans [22]. Enfin, dans un troisième travail [28], j'ai proposé une stratégie compatible avec les systèmes d'EDP. Les erreurs provenant des conditions initiales sont contrôlées par un observateur de Luenberger qui corrige l'état, tandis que les paramètres sont estimés à l'aide d'un filtre de Kalman réduit à l'espace paramétrique. L'efficacité de la stratégie a été évaluée sur des données d'électroporation de sphéroïdes tumoraux. Ces travaux sont présentés dans le chapitre 3 de cette thèse.

Le chapitre 4 conclut ce manuscrit en présentant brièvement mes projets de recherche à court et moyen termes. Je commence par aborder mes perspectives de recherche concernant la croissance tumorale, en mettant en évidence deux nouveaux axes de recherche. Le premier axe consiste à approfondir notre compréhension du processus métastatique en étudiant les cellules tumorales circulantes. Le deuxième axe consiste à développer une nouvelle collaboration axée sur l'utilisation du propranolol, un médicament initialement utilisé pour des troubles cardiaques, mais qui montre des résultats prometteurs dans le traitement de certaines tumeurs vasculaires. Ensuite, je décris mes perspectives de recherche dans le domaine de l'électroporation. Dans le cadre du projet ANR MIRE4VTach que je porte, je souhaite m'intéresser à l'électroporation pour l'ablation cardiaque. C'est l'occasion rêvée pour moi de coupler deux de mes champs d'expertise. Enfin, dans une dernière partie, j'aborde brièvement mes perspectives concernant le développement d'algorithmes pour l'assimilation de données. L'idée est de continuer à explorer les stratégies – combinant les aspects populationnels et les méthodes séquentielles – que nous avons développées.

Principales collaborations

Le travail présenté dans cette HDR est le fruit de collaborations. Mes principaux collaboratrices et collaborateurs sont listés ci-dessous :

Mathématiciennes/Mathématiciens :

C. Etchegaray, C. Poignard, O. Saut (Inria Bordeaux, MONC), S. Impériale, P. Moireau (Inria Saclay, M3DISIM), M. Prague (Inria Bordeaux, SISTM)
Doctorants/Doctorantes : T. Kritter (2015-18, 20%), A. Gérard (2015-19, 10%), S. Corridore (2016-20, 50%), P. Jaramillo-Agayo (2019-23, 50%), V. Montalibet (2021-.., 50%)

Biologistes :

G. Caluori (électrophysiologiste, IHU Lyric Bordeaux), T. García-Sánchez (Universitat Pompeu Fabra, Barcelona), J. Kolosnjaj, M. Golzio, M.-P. Rols (Université de Toulouse, CNRS, laboratoire IPBS), L. M. Mir (CNRS, Gustave Roussy, Université Paris-Saclay)

Cliniciens :

J. Engelhardt, H. Loiseau (neurochirurgiens, CHU Bordeaux), P. Jaïs (cardiologiste, IHU Lyric Bordeaux)

Principales contributions

Mes publications publiées dans des journaux et des actes de conférence avec comité de relecture sont listées en page 109. Des liens sont fournis pour accéder librement aux publications. Pour faciliter la lecture, les références chiffrées de ce manuscrit correspondent à mes publications et les références lettrées à la littérature. D'autres informations sont disponibles dans mon CV détaillé.

Introduction

In this chapter, I first present the general strategy I follow in my research, which is mainly focused on the biomedical field, and then my main contributions. The first step in my approach is to define biological or medical problems in consultation with experts in those disciplines. When these problems can be solved or at least understood through my areas of expertise – mathematical modeling with differential equations (ODE or PDE), theoretical and numerical study of these models, and data assimilation – collaboration ensues. Aiming for the most complete approach possible, I am developing innovative mathematical tools based mainly on the theoretical or numerical study of PDEs, asymptotic analysis, and data assimilation (including observers)– that can address both theoretical and practical aspects. In particular, a first part of my work deals with theoretical aspects of modeling or data assimilation. Another important part of my work is very application oriented, especially when it comes to working with real data. This chapter also gives me the opportunity to introduce several mathematical notions that will be used in the rest of this manuscript. Section A briefly introduces the modeling aspects, and Section B explains how to deal with the many uncertain quantities that must be specified for the models to be truly descriptive or predictive. Finally, Section C contains a summary of my main contributions.

A Modeling aspects

A.1 Mathematical models

Most classical mathematical models are based on the application of conservation principles and constitutive relations relevant to the physical, biological, or medical questions under investigation. A conservation law is usually expressed mathematically as a continuity equation, a partial differential equation that establishes a relationship between the quantity of a set and the “transport" of that set. It states that the quantity received at a point or in a volume can change only by the quantity flowing into or out of the volume. A constitutive equation is a relationship between two physical quantities that is specific to a material or substance and approximates the response of that quantity to external stimuli, usually in the form of applied fields or forces. These constitutive equations in the biomedical context can be physiological or phenomenological. A phenomenological model is based on observations of a system rather than a physical theory.

The choice of a model is a delicate trade-off between the best possible representation of reality, its numerical cost, and its identifiability with the available data. This choice must be made as a function of the ultimate goal. In [11], for example, where the goal was to study the effects of mechanical deformation on cardiac electrophysiology, we come back to the derivation of the equations governing ionic motion in the intracellular and extracellular regions in the conservation laws to ensure that we do not neglect any effect that is comparable to the effects we want to study. In contrast, in [17] we consider a very simple tumor growth model. One could probably consider a model for tumor growth that is closer to biology, but the major advantage of our model is that it depends on a very small number of parameters. In this case, we chose to keep the model simple to ensure that it could be effectively personalized for each patient using the sparse observations available in routine clinical practice.

A.2 Model order reduction

Part of my work concerns model order reduction. Model order reduction is a technique for reducing the computational complexity of mathematical models. On the one hand, the strategy can be based on a reduced state space dimension such as 0D integration in [17] or radial coordinates based on the spherical symmetry of the tumour in [21]. On the other hand, theoretically validated approximations to the original model can be written thanks to well-designed asymptotic analyses such as in [18] for a floating potential strategy or in [8] for a homogenization method by 2-scale convergence.

A.3 Theoretical investigation

By proving the existence and uniqueness of the solution of the model under consideration, it is possible to determine whether the problem is well posed. Although this question is important and regularly addressed in my papers, it is not the main topic of my research. Nevertheless, I cite the hard work done in this article [8] regarding the mathematical proof of the existence and uniqueness of the microscopic bidomain model, a very classical model of cardiac electrophysiology.

A.4 Numerical approximation

In most cases, the solution is not explicit and is then approximated using classical numerical methods such as finite difference methods, finite element methods, or volume element methods for the state variable. I use these methods rather than developing them myself, although a significant amount of my research time is devoted to writing code for numerical simulations. As we will see in the following section, in many situations we want to estimate the parameters of the model using available observations. Most strategies for estimating model parameters require solving the direct model multiple times. To achieve acceptable computational times, we choose numerical schemes very carefully and we rely on parallelization of the code – especially when working with 3D systems and a population of subjects that we want to couple together – with the goal of handling very large systems.

B Data assimilation aspects

When using ODE or PDE models in practical applications, a major difficulty is dealing with the many uncertain quantities that must be specified for the models to be truly predictive. These quantities include modeling errors, initial conditions, geometry, or parameters of the model. Fortunately, collected data provide additional information that can be used to circumvent the uncertainties associated with the definition of the dynamical system. The development and the application of appropriate estimation strategies occupy a significant portion of my research time. The main difficulties arise from the fact that observations can be sparse in content – for example, when only one of the unknowns is observed – in space – for example, when only a subdomain or part of the boundary is observed – and also in time. In addition, they can be difficult to compare with the solution of the models and are often noisy.

B.1 Problem setting

In this subsection, I briefly present the formalism of most of the cases I faced.

Model formulation We denote by u, the system state and by θ the vector containing all the parameters of the system. Let Ω be a bounded and smooth domain of $\mathbb{R}^d$, $d = 1, 2$ or 3, the state dynamics over the time window $[0, T]$ is modeled by an operator f – eventually nonlinear – such that

$$\left\{ \begin{array}{rcll} \partial_t u(t,x) & = & f(t, u(t,x), \theta), & [0,T] \times \Omega, \\ u(0,x) & = & u_0(x), & \Omega. \end{array} \right. \tag{1}$$

We assume that it is well-posed meaning that for a given vector θ of size N_θ and for a given sufficient regular initial solution $u_0 \in \mathcal{X}$, there exists a unique solution $u \in L^2(0, T; \mathcal{X})$, where $\mathcal{X}$ denotes the state space.

Observations In practice, we do not observe u directly, but we do have observations – also called measurements – $y \in \mathcal{Z}$. These observations y are related to u by the measurement process. Denoting by $h : \mathcal{X} \to \mathcal{Z}$ the observation operator, we have

$$y(t, \cdot) = h(u(t, \cdot)) + e(t, \cdot), \tag{2}$$

where e represents the error inherent to the measurement process. To simplify the presentation, we have chosen to consider continuous observations.

Discretization For the sake of simplicity, the presentation is done on the discretized version. Given $N_{\Delta t} \in \mathbb{N}^*$ and $\Delta t = \frac{T}{N_{\Delta t}}$, we define the $N_{\Delta t} + 1$ time points $t_n = n \times \Delta t$ for $n \in [\![0, N_{\Delta t}]\!]$. Then concerning the spatial discretization when PDE is considered, one could use indifferently finite element, finite volume or finite difference methods and we define $N_{\Delta x}$ the size of the discretized state. The lowercase will be used to denote the spatial discretization of the state-dependent variables. The subscript n designs the time discretization at time t_n of the time-dependent variables.

Uncertainties We assume that the initial state U_0 and the values of the parameters represented by a vector of size N_θ denoted by θ are not perfectly known. We quantify the level of uncertainty on U_0 and θ by assuming that they can be modeled as a Gaussian disturbance of $U_0^\diamond$ and $\theta^\diamond$ means (corresponding to the *a priori* parts) and P_U and P_θ covariances operators

$$U_0 = U_0^\diamond + \zeta_U, \;\; \theta = \theta^\diamond + \zeta_\theta,$$

where ζ_U and ζ_θ verify $\zeta_U \sim \mathcal{N}\big(0, P_U\big)$ and $\zeta_\theta \sim \mathcal{N}\big(0, P_\theta\big)$.

Measurement error By denoting W the covariance operator of the observation errors, we assume that the errors follow the centered Gaussian law

$$E_n \sim \mathcal{N}\big(0, W\big), \; \forall n \in [\![0, N_{\Delta t}]\!].$$

Objective We combine the uncertainties by defining

$$\zeta = (\zeta_U, \zeta_\theta) = (U_0 - U_0^\diamond, \theta - \theta^\diamond) \text{ and } P = \begin{pmatrix} P_U & \\ & P_\theta \end{pmatrix}.$$

The objective is to find the values of the uncertainties that maximize the probability of the uncertainties under the observations $\max_\zeta \mathbb{P}\big(\zeta \,|\, (Y_n)_{n\in[\![0,N_{\Delta t}]\!]}\big)$. The cases which interest us here correspond to cases for which it is difficult to directly known the uncertainties (ζ_U, ζ_θ) from the observations. This is why it is very classical to use Bayes theorem

$$\max_\zeta \mathbb{P}\big(\zeta \,|\, (Y_n)_{n\in[\![0,N_{\Delta t}]\!]}\big) = \max_\zeta \Big[\mathbb{P}\big((Y_n)_{n\in[\![0,N_{\Delta t}]\!]} \,|\, \zeta\big) \;\; \mathbb{P}\big(\zeta\big)\Big].$$

Assuming that all disturbances are Gaussian, the strategy relies on the *minimization* of the following least-square functional

$$\begin{aligned}
\mathcal{J}(\zeta) =& \frac{1}{2}\big(\zeta, P^{-1}\zeta\big) + \frac{1}{2}\sum_{n=0}^{N_{\Delta t}}\big(E_n, W^{-1}E_n\big),\\
=& \frac{1}{2}\big(U_0 - U_0^\diamond, P_U^{-1}(U_0 - U_0^\diamond)\big) + \frac{1}{2}\big(\theta - \theta^\diamond, P_\theta^{-1}(\theta - \theta^\diamond)\big)\\
&\qquad + \frac{1}{2}\sum_{n=0}^{N_{\Delta t}}\big(Y_n - H(U_n^{\{U_0^\diamond+\zeta_U,\theta^\diamond+\zeta_\theta\}}), W^{-1}(Y_n - H(U_n^{\{U_0^\diamond+\zeta_U,\theta^\diamond+\zeta_\theta\}}))\big),
\end{aligned}$$

where $(U_n^{\{U_0^\diamond+\zeta_U,\theta^\diamond+\zeta_\theta\}})_{n\in[\![0,N_{\Delta t}]\!]}$ is the approximated solution of the dynamics (1) with the initial condition $U_0^\diamond + \zeta_U$ and the parameters $\theta^\diamond + \zeta_\theta$.

Remark 1. *Some remarks are to be made on this section:*

- *The discretized version is presented for convenience only.*
- *Other models for measurement error could be considered, such as proportional models. It is straightforward to include other hypotheses in the least squares function.*
- *In some cases, we may also want to estimate the covariances P_U, P_θ or/and W. They can be easily integrated into the minimization.*
- *In many cases, the variables do not follow a Gaussian distribution. However, after a nonlinear transformation, they may approximate a Gaussian distribution. This is the case when they are nonnegative values that can be transformed with a* log *transform, or bounded values that can be transformed with a* logit *transform.*
- *It is possible to take into account in practice the fact that the data are sampled in time or in space.*

B.2 General strategy

Regarding the estimation strategy, I have gained experience with assimilating real data from biomedical problems into EDO and EDP systems. More specifically, I use very classical strategies in some cases when there are no real difficulties, and I develop very efficient strategies to deal with large systems (such as PDE systems), especially when a population of subjects is available.

Identifiability The minimization of the functional can be considered as an inverse problem. Inverse problems are usually ill-posed, in contrast to the well-posed problems usually encountered in mathematical modeling. There are two types of identifiability problems. We begin with **structural** identifiability. The task of uniqueness is crucial in uncertainty identification, since it is important that the given data be sufficient to uniquely identify the parameter or initial condition that is being sought. This question leads to the proof of cost function injection. We continue with **practical** identifiability. Perturbations in the data (*i.e.* W too large) or insufficient priors (*i.e.* P too large) may lead to an insufficiently robust estimation procedure. Identifiability must be investigated – theoretically, if possible – and, of course, practically.

Classical methods There are many methods to solve this type of problem numerically, such as a non-exhaustive list: gradient descent based methods, stochastic strategies such as Monte Carlo based strategies, or expectation maximisation algorithms. If we consider small ODE systems with no particular difficulty in identifiability, very classical strategies such as the Levenberg-Marquardt method [Lev44, Mar63] or the standard trust-region method [MS83] work very well, see for example [19]. In [15] we have also used a stochastic algorithm based on an unscented transform [JU04] for a static PDE model.

Nonlinear mixed-effects model However, this type of procedure is not sufficiently robust in many situations, such as when measurements are sparse and/or noisy and when there are many local minima. In this case, it is possible to compensate for the uncertainties in a given subject using the knowledge and data we have about a population of subjects of size N_S that follow the same dynamics. More precisely, the nonlinear mixed-effects model consists in pooling all subjects and estimating a global distribution of uncertainties in the population [LW82, Ver97, Lav14, RHM$^+$14]. For example, the uncertainties of the parameters of each subject $j \in [\![1, N_S]\!]$ are divided into two types of uncertainties

$$\zeta_\theta^j = \zeta_\theta^{\text{pop}} + \zeta_\theta^{\text{ind},j}, \tag{3}$$

where $\zeta_\theta^{\text{pop}}$ is common for all the subjects and corresponds to the fixed effect and $(\zeta_\theta^{\text{ind},j})_{j\in[\![1,N_S]\!]}$ are random effects. This strategy was used for example in [17] and [21].

B.3 Sequential approaches

The computational costs of the strategies presented above increase dramatically as soon as one increases the size of the dynamics (PDE or large ODE systems) and/or the size of the population in the case of mixed effects. An alternative is to use sequential data assimilation methods. In this context, System (1) with uncertainties on the initial condition ζ_u and on the parameters ζ_θ is called the *target* model:

$$\left\{\begin{array}{rcll} \partial_t u(t,x) &=& f(t,u(t,x),\theta(t)), & [0,T]\times\Omega, \\ u(0,x) &=& u_0^\diamond(x) + \zeta_u(x), & \Omega, \\ \theta &=& \theta^\diamond + \zeta_\theta. & \end{array}\right. \tag{4}$$

Sequential methods consist in adding a gain operator (also called a filter) denoted by g that defines a new system – called the *observer* system –

$$\left\{\begin{array}{rcll} \partial_t \begin{pmatrix} \hat{u}(t,x) \\ \hat{\theta}(t) \end{pmatrix} &=& \begin{pmatrix} f(t,\hat{u}(t,x),\hat{\theta}(t)) \\ 0 \end{pmatrix} + g(y(t,\cdot),\hat{u}(t,x)), & [0,T]\times\Omega, \\ \hat{u}(0,x) &=& u_0^\diamond(x), & \Omega, \\ \hat{\theta}(0) &=& \theta^\diamond. & \end{array}\right. \tag{5}$$

This filter should be build such that

$$\|\hat{u}(t,\cdot) - u(t,\cdot)\|_{\mathcal{X}} \to_{t\to\infty} 0 \text{ and } \|\theta - \hat{\theta}(t)\|_{\mathbb{R}^{N_\theta}} \to_{t\to\infty} 0.$$

Note that the parameters also have dynamics. These methods can be either of the Kalman type [KB61, JU97, Eve09] – which are optimal in the sense of a certain criterion [Ben71] – or either of the Luenberger type [Lue63, Lue71] or either a combination to obtain effective strategies [CMLT09].

Kalman filters More precisely, Kalman filters have the advantage that they can be fitted to all data and all models once the minimization is rewritten as a least squares functional. In linear cases, this leads to the well-known Kalman-Bucy filter – also called the Kalman filter – originally presented in [KB61]. This original filter is restricted to a linear – model and observation – operators. Various approximations have been developed for nonlinear cases. The most classical choice of gain for nonlinear configurations is the Extended Kalman Filter (EKF). The idea is to replace the nonlinear mappings by their tangent operators. The Unscented Kalman Filter (UKF) [JU97] is an alternative for state and parameter estimation in nonlinear cases. This newer method was originally introduced to circumvent the major computational drawback of the EKF method, namely, the computation of the tangent operators of the model and observation operators. Indeed, UFK does not require differentiation of the model and the discrepancy with respect to the trajectory, but instead relies on *particles* surrounding the trajectory to compute the sensitivities of the system to the data and uncertainties.

However, the Kalman filters have a major drawback, namely the time-consuming computation of the full covariance matrix (of size $(N_{\Delta x} + N_\theta) \times (N_{\Delta x} + N_\theta)$). A first strategy is to use a reduced order for the covariance operators. A typical example of reduced order is to restrict the uncertainty space to the parameter space. The main idea behind the reduced order strategy is to consider a SVD decomposition of the covariance matrix

$$P = LQ^{-1}L^{\mathrm{T}},$$

with Q an invertible matrix of small size r and L an extension operator.

For linear operators, the authors show in [MCLT08] that this decomposition is stable in time and that the equation of the covariance matrix reduces to two systems with admissible computation times. Extensions of these two systems have been developed for nonlinear cases. For example, one can cite the EKF of reduced order (RoEKF) [MCLT08] and the UKF of reduced order (RoUKF) [MC11a]. It should be noted that a specific analysis of the error generated by these nonlinear Kalman filters is required.

Luenberger filters An alternative method to the reduced-order strategy is to build a filter that is not based on an optimal criterion. This idea – originally introduced by Luenberger [Lue63, Lue71] and also called nudging in the PDE community [HA76, SS90] -– is based on defining a filter that is as simple as possible so that the error between the observed trajectory and the observer system tends to zero. However, these Luenberger observers must be adapted to any dynamics and are not compatible with parameter estimation, since – by definition – the parameters have no dynamics.

Joint state and parameters estimation One strategy is to combine the sequential strategies presented below to propose a joint state and parameter estimation. To do this, two different gains – one for the state and one for the parameters – must be defined. A Luenberger filter is considered for the state space, and the small dimension of the parameter space allows the use of an optimal reduced-order filter, typically a RoUKF. More precisely, the mean and covariance operators are computed from the empirical mean and empirical covariance based on N_σ sample points – the so-called sigma points [JU97]. Different choices of sigma-points can be used in practice, see [JU97, MC11a] for more details. We define for given sets of coefficients $\boldsymbol{\alpha} = (\alpha_j)_{1\leq j\leq N_\sigma}$ and particles $(v^{(j)})_{1\leq j\leq N_\sigma}$, the empirical mean and covariance by

$$\mathbb{E}_{\boldsymbol{\alpha},N_\sigma}(v_{(\cdot)}) \overset{\text{def}}{=} \sum_{j=1}^{N_\sigma} \alpha^i v^{(j)},\ \mathbb{C}\mathrm{ov}_{\boldsymbol{\alpha},N_\sigma}(v_{(\cdot)}, w_{(\cdot)}) \overset{\text{def}}{=} \sum_{j=1}^{N_\sigma} \alpha_j \Big(v^{(j)} - \mathbb{E}_{\boldsymbol{\alpha},N_\sigma}(v_{(\cdot)})\Big)\Big(w^{(j)} - \mathbb{E}_{\boldsymbol{\alpha},N_\sigma}(w_{(\cdot)})\Big)^{\mathrm{T}}.$$

The full algorithm (spatial discretized version and explicit Euler scheme) reads

Initialization

Priors on initial conditions: $\hat{U}_0^+$

Priors on parameters: $\hat{\theta}_0^+$

Priors on the covariance matrix of the parameters: Q_0

Initial extension matrix: L_0

Error covariances: $(W_n)_{n\in[\![0,N_{\Delta t}]\!]}$

Define sigma points: $\boldsymbol{e}^{(j)},\ \forall j \in [\![1, N_\sigma]\!]$

Loop $\forall n \in [\![0, N-1]\!]$

[1] *Sampling*

$$\begin{pmatrix}\hat{U}_n^{(j)+}\\ \hat{\theta}_n^{(j)+}\end{pmatrix} = \begin{pmatrix}\hat{U}_n^{+}\\ \hat{\theta}_n^{+}\end{pmatrix} + \delta L_n \sqrt{(Q_n^+)^{-1}}\,\boldsymbol{e}^{(j)},\ \forall j \in [\![1, N_\sigma]\!]$$

[2] *Prediction (Forward)*

$$\begin{pmatrix}\hat{U}_{n+1}^{(j)-}\\ \hat{\theta}_{n+1}^{(j)-}\end{pmatrix} = \begin{pmatrix}\hat{U}_n^{(j)+}\\ \hat{\theta}_n^{(j)+}\end{pmatrix} + \Delta t \begin{pmatrix}F(t_n, \hat{U}_n^{(j)+}, \hat{\theta}_n^{(j)+})\\ 0\end{pmatrix},\ \forall j \in [\![1, N_\sigma]\!] \tag{6a}$$

[3] *Correction (Analyze)*

<u>State Correction</u>

$$\begin{pmatrix}\hat{U}_{n+1}^{(j)+-}\\ \hat{\theta}_{n+1}^{(j)+-}\end{pmatrix} = \begin{pmatrix}\hat{U}_{n+1}^{(j)-}\\ \hat{\theta}_{n+1}^{(j)-}\end{pmatrix} + \Delta t \begin{pmatrix}G\big(\hat{U}_{n+1}^{(j)-}, Y_n\big)\\ 0\end{pmatrix},\ \forall j \in [\![1, N_\sigma]\!] \tag{6b}$$

<u>Parameter Correction</u>

$$L_{n+1} = \mathbb{C}\mathrm{ov}_{\boldsymbol{\alpha},N_\sigma}\big(\boldsymbol{e}_{(\cdot)}, \hat{U}_{n+1}^{(\cdot)+-}\big)$$

$$\Lambda_{n+1} = \mathbb{C}\mathrm{ov}_{\boldsymbol{\alpha},N_\sigma}\big(\boldsymbol{e}_{(\cdot)}, (H(\hat{U}_{n+1}^{(\cdot)+-}) - Y_n)\big)$$

$$Q_{n+1} = \mathbb{C}\mathrm{ov}_{\boldsymbol{\alpha},N_\sigma}\big(\boldsymbol{e}_{(\cdot)}, \boldsymbol{e}_{(\cdot)}\big) + (\Lambda_{n+1})^{\mathrm{T}}(W_n)^{-1}\Lambda_{n+1}$$

$$K_{n+1} = L_{n+1}(Q_{n+1})^{-1}\Lambda_{n+1}(W_n)^{-1}$$

$$\begin{pmatrix}\hat{U}_{n+1}^{+}\\ \hat{\theta}_{n+1}^{+}\end{pmatrix} = \begin{pmatrix}\mathbb{E}_{\boldsymbol{\alpha},N_\sigma}(\hat{U}_{n+1}^{(\cdot)+-})\\ \mathbb{E}_{\boldsymbol{\alpha},N_\sigma}(\hat{\theta}_{n+1}^{(\cdot)+-})\end{pmatrix} + K_{n+1}\big(Y_n - \mathbb{E}_{\boldsymbol{\alpha},N_\sigma}(\hat{U}_{n+1}^{(\cdot)+-})\big) \tag{6c}$$

One can notice regarding the algorithm that the time evolution of the parameters is conditioned only by the Kalman filter (6c), which means

$$\hat{\theta}_{n+1}^{(j)+-} = \hat{\theta}_{n+1}^{(j)-} = \hat{\theta}_{n}^{(j)-},\ \forall j \in [\![1, N_\sigma]\!],$$

while the state evolves first with the model dynamics (prediction (6a)), then with the state observer (state correction (6b)), and finally by the Kalman filter (parameter correction (6c)). This last step is fundamental to integrate the sensitivity of the parameters to the state and is the key point of the Reduced-order Unscented Kalman Filter (RoUKF) introduced in [MC11b].

In summary, the general strategy for applying joint state and parameter estimation using observers is divided into two steps:

(1) Construction and mathematical validation of a Luenberger observer assuming the uncertainties are reduced to the initial condition ($\zeta_\theta = 0$ in System (4)).
This consists of defining a gain observer for the state – denoted by $\gamma\, g_u$ – and proving the decrease of the energy of the *error* model corresponding to the system verified by $\tilde{u} = u - \hat{u}$,

$$\left\{ \begin{array}{rcll} \partial_t\, \tilde{u}(t,x) & = & f(t,u(t,x),\theta) - f(t,\hat{u}(t,x),\theta) - \gamma\, g_u(h(u(t,x)),\hat{u}(t,x)), & [0,T]\times\Omega, \\ \tilde{u}(0,x) & = & \zeta_u(x), & \Omega. \end{array} \right. \tag{7}$$

The strictly positive constant γ – called the parameter gain – balances the impact of the model correction using the data depending on the level of confidence in them. This justifies the *nudging* terminology used in the data assimilation community [LL08]. The gain is therefore typically adjusted by considering the level of noise in data, but also by evaluating the increased stability introduced by the correction. Sometimes an excessively large gain can be counter-productive – see a striking example in [MCLT09] – and in any case should eventually be optimized – see [VLDP03, SB93, ZNLD92].

(2) Combination of the Luenberger observer with a Kalman filter using for example Algorithm (6).

Contributions concerning sequential strategies In my research I have been involved in the development and theoretical investigation (proof of convergence) of Luenberger observers, but also in the application of this type of strategies. More specifically, I have acquired expertise in the development of estimation strategies for front propagation models – such as reaction-diffusion models, eikonal equations, or general hyperbolic/elliptic models – and front position data. Such models are considered in various applications, such as cardiac electrophysiology, wildfire propagation, and tumor growth modeling.

During my PhD, we proposed a Luenberger observer for reaction-diffusion models, validated it mathematically, and illustrated it numerically with synthetic data. Recent works are directly related to this observer. In the context of cardiac electrophysiology, this observer has been applied to real data [12] and a novel correction term based on topological gradients has been integrated to track solutions of complex patterns [5]. In the context of wildfire spread, a version compatible with an eikonal equation was proposed and illustrated with synthetic data in [9] and then with real data in [14]. In this context, a version compatible with a Lagrangian front-tracking model was also developed [13]. Finally, in the context of tumor growth, a Luenberger observer – inspired by our previous work – was developed, mathematically studied (proof of convergence), and numerically illustrated, see [20] for more details.

Another important research result concerning data assimilation is the design of a population-based Kalman filter. Our objective is to propose a strategy to deal with population-based estimation as introduced previously (see Eq. (3)) for large systems as for example PDE. To do so, we first define population-based estimators through maximum likelihood estimation. We then develop an equivalent robust sequen-

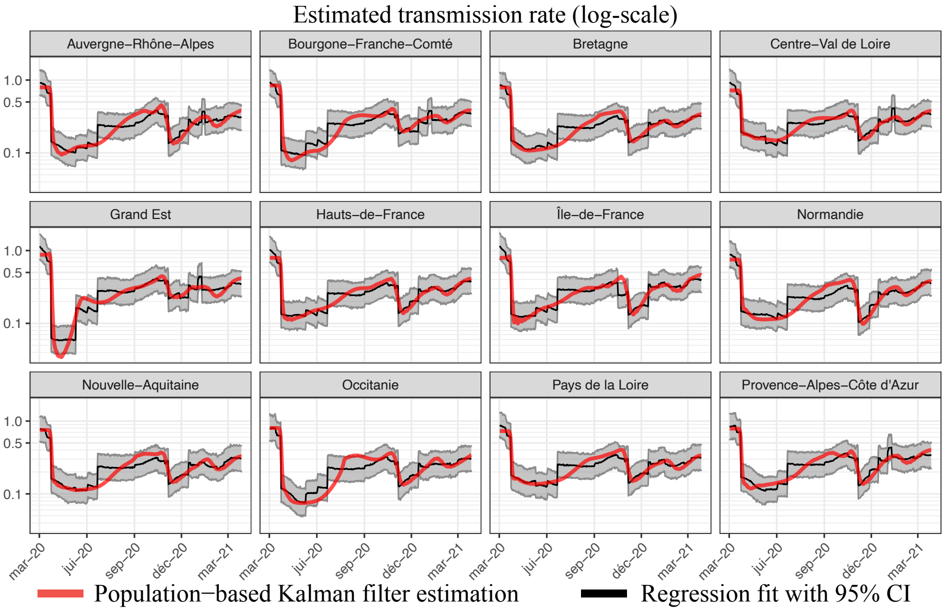

Covariate	Modification of the transmission rate	
NPIs		
Lockdown 1 - delay of 7 days	-78% [-82% ; -74%]	↘
Post lockdown 1 - Phase 1	-54% [-56% ; -52%]	↘
Post lockdown 1 - Phase 2	-48% [-50% ; -47%]	↘
Lockdown 2 - delay of 7 days	-54% [-57% ; -49%]	↘
Lockdown 2 with opened shops	-51% [-53% ; -49%]	↘
Closing schools	- 7% [- 8% ; - 5%]	↘
Barrier gestures	-46% [-48% ; -44%]	↘
Curfew at 6PM	-30% [-33% ; -26%]	↘
Curfew at 8PM	-28% [-31% ; -25%]	↘
Bar & restaurant closure (ref. $W = 0$)	-10% [-13% ; - 8%]	↘
Bar & restaurant closure, summer (vs. ref.)	- 8% [-11% ; - 4%]	↘
winter (vs. ref.)	-11% [-14% ; - 8%]	↘
Other factors		
100% of VoC circulating	22% [15% ; 28%]	↗
Weather effect during summer (ref. $W = 0$)	-22% [-24% ; -21%]	↘
during winter (ref. $W = 0$)	10% [9% ; 11%]	↗

Figure 2 – Top: Estimation of transmission rate with a population-based Kalman filter for the 12 French regions (red) and regression with seasonal weather conditions, the proportion of variants, and government measures (black). Bottom: Estimated associations with transmission rates.

tial estimator for large populations based on filtering theory that sequentially integrates data. Finally, we limit the computational complexity by defining a reduced-order version of this population-based Kalman filter that clusters subpopulations with common observational backgrounds. The performance of the resulting algorithm is evaluated against classical pharmacokinetics benchmarks. An important advantage of the developed method is that model errors can be easily included and estimated.

In [22], the strategy was used to assess associations between nonpharmaceutical interventions – such as lockdowns, curfews, or school closures – implemented to control the COVID -19 pandemic and transmission rates. The challenge was to work without prior knowledge of the dynamics of transmission rates and to use only hospitalization data, which are the only accurate data available. Figure 2 illustrates the results, which were used by the French government to adjust the measures and also cited in French newspapers, see for example [Ros21, Hec21, Don21].

However, our first goal in developing a population-based Kalman filter was to overcome the challenge of a nonlinear mixed-effects strategy for large systems such as PDE systems. Indeed, the nonlinear mixed-effects strategy is not applicable in practice for PDE systems due to its high computational cost. For this reason, we propose in [28] a population-based estimation for PDE systems. The errors arising from the initial conditions are controlled by a Luenberger observer that corrects for the state, and the parameters are estimated using a reduced-order population-based Kalman filter restricted to the parameter space. This sophisticated method for solving this difficult problem is based on two important existing methodological strategies: (1) the population-based Kalman filter presented in [23], and (2) the joint state-parameter estimation proposed in [CMLT09]. The performance of the resulting algorithm is evaluated on tumor spheroid electroporation (synthetic and real data), see Section 3.3.4 for details.

C Main contributions

This manuscript presents my research based on my three main areas of interest: Cardiac Electrophysiology, Tumor Growth, and Electroporation Modeling. Despite this chapter-by-chapter presentation, there are many interactions – highlighted in the manuscript – between these areas. However, before going into detail in the following chapters, I provide an overview of the major contributions in this section.

C.1 Contributions to cardiac electrophysiology

Cardiac electrophysiology is devoted to the study of the electrical wave that precedes contraction of the heart muscle. In Chapter 1, I present my significant contributions in this particular field. The following points serve as a concise summary of these contributions:

(1.1) Provide a mathematical analysis of the periodic homogenization process leading to the macroscopic bidomain model. In this work, we fill a gap in the literature by providing a mathematical analysis of the macroscopic bidomain model based on *2-scale convergence*. Our analysis is exhaustive in the sense that we provide *existence and uniqueness*, nondimensionalization, and *convergence* results within the same mathematical framework. This work, published in [8], is presented in Section 1.2.

(1.2) Extend the microscopic bidomain model to a microscopic bidomain model that accounts for cardiac muscle deformations. Our goal is to study the effects of cardiac deformations on cardiac electrophysiology. We go back to the origins of the bidomain model to integrate the effects directly into the *conservation laws* at the microscopic scale. This contribution is presented in Section 1.1.

(1.3) Determine a macroscopic bidomain model that integrates the cardiac deformations. Thanks to our understanding of the theoretical homogenization of classical bidomain equations, we perform a *formal homogenization* to determine the effects of mechanical deformations on the macroscopic equations. This work is presented in Section 1.3 and has been published (with Contribution 1.2) in [11].

(1.4) Assimilate depolarization front data. The previous works have given us an accurate understanding of direct models of cardiac electrophysiology. For the model to be truly descriptive or even predictive for a given patient, we need to control for uncertainties arising from the initial conditions or parameters of the model using the available medical data of this patient. In this part presented in Section 1.4, we worked with depolarization front data and developed an efficient Luenberger observer. This work has been published in two proceedings [5, 12].

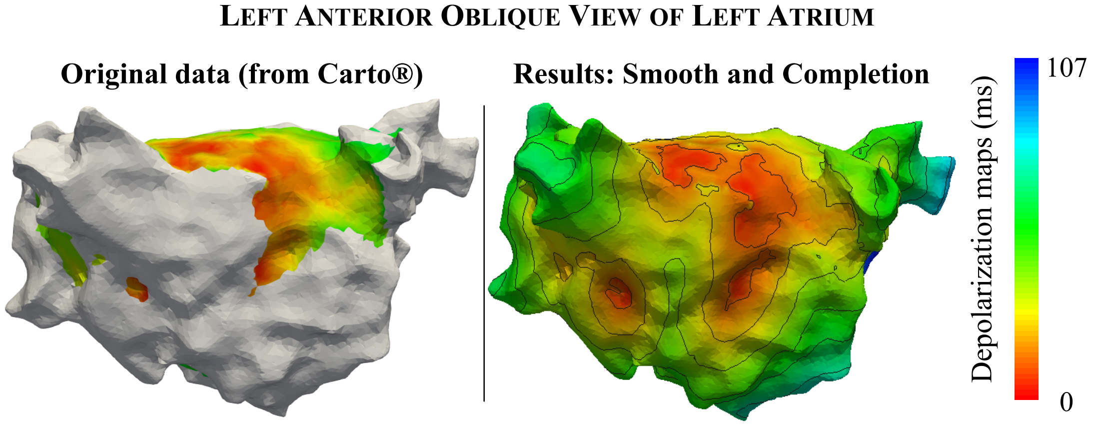

Figure 3 – Depolarization maps of a patient left atrium. Left: Data extracted with Carto$^{®}$ system. Right: Completion of the map using a Luenberger observer integrating depolarization fronts.

Illustrative example Our hard work on the bidomain model (Contributions 1.1, 1.2, and 1.3) has allowed us to gain a very good understanding of the direct model and, in particular, whether or not we need to consider mechanical deformations depending on the pathology of interest. A direct application of the observer we developed (Contribution 1.4) is its ability to smooth and complete activation maps. Figure 3 illustrates the potential of our approach on the left atrium of a patient. The left side of the figure shows the measured map of activation times corresponding to the times at which the depolarizing front reaches the area. This map is not smooth and is spatially incomplete due to the difficulty of the recording procedure. Our approach – a combination of a well-chosen PDE system and an efficient data assimilation strategy – allows us to smooth and complete the activation maps, as shown on the right side of Figure 3. A complete and realistic map is very useful for clinicians to identify pathological areas that need to be ablated.

C.2 Contributions to tumor growth

Chapter 2 presents my work on tumor growth whose the main contributions are:

(2.1) Select mechanistic models for tumor growth. Unlike cardiac electrophysiology, where there is a gold standard, there is no such consensus for modeling tumor growth. One explanation is that the unknowns of the system and the conservation laws are still open questions because of the many uncertainties about how tumor growth works. The models used by the MONC team are based on **advection equations** that model the time evolution of the densities of healthy and tumor cells.

(2.2) Develop an efficient estimation strategy to fit a tumor growth model to patients with meningioma. Tumor growth models need to be fitted to each patient to obtain predictive simulations. In this context, many medical data (volume, texture, shape of lesions, etc.) can be used to determine the parameters of the model. We developed an innovative strategy that combines a *0D scale model* and an *estimation strategy* based on nonlinear mixed effects. This strategy has been illustrated on a large cohort of meningiomas (benign brain tumors) providing reliable predictions of their volume and shape. This work – presented in Section 2.2 was highlighted by two publications [17, 24].

(2.3) Adapt this strategy to tumors with time-evolving shapes. The strategy described above is not effective when the shape of the tumor changes over time. In this work, a *Luenberger-type observer* has been *developed* and *mathematically analyzed* to solve this problem. This work – which is presented in Section 2.3 – has been published in [20].

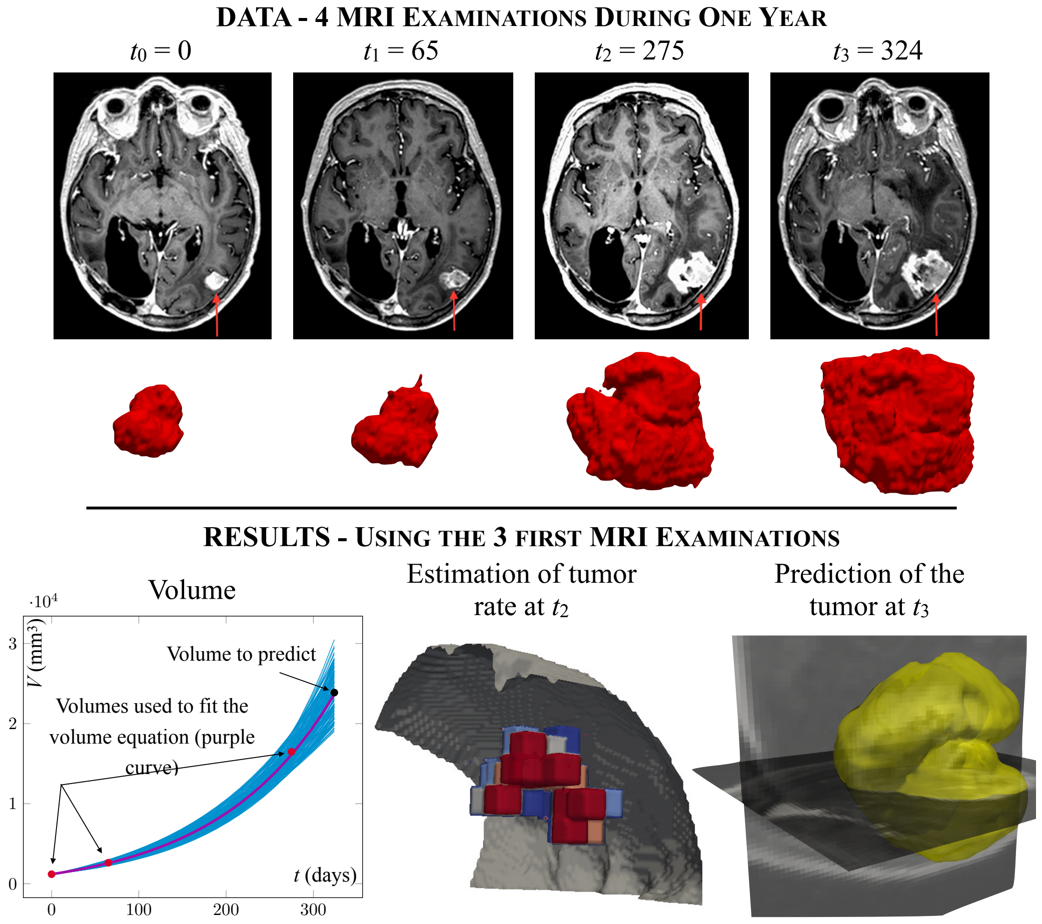

Figure 4 – Top: MRI examinations of a brain metastasis of a patient (HM Hospitales, Spain) at 4 different time points (given in days) and the 3D segmented tumors. Bottom: Volume description and prediction (left), growth rate estimation (middle) and shape prediction.

Illustrative example The accuracy of the model considered, despite its simplicity (contribution 2.1) in combination with a 0D scale model (contribution 2.2) and a Luenberger observer (contribution 2.3), allows us to describe and predict the volume and shape of a tumor. Our strategy is based on our ability to build a spatially distributed growth rate. Figure 4 illustrates the potential of our strategy on a patient brain metastasis. At the top, one can see the data and the segmented 3D tumors. At the bottom, one can see the volume evolution over time with a prediction of the last time point, the estimated spatial distribution of the growth rate, and the prediction of the shape of the tumor.

C.3 Contributions to electroporation modeling

Chapter 3 presents my work on modeling the electroporation phenomenon. Electroporation is the application of pulsed electric fields of high intensity and short duration to cells using catheters. The goal is to create defects – called pores – in the cell membrane. Reversible electroporation allows the introduction of non-permeable molecules into living cells without directly killing them, while irreversible electroporation leads to the death of cells in the target area. My mathematical contributions to this application area are as follows:

(3.1) Use mathematical modeling to better understand how the membrane becomes permeable. The goal is to develop mathematical approaches to track membrane dynamics. In an initial work presented in Section 3.1.1, we develop a robust calibration strategy for a 4-electrode experimental setup to measure the impedance of cellular myotubes exposed to electrical pulses, and we design and parameterize an equivalent circuit model. This allows us to quantify the short-term behavior of membrane conductance a few seconds after the pulse. In a second work presented in Section 3.1.2, we develop a PDE model of membrane electroporation that combines membrane water content and electric potential through a microscopic bidomain model. An innovative and efficient numerical strategy allows us to perform numerical simulations of pore formation on the membrane. These two papers have been published in [25] and [29].

(3.2) Compare and improve tissue-scale electroporation models. In a first work presented in Section 3.2.1, we compare solutions of different electroporation models from the literature and investigate their parameterizations using bioelectrical measurements on rabbit livers performed by Sel et al. [SCB+05]. In a second work presented in section 3.2.2, the choice of boundary conditions for passive electrodes – very conductive and thin – is investigated. In contrast to the active electrodes, which specify either the potential or the current (Dirichlet or Neumann conditions), the value of the equipotential of the inactive electrodes is an unknown factor of the PDE, regardless of the model considered. This leads to a nonlocal flux constraint along the conductive interface, the so-called floating potential problem. We develop a model to solve this problem in the context of electroporation. These two works have been published in [15, 18].

(3.3) Study the effects of electroporation on tumor growth. The aim of this work is to study the specificities of the growth of cancer cells in spheroids exposed to a pulsed electric field. Thanks to an advanced mathematical model (within the framework of the modeling presented in Chapter 2) and relevant estimation strategies, our modeling allows characterizing the growth of multicellular spheroids after permeabilization by an electric field pulse. This work, presented in Section 3.3 was published in [21].

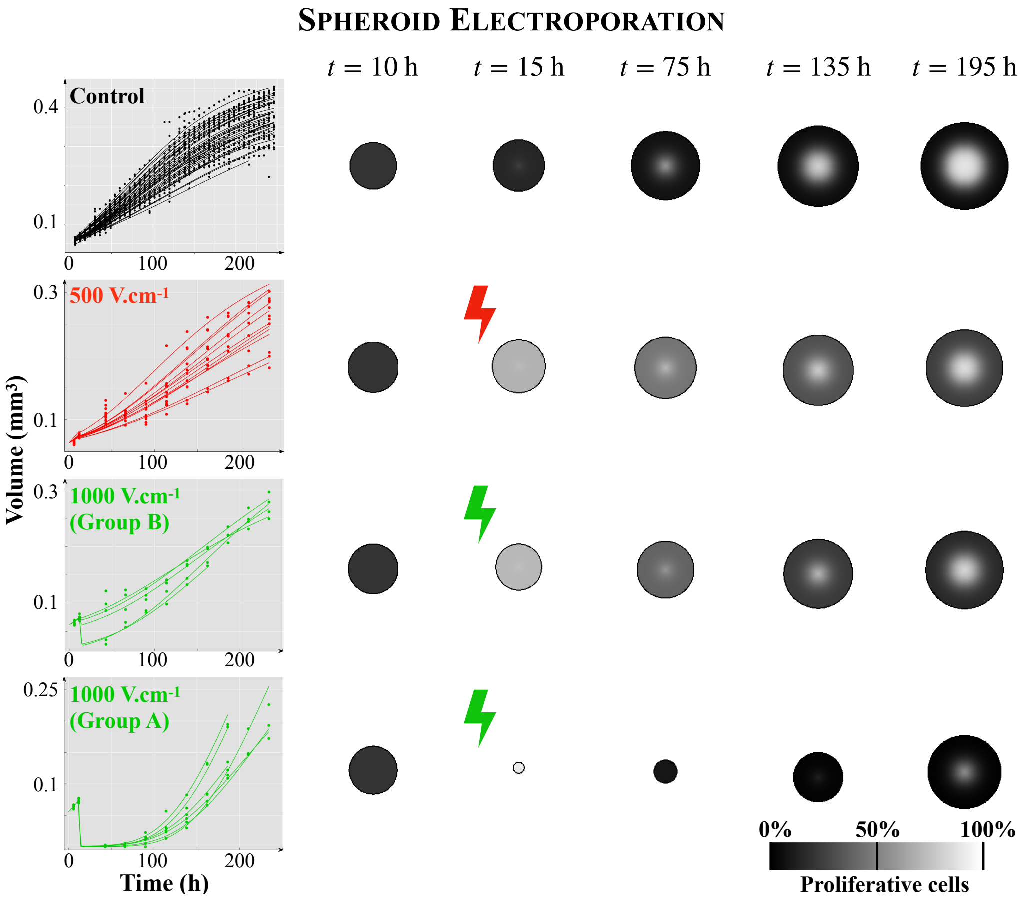

Figure 5 – Left: Fits of estimated volumes to measured volumes. Right: PDE simulation of the spheroids. Each column corresponds to a different case: control, electroporation field of 500V.cm^{-1}, electroporation field of 1000V.cm^{-1} (group B), electroporation field of 1000V.cm^{-1} (group A).

Illustrative example Our acquired knowledge of electroporation modeling (contributions 3.1 and 3.2) combined with a realistic tumor growth model (contribution 2.1) and relevant estimation strategies allowed us to characterize the growth of 3D *in vitro* tumors – called multicellular spheroids – after electroporation. The use of a PDE system allowed us to determine the percentage of cells destroyed and the percentage of cells whose functioning was altered by the effect of electroporation for different values of the electrical field. Figure 5 summarizes the results. It can be seen that for an electrical field close to 1000 V.cm^{-1} (see group A), the increase of the electrical field seems to boost the resumption of spheroid growth. This is a recurrent problem that also occurs in clinics, where clinicians observe either efficient treatment with reduced tumor growth or tumor relapse [SNdJ^{+}14]. The advantage of our model is that we can determine the trend of tumor growth shortly after electroporation. So, in practice, this model can be used to determine which patients have been treated efficiently and which patients are on the path to relapse. In this last case, this would alert the physician that the treatment was not efficient and that another electroporation cycle is needed to remove the tumor again.

Chapter 1

Contributions to cardiac electrophysiology

The innovative work presented in this chapter has been published in two articles [8, 11] and two proceedings [5, 12].

Introduction

The purpose of this chapter is to present my mathematical contributions to cardiac electrophysiology since the end of my PhD. Cardiac electrophysiology is the study of the electrical wave which precedes the cardiac contraction. Modeling of cardiac electrophysiology is a very mature field of research, and the so-called bidomain model [Tun78] is now considered the reference model, while some approximations to it are often considered, in particular the so-called monodomain model [Sac04, CFPT05], and also some specific forms of eikonal equations [Kee91, KS04, KCM^{+}10]. These macroscopic bidomain equations are the result of a complex homogenization process starting from a microscopic level associated with the cellular scale, where intracellular and extracellular domains – separated by the cell membrane – can be defined geometrically [NK93, CFS02, RC11].

My mathematical contributions aim to fill in some important gaps with respect to the very classical bidomain model, which can be summarized in the following points:

(1) **Provide a complete mathematical analysis of the periodic homogenization procedure that leads to the macroscopic bidomain model.** The aim of this work is to fill a gap in the literature by providing a complete mathematical analysis based on 2-scale convergence theory of the homogenization procedure that leads to the macroscopic bidomain model. Our analysis is exhaustive in the sense that we provide existence and uniqueness results, nondimensionalization of the equations and 2-scale convergence results – in particular, for the non-linear terms supported on the membrane surface – in the same mathematical framework. The results have been published in [8]. In this work, the cardiac mechanical deformations are neglected.

(2) **Extend the microscopic bidomain model by a microscopic bidomain model that considers deformations of the heart muscle.** Our objective is to examine the complete coupling between cardiac electrophysiology and mechanics, since this has not yet been fully elucidated. More specifically, the effect of mechanics on ionic models – *i.e.* ordinary differential equations designed to describe the local exchange of ions between different cellular compartments, including through cell membranes – has received considerable attention, see [KNP08, NP04], but in contrast, the effects on the conservation laws (of charges and ions) governing the spatial variations of all quantities of interest have not been

so actively studied before our work. We refer to [CFPS16] for a detailed overview of the latter aspect, see also [CFPS17, CFPS18, FPP$^+$16, QLRRB17]. To do this, it is essential to go back to the origins of the bidomain model to finally clarify the effects of mechanical deformations on it. This work allows to determine a bidomain model at the microscopic level *i.e.* at the cellular level including the effects of the mechanical deformations.

(3) **Determine a macroscopic bidomain model including the effects of the mechanical deformations.** Thanks to our understanding of the theoretical homogenization of the classical bidomain equations, we perform a formal homogenization to determine how the effects of mechanical deformations modify the macroscopic equations. The two last points have been published in [11].

(4) **Integrate data corresponding to the sparse location of the depolarization front into the macroscopic bidomain model**. An accurate understanding of the direct model has been achieved thanks to the previous works. For the model to be truly descriptive or even predictive for a given patient, the uncertainties arising from, among other things, the initial conditions or the parameters of the model must be estimated or controlled using the medical data available for that patient. In this work, we focus on data corresponding to depolarization fronts and we manage them with sequential data assimilation methods. The results have been published in [5, 12].

Since the second contribution allows us to explain the origin of the microscopic bidomain model – even without including the deformations of the myocardium –, we start with this point, see Section 1.1. In Section 1.2, the mathematical analysis of the periodic homogenization procedure leading to the macroscopic bidomain model – corresponding to the first contribution – is presented. In this section, the mechanical deformations are neglected, but it allows to present the homogenization procedure leading to the macroscopic bidomain model, which allows a better illustration of the formal homogenization performed to obtain the macroscopic bidomain model including the heart deformations presented in Section 1.3 corresponding to the third contribution. Some numerical illustrations are included. These simulations show, first, that we are now able to obtain very realistic simulations of cardiac electrophysiology, and second, they allow quantification of the effects of mechanical deformations on cardiac electrophysiology. Based on this very good understanding of the direct model, Section 1.4 – corresponding to the fourth contribution – presents our strategy for dealing with the uncertain quantities that must be preserved when performing model simulations for a given patient.

1.1 Microscopic bidomain model

The purpose of this section is to recall the microscopic model – governing ionic motion and electric potentials – underlying the bidomain model and to derive extensions of these equations to account for mechanical deformations. This section is a summary of Section 2 of our article [11]. The novelty arises from the consideration of mechanical deformations.

1.1.1 Definitions and notation

The geometric domain occupied by the cardiac tissue at any time t is denoted by $\Omega(t)$, with boundary $\partial\Omega(t)$. We use a Lagrangian description, for which we introduce a reference configuration Ω_0 – not necessarily corresponding to $\Omega(0)$ – and the one-to-one deformation mapping $\underline{\phi}$ from the reference configuration to the current configuration, giving the position of each material point over time, $\underline{\phi} : \overline{\Omega}_0 \times [0, T] \to \mathbb{R}^3$ such that $\underline{x}(t) = \underline{\phi}(\underline{\xi}, t)$. We define the displacement $\underline{y}$ by $\underline{y}(\underline{\xi}, t) = \underline{x} - \underline{\xi} = \underline{\phi}(\underline{\xi}, t) - \underline{\xi}$, and the deformation

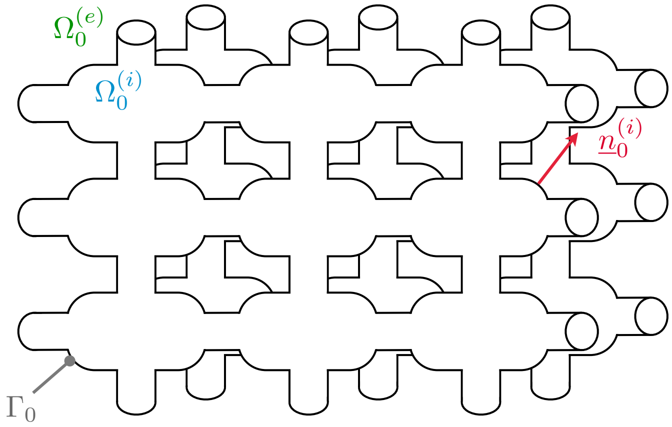

Figure 1.1 – Intracellular and extracellular regions of the heart.

gradient by $\underline{\underline{F}}(\underline{\xi}, t) = \vec{\nabla}_{\vec{\xi}}\, \underline{\phi} = \underline{\underline{1}} + \vec{\nabla}_{\vec{\xi}}\, \underline{y}$. We will assume that $J = \det \underline{\underline{F}}$ is strictly positive for any $\underline{\xi} \in \overline{\Omega}_0$, meaning that the deformation mapping does not degenerate anywhere and that $\underline{\underline{F}}$ is invertible.

In fact, this geometric domain Ω_0 is decomposed into two parts, *i.e.* $\Omega_0^{(i)}$ the intracellular region and $\Omega_0^{(e)}$ the extracellular region, see Figure 1.1, with the associated regions $\Omega^{(i)}(t)$ and $\Omega^{(e)}(t)$ in the deformed configuration. Geometrically, $\Omega_0^{(i)}$ and $\Omega_0^{(e)}$ are two connected domains verifying $\overline{\Omega}_0 = \overline{\Omega}_0^{(e)} \cup \overline{\Omega}_0^{(i)}$ and $\Omega_0^{(e)} \cap \Omega_0^{(i)} = \varnothing$. We suppose that the membrane separating the two regions $\Gamma_0 = \partial\Omega_0^{(e)} \cap \partial\Omega_0^{(i)}$ is regular, and we define $\underline{n}_0^{(i)}$ and $\underline{n}_0^{(e)}$ as the unit outward-pointing normal vectors associated with $\Omega_0^{(e)}$ and $\Omega_0^{(i)}$, respectively, with of course $\underline{n}_0^{(i)} = -\underline{n}_0^{(e)}$. Accordingly, $\underline{n}^{(e)}(t)$ and $\underline{n}^{(i)}(t)$ denote the unit normal vectors on the deformed membrane $\Gamma(t)$. In what follows, we will often drop the explicit time dependence in the notation pertaining to the deformed configuration, as in $\Omega^{(e)}$ and $\Omega^{(i)}$.

1.1.2 General model of ion motion

In this section, we give an overview of the derivation of the equations governing ionic motion in the intracellular and extracellular regions, namely, the so-called Nernst-Planck-Poisson equations, see e.g. [Kir10]. We consider ion motion in an isothermal medium with negligible solvent flows. We suppose that we have $N^{(i)}$ and $N^{(e)}$ different species of mobile ions in the intra- and extracellular regions, respectively. The individual conservation gives,

$$\partial_t c_k^{(\alpha)}{}_{|_{\underline{x}}} + \vec{\nabla}_{\vec{x}} \cdot \underline{\jmath}_k^{(\alpha)} = 0,\ k = 1, \ldots, N^{(\alpha)},\ \alpha = i, e, \tag{1.1}$$

where $c_k^{(\alpha)}$, $\underline{\jmath}_k^{(\alpha)} = c_k^{(\alpha)}\, \underline{v}_k^{(\alpha)}$ are the concentration and the flux of the k-th ionic species, respectively, in the given region, and with $\underline{v}_k^{(\alpha)}$ the corresponding velocity. Denoting by $\underline{v}_{k,r}^{(\alpha)}$ the relative velocity of the ions with respect to the substrate, we will use the decompositions

$$\underline{v}_k^{(\alpha)} = \underline{v}_s + \underline{v}_{k,r}^{(\alpha)}, \quad \underline{\jmath}_k^{(\alpha)} = \underline{\jmath}_{k,s}^{(\alpha)} + \underline{\jmath}_{k,r}^{(\alpha)} = c_k^{(\alpha)}\big(\underline{v}_s + \underline{v}_{k,r}^{(\alpha)}\big).$$

The total charge density $\rho^{(\alpha)} = \rho_b^{(\alpha)} + \mathrm{F} \sum_k z_k c_k^{(\alpha)}$ – with $\rho_b^{(\alpha)}$ the background charge density, F the

Faraday constant, and z_k the signed number of elementary charges carried by this ion – is related to the electric field $\underline{E}^{(\alpha)}$ by the Gauss law of electrostatics

$$\vec{\nabla}_{\vec{x}} \cdot \underline{E}^{(\alpha)} = \frac{\rho^{(\alpha)}}{\varepsilon_0 \varepsilon_s} = \frac{1}{\varepsilon_0 \varepsilon_s} \Big(\rho_b^{(\alpha)} + \mathrm{F} \sum_{k=1}^{N^{(\alpha)}} z_k c_k^{(\alpha)} \Big), \tag{1.2}$$

with ε_s the relative permittivity of the medium, and ε_0 the permittivity of free space. In order to determine the flux $\underline{\jmath}_k^{(\alpha)} = c_k^{(\alpha)} \underline{v}_k^{(\alpha)}$ of the species k, we apply Newton's second law to an ion of this species. The forces undergone by this ion are:

- the friction force $\underline{F}_k^{\text{frict}} = -\frac{\underline{v}_{k,r}^{(\alpha)}}{m_k}$, where m_k denotes the so-called mobility of the ion;
- the electric force $\underline{F}_k^{\text{elec}} = z_k q \underline{E}^{(\alpha)}$, with q the charge of a proton;
- the diffusion force (Einstein's diffusion law) $\underline{F}_k^{\text{dif}} = -\frac{k_B T}{c_k^{(\alpha)}} \vec{\nabla}_{\vec{x}}\, c_k^{(\alpha)}$, where k_B denotes the Boltzmann constant and T the absolute temperature.

Neglecting the inertia and using the equilibrium equation $\underline{F}_k^{\text{dif}} + \underline{F}_k^{\text{frict}} + \underline{F}_k^{\text{elec}} = 0$, we infer the Nernst-Planck equation for the flux $\underline{\jmath}_k^{(\alpha)} = c_k^{(\alpha)} \underline{v}_k^{(\alpha)}$ of the species k,

$$\underline{\jmath}_k^{(\alpha)} = -D_k \Big(\vec{\nabla}_{\vec{x}}\, c_k^{(\alpha)} - \frac{q z_k c_k^{(\alpha)}}{k_B T} \underline{E}^{(\alpha)} \Big) + c_k^{(\alpha)} \underline{v}_s, \tag{1.3}$$

with $D_k = m_k k_B T$ the diffusion coefficient of the species k. The electric field is related to an electric potential u by $\underline{E}^{(\alpha)} = -\vec{\nabla}_{\vec{x}}\, u^{(\alpha)}$. Using (1.1), (1.2) and (1.3), we finally obtain

$$\left|\begin{array}{l} \text{Charge conservation : } \partial_t c_k^{(\alpha)}{}_{|_{\underline{x}}} = -\vec{\nabla}_{\vec{x}} \cdot \underline{\jmath}_k^{(\alpha)}, \ \forall k \in [\![1; N^{(\alpha)}]\!], \\ \text{Drift-diffusion flux : } \underline{\jmath}_k^{(\alpha)} = -D_k \Big(\vec{\nabla}_{\vec{x}}\, c_k^{(\alpha)} + \dfrac{q z_k c_k^{(\alpha)}}{k_B T} \vec{\nabla}_{\vec{x}}\, u^{(\alpha)} \Big) + c_k^{(\alpha)} \underline{v}_s, \ \forall k \in [\![1; N^{(\alpha)}]\!], \\ \text{Gauss law : } \Delta_{\underline{x}}\, u^{(\alpha)} = -\dfrac{1}{\varepsilon_0 \varepsilon_s} \Big(\rho_b^{(\alpha)} + \mathrm{F} \displaystyle\sum_{k=1}^{N^{(\alpha)}} z_k c_k^{(\alpha)} \Big). \end{array}\right. \tag{1.4}$$

This system is an extension of the Nernst-Planck-Poisson system, with the additional term $c_k^{(\alpha)} \underline{v}_s$ results from the substrate motion.

1.1.3 Electroneutrality, transmembrane equations and summary of equations

By examining the orders of magnitude of the physical parameters in the above Gauss law, compared to the time and space scales in consideration, it can be argued – and justified by a mathematical asymptotic analysis, indeed [Mor09, Ric09] – that electroneutrality must prevail away from the membranes, *i.e.*

$$\rho_b^{(\alpha)} + \mathrm{F} \sum_{k=1}^{N^{(\alpha)}} z_k c_k^{(\alpha)} = 0,$$

everywhere in the interior of the intra- and extracellular regions. In order to obtain an equation for the electric potential, we need to consider the total electric current and apply to it the electroneutrality assumption. This gives the following equations, see [11] for more details,

$$\underline{j}_r^{(\alpha)} = -\Big(\sigma^{(\alpha)}\vec{\nabla}_{\vec{x}}\, u^{(\alpha)} + \mathrm{F}\sum_{k=1}^{N^{(\alpha)}} z_k D_k \vec{\nabla}_{\vec{x}}\, c_k^{(\alpha)}\Big) \text{ and } \vec{\nabla}_{\vec{x}} \cdot \underline{j}_r^{(\alpha)} = 0.$$

To close the system, the drift-diffusion flux at the membrane interface is modeled: the ions that hit the membrane can be blocked on the surface on each side, or cross the membrane through so-called ionic channels. We denote by $\mu_k^{(\alpha)}$ the molar density per unit surface for species k on either side, and by I_k^{ion} the molar quantity crossing the membrane from $\Omega^{(i)}$ to $\Omega^{(e)}$, per unit time and per unit surface of the reference configuration. We also introduce the total quantities $I^{\text{ion}} = \mathrm{F}\sum_{k=1}^{N} z_k I_k^{\text{ion}}$ and $\mu^{(\alpha)} = \mathrm{F}\sum_{k=1}^{N} z_k \mu_k^{(\alpha)}$. By considering that conservation dictates that the variation of molar quantity attached to the membrane equals the quantity crossing the membrane from $\Omega^{(e)}$ to $\Omega^{(i)}$ plus the quantity associated with ions coming from $\Omega^{(i)}$ and hitting the membrane, the full system of unknowns $c_k^{(\alpha)}$ and $u^{(\alpha)}$ reads

$$\begin{cases} \partial_t c_k^{(\alpha)}{}_{|\underline{x}} = -\vec{\nabla}_{\vec{x}} \cdot \underline{j}_k^{(\alpha)}, & \text{in } \Omega^{(\alpha)} \\ \underline{j}_k^{(\alpha)} = -D_k\Big(\vec{\nabla}_{\vec{x}}\, c_k^{(\alpha)} + \dfrac{q z_k c_k^{(\alpha)}}{k_B T}\vec{\nabla}_{\vec{x}}\, u^{(\alpha)}\Big) + c_k^{(\alpha)}\underline{v}_s, & \text{in } \Omega^{(\alpha)} \\ s_\Gamma\, \underline{j}_{k,r}^{(\alpha)} \cdot \underline{n}^{(\alpha)} = \partial_t \mu_k^{(\alpha)}{}_{|\underline{\xi}} \pm I_k^{\text{ion}}, & \text{on } \Gamma \\ \vec{\nabla}_{\vec{x}} \cdot \underline{j}_r^{(\alpha)} = 0, & \text{in } \Omega^{(\alpha)}, \\ \underline{j}_r^{(\alpha)} = -\Big(\sigma^{(\alpha)}\vec{\nabla}_{\vec{x}}\, u^{(\alpha)} + \mathrm{F}\displaystyle\sum_{k=1}^{N^{(\alpha)}} z_k D_k \vec{\nabla}_{\vec{x}}\, c_k^{(\alpha)}\Big), & \text{in } \Omega^{(\alpha)}, \\ s_\Gamma\, \underline{j}_r^{(i)} \cdot \underline{n}^{(i)} = -s_\Gamma\, \underline{j}_r^{(e)} \cdot \underline{n}^{(e)} = C_m \partial_t u^{(m)}{}_{|\underline{\xi}} + I^{\text{ion}}, & \text{on } \Gamma, \end{cases} \tag{1.5}$$

where $s_\Gamma = J\|\underline{\underline{F}}^{-T} \cdot \underline{n}_0^{(\alpha)}\|$ represents the stretch ratio of the membrane in the current configuration with respect to the reference one, $u^{(m)} = u^{(i)} - u^{(e)}$ denotes the transmembrane potential and C_m the capacitance per unit area of the membrane, see [11] for all details. In addition, the auxiliary unknowns $\mu_k^{(\alpha)}$ and $\mu^{(\alpha)}$ are given by $\mu_k^{(\alpha)} = (z_k c_k^{(\alpha)} \mu^{(\alpha)})/(\sum_{\ell} (z_\ell)^2 c_\ell^{(\alpha)} \mathrm{F})$ and $\mu^{(i)} = -\mu^{(e)} = C_m u^{(m)}$ on Γ.

1.1.4 Bidomain model simplifications

In order to derive the classical bidomain equations, it is assumed that diffusion can be neglected compared to drift in ionic fluxes [Mor09]

$$\begin{cases} \vec{\nabla}_{\vec{x}} \cdot (\sigma^{(\alpha)}\vec{\nabla}_{\vec{x}}\, u^{(\alpha)}) = 0, & \text{in } \Omega^{(\alpha)} \\ \sigma^{(i)}\vec{\nabla}_{\vec{x}}\, u^{(i)} \cdot \underline{n}^{(i)} = \sigma^{(e)}\vec{\nabla}_{\vec{x}}\, u^{(e)} \cdot \underline{n}^{(i)}, & \text{on } \Gamma \\ -s_\Gamma\, \sigma^{(i)}\vec{\nabla}_{\vec{x}}\, u^{(i)} \cdot \underline{n}^{(i)} = C_m \partial_t u^{(m)}{}_{|\underline{\xi}} + I^{\text{ion}}, & \text{on } \Gamma. \end{cases} \tag{1.6}$$

Whether or not this assumption is valid in practice is an open question that goes beyond the scope of this work. Finally, one can observe that the previous equations define $u^{(i)}$ or $u^{(e)}$ up to the same constant. Therefore, we choose to impose $\int_\Gamma u^{(e)}\, d\gamma = 0$. To conclude the description of the microscopic bidomain model, the last subsection is dedicated to the description of the transmembrane currents.

1.1.5 Ionic models and mechanical effects

Physiological or phenomenological ionic models Physiological ionic models aim at describing ionic exchanges up to some varying degree of detail. The first such model was proposed for neurons by Hodgkin and Huxley [HH52]. Some models were later introduced to more specifically address cardiac electrophysiology with – to cite just a few classical ones – the models proposed in [CRN98, NFF$^+$98] for atrial cells and in [tTNNP04, tTP06, OVVR11] for ventricular cells. By contrast, so-called phenomenological ionic models are intended to focus on reproducing the variations of the transmembrane potential with much fewer state variables. The first one was independently proposed by FitzHugh and Nagumo [Fit61, NAY62] for neurons, and was later adapted to cardiac cells in [BCP94, AP96]. More recent phenomenological model were proposed in [MS03, BOCF08]. Since most ionic models can be rewritten as follows

$$I^{\text{ion}} := I^{\text{ion}}(u^{(m)}, w), \quad \partial_t w + g(u^{(m)}, w) = 0,$$

where w corresponds to one (or more) additional variable(s) called state variable(s), we will consider this formulation in what follows, see [8] for more details.

Stretch-Activated Channels To a first approximation, cardiac electrophysiology and mechanics are often assumed to be *weakly coupled*, that is, electrophysiology is considered to be an input that drives the active part of mechanical behavior. However, it is known that mechanical deformation alters electrical properties. This is the so-called mechano-electrical feedback (MEF), which is thought to be involved in cardiac arrhythmias and other pathologies, see, e.g., [ABE16] and references therein. One of the mechanisms of MEF is provided by the stretch-activated channels (SAC). To model this effect, some parts of ionic models are made to depend on deformation, which usually leads to a decrease in action potential duration and amplitude and an increase in resting transmembrane potential [HM05, AHZ$^+$13, PKN05, AHZ$^+$13, AHZ$^+$13]. However, as the role and mechanisms of SAC are still not fully understood [WGRS12], we disregard the direct dependence on mechanical deformations of ionic model to evaluate other effects.

1.2 Mathematical analysis of the periodic homogenization

In this section we neglect the mechanical deformations, which means that we consider System (1.6) in which ϕ is the identity, which means that $\underline{x}(t) = \underline{\xi}, \forall t, \; s_\Gamma = 1,$ and $\underline{v}_s = 0.$

This section is a summary of our article [8]. The goal of our work is to fill a gap in the literature by providing a complete mathematical analysis based on the 2-scale convergence theory of the homogenization process leading to the macroscopic bidomain model. Our analysis is exhaustive in the sense that we provide existence and uniqueness results, non-dimensionalization of equations, and 2-scale convergence results – in particular, for the nonlinear terms supported on the membrane surface – within the same mathematical framework. To anticipate reasonable modeling assumptions, we assume that the electric conductivities are tensorial and spatially variable at the microscopic scale. We also consider ionic models of both types (physiological and phenomenological) that can vary uniformly in space (to consider ventricular or atrial cells, for example). We carefully introduce the various standard assumptions satisfied by ionic terms and distinguish the models that are compatible with our analysis. We believe that this work will enable the analysis of more complex models by laying the foundation for the 2-scale analysis of the bidomain equations. More specifically, we study the following system

$$\left\{\begin{array}{rcll} \vec{\nabla}_{\vec{x}} \cdot (\vec{\vec{\sigma}}^{(\alpha)}\, \vec{\nabla}_{\vec{x}}\, u^{(\alpha)}) & = & 0 & \Omega^{(\alpha)}, \\ \vec{\vec{\sigma}}^{(i)}\, \vec{\nabla}_{\vec{x}}\, u^{(i)} \cdot \vec{n}^{(i)} & = & \vec{\vec{\sigma}}^{(e)}\, \vec{\nabla}_{\vec{x}}\, u^{(e)} \cdot \vec{n}^{(i)} & \Gamma^{(m)}, \\ -\vec{\vec{\sigma}}^{(i)}\, \vec{\nabla}_{\vec{x}}\, u^{(i)} \cdot \vec{n}^{(i)} & = & C_m u^{(m)} + I^{\text{ion}}(u^{(m)}, w) & \Gamma^{(m)}, \\ u^{(m)} & = & u^{(i)} - u^{(e)} & \Gamma^{(m)}, \\ \partial_t w & = & -g(u^{(m)},\, w) & \Gamma^{(m)}, \\ \vec{\vec{\sigma}}^{(\alpha)} \vec{\nabla}_{\vec{x}}\, u^{(e)} \cdot \vec{n}^{(\alpha)} & = & 0 & \partial\Omega^{(\alpha)} \cap \partial\Omega, \\ \displaystyle\int_{\Gamma^{(m)}} u^{(e)}\, d\gamma & = & 0. & \end{array}\right. \tag{1.7}$$

Among the modeling ingredients that might fit our context, one might consider: heterogeneous concentrations of ionic species within cells, gap junctions [HP10], and microscopic cardiac fiber structure in the context of local 2-scale convergence [Bri93, Pta17]. In Section 1.2.1, the main results of the existence and uniqueness of the heterogeneous microscopic bidomain model are given. In Section 1.2.2 the main results of the homogenization process of the heterogeneous microscopic bidomain model are given.

1.2.1 Analysis of the microscopic bidomain model

In [8], the assumptions used to prove existence and uniqueness of the microscopic bidomain model for various ionic models are very carefully selected.

Assumption 1. *Summary of the assumptions:*

(a) *Regularity of the diffusion tensors.* $\vec{\vec{\sigma}}^{(\alpha)}$ *are bounded, symmetric, definite, positive and coercive and allow to define norms in* $L^2(\Omega^{(\alpha)})$.

(b) *Regularity of the initial conditions.* $\overline{u^{(m)}}^0 \in L^2(\Gamma^{(m)})$ *and* $\overline{w}^0 \in L^2(\Gamma^{(m)})$.

(c) *Regularity condition of the ionic terms.* $I^{ion} \in C^0(\overline{\Omega} \times \mathbb{R}^2)$ *and* $g \in C^0(\overline{\Omega} \times \mathbb{R}^2)$.

(d) *Growth conditions of the ionic terms.* $\exists C_\infty > 0, \forall \vec{x} \in \Omega, \forall (v, w) \in \mathbb{R}^2$,

$$|I^{ion}(\vec{x}, v, w)| \leq C_\infty(|v|^3 + |w| + 1) \text{ and } |g(\vec{x}, v, w)| \leq C_\infty(|v|^2 + |w| + 1). \tag{1.8}$$

(e) *Signed condition of the ionic terms. There exist* $\mu > 0$ *and* $C_I > 0$ *such that for all* $\vec{x} \in \Omega$ *and* $(v, w) \in \mathbb{R}^2$*, we have*

$$v\, I^{ion}(\vec{x}, v, w) + \mu\, w\, g(\vec{x}, v, w) \geq -C_I(\,|v|^2 + |w|^2\, + 1). \tag{1.9}$$

(f) *Compensation of the lack of regularity on the gating variables. Depending on whether the model is physiological or phenomenological, one of the following assumptions applies*

  (i) *Global lipschitz property. There exists a positive scalar* $L_g > 0$*, such that for all* $\vec{x} \in \Omega$*,* $(v_1, v_2) \in \mathbb{R}^2$ *and* $(w_1, w_2) \in \mathbb{R}^2$*,*

$$|g(\vec{x}, v_1, w_1) - g(\vec{x}, v_2, w_2)| \leq L_g\, |v_1 - v_2| + L_g\, |w_1 - w_2|. \tag{1.10}$$

(ii) *Decomposition of the nonlinear terms. There exist continuous functions*

$$(f_1, f_2, g_1, g_2) \in [C^0(\Omega \times \mathbb{R}^2)]^4$$

such that

$$\begin{cases} I^{ion}(\vec{x}, v, w) = f_1(\vec{x}, v) + f_2(\vec{x}, v)\, w, \\ g(\vec{x}, v, w) = g_1(\vec{x}, v) + g_2(\vec{x})\, w, \end{cases}$$

and there exist positive constants C_1, c_1 and C_2 such that for all $\vec{x} \in \Omega$ and $v \in \mathbb{R}$,

$$v\, f_1(\vec{x}, v) \geq C_1\, |v|^4 - c_1\, (\, |v|^2 + 1) \quad \textit{and} \quad |f_2(\vec{x}, v)| \leq C_2\, (\, |v| + 1). \tag{1.11}$$

(g) *One-sided Lipschitz condition for the uniqueness of a solution. There exist $\mu > 0$ and $L_I > 0$ such that for all $\vec{x} \in \Omega$, $(v_1, w_1) \in \mathbb{R}^2$ and $(v_2, w_2) \in \mathbb{R}^2$*

$$\Big(I^{ion}(\vec{x}, v_1, w_1) - I^{ion}(\vec{x}, v_2, w_2)\Big)(v_1 - v_2) + \mu\, \Big(g(\vec{x}, v_1, w_1) - g(\vec{x}, v_2, w_2)\Big)(w_1 - w_2) \\ \geq -L_I\, \big(|v_1 - v_2|^2 + |w_1 - w_2|^2\big). \tag{1.12}$$

Assumptions from 1(a) to 1(f) are satisfied for classical ionic models, see Table 1.1 for a classification. Assumption 1(g) is not satisfied for the Aliev-Panfilov [AP96], the MacCulloch [BCP94], and the Mitchell-Schaeffer [MS03] models. The uniqueness of a solution for these models is still an open problem.

Assumption	1(d)	1(e)	1(f)	1(g)
FitzHugh-Nagumo	✓	✓	(i)	✓
Roger MacCulloch	✓	✓	(i)	
Aliev-Panfilov	✓	✓	(ii)	
Regularized Mitchell-Schaeffer	✓	✓	(i)	
Physiological models	✓	✓	(i)	✓

Table 1.1 – Ionic models and verified assumptions

1.2.1.1 Existence and uniqueness analysis

In the literature, the analysis of the classical bidomain model is mostly performed at the macroscopic scale, see [CFPS14] for a presentation of the different approaches. In any case, to justify the homogenization process, a mathematical analysis at the microscopic scale is required. In this section, we give existence and uniqueness results for solutions of System (1.7) using the Faedo-Galerkin approach. The main five steps are quickly detailed below.

Step 1 - Elimination of the unknown electric potentials Following an idea developed in [BCP09] for the bidomain equation at the macroscopic level or in [KLPW14] for an electroporation model at the microscopic level, one can prove, see [8, Section 3.1], that there exists a regular linear operator $\mathcal{A}$ defined as a combination of Dirichlet-to-Neumman type of operators such that solutions of System (1.7) verify

$$\begin{cases} C_m \partial_t u^{(m)} + I^{\text{ion}}(u^{(m)}, w) &=& -\mathcal{A}(u^{(m)}), & \Gamma^{(m)}, \\ \partial_t w &=& -g(u^{(m)}, w), & \Gamma^{(m)}. \end{cases} \tag{1.13}$$

Step 2 - Evolution equation of the gating variable. Let $U \in C^0([0,T];L^2(\Gamma^{(m)}))$, a given electrical potential. The term $g(u^{(m)},w)$ in (1.13) is replaced by $g(U,w)$ with $w = w_U$ the corresponding solution.

Lemma 1. *If Assumption 1(b), 1(c), 1(d) and 1(f)(i) hold, there exists a unique function* $w_U \in C^1([0,T];L^2(\Gamma^{(m)}))$, *which is a solution of*

$$\begin{cases} \partial_t w_U + g(\vec{x},U,w_U) = 0, & \Gamma^{(m)},\ \forall\, t \in [0,T], \\ w_U(\vec{x},0) = \overline{w}^0(\vec{x}), & \Gamma^{(m)}. \end{cases} \tag{1.14}$$

and there exists a positive scalar C_w, *that depends only on* T *and* L_g, *such that for any function* $V \in C^0((0,T);L^2(\Gamma^{(m)}))$,

$$\int_0^T \|w_U(t) - w_V(t)\|^2_{L^2(\Gamma^{(m)})} \leq C_w \int_0^T \|U(t) - V(t)\|^2_{L^2(\Gamma^{(m)})}\, dt.$$

The proof of Lemma 1 is done by considering smooth approximations of U and $\overline{w}^0$. Then, the problem reduces to the analysis of an ODE where the space variable plays the role of a parameter. Finally, the solution of (1.14) is constructed by a limit process using the density of smooth functions into $L^2(\Gamma^{(m)})$.

Step 3 - Existence result for the microscopic bidomain equation

Theorem 1. *If Assumptions from 1(a) to 1(f) hold, there exist*

$$u^{(m)} \in C^0([0,T];L^2(\Gamma^{(m)})) \cap L^2((0,T);H^{1/2}(\Gamma^{(m)})), \quad \partial_t u^{(m)} \in L^2((0,T);H^{-1/2}(\Gamma^{(m)})),$$

and $w \in H^1((0,T);L^2(\Gamma^{(m)}))$, *which are solutions of*

$$\begin{cases} C_m\,\partial_t u^{(m)} + \mathcal{A}\big(u^{(m)}\big) + I^{\text{ion}}\big(u^{(m)},w\big) = 0, & \widetilde{H}^{-1/2}(\Gamma^{(m)}), & \text{a.e. } t \in (0,T), \\ \partial_t w + g\big(u^{(m)},w\big) = 0, & \Gamma^{(m)}, & \text{a.e. } t \in (0,T), \end{cases} \tag{1.15}$$

$$\textit{and } u^{(m)}(\vec{x},0) = \overline{u^{(m)}}^0(\vec{x}),\ w(\vec{x},0) = \overline{w}^0(\vec{x}),\ \Gamma^{(m)}.$$

The proof of Theorem 1 is done using the Faedo-Galerkin method. More precisely, the equations are first space-discretized using a finite dimensional basis of $L^2(\Gamma^{(m)})$ constructed with the eigenvectors of $\mathcal{A}$. After the discretization, it is proven that semi-discrete solutions exist by applying the Cauchy-Peano theorem (to be more specific, we use the more general Carathéodory's existence theorem) on systems of ordinary differential equations. Finally, by a limit procedure, the existence of solutions is proven for the weak form of (1.15).

Step 4 - Uniqueness results for the microscopic bidomain equation Uniqueness is proven by standard energy techniques for models satisfying Assumption 1(g).

Step 5 - Post-processing of the intra- and extra-cellular potentials From the solution $u^{(m)} = u^{(i)} - u^{(e)}$ given by Theorem 1, we can recover the intra- and extra-cellular potentials

$$u^{(i)} \in L^2((0,T);H^1(\Omega_0^{(i)})) \text{ and } u^{(e)} \in L^2((0,T);H^1(\Omega_0^{(e)}))$$

following the strategy given in Section 3.4 of [8].

1.2.2 Homogenization of the bidomain equations

Context After existence and uniqueness, we are now in a position to perform a rigorous homogenization of the microscopic bidomain model (1.6). The microscopic model is useless for the whole heart in terms of numerical applications. At the macroscopic scale, the heart appears as a continuous material with a fiber-based structure. At this scale, the intracellular and extracellular media are indistinguishable. Our goal is to use a homogenization of the microscopic bidomain model to obtain a bidomain model in which all unknowns are defined everywhere. Formally, the heart volume after homogenization is "$\Omega = \Omega^{(i)} = \Omega^{(e)}$" (for simplicity, the subscript 0 has been removed but as the mechanical deformations are not considered, it corresponds to the reference domain). Homogenization of partial differential systems is a well-known technique, see [BLP78] for a reference book on this subject. Here the medium is considered periodic of period ε, and equations are derived by asymptotic analysis with respect to ε. The periodicity allows to use the results of 2-scale convergence, see [All92], a method which has been used in many areas of science and engineering. We denote by Y the open reference domain that is used to define the idealized micro-structure corresponding to the periodic arrangement of cardiac cells. This micro-structure is decomposed into two open connected subdomains: the intracellular part $Y^{(i)}$ and the extracellular part $Y^{(e)}$. We have $Y_i \cap Y_e = \emptyset, \quad \overline{Y} = \overline{Y}_i \cup \overline{Y}_e$. The intra- and the extra-cellular domains are separated by Γ_Y. The global position vector is denoted by $\vec{x}$ and the local position vector by $\vec{t}$. In this context, the domain $\overline{\Omega} = \overline{\Omega_\varepsilon^{(i)}} \cup \overline{\Omega_\varepsilon^{(e)}}$ is then defined by ε-periodicity and we denote by $\Gamma_\varepsilon^{(m)}$ the boundary between the intra- and the extra-cellular domains $\Omega_\varepsilon^{(i)}$ and $\Omega_\varepsilon^{(e)}$ *i.e.* $\Omega_\varepsilon^{(\alpha)} = \bigcup_k (\varepsilon Y^{(\alpha)} + \varepsilon \vec{w}_k)$ and then $\Gamma_\varepsilon^{(m)} = \bigcup_k (\varepsilon \Gamma_Y + \varepsilon \vec{w}_k)$, where $\vec{w}_k$ (with $\vec{w}_0 = \vec{0}$) is the vector corresponding to the translation between the considered cell and the reference cell. Note that by construction, we have $\vec{t} = \vec{x}/\varepsilon$. We assume that the diffusion tensors depend on the two scales *i.e.* $\vec{\vec{\sigma}}_\varepsilon^{(\alpha)}(\vec{x}) = \vec{\vec{\sigma}}^{(\alpha)}\left(\vec{x}, \frac{\vec{x}}{\varepsilon}\right)$.

A classical article for the formal homogenization of the microscopic bidomain model – when the conductivities $\sigma^{(\alpha)}$ are strictly positive constants – is [NK93]. In [CFS02], the homogenization of the microscopic bidomain equations (with constants conductivities) is presented using formal asymptotic analysis. It should also be noted that in [ACFS00, PSCF05], the same type of results have be proven using the theory of Γ-convergence in some simplified situations. The approach presented below uses the 2-scale convergence method, see [All92], to extend the results obtained in [ACFS00, PSCF05]. As typical for this kind of homogenization problem, we adopt the following approach, see [8]:

Step 1 - Nondimensionalization of the problem. The microscopic bidomain equations are scaled in space and time, and written unitless. Using the characteristic values of the physical parameters of our problem (cells size, conductivities, ionic current,...), a small parameter ε is introduced in the equations and in the geometry. We obtain in [8, Section 4.1] the following system

$$\left\{\begin{array}{rcll}
\vec{\nabla}_{\vec{x}} \cdot (\vec{\vec{\sigma}}_\varepsilon^{(\alpha)} \, \vec{\nabla}_{\vec{x}} \, u_\varepsilon^{(\alpha)}) & = & 0 & \Omega_\varepsilon^{(\alpha)}, \\
\vec{\vec{\sigma}}_\varepsilon^{(i)} \, \vec{\nabla}_{\vec{x}} \, u_\varepsilon^{(i)} \cdot \vec{n}^{(i)} & = & \vec{\vec{\sigma}}_\varepsilon^{(e)} \, \vec{\nabla}_{\vec{x}} \, u_\varepsilon^{(e)} \cdot \vec{n}^{(i)}, & \Gamma_\varepsilon^{(m)} \\
\vec{\vec{\sigma}}_\varepsilon^{(i)} \, \vec{\nabla}_{\vec{x}} \, u_\varepsilon^{(i)} \cdot \vec{n}^{(i)} & = & -\varepsilon C_m \partial_t (u_\varepsilon^{(i)} - u_\varepsilon^{(e)}) - \varepsilon I^{\text{ion}}(u_\varepsilon^{(i)} - u_\varepsilon^{(e)}, w_\varepsilon) & \Gamma_\varepsilon^{(m)}, \\
\partial_t w_\varepsilon & = & -g(u_\varepsilon^{(i)} - u_\varepsilon^{(e)}, w_\varepsilon), & \Gamma_\varepsilon^{(m)}. \\
\vec{\vec{\sigma}}_\varepsilon^{(i)} \, \vec{\nabla}_{\vec{x}} \, u_\varepsilon^{(\alpha)} \cdot \vec{n}^{(\alpha)} & = & 0, & \partial\Omega \cap \partial\Omega_\varepsilon^{(\alpha)}, \\
u_\varepsilon^{(i)}(\cdot, 0) - u_\varepsilon^{(e)}(\cdot, 0) & = & \overline{V_{m,\varepsilon}}^{0}, & \Gamma_\varepsilon^{(m)} \\
w_\varepsilon(\cdot, 0) & = & \overline{w}_\varepsilon^0, & \Gamma_\varepsilon^{(m)}, \\
\int_{\Gamma_\varepsilon^{(m)}} u_\varepsilon^{(e)} \, d\gamma & = & 0. &
\end{array}\right.$$

Step 2 - Uniform estimate of solutions. Using energy estimates, we prove that the norms of the solutions – as well as norms of the nonlinear terms – are uniformly bounded with respect to ε if the initial conditions follow uniform estimates, see [8, Section 4.2].

Step 3 - Two-scale convergence. The limit equations are deduced by application of the 2-scale convergence theory. One of the main difficulties of this step is the convergence analysis of the nonlinear terms. We quickly detail this part below. In [8], one can find a detailed proof of the 2-scale convergence of $u_\varepsilon^{(\alpha)}$ to the sought macro-scale solutions $u_0^{(\alpha)}$ verifying

$$\left\{\begin{array}{rll}
-\vec{\nabla}_{\vec{x}} \cdot \vec{\vec{T}}^{(i)}\, \vec{\nabla}_{\vec{x}}\, u_0^{(i)} + A_m C_m (u_0^{(i)} - u_0^{(e)}) + A_m I^{\text{ion}}(u_0^{(i)} - u_0^{(e)}, w_0) & = 0, & \Omega \times (0,T), \\
-\vec{\nabla}_{\vec{x}} \cdot \vec{\vec{T}}^{(e)}\, \vec{\nabla}_{\vec{x}}\, u_0^{(e)} - A_m C_m (u_0^{(i)} - u_0^{(e)}) - A_m I^{\text{ion}}(u_0^{(i)} - u_0^{(e)}, w_0) & = 0, & \Omega \times (0,T), \\
\partial_t w_0 + g(u_0^{(i)} - u_0^{(e)}, w_0) & = 0, & \Omega \times (0,T), \\
(\vec{\vec{T}}^{(\alpha)} \cdot \vec{\nabla}_{\vec{x}}\, u_0^{(\alpha)}) \cdot \vec{n} & = 0, & \partial\Omega \times (0,T), \\
(u_0^{(i)} - u_0^{(e)})(\vec{x}, 0) & = \overline{u^{(m)}}^{0}(\vec{x}), & \Omega, \\
w_0(\vec{x}, 0) & = \overline{w}^{0}(\vec{x}), & \Omega, \\
\displaystyle\int_\Omega u_0^{(e)}\, \mathrm{d}\vec{x} & = 0 &
\end{array}\right.$$

The tensors $\vec{\vec{T}}^{(\alpha)}$, $\alpha = (i, e)$ are the associated effective medium tensors

$$(\vec{\vec{T}}^{(\alpha)})_{j,k} = \frac{1}{|Y|} \int_{Y^{(\alpha)}} \vec{\vec{\sigma}}^{(\alpha)}\, (\vec{\nabla}_{\vec{y}}\, \mathcal{X}_j^{(\alpha)} + \vec{e}_j) \cdot (\vec{\nabla}_{\vec{y}}\, \mathcal{X}_k^{(\alpha)} + \vec{e}_k) \mathrm{d}\vec{t}, \tag{1.16}$$

where the canonical functions $\mathcal{X}_j^{(\alpha)}$, $j = 1..3$ belong to $H^1_\sharp(Y^{(\alpha)})$ and are uniquely defined by the following variational formulation – called the cell problem

$$\left\{\begin{array}{l}
\left(\vec{\vec{\sigma}}^{(\alpha)}\, (\vec{e}_j + \vec{\nabla}_{\vec{y}}\, \mathcal{X}_j^{(\alpha)}),\, \vec{\nabla}_{\vec{y}}\, \psi\right)_{Y^{(\alpha)}} = 0, \;\; \forall\, \psi \in H^1_\sharp(Y^{(\alpha)}), \\
\displaystyle\int_{Y^{(\alpha)}} \mathcal{X}_j^{(\alpha)}\, \mathrm{d}\vec{t} = 0.
\end{array}\right. \tag{1.17}$$

For the proof, we use the 2-scale convergence theory developed in [All92] and [Ngu89]. The treatment of the nonlinear ionic terms represents one of the main difficulties. To solve this problem, we present an approach using the general ideas of [All92]. It is based on the one-sided Lipschitz assumption (Assumption 1(g)). The final difficulty is that the nonlinear terms are at the boundary of the domain. The 2-scale convergence theory must be adapted, and for this we use the results given in [ADH95].

Since the analysis has already been performed for the microscopic bidomain model, we can infer – up to a subsequence – the existence of a solution for the macroscopic bidomain model. The proposed model is a generalization of the very classical macroscopic bidomain model in which constant electric conductivities are considered. Compared to previous studies, see for example [ACFS00] and [PSCF05], and in order to anticipate meaningful modeling assumptions, we have considered at the microscopic level that the electric conductivities are tensorial. This appears in the definition of the cell problem (1.17) and in the definition of the tensor (1.16). Moreover, we have shown that the classical macroscopic bidomain model formally obtained in [CFS02] and [NK93] is valid for the ionic terms under some more general conditions than those assumed in [ACFS00] and [PSCF05]. More precisely, we extended the validity of the macroscopic bidomain equations to spatially variable physiological models.

1.3 Effects of mechanical deformations on the bidomain model

1.3.1 Macroscopic bidomain incorporating the mechanical deformations

Now we return to the incorporation of the mechanical deformations. We use our expertise acquired in the full analysis of the modeling when the mechanical deformations are neglected to perform a formal asymptotic analysis on System (1.5), which we rewrite here in the Lagrangian framework, *i.e.* in terms of the spatial variable associated with the reference configuration. For this purpose, it is classical, as is usual in the derivation of conservation laws in moving domains [TM05], to introduce the following modified concentration and (relative) flux quantities

$$C_k^{(\alpha)} = J\, c_k^{(\alpha)}, \quad \underline{J}_k^{(\alpha)} = J\underline{\underline{F}}^{-1} \cdot \underline{j}_{k,r}^{(\alpha)}.$$

Our homogenization *Ansatz* is that each main unknown of the microscopic problem defined on the reference domain is the sum of two terms defined everywhere in Ω_0:

- a leading term independent of ε,
- correction terms dependent on ε and with local variations inside each cell.

Regarding the membrane equations, we consider asymptotic assumptions consistent with the nondimensionalized system presented in the previous section meaning that they are scaled by like ε.

We then incorporate the equations of our homogenization Ansatz into the governing equations and we identify the equations satisfied by the leading order terms $C_{k,0}^{(\alpha)}$ and $u_0^{(\alpha)}$. It should be noted, however, that these terms will be mixed with higher order terms in the equations that we will directly infer, due to space differentiation with the coexistence of the $\underline{\xi}$ and $\underline{\xi}/\varepsilon$ variables in various terms.

We only give the results but all the computations are in [11]. First, we introduce the basic cell problem in which, for any vector $\underline{v} \in \mathbb{R}^3$, we call $\mathcal{X}^{(\alpha)}(\underline{v})$ the periodic solution (defined up to a constant) of

$$\begin{cases} \vec{\nabla}_{\vec{\eta}} \cdot \left[\left(\underline{\underline{F}}^T \cdot \underline{\underline{F}}\right)^{-1} \cdot \vec{\nabla}_{\vec{\eta}}\, \mathcal{X}^{(\alpha)}(\underline{v}) \right] = 0, & \text{in } Y^{(\alpha)} \\ \left[\left(\underline{\underline{F}}^T \cdot \underline{\underline{F}}\right)^{-1} \cdot \vec{\nabla}_{\vec{\eta}}\, \mathcal{X}^{(\alpha)}(\underline{v}) \right] \cdot \underline{n}_Y^{(\alpha)} = -\left[\left(\underline{\underline{F}}^T \cdot \underline{\underline{F}}\right)^{-1} \underline{v} \right] \cdot \underline{n}_Y^{(\alpha)}, & \text{on } \Gamma_Y \end{cases} \tag{1.18}$$

Using this solution and as it is classical in periodic homogenization analysis (see. [All12, Chapter 1]), we introduce the tensor $\underline{\underline{T}}^{(\alpha)}$ defined by

$$\underline{\underline{T}}^{(\alpha)} \cdot \underline{u} = \frac{1}{|Y^{(\alpha)}|} \int_{Y^{(\alpha)}} \left(\underline{\underline{F}}^T \cdot \underline{\underline{F}}\right)^{-1} \cdot \left(\underline{u} + \vec{\nabla}_{\vec{\eta}}\, \mathcal{X}^{(\alpha)}(\underline{u})\right) d\underline{\eta}. \tag{1.19}$$

Note that $\underline{\underline{T}}^{(\alpha)}$ only depends on the geometry of the cell and on the deformation through $\underline{\underline{F}}$. We obtain

$$\begin{cases} \phi^{(\alpha)} \partial_t C_{k,0}^{(\alpha)} + \vec{\nabla}_{\vec{\xi}} \cdot \phi^{(\alpha)} \underline{\widehat{J}}_{k,0}^{(\alpha)} + A_m\, p_{k,0}^{(\alpha)} = 0, \\ \underline{\widehat{J}}_{k,0}^{(\alpha)} = -J\, D_k\, \underline{\underline{T}}^{(\alpha)} \cdot \Big(\vec{\nabla}_{\vec{\xi}} \left(J^{-1} C_{k,0}^{(\alpha)}\right) + \dfrac{q z_k \left(J^{-1} C_{k,0}^{(\alpha)}\right)}{k_B T} \vec{\nabla}_{\vec{\xi}} u_0^{(\alpha)} \Big), \end{cases} \tag{1.20}$$

with $\phi^{(\alpha)} = \dfrac{|Y^{(\alpha)}|}{|Y|}$, the volume fractions of intra- and extra-cellular media in the reference configuration and

$$p_{k,0}^{(i)} = \mu_{k,0}^{(i)} + I_{k,0}^{\text{ion}},\ p_{k,0}^{(e)} = \mu_{k,0}^{(e)} - I_{k,0}^{\text{ion}}.$$

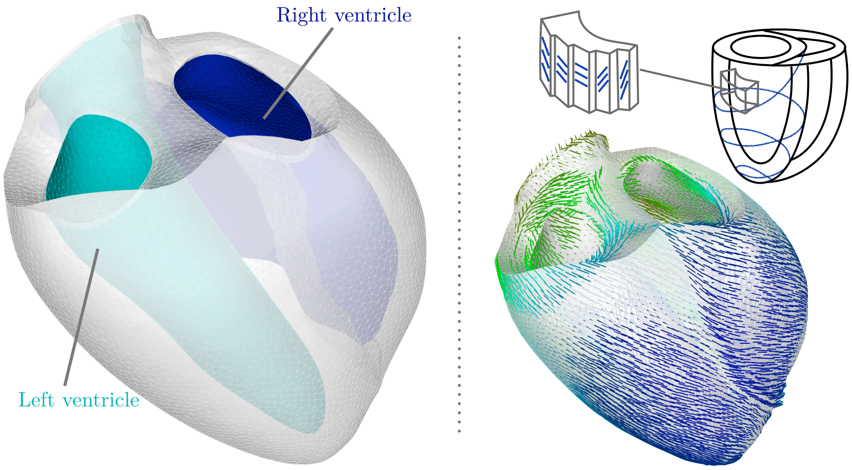

Figure 1.2 – Left: Mesh of the ventricles. Right: Fibers in the ventricles.

The additional relations pertaining to surface charges read

$$\mu_{k,0}^{(\alpha)} = \frac{z_k C_{k,0}^{(\alpha)}}{\sum_\ell (z_\ell)^2 C_{\ell,0}^{(\alpha)}} \frac{\mu_0^{(\alpha)}}{\mathrm{F}}, \; \mu_0^{(i)} = -\mu_0^{(e)} = \widehat{C}_m V_{m,0}.$$

Note that the terms $A_m \, p_{k,0}^{(\alpha)}$ in (1.20) represent the quantity of ions going from the volume to the membrane, for each species and in each domain. Finally, we complete this set of equations with

$$\begin{cases} \vec{\nabla}_{\vec{\xi}} \cdot \phi^{(\alpha)} \underline{\widehat{J}}_0^{(\alpha)} + A_m \, p_0^{(\alpha)} = 0, \\ \underline{\widehat{J}}_0^{(\alpha)} = -J \, \underline{\underline{T}}^{(\alpha)} \cdot \left(\sigma_0^{(\alpha)} \vec{\nabla}_{\vec{\xi}} u_0^{(\alpha)} + \mathrm{F} \sum_{k=1}^{N^{(\alpha)}} z_k D_k \vec{\nabla}_{\vec{\xi}} \left(J^{-1} C_{k,0}^{(\alpha)} \right) \right), \end{cases} \tag{1.21}$$

where $p_0^{(i)} = -p_0^{(e)} = \widehat{C}_m V_{m,0} + I_0^{\text{ion}}$, $\sigma_0^{(\alpha)} = \mathrm{F} q \sum_{k=1}^{N^{(\alpha)}} m_k (z_k)^2 \, J^{-1} \, C_{k,0}^{(\alpha)}$ and $I_0^{\text{ion}} = \mathrm{F} \sum_{k=1}^{N} z_k I_{k,0}^{\text{ion}}$.

To obtain a macroscopic bidomain equation including the effects of mechanical deformations, we need the last hypothesis. Indeed, assuming that the diffusion is negligible compared to the drift and denoting $\underline{\underline{\Sigma}}_0^{(\alpha)} = J \sigma_0^{(\alpha)} \phi^{(\alpha)} \underline{\underline{T}}^{(\alpha)}$, one can simplify System (1.21) into

$$\begin{cases} \vec{\nabla}_{\vec{\xi}} \cdot \left(\underline{\underline{\Sigma}}_0^{(i)} \cdot \vec{\nabla}_{\vec{\xi}} u_0^{(i)} + \underline{\underline{\Sigma}}_0^{(e)} \cdot \vec{\nabla}_{\vec{\xi}} u_0^{(e)} \right) = 0, \\ A_m \left[\widehat{C}_m \frac{\partial V_{m,0}}{\partial t} + I_0^{\text{ion}} \right] - \vec{\nabla}_{\vec{\xi}} \cdot \left(\underline{\underline{\Sigma}}_0^{(i)} \cdot \vec{\nabla}_{\vec{\xi}} u_0^{(i)} \right) = 0, \end{cases} \tag{1.22}$$

Of course, these equations can also be rewritten in the Eulerian framework, see [11].

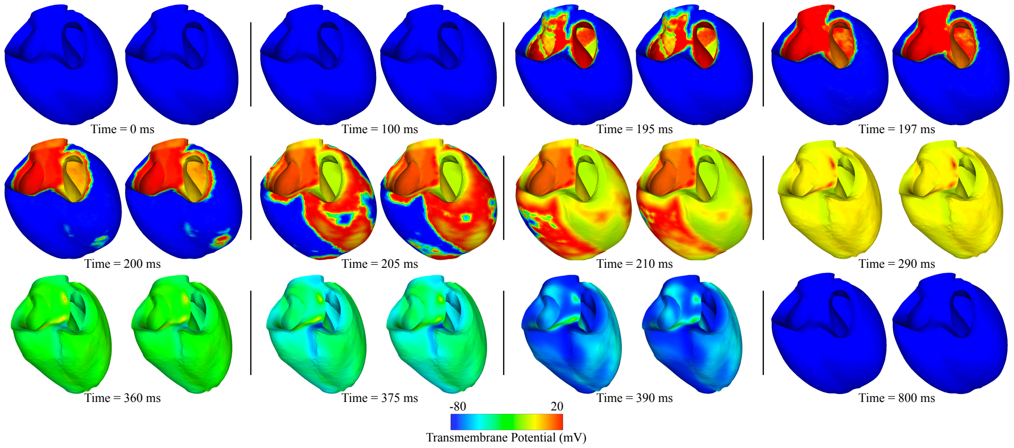

Figure 1.3 – Comparison between the results of the bidomain model with (left) and without (right) deformations.

1.3.2 Numerical illustrations

In this section, we would like to make a comparison between a simulation in which the mechanical deformations are taken into account and a simulation in which they are neglected. The goal is to see if neglecting the mechanical effects is reasonable in practice, and which geometry is most appropriate when neglecting them.

All the main components required to run a simulation – as variational formulation, parameters values, geometry, mesh and fiber directions (see Figure 1.2), ionic model, external stimulus, space and time discretizations and mechanical displacements – are given in [11].

Simulation results and discussion We display the simulation results in Figure 1.3 and in Figure 1.4 for a cut of the heart, where we compare for each time considered the potential maps obtained with and without taking the deformations into account, albeit applying the same deformation in the visualization to ease the comparison. The simulation starts when the atria contract and eject the blood in the ventricles between $t = 0$ and 190 ms, *i.e.* when the volumes of the ventricles are near their maximum. The applied current I^{app} stimulates the endocardium at $t = 190$ ms. As we can see in Fig. 1.3 and 1.4, the depolarization is faster when deformations are considered, which is explained by the fact that the signal mainly propagates through the ventricular wall thickness from the endocardium to the epicardium. Indeed, the wall thickness is thinner when the walls are stretched. The depolarizations are complete at 211 ms vs. 214 ms with and without deformations, respectively, which gives a delay of 3 ms on a depolarization duration of 21 ms, *i.e.* a difference of 15%. Near the end of depolarization (around $t = 210$ ms), ejection begins. Before the end of ejection (around $t = 365$ ms), repolarization occurs. We can see ($t = 390$ ms) that the repolarization appears somewhat faster when the deformations are considered, but the advance of 3 ms due to depolarization has to be considered. The repolarizations are complete at 410 ms vs. 411 ms with and without deformations, respectively, which gives a small difference in the end.

We can summarize our observations by saying that the effects of deformations as represented by our model are predominantly seen in the depolarization phase, where they speed up the propagation through the wall, with an impact on the depolarization timings that is comparable – in relative value – to

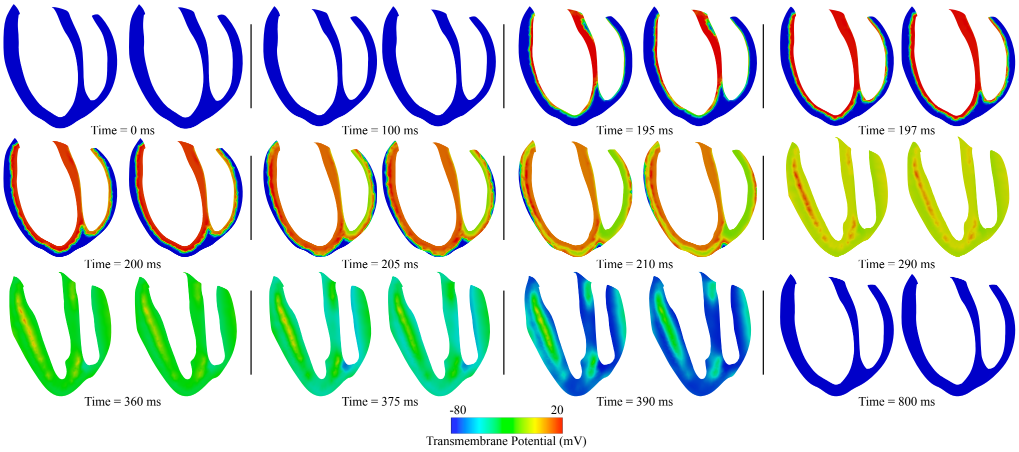

Figure 1.4 – Comparison between the results of the bidomain model with (left) and without (right) deformations in a cut of the heart.

the deformation amplitude. We point out that this is also comparable to the impact obtained when only considering changes in the constitutive laws to account for the MEF. Note that changing the geometry on which the fixed-domain electrophysiology problem is solved to one closer to end-diastolic configuration would most probably reduce the discrepancy in the depolarization phase with the solution of the model incorporating mechanical deformations. Nevertheless, this would not be satisfactory in our context where only the mechanical reference configuration (close to end-systole) is assumed to be given, and moreover in this case it would instead introduce discrepancies in the repolarization phase. In other words, if conductivity parameters are calibrated in one given configuration (end-systolic or end-diastolic), using the same parameters in a phase where the deformed geometry is far from this configuration will introduce discrepancies between the solutions of the electrophysiology problem with and without deformations.

Electrocardiogram simulations An ECG is a recording of the electrical activity of the heart [MP95, War75] measured at the outer surface of the body. This procedure – which is non-invasive and inexpensive – is the most standard diagnosis tool for cardiologists to detect cardiac pathologies. The literature on the simulation of ECG is abundant, see e.g. [BP11, Hui98, LBG$^+$03, KSW$^+$07]. The simulation of 12-lead ECGs based on partial differential equations (PDEs) – as proposed here – appeared during the last decade [BCF$^+$10, MDFG12, PDG03, PDV09, TDP$^+$04], more recently than simulations based on cellular automata [WOH$^+$95].

To model an ECG, the coupling between the heart and the body must be taken into account. It can be done through a diffusion problem with well-chosen transmission conditions at the heart-body interface. Our modeling choice has been detailed in [11].

Because the ECG is the most commonly used examination to assess the heart, it is important to understand the effects of mechanical deformation on the ECG in order to assimilate this type of data to estimate for example parameters of bidomain model.

Figure 1.5 displays the simulated ECGs with (blue) and without (red) deformations. The simulated ECGs can be validated against numerous criteria used and those considered in this work are given in [11] and allows to validate our modeling. The quality if these ECGs is discussed in [6] and in [11].

The main difference between the two simulations is the duration of the R-wave in the limb leads,

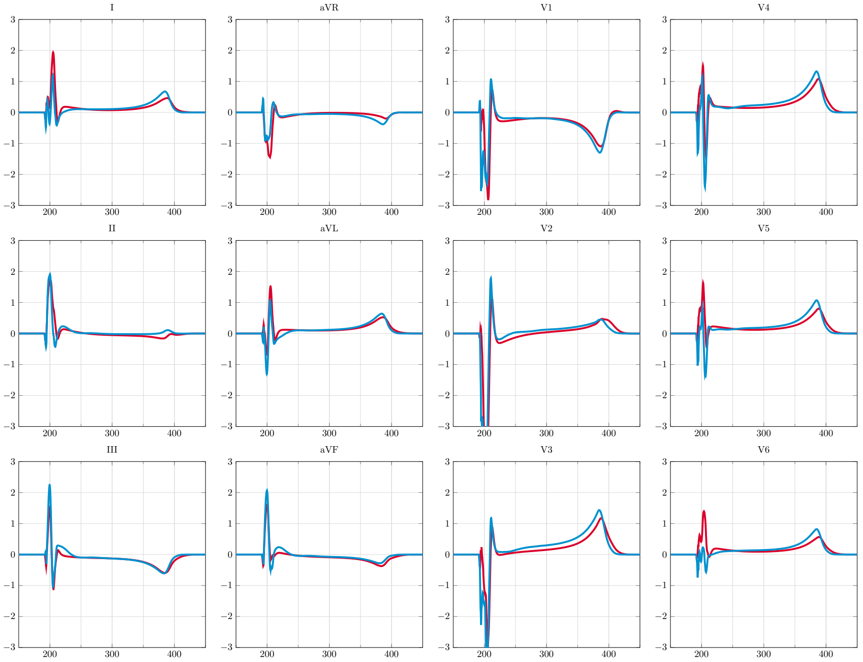

Figure 1.5 – Simulated ECGs with (blue) and without (red) deformations.

which is smaller when the displacements are considered. This is due to the faster depolarization.

Our simulations reveal a significant – although not predominant – impact of mechanical deformations on the ECGs. One natural perspective would be to compare our mechanically deformed bidomain model – which takes into account the heart deformation in conservation laws – with the classical mechano-electrical feedback model in a realistic case of ECG simulation.

1.4 Contributions to data assimilation aspects

As just seen, we are now able to obtain very realistic simulations of the electrophysiology of the heart. We have also seen that in most cases, the mechanical deformations can be neglected. As for all natural and physical systems, a great difficulty consists now in dealing with the many uncertain quantities which must be preserved for running model simulations for a given patient. These quantities include initial conditions and physical parameters of the model – as for example the conductivity tensors – which are difficult to measure. Fortunately, other types of measurement exist and the objective is to use these available data in order to circumvent the uncertainties corresponding to the dynamical model.

Here, we consider the propagation maps corresponding to the position of the front at different times. These maps give the position of the depolarization fronts over time. Mathematically, we assume that the data correspond to the position of the front of the transmembrane potential $u^{(m)} = u^{(i)} - u^{(e)}$. The proposed methods can be used in other application fields where models (reaction-diffusion) and data (front position) are very similar, as for fire propagation or tumor growth. Our methods are based on sequential observers, see Section B.3 of the introduction chapter for a quick presentation.

We will first start by presenting the *Luenberger* observer for reaction-diffusion models what we have proposed in my PhD in Section 1.4.1. In Section 1.4.2, we present a state observer based on the topological gradient that we have developed afterwards. This observer is very efficient to deal with complex patterns as one could observe when dealing with real data. In Section 1.4.3, the work that we have done in collaboration with the Carmen team, a Inria team localized at Bordeaux and specialized in modeling of cardiac electrophysiology. Our aim is to evaluate the sensitivity of our estimation strategy based on synthetic data generated with a validated realistic atrial model and then inverted with simpler modeling components. In particular, the effects of defining the muscle fibers and the corresponding anisotropic conductance parameters are examined. Finally, an application of the method to real data is presented, showing promising results. In particular, the resulting simulation smooths and completes activation maps that were spatially incomplete.

This section corresponds to very applied works. It is indeed very important for me that the innovative mathematical tools I develop are actually applicable in practice. Therefore, I try to go as far as possible to the proof of concept and also to communicate about our work in the application discipline. In this objective, the presented works have been published in two proceedings [5, 12] of the FIMH conference that aims to integrate the state of the art research and novel development efforts among others in heart modeling.

1.4.1 Context: a state observer using shape derivatives

Presentation During my PhD, we proposed, mathematically validated and numerically illustrated with synthetic data a *Luenberger* observer for reaction-diffusion models in the case where the uncertainties are reduced to the initial condition, see [4] for a full presentation. Following the definitions of Section B.3 of the introduction chapter, we consider the following *target* model

$$\left\{\begin{array}{lcll} \partial_t\, u & = & \nabla\cdot(\sigma\cdot\nabla u)+kf_r(u), & [0,T]\times\Omega, \\ u(0,x) & = & u^0(x)+\zeta_u(x), & \Omega, \end{array}\right.$$

where f_r is a reaction term, k a modeling coefficient and u^0 (resp. ζ_u) the known (resp. the unknown) part of the initial condition. We assume that the problem is well posed *i.e.* there exists a unique solution $u \in L^2(0,T;\mathcal{X})$, where $\mathcal{X}$ is for example $H^1_0(\Omega)$ if we consider homogenous Dirichlet conditions. The data correspond to the position of the front of u meaning that the observer operator is

$$\begin{array}{rccc} h: & L^2(0,T;\mathcal{X}) & \to & L^2(0,T;\mathcal{X}), \\ & u & \mapsto & \phi_u, \end{array}$$

where ϕ_u is a level set associated with u and a certain threshold value c_{th} *i.e.* $\phi_u(t,x)\geq 0$ if and only if $u(t,x)\geq c_{th}$. One possible choice for ϕ_u is $(t,x)\mapsto u(t,x)-c_{th}$ but we will show in what follows that the front in the data needs to be sufficient sharp to have the convergence. Assuming that there is no measurement error, the observations become $y = h(u)$. In [4], we propose the following *observer* model

$$\left\{\begin{array}{lcll} \partial_t\, \hat{u} & = & \nabla\cdot(\sigma\cdot\nabla \hat{u})+kf_r(\hat{u})+\gamma\, g_u(y,\hat{u}), & [0,T]\times\Omega, \\ \hat{u}(0,x) & = & u^0(x), & \Omega. \end{array}\right.$$

where the gain observer is defined by

$$g_u(y,\hat{u}) = \delta_{\{x\in\Omega,\hat{u}(t,x)=c_{th}\}}(t)\,\alpha(\nabla\hat{u})\,((y-C_{max}(y,\hat{u}))^2-(y-C_{min}(y,\hat{u}))^2),$$

where

- $\delta_{\{x\in\Omega,\hat{u}(t,x)=c_{th}\}}$ is a Dirac delta-function that ensures that the correction is only active along the front to correct,
- α is a strictly positive function that could be optimized to accelerate the convergence,
- and $C_{min} = \min(C_{in}, C_{out})$ and $C_{max} = \max(C_{in}, C_{out})$ with

$$C_{in}(y,\hat{u}) = \frac{\int_{\hat{u}>c_{th}} y(t,x)\,dx}{\int_{\hat{u}>c_{th}} dx} \text{ and } C_{out}(y,\hat{u}) = \frac{\int_{\hat{u}<c_{th}} y(t,x)\,dx}{\int_{\hat{u}<c_{th}} dx}.$$

One could remark that C_{in} measures the level of agreement between the observed and simulated interior areas and C_{out} measures the level of disagreement between the observed and simulated exterior areas.

To prove the convergence, we study the following *error* system

$$\left\{ \begin{array}{rcll} \partial_t\,\tilde{u} & = & \nabla\cdot(\sigma\cdot\nabla\tilde{u}) + k(f_r(u) - f_r(\hat{u})) - \gamma\, g_u(y,\hat{u}), & [0,T]\times\Omega, \\ \tilde{u}(0,x) & = & \zeta_u(x), & \Omega, \end{array} \right.$$

whose the energy estimate is

$$\frac{d}{dt}\Big(\frac{1}{2}\|\tilde{u}\|^2_{L^2(\Omega)}\Big) = -\int_\Omega \sigma\cdot\nabla\tilde{u}\cdot\nabla\tilde{u}\,dx + \int_\Omega (k(f_r(u) - f_r(\hat{u})))\tilde{u}\,dx - \gamma\int_\Omega g_u(y,\hat{u})\tilde{u}\,dx.$$

In a general context, one would like to prove the exponential or linear decrease of the energy. However, a complete mathematical analysis of the observer error is here out of the scope, due to the complexity induced by both the nonlinear reaction term and the observer correction. In [4], we were satisfied with proving the negativity of the linearized version of the observer term proving that the gain term has a stabilization effect.

Theorem 2. *Under a condition of a sufficient sharpness of the data front detailed in [4] and when the measurement error e is identically zero, the observer term is energy-decreasing in the linearized error.*

This observer is compatible with the bidomain model when it is rewritten in terms of $u^{(m)} = u^{(i)} - u^{(e)}$ and $u^{(e)}$ and when the gain correction is added to the equation on $u^{(m)}$. Always is [4], numerical illustrations including parameters estimation were performed to validate the strategy.

***Mumford-Shah* functional** As discussed in [4], the observer design originates from an analogy with the dynamical behavior of contours tracking an object in a *Mumford-Shah*-based segmentation. The observer term corresponds to the *shape derivative* of the data-fitting term of the functional given in [CV91]

$$\mathcal{J}_u(u) = \int_{u>c_{th}} (y - C_{max}(y,u))^2\,dS + \int_{u<c_{th}} (y - C_{min}(y,u))^2\,dS,$$

that could also be seen as a functional of $\Omega_u = \{x\in\Omega, u > c_{th}\}$

$$\mathcal{J}_u(\Omega_u) = \int_{\Omega_u} (y - C_{max}(y,\Omega_u))^2\,dS + \int_{\Omega\setminus\Omega_u} (y - C_{min}(y,\Omega_u))^2\,dS,$$

as C_{in} and C_{out} could be rewritten easily in terms of Ω_u.

1.4.2 A new state observer based on the topological gradient

Our objective in this work was to extend the state observer introduced in [4]. Indeed, this observer is limited in the sense that it can only correct the front that is already present in the simulation. This means that, if we do not have a propagation front to be associated with the data, we are not able to compute any observer correction. Our goal here is to circumvent this limitation, in order to track complex types of propagation patterns such as cardiac fibrillations corresponding to irregular and often very rapid heart rhythms. This work was published in the proceeding [5].

In order to improve the observer formulation, we intend to follow a strategy of increasing importance in shape optimization [BHR04] or *level-set*-based image segmentation [HKO07, HL09]. The central idea is to complement the required shape derivatives, used to modify the shape contours, by a topological derivative that represents the sensitivity of $\mathcal{J}_u$ when removing a small part of the domain. Following [BHR04], we formally define the topological derivative of our functional by

$$d\mathcal{J}_u(\Omega_u) = \lim_{x \to 0} \frac{\mathcal{J}_u(\Omega_u \setminus B_{\rho,x}) - \mathcal{J}_u(\Omega_u)}{|\Omega_u \cap B_{\rho,x}|},$$

where $B_{\rho,x}$ denotes a ball of radius ρ and center x. This gives in our case as in [HL09]

$$d\mathcal{J}_u(\Omega_u) = (y - C_{in}(y, \Omega_u))^2 - (y - C_{out}(y, \Omega_u))^2.$$

Then, we incorporate this topological derivative in our observer as a new reaction term, when we detect a topological difference between the target solution and the observer solution. In this respect, we follow a simple reasoning inspired from [HKO07]. Using illustrations, we show in [5] that we only want to act in the region where $d\mathcal{J}_u \times (u - c_{th})$ is positive. We infer that we should consider a *topological gradient* term of the form

$$\vec{\nabla}_{\text{top}}\mathcal{J}_u = \Big(1 + \text{sign}\Big(d\mathcal{J}_u \times (u - c_{th})\Big)\Big) d\mathcal{J}_u,$$

where the first term selects the region where we want to act while the topological derivative $d\mathcal{J}_u$ provides the direction (creation or destruction).

We illustrate this observer on a realistic configuration where we purport to track an atrial fibrillation starting from a physiologically *healthy* initial condition. In order to synthetically generate the atrial fibrillation, we use a standard S1-S2 protocol [CFPS14]. The location of the stimulation S2 is near the left pulmonary inferior vein. Indeed, the pulmonary veins are known to be prone to frequent re-entries. The S1 stimulus corresponds to a standard sinus stimulation (natural pacemaker of the heart) at t = 0 and t = 700 ms, corresponding to the cardiac cycle period considered here. The S2 stimulus is triggered at t = 290 ms. The results of the simulation of the target atrial fibrillation are displayed in Figure 1.6 (left column). The figure shows successive time steps between t = 300 ms (note that before the S2 stimulus the simulation is the same as in the healthy case) and t = 820 ms, and compares the reference solution with the results obtained with our observer, and with a direct model simulation undergoing S1 stimulation only like the observer. We see that the observer very quickly and accurately captures the complex nature of the fibrillation solution.

1.4.3 Application to real data

This part is in collaboration with the Inria team Carmen. This team is a partnership between Inria and IHU Liryc and is specialized in modeling of cardiac electrophysiology. IHU Liryc is a unique center in

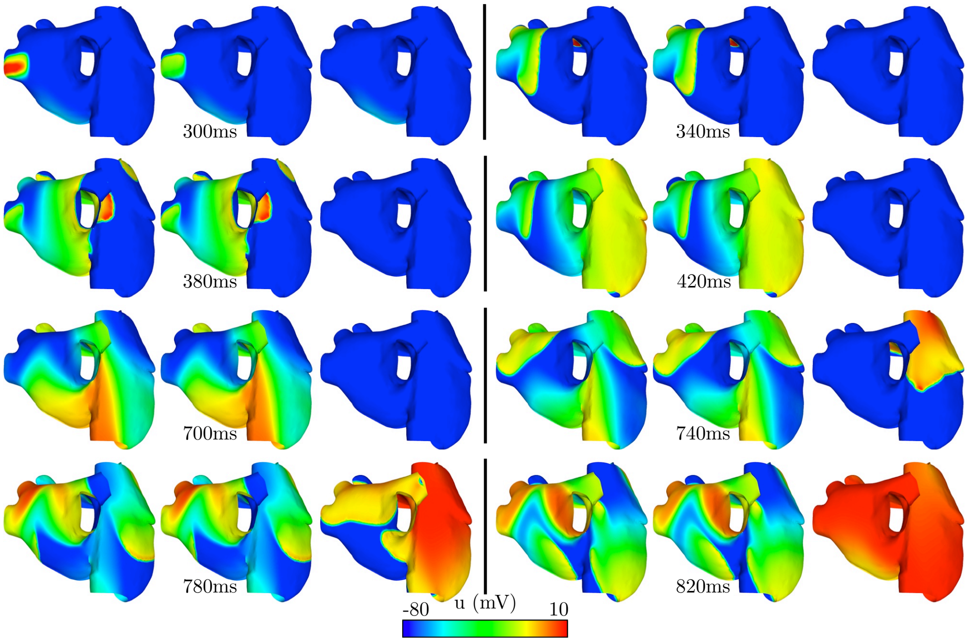

Figure 1.6 – Atrial fibrillation: target solution (left), observer solution (middle) and direct simulation without data (right)

the world which aims to understand and treat heart rhythm disorders better. This collaboration gave us access to a depolarization map of one patient extracted from Carto® system.

Strategy sensitivity Before applying it to real data, we evaluate the robustness of our data assimilation method when confronted with model simplifications. The model sensitivity is evaluated on the basis of synthetic data generated with a validated realistic atrial model that accounts for the specific atrial structure and fibers at endocardium and epicardium. The problem inverse is solved with simpler modeling components and this numerical analysis shows that, among other things, conductance anisotropy and knowledge of fiber distribution are essential to produce a model that matches observations, see [12]. Always in this article, we also work with real data but we do not present this result here. We will focus on another application detailed in the thesis of Antoine Gérard [Gér19] (in French).

Data presentation and application The goal of electro-anatomical mapping systems for clinicians is to give an anatomical representation of the chamber considered in the acquisition and to give electrical signal amplitude, signal complexity, local activation times... The functioning of the Carto® system used to register the data and the pre-processing steps to obtain data that can be used in practice are presented in the thesis of Antoine Gérard [Gér19] (in French). The data concerns the left atrium. The geometry and the depolarization map are presented in Figure 1.7-Top. One can see that even if the geometry is complete, the depolarization maps are partial. To deal with this problem, we consider instead of a constant gain parameter γ a spatial gain $\gamma : x \mapsto \mathbb{1}_{\omega^{\text{obs}}}(x)$ where ω^{obs} is the domain in which the data are available allowing to act only if the data are available.

A direct application of our observer is its capability to smooth and complete the activation maps using both corrections: the one based on shape gradient allow to smooth and to complete and the ones based on topological gradients to deal with the appearance of new fronts. Figure 1.7-Bottom illustrates the potential of the approach.

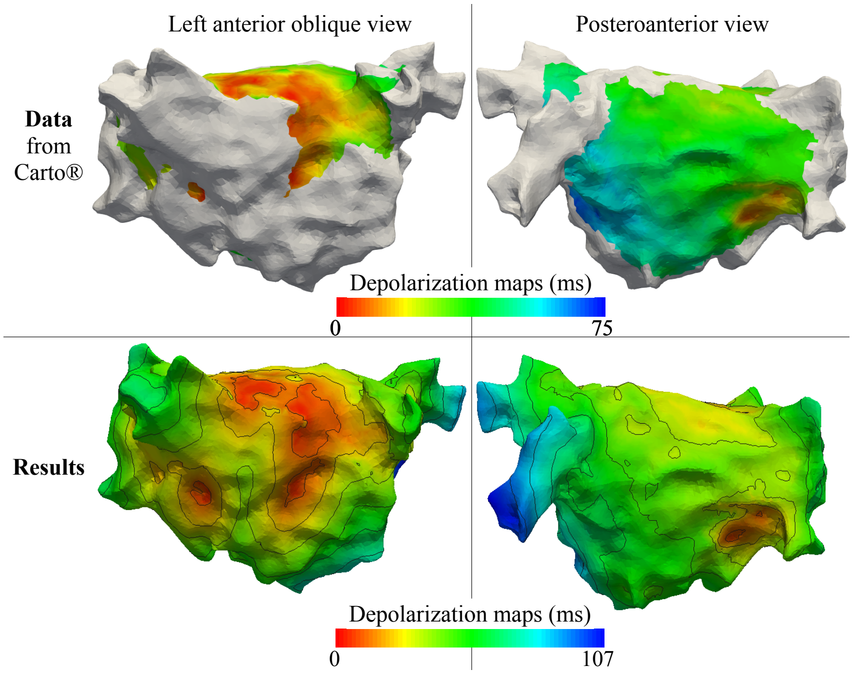

Figure 1.7 – Two views (left: leftanterior, right: posteroanterior) of depolarization maps of a patient left atrium. Top: Data extracted with Carto$^{®}$ system. Bottom: Map completion using sequential observers.

Remark 2. *The observer presented in Section 1.4.1 has also led to other applications. In the context of wildfire spread, a version compatible with an eikonal equation was proposed and illustrated with synthetic data in [9] and then illustrated with real data in [14]. In this context, a version compatible with a Lagrangian front-tracking model was also developed [13]. In Chapter 2 (see Section 2.3), we also present a work directly inspired from the design of this observer in the context of tumor growth.*

Conclusion

This chapter presents my contributions to cardiac electrophysiology modeling. As for the modeling aspects, the origin of the very classical bidomain model was studied. A complete and exhaustive mathematical analysis of the periodic homogenization procedure leading to the macroscopic bidomain model when the mechanical deformations of the heart are neglected has been presented. An extension of the microscopic bidomain model by a microscopic bidomain model taking into account the deformations of the myocardium was also proposed and derived thanks to a formal homogenization inspired by our previous mathematical analysis. Very realistic simulations of cardiac electrophysiology validate our approaches. As for the aspects of the inverse problem, whose aim is to illustrate our desire to get as close as possible to clinical applications, the strategy – we developed and validated from a mathematical point of view – was applied to the data of a patient. This underlines that our approach has great potential. In my research project given in Chapter 4, I will present my future work in this area.

Chapter 2

Contributions to tumor growth modeling

The innovative work presented in this chapter has been published in four accepted articles [20, 19, 17, 24].

Introduction

The purpose of this chapter is to present my mathematical contributions to tumor growth modeling. This work has started since I arrived in Bordeaux in 2015. Developing models able to accurately describe tumor growth may help monitoring the disease evolution or even predicting the efficacy of different therapeutic strategies. Mathematical modeling of tumor growth has recently drawn interest from the medical community. Indeed, since the pioneering work on glioblastomas [SBMAJ03], the development of such reliable models has helped better understand biological mechanisms and clinical behaviors of several types of tumor such as lung metastases [CCJ$^+$15], renal cell carcinoma [BBB$^+$15], and glioblastoma [SLCFS14, SBMAJ03] or the effects of treatments [BAB$^+$12, RKP$^+$12, RSC$^+$06]. Such applications are made possible mainly thanks to the development of realistic mathematical models which are personalized using patients' imaging.

My mathematical contributions to this application field can be summarized in the following points:
(1) **Select mechanistic models for tumor growth.** Unlike cardiac electrophysiology, where there is a reference model in the form of the bidomain model, there is no such consensus when modeling tumor growth. In my opinion, this can be explained by the fact that the unknowns of the system and the corresponding conservation laws and constitutive equations are still open questions due to the many uncertainties of how tumor growth works. Even though the roles of oxygen, nutrients, and angiogenesis (development of new vessels by the tumor itself) are becoming better understood, it can be difficult to translate them into mathematical equations, especially if one wants to obtain a parameterizable model with clinical data. In the Inria team MONC, we therefore decided to consider advection models for the temporal evolution of the densities of healthy and tumor cells.
(2) **Develop an efficient estimation strategy to adapt a tumor growth model to patients with meningioma.** Tumor growth models must be adapted to each individual case to generate predictive simulations for a given patient. In this context, abundant medical data – especially lesion volume, texture, and shape – can be used to identify model parameters. We develop an innovative strategy that combines a 0D reduction and population estimation approach to generate reliable predictions of the volume and the shape of tumors within a reasonable time frame. This strategy is illustrated using a large cohort of meningiomas (intracranial tumors). The results have been published in [17, 24].

(3) **Adapt this strategy when the tumor shapes are time-evolving.** The strategy described above is not efficient when the tumors have a time-evolving shape. To deal with this situation, we develop a sequential strategy. The main contribution is the development and the mathematical analysis of a *Luenberger* observer. This work has been published in [20].

These contributions are presented into three sections. Section 2.1 quickly presents the type of models used in the Inria team MONC and focus on a free growth model with only one density of tumor cells. The strategy developed to estimate its parameters very efficiently and using very few medical imaging is also presented. It corresponds to a part of the work published in [17]. In Section 2.2, the strategy is illustrated with a large cohort of intracranial meningiomas. Finally, in Section 2.3, we present the *Luenberger* observer to deal with time-evolving shapes whose the design is very inspired from the observers presented in Section 1.4.1 of Chapter 1.

2.1 Advection type models

2.1.1 General presentation

Let $\mathcal{B}$ be a bounded and smooth domain of $\mathbb{R}^3$. The tumor growth can be represented by mechanistic descriptions of the healthy and tumor cell densities evolution over time. We consider one (or more) tumor densitie(s) P_i, $\forall i \in [\![1; N_{TD}]\!]$ – corresponding to multiple cell lines or at different status of the cell (proliferative, quiescent, necrotic) – and one healthy density S such that $\sum_{i=1}^{N_{TD}} P_i + S = 1$. Historically in the MONC [RSC⁺06, BRS⁺09, BCG⁺10] team, the models used are advection type models

$$\begin{cases} \partial_t P_i + \nabla \cdot (\vec{v}\, P_i) &= \displaystyle\sum_{j=1}^{N_{TD}} f_{ij}(P_i, P_j), \quad \mathcal{B}, \quad \forall i \in [\![1; N_{TD}]\!], \\ \partial_t S + \nabla \cdot (\vec{v}\, S) &= 0, \quad \mathcal{B}. \end{cases} \tag{2.1}$$

One can see that we assume that S is only advected at the velocity $\vec{v}$ due to cellular division of cancer cells. This velocity corresponds to the motion of tumor cells. This is clearly not true as there is a biological action of the tumor on the extracellular matrix but in our setting, this assumption means that the global evolution of the tumor is not modified by the extra-tumoral medium. The saturation assumption leads to

$$\nabla \cdot \vec{v} = \sum_{i=1}^{N_T} \sum_{j=1}^{N_{TD}} f_{ij}(P_i, P_j).$$

To close the system, the Darcy's law is often considered $\vec{v} = -\nabla \pi$, where π is the pressure that tumor cells exert on healthy cells. The functions f_{ij} model the interactions between the different cells or the treatments impact. These complex models must be adapted to each individual case in order to produce predictive simulations for a given patient. In this context, the abundant available medical data – especially volumes, textures and shapes of the lesions – can be used to identify the model parameters.

2.1.2 Free growth tumor model

2.1.2.1 Modeling

In this section, we present a growth model with only one tumor density (*i.e.* $N_{TD} = 1$). We assume that it is free growth meaning that there is no treatment. This implies that the function f_{11} corresponds to the multiplication between P and a growth rate denoted in that follows by τ_G. The system reads

$$\left\{\begin{array}{rcll} \partial_t P + \nabla \cdot (\vec{v}\, P) & = & \tau_G(t,P)P, & \mathcal{B}, \\ \partial_t S + \nabla \cdot (\vec{v} S) & = & 0, & \mathcal{B}, \\ \nabla \cdot \vec{v} & = & \tau_G(t,P)P, & \mathcal{B}, \\ \vec{v} & = & -\nabla \pi, & \mathcal{B}. \end{array}\right. \tag{2.2}$$

Different dynamics could be considered for the growth rate:

(1) a constant growth rate: $\tau_G(t,P) = a$,

(2) a time dependent decreased growth rate to model its consumption by the tumor: $\tau_G(t,P) = ae^{-bt}$, where b^{-1} corresponds to the characteristic time at which the tumor growth capacity decreases and a to the initial growth rate,

(3) or a spatial and time dependent growth rate: $\tau_G(t,P) = ae^{-b\int_0^t P(s,\cdot)\mathrm{d}s}$ meaning that the consumption of the rate takes place only inside the tumor.

The two parameters a and b are assumed to be strictly positive constants. The modeling choices proposed here do not allow to obtain time-evolving shapes. To do so, one strategy consists in considering an initial growth rate distributed spatially meaning that a is not anymore a constant. We will come back to this case in Section 2.3. It is clear than one could probably consider models for tumor growth closer to biology but the major advantage of these three models is that they depend only on one or two parameters: a and b. We choose to keep the model simple to ensure that it can effectively be personalized for each patient using the sparse observations that are available in the clinical routine.

Concerning the boundary conditions (BC), it is quite easy to consider rigid constraints at the skull for example by considering that $\partial\mathcal{B} = \Gamma_c \cup \Gamma_f$, where Γ_c is the boundary corresponding to the rigid constraint and Γ_f the rest of the boundary. We then consider the following BC for the pressure

$$\pi = 0 \text{ on } \Gamma_f \text{ and } \nabla\pi \cdot \vec{n} = \vec{v} \cdot \vec{n} = 0 \text{ on } \Gamma_c. \tag{2.3}$$

We assume that the domain $\mathcal{B}$ is taken large enough such that the Dirichlet BC on Γ_f has no significant influence on the growth.

Developing first equation on (2.2) yields

$$\partial_t P + \vec{v} \cdot \nabla P = \tau_G(t,P)P(1-P). \tag{2.4}$$

Let the initial condition of P equal to $P(0,x) = 1$ inside the tumor and 0 elsewhere, one can easily see that $P(t,X) = 1$ inside the tumor and 0 elsewhere at any time. We define by $\Omega(t) = \{x, P(t,x) > 0.5\}$ the domain corresponding to the tumor at time t.

These models are simplified versions of the general model presented in Section 2.3.1 whose the existence and uniqueness is given in Propositions 2 and 3 under the hypothesis of Dirichlet boundary conditions for π (see [20] for the proof). Simulation of these PDE systems could be done using a following split-step scheme described in [17].

2.1.2.2 ODE systems embedded in PDE systems

Let us denote by $V(t)$ the volume of the lesion $\Omega(t)$ at time t. We have

$$V(t) = \int_{\mathcal{B}} P(t,X)dX = \int_{\Omega(t)} dX$$

by definition of P. One can prove the following proposition using Reynolds and Green theorems, see [17].

Proposition 1. *We have*

$$\begin{aligned}
&V(t) = V_0 e^{at}, \text{ if } \tau_G(t,P) = a,\\
&V(t) = V_0 e^{\frac{a}{b}(1-e^{-bt})}, \text{ if } \tau_G(t,P) = ae^{-bt},\\
&V(t) = V_0\left(1 + a\frac{e^{(a-b)t}-1}{a-b}\right), \text{ if } \tau_G(t,P) = ae^{-b\int_0^t P(s,\cdot)ds} \text{ and } a \neq b.
\end{aligned}$$

The first case corresponds to an exponential increase of the volume. One can recognize in the second case the formula of the Gompertz model, a very classical growth model, see [BLB$^+$14] for a full study and [Gom25, Cas34, Lai64, Lai65, Nor88] for validations of Gompertz model for tumor growth.

2.1.2.3 Estimation strategy

Descriptive power We will consider a cohort of N_P patients with for each individual $j \in [\![1;N_P]\!]$, N^j_{obs} MRI or CT scan examinations acquired at different times $(t^j_k)_{k\in[\![1;N^j_{\text{obs}}]\!]}$ are available. From these data, one can then extract – using for example a semi-automatic segmentation algorithm – the tumor volumes denoted $(\overline{V}^j_k)_{k\in[\![1;N^j_{\text{obs}}]\!]}, \forall j \in [\![1;N_P]\!]$. As PDE and ODE systems share the same parameters, they can be both estimated for a given patient j by fitting the ODE systems to the tumor volumes denoted $(\overline{V}^j_k)_{k\in[\![1;N^j_{\text{obs}}]\!]}$. This allows us to be able to deal with large cohort of real data.

Concerning theoretical identifiability, one can easily show that at least two (resp. three) measured volumes at two (resp. three) different times are necessary for the first (resp. second and third) case(s). However, only two or three medical imaging lead to overfitting and do not allow to integrate the fact that the data are noisy. One way to compensate for sparse sampling times and measurement uncertainties, is to consider a population approach allowing to constrain the variability of the parameters in the population of the N_P patients. More precisely, one can for example consider mixed-effects approach, see Section B.2 of the introduction chapter. The initial volume instead of be fixed with the volume computed using the first MRI examination is then considered as a covariate of $\overline{V}^j_0$

$$V^j_0 = \overline{V}^j_0(1+e^j_0), \ \forall j \in [\![1;N_P]\!],$$

where $e^j_0 \sim \mathcal{N}(0,\sigma^2_{V_0})$. The parameters a and b are decomposed as

$$\log(\{a^j, b^j\}) = \log(\{a^{\text{pop}}, b^{\text{pop}}\}) + \{\zeta^j_a, \zeta^j_b\}, \forall j \in [\![1;N_P]\!]$$

where $\{a^{\text{pop}}, b^{\text{pop}}\}$ are common for all the subjects and corresponds to fixed effects and $\{\zeta^j_a, \zeta^j_b\}$ – assumed to be centered – and are random effects. The Log-normal distribution allows to constraint the positivity of the parameters. Concerning the measurement error, we consider it proportional

$$\overline{V}_k^j = V^j(t_k)(1+e),\ \forall j \in [\![1; N_P]\!].$$

We assume that e follows a centered Gaussian law. The standard deviation σ_e is estimated and is used to define the 95% confidence interval: $[V^j(t)(1-1.96\sigma_e); V^j(t)(1+1.96\sigma_e)]$.

Predictive power We also develop a strategy to make prediction with only two medical imaging. More precisely, to answer the following question: using only two MRI examinations given at time t_0 and t_1, can we predict the volume and the shape of the tumor, at a later time t_2? It is a very difficult question because using only two time points, it is impossible to determine the behavior of the volume evolution for not constant growth rates, namely whether the volume evolution is linear, strictly convex or strictly concave. To answer this difficult question, we propose the following strategy. Let a patient denoted by j for which only two time data are available, we assume that a population of patients with at least 3 times is available and we will use this population to estimate the parameters of the patient j using once again the mixed-effects approach. Our strategy can be seen as a way to compensate the lack of available times of the given patient j by an available population of $N_P - 1$ patients.

The estimation strategies have been done using the stochastic approximation expectation maximization (SAEM) algorithm [KL05] implemented in `Monolix` [Ant19]. For all results, the convergence of the algorithm has been reached. In [24], a validation of the strategy has been done using synthetic data.

2.2 Illustration on a large cohort of meningiomas

2.2.1 Meningiomas

Arising from arachnoidal cap cells, they account for a third of primary adult intracranial tumors [BGA+11, OGF+13]. They become a major public health issue: (1) an annual increasing incidence ranging from 2-4.5% has been reported [BEB+18, BGA+11, OGF+13] and (2) one third of these tumors are asymptomatic at the time of diagnosis [BEB+18, BGA+11, HHI+09, NFN+05, OGF+13]. While most meningiomas are slow-growing tumors, some may exhibit important growth over a short period of time. Recent data have shown that asymptomatic meningiomas are observed in 1% to 2% of the population, especially in women over 60 years of age [JOV+11, KNP+04, VIT+07]. Surgery or radiation therapy remain the cornerstone of the treatment for meningiomas, and, following the diagnosis of asymptomatic lesions, clinicians struggle with the decision of either immediately treating the lesion using these invasive procedures, or simply planning periodical radiological examinations [BV97, GXCI+19, IMM+19a, KKC+18, MCZ+17, RRBP18, ZLJ+15]. In most cases, the frequency of such a monitoring is based on empirical strategies [Cou06, HHI+09, IMM+19b, JKK+11, MCZ+17, NRM+03, NNF+11, OKSL11, RRBP18, SRA+10, ZAD+08, ZLJ+15]. This is not optimal due to the potential toxicity of repeated Gadolinium infusions [LDAW18] and from a medico-economic point of view. Consequently, predicting the progression of asymptomatic lesions is paramount to inform decision-making. However, to our knowledge, only one predictive tool [BBRRH+19, LKP+17, LPPK17] is available to assess the growth rate of untreated meningiomas and help clinicians in selecting which patients to treat or simply monitor. This tool was developed based on statistical predictions using various clinical and imaging data collected at the time of diagnosis. Our objective is to use mathematical modeling of the underlying physiopathological processes to offer an accurate alternative in terms of prediction of growth.

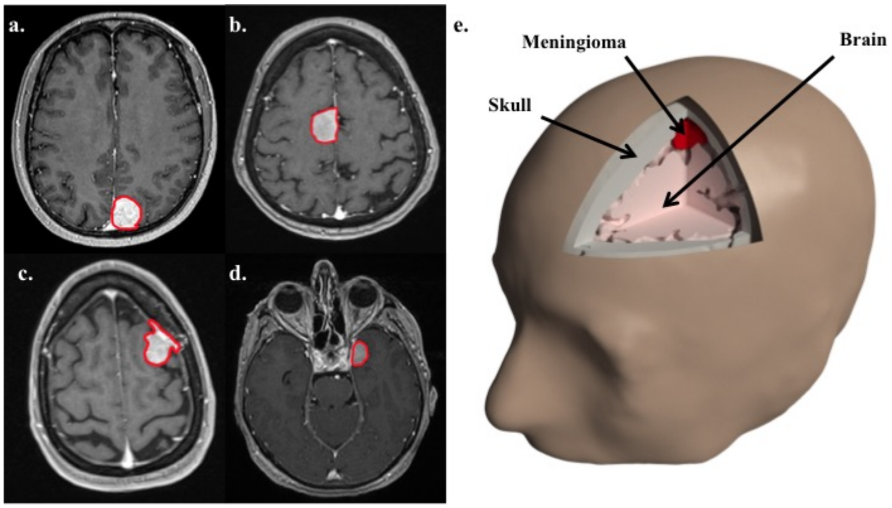

Figure 2.1 – Left: MRI T1 of 4 patients with tumor boundaries in red. Right: Anatomical view of a meningioma with skull, brain and meningioma geometries delineated in 3D from the MRI examination.

2.2.2 Clinical data

Study design and participants - In this retrospective study, we analyze the clinical, radiological and volumetric data of all the consecutive patients who were referred to the neurosurgical consultation of H. Loiseau between December 2013 and August 2021 for an incidental meningioma. All the patients had regularly empirically defined clinical and radiological follow-up. Treatment (surgery, stereotactic or fractioned radiotherapy) was proposed according to volumetric progression and/or neurological symptoms as done in daily practice and was approved by the tumor board.

Procedure and variable extraction - All the imaging (MRI scans with 3D millimetric T1 WI sequence with gadolinium or CT-scans with contrast product injection if contraindications to MRI) were analyzed with the Sophia Radiomics$^{©}$ software which allows 3D volumetric measures by a semi-automatically segmentation algorithm. Illustrations of the segmentation process are given in Fig 2.1. Using this tool, we have extracted for each patient of the cohort the volumes and the shapes of the tumor at each time. For very few of them (9 patients), the skull has also been segmented to perform 3D simulations.

Inclusion and exclusion criteria for mathematical modeling - Only tumors with at least three imaging at different time points were included. Exclusion criteria were missing baseline radiological data, cyproterone, nomegestrol and chlormadinone acetate treatment at the time of meningioma diagnosis, type 2 neurofibromatosis, and a statistically significant decrease in volume over time. During the study period, 294 consecutive patients with $N_P = 333$ tumors met the inclusion criteria.

Clinical questions - Using these data, we want to answer three questions:
(1) Descriptive power: Can we model the dynamics of meningioma *volume* evolution?
(2) Classification: Can we classify the meningiomas depending of their agressiveness?
(3) Predictive power: Using only 2 MRI examinations, can we predict the tumor *volume* and the *shape* at a later time?

Model	AIC	BIC	$\frac{1}{N_P}\sum_{j=1}^{N_P}\text{MSE}^j$	$\frac{1}{N_P}\sum_{j=1}^{N_P}E^j_{L^1}$	$\frac{1}{N_P}\sum_{j=1}^{N_P}E^j_{L^\infty}$
Linear	1279	820	0.085 [0.056;0.14]	0.066 [0.045;0.11]	0.14 [0.091;0.24]
Exponential	983	1002	0.075 [0.047;0.13]	0.060 [0.038;0.10]	0.13 [0.077;0.22]
Power	802	829	0.074 [0.045;0.12]	0.056 [0.035;0.10]	0.12 [0.076;0.18]
Gompertz	**793**	**819**	**0.066 [0.044;0.11]**	**0.053 [0.036;0.089]**	**0.11 [0.072;0.18]**

Table 2.1 – Descriptive power: Fit performances according to AIC and BIC criteria, MSE and errors of the four volume models.

2.2.3 Descriptive power

Concerning the volume evolution, we will consider the Gompertz model ($\tau_G(t) = ae^{-bt}$) and the exponential model ($\tau_G = a$). For the results with the spatial growth rate on a small cohort (40 patients), we refer to [17]. To answer the **first question**, the two models are also compared to two other very classical growth models which are not related to a PDE system:

- Linear model: $V(t) = V_0 + at$ $(V_0 > 0, a > 0)$,
- Power model: $V(t) = (V_0^{1-\gamma} + a(1-\gamma)t))^{\frac{1}{1-\gamma}}$, solution of $V' = bV^\gamma$ $(V_0 = V(0) > 0,\ a > 0,\ 0 < \gamma < 1)$.

To estimate the parameters of the four 0D models, the population approach presented in Section 2.1.2.3 is applied. The goodness of fit are compared by the Akaike (AIC) and the Bayesian information criterion (BIC). For each meningioma j, we also compute the errors between estimated and real volumes calculated according the relative L^1 and L^∞ norms and the Mean Squared Error (MSE):

$$E^j_{L^1} = \frac{1}{N^j_{\text{obs}}}\sum_{k=1}^{N^j_{\text{obs}}}\frac{|V^j(t_k) - \overline{V}^j_k|}{\overline{V}^j_k},\ E^j_{L^\infty} = \max_{k=1\cdots N^j_{\text{obs}}}|V^j(t_k) - \overline{V}^j_k|,\ \text{MSE} = \frac{1}{N^j_{\text{obs}}}\sum_{k=1}^{N^j_{\text{obs}}}\frac{(V^j(t_k) - \overline{V}^j_k)^2}{(\overline{V}^j_k)^2}.$$

Table 2.1 gives AIC, BIC and errors. The Power and Gompertz models gave similar results with fairly close AIC and BIC and no significant difference between errors calculated by the 3 metrics. The Power and Gompertz models gave significantly smaller errors. Because the Gompertz model gave the best results in all the metrics used, it was selected to model the meningiomas growth. This model has also the advantage to be compatible with one of the PDE system allowing to test the availability to describe the shape of the meningiomas. The standard deviation σ_e of the proportional error was estimated at 14.6%. Figure 2.2 depicts six representative growth curves of meningiomas fitted with the four models. Note how the linear model (resp. the exponential model) does not fit the data for ID 120 (resp. for ID 305). ID 50 and ID 53 are two tumors with very close initial volumes (9.2 and 9.9 cm^3 resp.) at first imaging and with the same length of follow-up but with different growth pattern over time and thus for ID 53, only Gompertz model fits well the data. For ID 50 and ID 164, the 4 models are similar. ID 12 had similar dynamics to ID 53 despite a very smaller initial volume and once again, only Gompertz model fits well the data.

2.2.4 Classification

Once the parameters estimated, the estimated volume V is known for all times using explicit formulas of the models. We then estimate the relative growth-rate (RGR) during the X months before and after as

$$\text{RGR}^j_{-X}(t) = \frac{V^j(t) - V^j(t-X)}{V^j(t)} \text{ and } \text{RGR}^j_{+X}(t) = \frac{V^j(t+X) - V^j(t)}{V^j(t)},\ \forall t \geq 0.$$

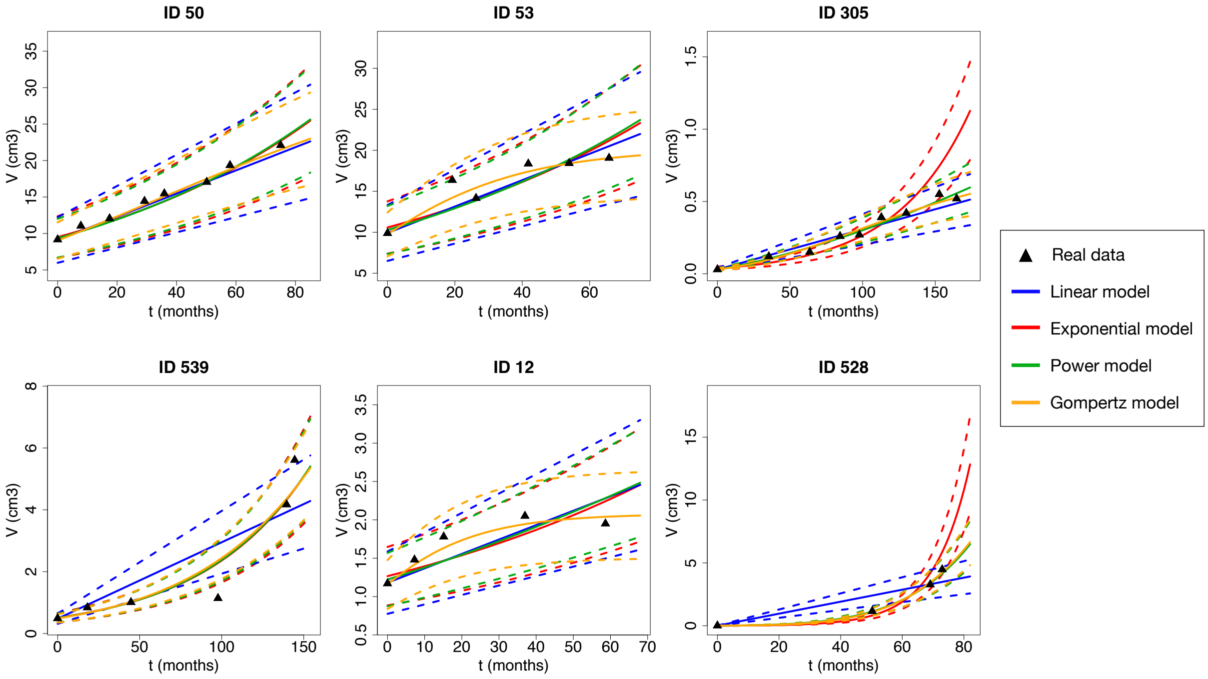

Figure 2.2 – Descriptive power - Six illustrative examples of tumor growth modeling with the four models.

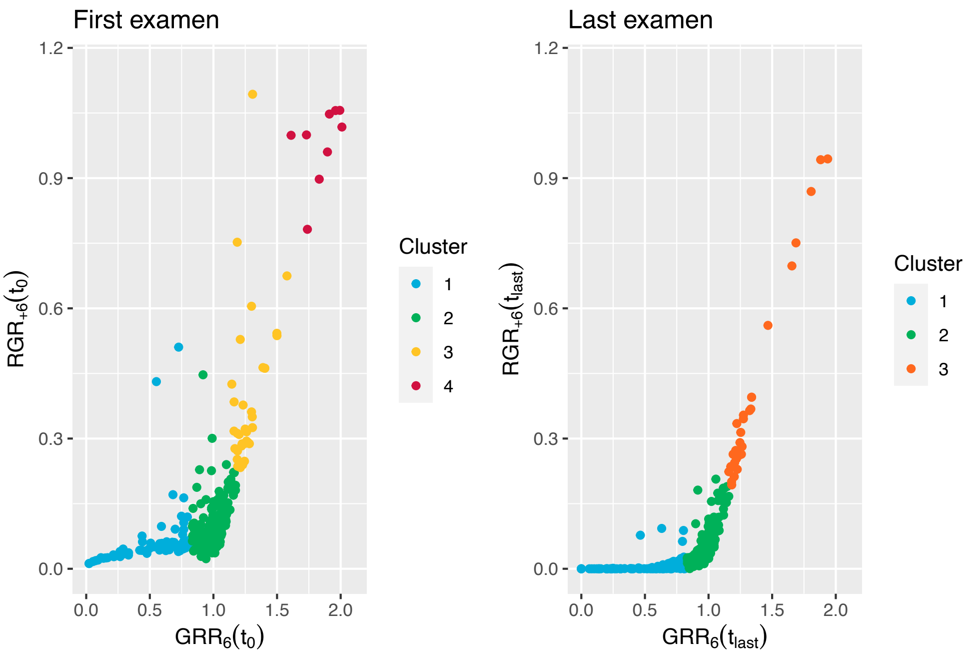

Figure 2.3 – Classification - Hierarchical clustering results.

Error (mean of 33 patients)	$E^{t_2}_{L^1}$	$B^{t_2}_{L^1}$
Gompertz model	9.9 %	0.007
Linear model	12.5%	0.024

Table 2.2 – Predictive power - Relative error $E^{t_2}_{L^1}$ and relative bias $B^{t_2}_{L^1}$ (see Eq. (2.5)).

To estimate if at a given time t, the RGR was increasing or decreasing, the following growth rate ratio (GRR) was computed $\mathrm{GRR}^j_X(t) = \dfrac{\mathrm{RGR}^j_{+X}}{\mathrm{RGR}^j_{-X}}$. If GRR^j_X is strictly inferior to 1, it means that the growth of the meningioma slows down, if GRR^j_X equals to 1, the growth is linear and if GRR^j_X is strictly superior to 1, the growth of the meningioma accelerates. One can easily prove that when volume follows a Gompertz model, the relative growth rates and the growth ratio are decreasing functions over time. To answer the **second question**, a hierarchical clustering of the meningiomas was done using RGR_{+6} and GRR_6. The value of 6 months has been selected based on two facts: (1) our ability to well estimate the quantities at 6 months has been validated on synthetic data (see [24]) and (2) the period of time is sufficiently long to detect a change in growth rate. The dendrogram obtained was computed using the Ward.D2 agglomeration method of the `hclust` function of `R`. The number of clusters is selected using the dendrogram. Figure 2.3 gives the results of the classification. At the first examen time, the hierarchical clustering identifies 4 clusters – that could name – as

- **Cluster 1** - slowing-growth pattern meningiomas: $\mathrm{GRR}_6 = 0.3\,[0.2; 0.4]$,
- **Cluster 2** - linear pattern meningiomas: $\mathrm{GRR}_6 = 1.0\,[0.9; 1.0]$,
- **Cluster 3** - accelerating pattern meningiomas: $\mathrm{GRR}_6 = 1.1\,[1.1; 1.2]$ and $\mathrm{RGR}_{+6} = 19.4\%\,[14.3\%; 28.8\%]$,
- **Cluster 4** - very accelerating pattern: $\mathrm{GRR}_6 = 1.6\,[1.4; 1.9]$ and $\mathrm{RGR}_{+6} = 79.1\%\,[53.7\%; 102.8\%]$.

and at the last examen time, it identifies 3 clusters – that once again could name –

- **Cluster 1** - slowing-growth pattern meningiomas: $\mathrm{GRR}_6 = 0.3\,[0.2; 0.5]$,
- **Cluster 2** - linear pattern meningiomas: $\mathrm{GRR}_6 = 0.9\,[0.9; 1.0]$,
- **Cluster 3** - and accelerating pattern meningiomas: $\mathrm{GRR}_6 = 1.2\,[1.1; 1.3]$.

The clinical and radiological features of the meningiomas by cluster have been studied by our collaborating clinicians. We only give a small summary to show how our work could be use useful but we refer to [24] for more details. We observe that age at diagnosis and the initial volume of the tumors significantly increased from cluster 4 to cluster 1 (from 56.9 to 64.7 years-old and from 0.34 to 1.43 cm^3 respectively). We also observe a significantly increasing proportion of patients who have had a cranial radiotherapy before the diagnosis of meningioma from the cluster 4 to 1 (from 26.3% to 3.4% respectively). We did not find any correlation between the proportion of meningiomas with a hypersignal FLAIR, calcifications or edema and the clustering. Consistently, we do not observe any correlation between the clustering and the AIMSS risk score. We observe a significantly increasing proportion of treated meningiomas from cluster 1 to 4 (from 3.4% to 68.4% respectively) without any significant difference between the delay to treatment and volume at treatment. Among the meningiomas operated on, we observe a significantly increasing proportion of WHO grade II tumors from cluster 1 to 4 (from 0% to 64% respectively). The main perspective of this research is to try to predict the cluster using only the initial imaging features through radiomics approach. This work is in progress in the context of the PhD of Virginie Montalibet.

Pat	2	4	7	8	9	11	18	20	22	23
PDE model	95%	93%	83%	87%	65%	85%	86%	90%	85%	87%
Redist.	94%	93%	74%	69%	52%	82%	86%	87%	66%	88%

Table 2.3 – Predictive power - Sørensen-Dice coefficient SDC_2 (see Eq. (2.6))

2.2.5 Predictive power

Concerning the predictive power, the population strategy presented at the end of Section 2.1.2.3 has been applied in [17] on 33 patients for the volume prediction and on 10 patients for the shape prediction. Extend this database is one of the perspective of the PhD of Virginie Montalibet. The two main issues concern the optimization of the PDE resolution and the development of an automatic strategy to segment the skull.

To validate the strategy, we first compute the relative error $E_{L^1}^{t_2}$ and the relative bias $B_{L^1}^{t_2}$ between the predicted volume at t_2 and the measured volume given by

$$E_{L^1}^{t_2} = 100 \sum_{j=1}^{N_P} \frac{|V^j(t_2) - \overline{V}_2^j|}{\overline{V}_2^j} \text{ and } B_{L^1}^{t_2} = \sum_{j=1}^{N_P} \frac{V^j(t_2) - \overline{V}_2^j}{\overline{V}_2^j}. \tag{2.5}$$

Regarding the results given in Table 2.2, the prediction strategy gives very interesting results. Indeed, the results are excellent: using the ODE system, we can predict the volume at t_2 with an error inferior to 10 $\%$ *i.e.* with the same order of magnitude of the segmentation error. Concerning the bias, it is smaller using the ODE system than linear model.

Second, concerning the shape, we will compare then using the Sørensen-Dice coefficient. To do so, we denote by $\overline{\Omega}_2^j$ the segmented 3D domain using the MRI at time t_2 for a given patient j and we denote by Ω_2^j the 3D domain corresponding to $\Omega_2^j = \{x \in \mathcal{B}, P^j(t_2, x) > 0.5\}$, where P^j is the solution of the PDE system (2.2) for a given patient j. The Sørensen-Dice coefficient is defined as

$$\text{SDC}_2^j = 100 \frac{2|\Omega^j \cap \overline{\Omega}^j|}{|\Omega^j| + |\overline{\Omega}^j|}. \tag{2.6}$$

On can easily see that for an individual meningioma SDC_2^j is in [0, 100]% and that if SDC_2^j is close to 100% (resp. to 0%), the predicted shape is close (far away) to the measured shape at t_2. We compare the solutions of the PDE model with the shape obtained by doing an expansion of the shape of the initial tumor using a redistancing process. To do that, we consider the level set of the initial shape with a volume equals to the volume predicted using the linear 0D model. Table 2.3 gives the results. One can see that the shape of the tumor is very well estimated with a mean of 85% for PDE systems and 79% for the linear model. The results are very encouraging. Figure 2.4 shows the shape for 10 patients. The limitation of the linear model (which is not able to take into account the boundary of the skull) can be seen on the results of Patients 7, 8, 9 and 22. Concerning the PDE system, one can see that – expected Patient 9 – the results are very encouraging. Concerning Patient 9, its shape evolves in time. It is one of the main limitation of the PDE model – presented in Section 2.1.2.1 – to not be able to integrate this phenomenon. In the next section, we will explain the approach that could be applied in this context.

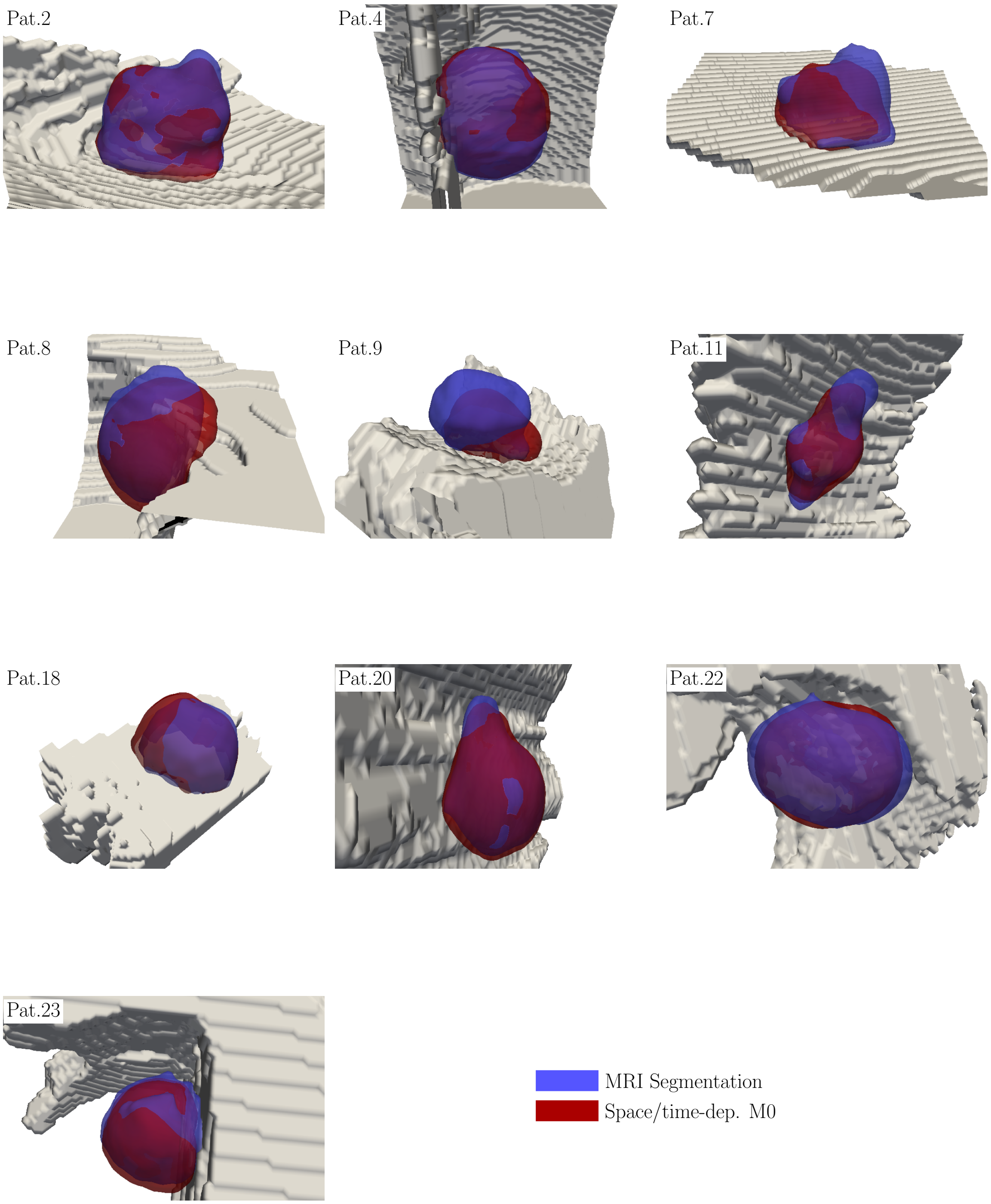

Figure 2.4 – Predictive power - 3D views of the solution of PDE system (red) compared to the MRI segmentation (blue) at the last available time for 10 patients. The supportive arachnoid tissue (skull) is represented by the grey surface.

2.3 Tumor model with time-evolving shapes

In this section, we present work published in [20] that aims to address the estimation of tumor evolution when they have a nontrivial shape. This estimation provides crucial information, for example, in brain or lung tumors, since the tumor may affect vital functions or structures of the diseased organ. Our strategy is based on the development of a joint state and parameter observer as presented in Algorithm (6) of the introduction chapter. Section 2.3.1 presents the model – which is a generalization of System (2.2) – and the existence and uniqueness results. The state observer is then given and studied in Section 2.3.2. Results of existence and uniqueness and convergence theorems are also given. In Section 2.3.3, the strategy to use in practice is presented. Numerical illustrations are given.

2.3.1 Tumor model and analysis

We consider a generalization of System (2.2) (corresponding to $\tau_G^0(t,P) = \tau_G^1(t,P) = \tau_G(t,P)P$) and with Dirichlet boundary conditions for the pressure

$$\left\{\begin{array}{rcll} \partial_t P + \nabla\cdot(\vec{v}\,P) & = & \tau_G^0(t,P), & \mathcal{B}, \\ S+P & = & 1, & \mathcal{B}, \\ \nabla\cdot\vec{v} & = & \tau_G^1(t,P), & \mathcal{B}, \\ \vec{v} & = & -\nabla\pi, & \mathcal{B}. \end{array}\right. \tag{2.7}$$

The functional τ_G^0 describes the tumor evolution and the functional τ_G^1 the induced pressure due to tumor expansion. We make the following assumptions on these two functionals.

Assumption 2 (Assumptions on the functional mappings τ_G^i, $i = 0,1$)**.**

- *For $i = \{0,1\}$, τ_G^i are uniformly bounded and smooth functionals which map $\mathbb{R}^+ \times L^\infty(0,T;H^s(\mathcal{B}))$ into $L^\infty(0,T;H^s(\mathcal{B}))$ for any $s \geq d/2$.*
- *For any $P \in L^\infty(0,T;H^s(\mathcal{B}))$, the function g_P is defined on $\mathbb{R}^+ \times \mathcal{B}$ by*

  $$g_P(t,x) = \tau_G^0(t,P(t,x)) - P\tau_G^1(t,P(t,x)).$$

  The function g_P is such that for any $P \in L^\infty(0,T;H^s(\mathcal{B}))$, g_P belongs to $L^\infty(0,T;H^s(\mathcal{B}))$. Moreover if $P(t,\cdot)$ compactly supported in $\mathcal{B}$, then $g_P(t,\cdot)$ is compactly supported in $\mathcal{B}$.

The following propositions study the existence and uniqueness in case of Dirichlet boundary conditions on π ($\Gamma_c = \emptyset$ in Equation (2.3)).

Proposition 2. *Assume that the initial condition of P belongs to $H^s(\mathcal{B})$ such that its support is compactly embedded in $\mathcal{B}$. Then there exists T small enough such that Problem (2.7) coupled with $\pi = 0$ on $\partial\mathcal{B}$ admits a unique solution in $L^\infty(0,T;H^s(\mathcal{B}))$ whose support is compactly embedded in $\mathcal{B}$.*

Proposition 3. *Let $s \geq 5/2$ and assume that the initial condition of P belongs to $H^s(\mathcal{B})$ such that its support is compactly embedded in $\mathcal{B}$, and assume in addition that its values belong to the interval $[0,1]$. Let $\mathcal{L}_{\tau_G}^0$ satisfy Assumption 2, and set*

$$\forall u \in L^\infty(0,T;H^s(\mathcal{B})), \qquad \tau_G^0(t,u) = \tau_G^1(t,u) = u\mathcal{L}_{\tau_G}^0(t,u).$$

For $i = 0, 1$, it is obvious that τ_G^i satisfies Assumption 2, and let T be such that the unique solution P of (2.7) exists in $L^\infty(0,T;H^s(\mathcal{B}))$, and such that the support of P is compactly embedded in $\mathcal{B}$ then for any $t \in (0,T)$, $0 \le P(t,x) \le 1$.

The proofs given in [20] rely on the hyperbolic properties of the tumor model, combined with Gagliardo-Nirenberg estimates in Sobolev spaces.

2.3.2 State observer: design and study

Data As previously, we consider that we have at our disposal MRI or CT scan examinations at different times. In the previous presented work, only the segmented volumes are used to estimate the parameters. In this work, we investigate how the shape of the tumor may be used to circumvent the uncertainties associated with the dynamical model. More precisely, we consider that the measurements (denoted by y) are time-continuous sequences of tumor masks, namely, maps taking essentially two different values inside and outside the tumor region, up to some perturbations and regularization across the front.

Context We consider the particular case: $\tau_G^0(\cdot,P) = \tau_G^1(\cdot,P) = \mathcal{L}^0_{\tau_G}(\cdot,P)P$ where τ_G^i, $i = \{0,1\}$ verify Assumption 2. The *target* system reads

$$\left\{\begin{array}{rcll} \partial_t P + \nabla\cdot(\vec{v}\,P) &=& \mathcal{L}^0_{\tau_G}(t,P)P, & \mathcal{B}, \\ \nabla\cdot\vec{v} &=& \mathcal{L}^0_{\tau_G}(t,P)P, & \mathcal{B}, \\ \vec{v} &=& -\nabla\pi, & \mathcal{B}, \\ P(0,\cdot) &=& P^0_\diamond + \zeta_P, & \mathcal{B}, \end{array}\right. \tag{2.8}$$

where ζ_P is the initial condition uncertainty that we would like to control with the *observer* system

$$\left\{\begin{array}{rcll} \partial_t \hat{P} + \nabla\cdot(\hat{\vec{v}}\,\hat{P}) &=& \mathcal{L}^0_{\tau_G}(t,\hat{P})\hat{P} + \gamma g_P(y,\hat{P}), & \mathcal{B}, \\ \nabla\cdot\hat{\vec{v}} &=& \mathcal{L}^0_{\tau_G}(t,\hat{P})\hat{P}, & \mathcal{B}, \\ \hat{\vec{v}} &=& -\nabla\hat{\pi}, & \mathcal{B}, \\ \hat{P}(0,\cdot) &=& \hat{P}^0_\diamond, & \mathcal{B}. \end{array}\right. \tag{2.9}$$

In this work, we consider that g_P designs a consistent observer providing physically realistic solutions.

Assumption 3. *We assume that g_P satisfies the following assumptions:*
- *If P is the solution of the target system (2.8), then $g_P(y,P) = 0$,*
- *For any $u \in L^\infty(0,T;H^s)$ for s large enough,*

$$\begin{cases} \text{If } u \le 0 \text{ then } g_P(y,u) \ge 0, \\ \text{If } u \ge 1 \text{ then } g_P(y,u) \le 0. \end{cases} \tag{2.10}$$

Proposition 4. *Assume that $P^0_\diamond$ and ζ_P are such that*

$$0 \le P^0_\diamond \le 1, \qquad 0 \le P^0_\diamond + \zeta_P \le 1, \qquad \text{in } \mathcal{B}.$$

Assume in addition that $\mathcal{L}^0_{\tau_G}$ is such that the solution to Problem (2.8) exists in $L^\infty(0,+\infty;H^s)$. Finally assume that g_P satisfies Hypothesis 3 and is such that for any $\gamma > 0$, the solution to Problem (2.9) exists in

$L^\infty(0,+\infty;H^s)$. *Then*

$$0 \le \hat{P} \le 1, \qquad \textit{a.e. in } (0,+\infty)\times\mathcal{B}.$$

The proof is obvious thanks to Assumption (2.10).

In order to investigate the convergence of the state observer towards the target solution, we consider the linearization of the observer term g_P

$$g_P(y,\hat{P}) \approx -dg_P(y,P)(P-\hat{P}).$$

This approximation is valid when the difference between $\hat{P}$ and P is assumed to be small (*i.e.* the uncertainty of the initial condition is assumed to be reasonable). We denote by $\hat{P}$ the solution to the following linearized state observer model in the sense of distribution:

$$\begin{cases} \partial_t \hat{P} + \nabla\cdot(\vec{\hat{v}}\,\hat{P}) &= \mathcal{L}^0_{\tau_G}(t,\hat{P})\hat{P} + \gamma\, dg_P(y,P)(\hat{P}-P), & \mathcal{B}, \\ \nabla\cdot\vec{\hat{v}} &= \mathcal{L}^0_{\tau_G}(t,\hat{P})\hat{P}, & \mathcal{B}, \\ \vec{\hat{v}} &= -\nabla\hat{\pi}, & \mathcal{B}, \\ \hat{P}(0,\cdot) &= \hat{P}^0_\diamond, & \mathcal{B}. \end{cases} \tag{2.11}$$

According to Proposition 2 there exists T small enough such that the unique solution to Problem (2.8) exists and belongs to $L^\infty(0,T;H^s)$, $s>5/2$. In addition if $dg_P(y,P)$ maps $L^\infty(0,T;H^s)$ into itself for $s>5/2$, thus for any $\gamma>0$, there exists a unique solution to Problem (2.11) in $L^\infty(0,T^\gamma;H^s)$, $s>5/2$ with $T^\gamma<T$. However we are not interested in the condition to ensure global existence. We assume in the following proposition that $\mathcal{L}^0_{\tau_G}$ and g_P are well-chosen to ensure a global existence of the solution to the two problems (2.8) and (2.11) and we focus on the convergence proof.

Proposition 5. *Assume also that $P^0_\diamond$ and ζ_P are such that*

$$0 \le P^0_\diamond \le 1, \qquad 0 \le P^0_\diamond + \zeta_P \le 1, \qquad \textit{in } \mathcal{B}.$$

Assume in addition that $\mathcal{L}^0_{\tau_G}$ is such that the solution to Problem (2.8) exists in $L^\infty(0,+\infty;H^s)$ and that $g_P(y,P)$ is such that for any $\gamma>0$, the solution to Problem (2.11) exists in $L^\infty(0,+\infty;H^s)$.

- *If there exist $\alpha>0$ and $\beta>0$ such that*

$$\int_{\mathcal{B}} dg_P(y,P)(u)u\,dx \ge \alpha\|u\|^2_{L^2(\mathcal{B})} - \beta, \qquad \forall u \in L^\infty(0,+\infty;H^s), \tag{2.12}$$

then there exists $c>0$ such that for any $t>0$, for any $\gamma>0$,

$$\|(\hat{P}-P)(t)\|^2_{L^2(\mathcal{B})} \le \|(\hat{P}-P)(0)\|^2_{L^2(\mathcal{B})} e^{-(\gamma\alpha-c)t} + \frac{\gamma\beta\left(1-e^{-(\gamma\alpha-c)t}\right)}{\gamma\alpha-c}. \tag{2.13}$$

In particular if $\beta=0$, for any $\gamma>\frac{c}{\alpha}$, $t\mapsto\|(\hat{P}-P)(t)\|_{L^2(\mathcal{B})}$ decreases exponentially towards 0.

- *If there exists $\alpha>0$ and $p\ge1$ such that*

$$\int_{\mathcal{B}} dg_P(y,P)(u)u\,dx \ge \alpha\|u\|_{L^p(\mathcal{B})}, \qquad \forall u \in L^\infty(0,+\infty;H^s), \tag{2.14}$$

there exists $\gamma_{0,p}$ such that for any $\gamma > \gamma_{0,p}$, $t \mapsto \|(\hat{P}-P)(t)\|^2_{L^2(\mathcal{B})}$ decreases linearly towards 0. In addition, if $p=2$, then $t \mapsto \|(\hat{P}-P)(t)\|_{L^2(\mathcal{B})}$ decreases linearly towards 0.

The proof given in [20] consists in the study of the *error* system as explained in the first chapter. Inspiring from the observer presented in Section 1.4.1 of Chapter 1, we consider

$$g_P(y,\hat{P}) = \delta_{\{x\in\mathcal{B},\hat{P}(t,x)=c_{th}\}}(t)\,\|\nabla\hat{P}\|\,((y-C_{max}(y,\hat{P}))^2-(y-C_{min}(y,\hat{P}))^2), \tag{2.15}$$

where c_{th} is the threshold constant allowing to compare $\hat{P}$ to the segmented MRI domain. We refer to Section 1.4.1 of Chapter 1 for all the other notations. Always in [20], we show the following proposition.

Proposition 6. *Assume that the data y is sharp enough and satisfies the assumption given in [4]. Assume that there exists $\varepsilon > 0$ to be assumed small such that at any time t the solution $\hat{P}$ of (2.11) with g_P defined by Eq. (2.15) is such that $\tilde{P} = P - \hat{P}$ has a compact support included in a tubular neighborhood of $\Gamma_P(t) = \{x, P(t,x) = c_{th}\}$ of width ε.*
Then for any $\gamma > 2c\varepsilon/\alpha$, for any $t > 0$

$$\|\tilde{P}(t)\|^2_{L^2(\mathcal{B})} \leq \|\tilde{P}(0)\|^2_{L^2(\mathcal{B})} e^{-(\frac{\gamma\alpha}{\varepsilon}-c)t} + 4\frac{\varepsilon^2\bar{C}}{\alpha}.$$

The proof of the proposition is inspired from [4] and is based on the Fréchet derivative formalism. Regarding the choice of the gain parameter, the value of γ through the proposition is probably not optimal and only roughly evaluable in practice. In [Kri18] (in French), a practical study to choose γ is proposed.

Remark 3. *Concerning the above proposition, the second hypothesis is similar to assume that the error is localized to the tumor front which is coherent in our context, where data consists mainly of tumor segmentation. The proposition also shows that the observer decreases the error exponentially fast from ε to ε^2 in L^2 norm. Since the observer term only acts on the front, one cannot show the exponential decay over time.*

2.3.3 And in practice?

To use the following state observer in practice, some points need to be lifted:

(1) **Selection of a model for τ_G^0 (= τ_G^1).** In [20], we consider $\tau_G^0(t,P) = ae^{-b\int_0^t P(s,\cdot)\mathrm{d}s}$ in the case where the initial growth rate a is spatially distributed allowing to consider time-evolving shapes. When it is spatially distributed, it is denoted a^s.

(2) **Dealing with the very few available data.** In practical situations, data is not a time-continuous sequence of images, but a sequence of very few images acquired at distant times. In order to calculate the correction terms at a given time t, the idea is to interpolate data. The easiest way is to use a linear interpolation. However, when the tumor volume satisfies a solvable ODE, it is more accurate to use it to interpolate data. A redistanciation process has been taken in place, see [20] for all details.

(3) **Strong correlation between a and b.** A correlation between the parameters a and b in a population of tumors has been observed frequently in Gompertz model. In [VRF$^+$20], a reduced Gompertz model is even introduced: b is estimated as explained in Section 2.1.2.2 and $k = \frac{a}{b}$ as a constant parameter in the population. In this context, we cannot consider this kind of strategy as we do not have a large database at our disposal. We only fix b using the 0D estimation obtained assuming a constant. Only the initial distribution of the growth rate a^s is estimated using the sequential strategy.

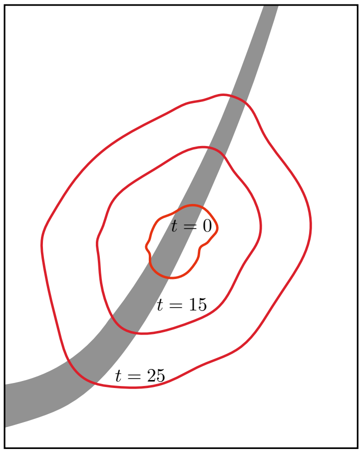

Figure 2.5 – Synthetic data obtained at time $t_0 = 0$, $t_1 = 15$ and $t_2 = 25$. This simulation is obtained with a^s taking a value $a^{\text{in}} = 0.3$ inside the synthetic vessel (white front), and $a^{\text{out}} = 0.08$ outside the vessel.

(4) **Dealing with the fact that the shape of a^s is often not known.** Considering that a^s is spatially distributed allows to integrate structures in the modeling. For example, a^s can take different values in white and grey matters of the brain, because tumor propagation is faster in white matter than in grey matter [SAM00, HAS07]. We could consider also fibers and vessels surrounding the tumor that may also lead to shape changes. However, the locations of fibers and vessels are not visible using medical imaging and the segmentation of white and grey matter contains uncertainties and is computationally costly. Our objective is then to develop a strategy in which we have no prior on the structure of a^s and to estimate it. We develop a strategy in which a^s is estimated on a grid. Each case of the grid corresponds to a value that has to be estimated. The chosen grid is less refined that the computation grid, as Kalman filter is a costly algorithm.

(5) **Extend the value of a^s outside the tumor to make prediction.** A smoothing and thresholding strategy has been developed and is presented in [Kri18] (in French).

In [20], numerical simulations with synthetic data allow to validate the Luenberger observer and the joint state and parameter observer on cases where the shape of a^s is known with very few medical imaging. The last numerical simulation concerns the estimation in a case where the shape of a^s is unknown. In order to simulate the growth of a tumor along a vessel, a target simulation is launched with a^s taking a higher value inside a synthetic vessel. The simulation is shown on Figure 2.5, with the vessel front represented in white. Let us note that the tumor expands in the direction of the vessel as expected. The parameters used for this simulation are $(b, a^{\text{in}}, a^{\text{out}}) = (0.02, 0.3, 0.08)$, with a^{in} and a^{out} the values of a^s inside and outside the vessel. Our objective is here to predict the tumor shape and to compare the real value of a^s to the one estimated by our model. Only three times are used for the estimation process.

The volume calibration – done after assuming a constant – gives $(b, a) = (0.029, 0.132)$. We will use the estimated value of b for the PDE system and we will use the value of a as an initial prior value for a^s. On the top of the first column of Figure 2.6, the first grid considered for a^s is represented. On the bottom, the solutions of the target model in red and of the observer model in green are compared at time $t = 25$. We notice that the grid 5x5 contains three types of zones. Grey zones are those which are not reached by the tumor: parameters are not corrected, and stay at initial value. Red and blue zones are

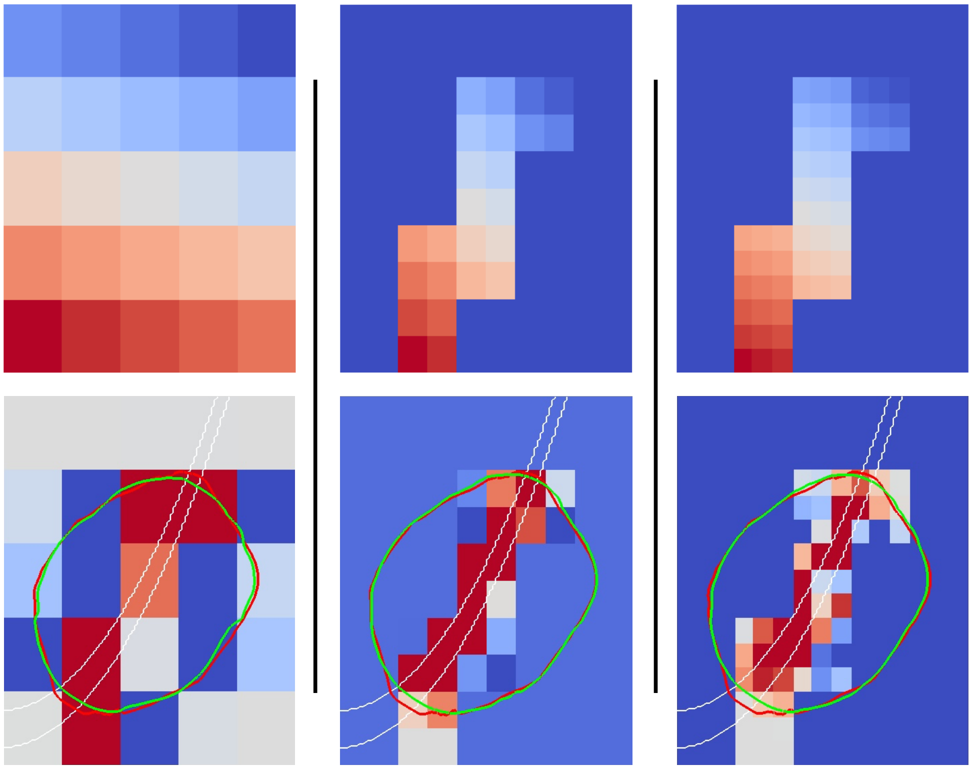

Figure 2.6 – Initial shapes of a^s (first line) and comparison between the solution of the target model and the solution of the observer model at time $t = 25$ (second line). First column: initial grid. Second and third columns: evolution of the grid using the previous results.

those where the parameter increase or decrease respectively. In these simulations, we choose $\lambda = 0.001$ and an error of covariance of 0.08. It is interesting to notice that the red zones are those located inside the vessel. It shows that it is possible to extract information on the structure of a^s, even when we have no *a-priori* on it. In order to improve the prediction, the grid is refined like this: red zones are refined and blue and grey zones are unified to form a single zone. The aim is to refine interesting zones only. Unifying other zones aims at reducing the number of parameters and have reasonable computation time. We obtain successively the grids represented on the top of the second and third columns of Figure 2.6.

Solutions of the target and the observer models at time $t = 25$ on these grids are represented on the bottom of the second and third columns of Figure 2.6. We notice as before that red zones are those located in the synthetic vessel. We also notice that the most refined grid is not the one that gives the best result. Each zone being correlated to its neighbors, this method cannot give a precise vascularization map. However, the method is efficient to estimate a global behavior of the shape of a^s.

In this example, the strategy has been validated with synthetic data but in a clinical context. As these results are very encouraging, we also apply on a brain metastasis whose the shape evolves in time (see Figure 2.7-Top). The results – summarized here – are detailed in [Kri18] (in French). The question of our collaborator was: can we determine the area with a large growth rate and which explains why the shape of the tumor evolves in time? We also add one: can we predict the volume and the shape at a later time using three MRI examinations? Figure 2.7-Middle/Bottom gives the results. The strategy allows us

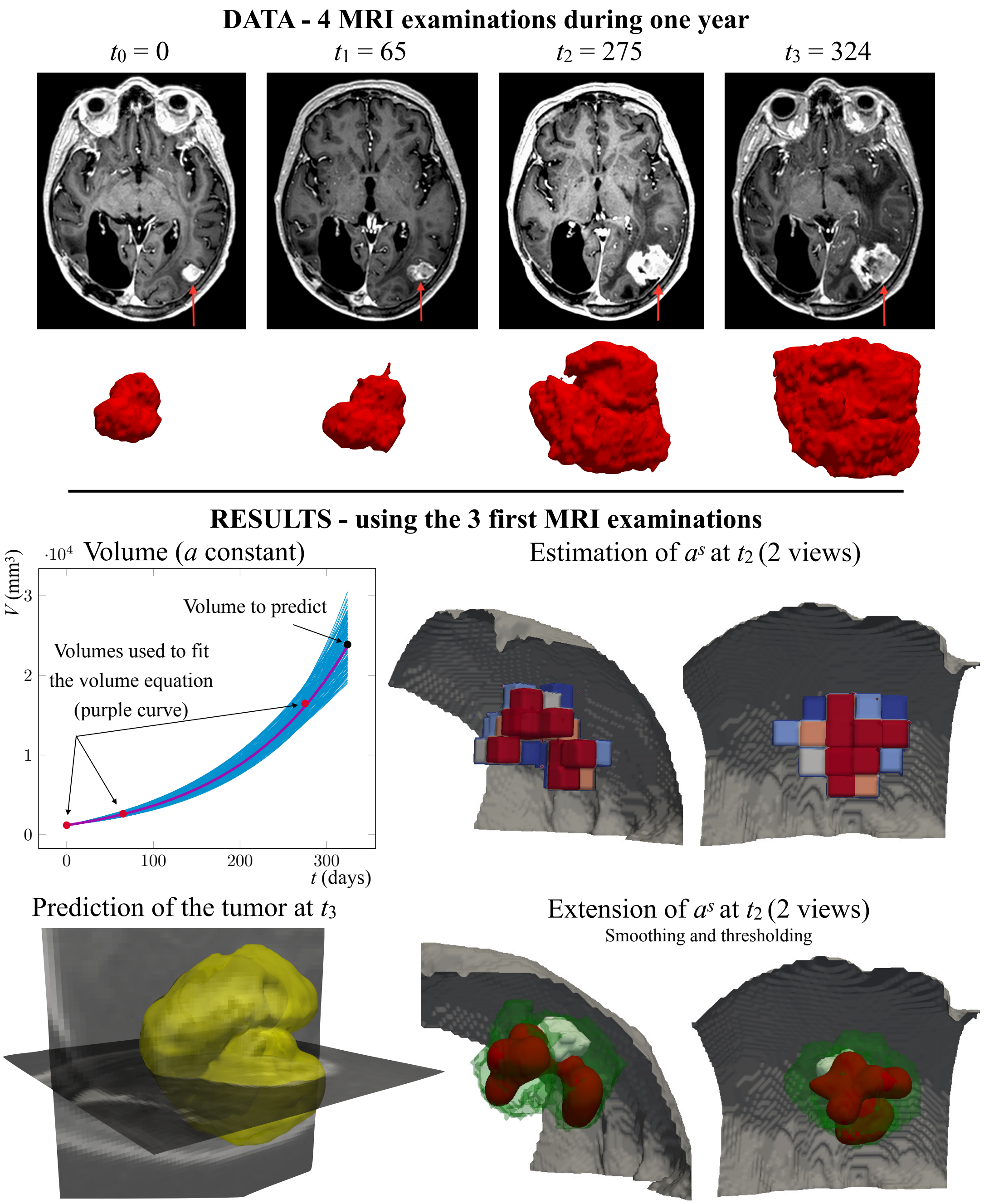

Figure 2.7 – Top: MRI examinations of a brain metastasis of a patient followed by Ana Ortiz de Mendivil Arrate of HM Hospitales in Spain at 4 different times (given in days) and the 3D segmented tumors. Bottom: Tumor rate estimation. Volume and shape prediction.

to well describe and even predict the volume of the tumor. Concerning the shape, one can first see that our strategy allows to determine the shape of the growth rate allowing to make prediction of the tumor. This example on real data validates the proof of context of our strategy.

Conclusion

This chapter presents my contributions to tumor growth modeling. The tumor models that we classically use in the MONC team to model tumor growth are presented. Different strategies to fit these models to each patient using available medical data are presented, as well as the results obtained in a large cohort of meningiomas.

In all examples presented here, no treatment was considered, but our approaches may be valid in this context as well. As an example, we present in [19] a model that integrates chemotherapy by considering two different cell densities ($N_{TD} = 2$ in System (2.1)). To parameterize it, lesion textures were considered in addition to volume data. The strategy is illustrated on a small cohort of 17 patients with EGFR-mutated non-small cell lung cancer treated with tyrosine kinase inhibitors (TKI) who relapsed after an initial response to treatment (enlargement of the primary tumor, appearance of aggressive metastases, deterioration of the patient's general condition). We identified a biomarker calculated thanks to our mathematical model that allows us to determine whether the patient will have a survival under TKI based on only three initial CT scans.

Always in the context of cancer therapies, an increasing amount of my research focuses on electroporation. Electroporation is a complex phenomenon that occurs when biological tissue is subjected to electrical pulses that allow either the direct killing of cells in the target tumor area or the introduction of molecules into living cells. The next chapter is devoted to the presentation of my work on this innovative therapy.

Chapter 3

Contributions to electroporation modeling

The innovative work presented in this chapter has been published in six articles [15, 18, 21, 25, 29, 28].

Introduction

This chapter is dedicated to the innovative medical therapy called electroporation. Electroporation consists in applying pulsed electric fields of high intensity and short duration (usually several hundred volts per centimeter for a hundred microseconds) to cells using catheters containing active electrodes (to apply the electric field) and often passive/inactive electrodes (which can be used to measure). The objective to create defects – called pores – at the surface of the cell membrane. Over the past two decades, this phenomenon has been studied in detail both *in vivo* and *in vitro*. Interestingly, this method has been shown to selectively affect cell membrane structures and their properties [TGR05], leading to therapeutic innovations. In particular, reversible electroporation allows the introduction of non permeant molecules (cytotoxic drugs such as bleomycin, DNA plasmids) into living cells without directly killing them [Mir01, AM10, Geh08, MSB+12], whereas at higher electric pulse intensity or duration, cells in the target region die by a nonthermal mechanism called irreversible electroporation (IRE) [DMR05]. IRE is then used as a novel nonthermal ablation modality: pulsed electric field ablation (PFA). It appears that PFA represents an interesting alternative to the usual nonsurgical ablation techniques – radiofrequency electromagnetic field (RFA) or cryotherapy – to treat deep-seated, inoperable tumors [MLR05, CEH+13] and, more recently, to perform cardiac ablations [KKI+19b, COJ+20a, RDN+21].

However, one of the main limitations to the use of electroporation in routine clinical practice arises from the technical difficulties associated with this therapy, in particular the difficulty of (1) accurately understanding cell death and (2) determining the treated zone. Mathematical modeling of the electroporation process at the cellular level could provide information that contributes to the understanding of this phenomenon, while modeling of the electroporation process at the tissue level could evaluate the efficacy of the treatment thanks to a prediction of the electric field distribution based on a mathematical modeling . My mathematical contributions to this field are summarized in the following points:
(1) **Use mathematical modeling to better understand how the membrane becomes permeable.** The goal of this first contribution is to develop mathematical approaches to track cell membrane dynamics. In a first work, we develop a robust calibration strategy for the 4-electrode experimental setup – developed by our collaborators Tomás García-Sánchez and Luis M Mir, among others – that allows us to measure the impedance of cell myotubes subjected to electrical pulses [GSAL+15]. We then design and parameterize

an equivalent circuit model that allows to quantify the short-term behavior of membrane conductance few seconds after the pulse. This first work gives us informations about the global behavior of the cell membrane and in parallel, we work on the local behavior of the membrane. To do so, we develop a PDE model of membrane electroporation that combines membrane water content and transmembrane voltage, and an efficient numerical strategy that allows us to obtain numerical simulations of pore formation on the membrane. This work corresponds to the two articles [29] [25].

(2) **Compare and improve electroporation models at the tissue scale.** The objective of the second contribution is to develop mathematical approaches to model the electroporation process at the tissue scale. We first compare the solutions of the phenomenological electroporation models available in the literature. We also examine their calibrations using bioelectric measurements on rabbit livers performed by Sel et al. [SCB$^+$05]. In a second work, we focus on the boundary conditions of the – very conductive and thin – passive electrodes. It is a difficult question because, unlike the active electrodes on which either the potential or the current is imposed – corresponding to Dirichlet or Neumann boundary conditions – for the inactive electrodes the value of the equipotential is an unknown of the PDE. This leads to a non-local constraint of the flux along the conductor interface, the so-called floating potential problem. We develop a strategy to address this problem in the context of electroporation. This strategy is compatible with all of the models of the literature. This work has been published in these two articles [15, 18].

(3) **Investigate the effects of irreversible and reversible electroporation on tumor growth.** The aim of this third contribution is to study the growth specificities of cancer cells subjected to a pulsed electric field. To do so we work on data on 3D tumor spheroids obtained by our collaborators Jelena Kolosnjaj, Muriel Golzio and Marie-Pierre Rols (IPBS, Toulouse University). Our strategy is based on an advanced advection model (compatible with System 2.1 of Chapter 2) and well-fitted estimation strategies and has been published in [21].

These contributions are presented in three sections. Section 3.1 presents work at the cellular scale. Section 3.2 presents the tissue-scale work. Finally, in Section 3.3, the study of the effects of electroporation on tumor spheroids is presented. The population-based estimation strategy for PDE systems presented in [28], is also introduced as it was applied on the same data.

Remark 4. *The work corresponding to the first two contributions focuses on application in oncology but one can see that most of it could be adapted for use in cardiology as well. This point is further develop in my research project (see Chapter 4).*

3.1 Membrane dynamics

One of the most important properties of a biological cell membrane is that it is a semipermeable layer, meaning that it allows only certain molecules to pass through. For example, a cell can regulate the concentration of certain ions inside it by letting in more or fewer ions from its environment through its membrane. The membrane of a cell consists largely of a lipid layer, which is why it behaves like a dielectric under the influence of an electric field. In contrast, the interior of the cell usually behaves like an electrolyte. When an electric field is applied to a cell, charge accumulation occurs at the membrane, resulting in a transmembrane voltage. This phenomenon has already been studied in Chapter 1 for cardiac cells, which have the peculiarity of being excitable and has been modeled with the microscopic bidomain model coupled with a ionic model, see Section 1.1.

When this voltage exceeds a certain threshold, the permeability of the cell membrane increases dramatically, so that molecules that previously could not enter the cell can now do so. This phenomenon is known as electroporation. Although the phenomenon was discovered in the late 1960s, the way in which membranes become permeable through the action of a strong electric field is still not well understood. Mir's group has shown that the cell membrane remains permeable for several minutes after microsecond pulses, which has led to a well-designed clinical protocol for electrochemotherapy [MOBP91, MNS+22], and Pakhomov *et al.* have shown similar results for nanosecond pulses [PKW+07]. Mir's group has also demonstrated the dual phenomenon of electroporation: rapid pore formation that closes quickly and a long-term change in membrane permeability confirmed by molecular dynamics simulations [BDS+12].

It is worth noting that despite extensive experimental evidence of increases in membrane permeability following electrical pulses, there is still a lack of knowledge about the electrical properties of the membrane in the minutes following the pulses. In this section, we present mathematical work that attempts to fill these gaps. In a first subsection, we study the global behavior of the membrane based on the time evolution of its resistance using bioimpedance measurements. In a second subsection, we focus on the local behavior of the membrane by designing a microscopic bidomain model that integrates the state of membrane evolution through a continuous phase order function $\phi : x \in \Gamma \mapsto \phi(x) \in [0, 1]$, where $\phi = 0$ represents the ideal pure lipid phase and $\phi = 1$ represents the ideal pure water phase.

3.1.1 Bioimpedancemetry

Bioimpedance measurement seems to be the method of choice to track the evolution of the electrical properties of the membrane in the minutes following the pulses, since a large number of measurements can be made. However, it is confronted with the difficult problem of electrode-solute interactions that affect the measurements and their interpretations. Namely, when an electrode is immersed in an ion-containing solute, a boundary layer called the Gouy-Chapman-Stern layer forms around the electrode. In this layer, the ion concentrations - and thus the conductivity of the solute - differ significantly from the concentrations in the bulk (far from the electrode). In other words, the electrode measurements are greatly disturbed by this layer, and the conductivity of the medium can hardly be accurately recovered [Lvo12]. Moreover, the thickness of the layer increases (nonlinearly) with the electric current injected into the electrode [Sch66, ITC+13]. Therefore, a standard impedance measurement setup leads to noisy and unusable results in biological experiments. Schwan et al. proposed an experimental setup with 4 electrodes to limit the size of the solute-electrode interface of the measurements [SF68]. Roughly speaking, 2 electrodes deliver the current and 2 others connected to a high input impedance measure the potential. However, calibration of the system is far from trivial. Bao *et al.* proposed a well-designed setup and the corresponding numerical calibration method for impedance spectroscopy of erythrocytes in [BDS93]. The calibration method is based on impedance measurements of 3 samples whose electrical properties are known. The resolution of a nonlinear system then allows the determination of the calibration functions. García-Sánchez *et al.* proposed a different 4-electrode experimental setup that requires a special calibration [GSAL+15] because the method of Bao *et al.* leads to an unstable calibration. Normally, impedance measurements of cells in culture are performed using very dense cell suspensions to increase the cell volume to buffer volume ratio. By using fixed cells in a setup that does not require cell separation (and respects the cell geometry and membrane characteristics), impedance measurements can be performed under more physiological conditions. García-Sánchez *et al.* recently proposed such a well-designed setup. In particular, they proposed an experimental setup for fast electrical impedance spectroscopy measurements (1 spectrum per millisecond) to study the evolution of the electrical properties of adherent cell myotubes within milliseconds after the electroporation pulse [GSAL+15].

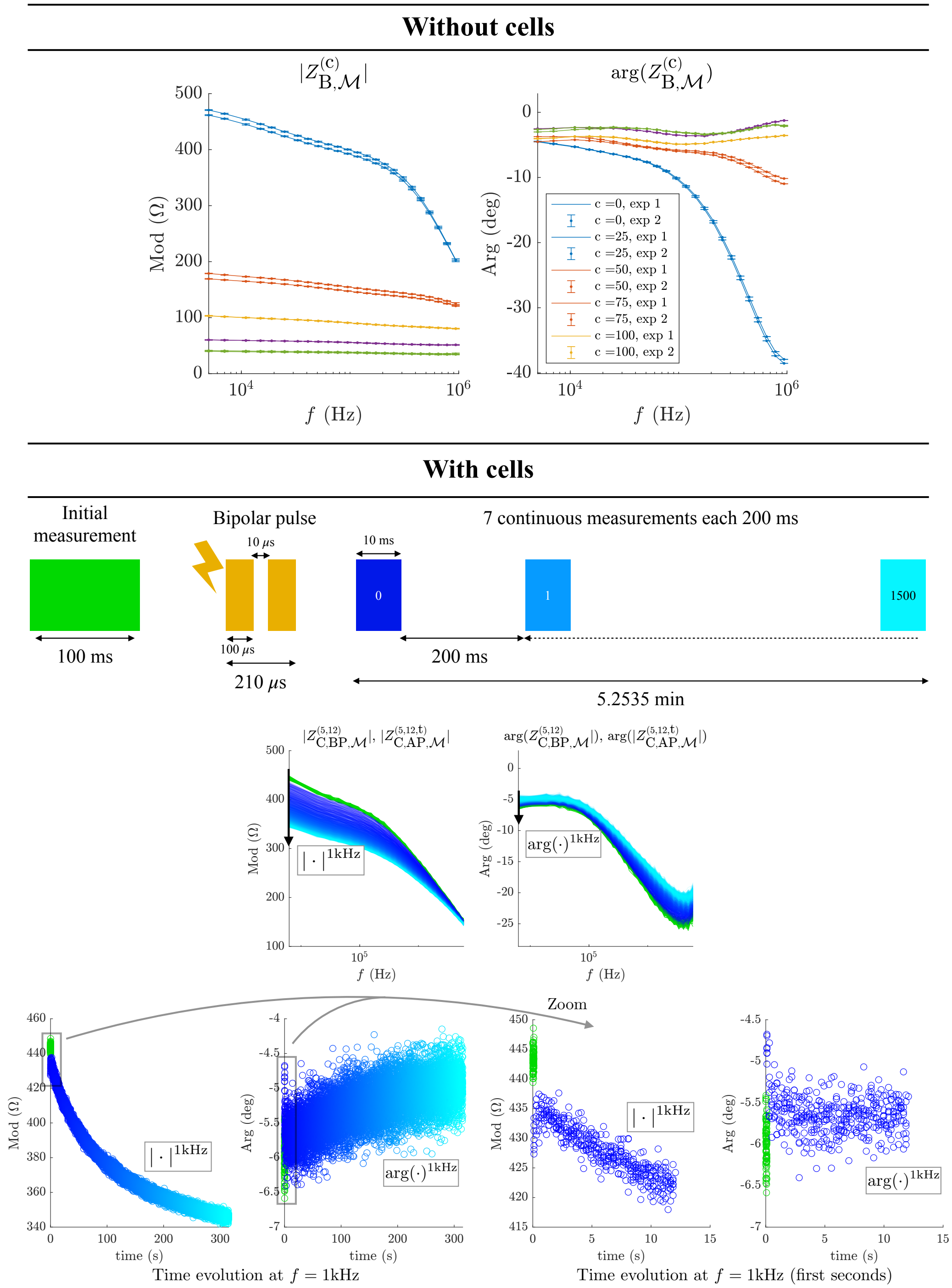

Figure 3.1 – Top: Bode plots of the impedances $Z^{(c)}_{B,\mathcal{M}}$. The error bars represent the 95% of the impedance measured at a given frequency. Bottom: Scheme of the experiment and bode plots of the $Z^{(5,12)}_{C,BP,\mathcal{M}}$ and $Z^{(5,12,t)}_{C,AP,\mathcal{M}}$ with measurements before the pulse (in green) and those done after the pulse during five minutes in blue – increasingly clear at the passage of the time, as explained by the scheme. Left: Corresponding time evolving curves for the frequency 1 kHz. Right: Zoom on the beginning.

Quick presentation of the data The full setup used to obtain the bioimpedance measurements is presented in [29]. We introduce the following datasets:

$$\begin{aligned}
F_{\text{kHz}} &= \{1, 3, 5, 7, 11, 15, 19, 25, 33, 41, 51, 63, 77, 95, 117, 143, \\
&\qquad 173, 209, 253, 307, 371, 447, 539, 649, 781, 939\} \text{ kHZ (frequencies)}, \\
C_{\text{B}} &= \{0, 25, 50, 75, 100\} \text{ mM (concentration without cells)}, \\
C_{\text{C}} &= \{0, 5, 10, 20, 30\} \text{ mM (concentration with cells)}, \\
V &= \{12, 30\} \text{ V (considered voltages)}, \\
T &= \{t_n = n \times 210 \text{ ms}, n = 0, 1, \cdots, 1500\} \text{ (time after pulse)}.
\end{aligned}$$

The following notations are also used: B for buffer, $\mathcal{M}$ for measures, BP for before pulse and AP for after pulse. The measured impedances given in Figure 3.1 can be summarized as:

(1) *Impedance without cells* in the buffer denoted $Z^{(\text{c})}_{\text{B},\mathcal{M}} : f \mapsto Z^{(\text{c})}_{\text{B},\mathcal{M}}(f)$, for all $(\text{c}, f) \in C_{\text{B}} \times F_{\text{kHz}}$, see Figure 3.1 (top),

(2) *Impedance with cells* in the buffer:

(a) 100 ms (only the mean is considered) in *pre-electroporation* context denoted $Z^{(\text{c,v})}_{\text{C,BP},\mathcal{M}} : f \mapsto Z^{(\text{c,v})}_{\text{C,BP},\mathcal{M}}(f)$, for all $(\text{c}, \text{v}, f) \in C_{\text{B}} \times V \times F_{\text{kHz}}$, see Figure 3.1 (bottom, green curves),
(b) ∼5 min *after one biphasic microsecond electroporation pulse* of $v \in V$ denoted $Z^{(\text{c,v,t})}_{\text{C,AP},\mathcal{M}} : f \mapsto Z^{(\text{c,v,t})}_{\text{C,AP},\mathcal{M}}(f)$, for all $(\text{c}, \text{v}, \text{t}, f) \in C_{\text{B}} \times V \times T \times F_{\text{kHz}}$, see Figure 3.1 (bottom, blue curves).

For almost all cases, several experiments were performed. The measured impedances $Z^{(\text{c})}_{\text{B},\mathcal{M}}$, $Z^{(\text{c,v})}_{\text{C,BP},\mathcal{M}}$ and $Z^{(\text{c,v,t})}_{\text{C,AP},\mathcal{M}}$ differ from the true sample impedances – respectively denoted by $Z^{(\text{c})}_{\text{B},\mathcal{T}}$, $Z^{(\text{c,v})}_{\text{C,BP},\mathcal{T}}$ and $Z^{(\text{c,v,t})}_{\text{C,AP},\mathcal{T}}$ – because of distortion due to the experimental setup. The strategy to deal with this issue is presented in [29].

Equivalent circuit model Our strategy to study the impact of electroporation on the electrical properties of the cells consists in analyzing impedance data using an equivalent electrical model of the experimental setup. It is composed of two parallel branches: one for the buffer compartment and one for the cell compartment. An important – and hardly measurable – phenomenon lies in the ion exchanges between the cells and the buffer. This phenomena is particularly important at low buffer conductivity. Therefore the buffer impedances obtained by the calibration are modified – and thus need to be estimated – in the experiments with cells. Denoting by $\sigma_{0,b}$ the buffer conductivity without KCl, the buffer conductivity as a function of the KCl concentration is deduced from the Kohlrausch law:

$$\sigma_b([\text{KCl}]_b) = \sigma_{0,b} + [\text{KCl}]_b(\Lambda_0 - K\sqrt{[\text{KCl}]_b}).$$

To account for the cells-buffer ion exchange, we set $\sigma_{0,b} = \sigma_0 + \Delta\sigma_0$, where $\Delta\sigma_0$ is the change of conductivity due to ions exchange between cells and the buffer that has to be fit. More precisely, in Figure 3.2, one can remark the data variability (dot points) between two same experiments, as for example for $\text{c} = 10$ or 20 mM with $\text{v} = 12$ V (top, left) or for $\text{c} = 5$ mM with $\text{v} = 30$ V (bottom, left). We assume that this variability is due to different states of the cells and exchanges between the cell monolayer and the buffer. The parameter $\Delta\sigma_0$ has been added to the buffer conductivity in order to account for this phenomenon.

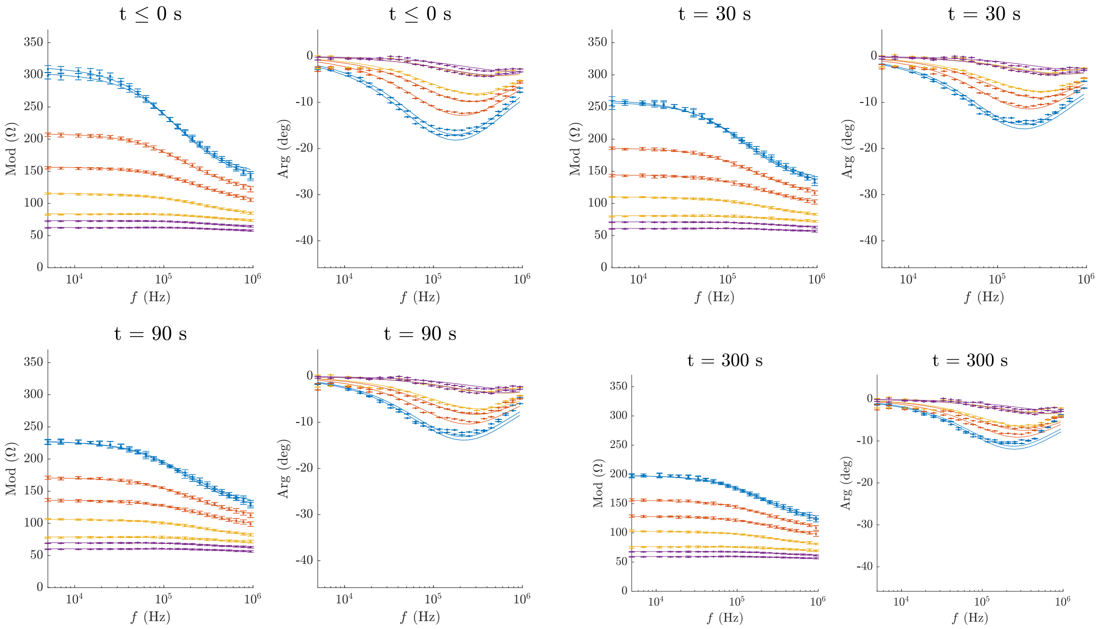

Figure 3.2 – Bode plot of $Z^{(c,12)}_{\mathrm{C,BP},\mathcal{T}}$ (top-left) and $Z^{(c,12,t)}_{\mathrm{C,AP},\mathcal{T}}$ at different times for $\mathrm{c} \in C$.

The buffer resistance is then modeled as

$$R_b^{\mathrm{r}} = \frac{R_b}{\phi} = \frac{k}{\sigma_b([\mathrm{KCl}]_b)\phi}, \text{ with } k = 40 \text{ m}^{-1},$$

where $1-\phi$ is the volume fraction of the cells.

The influence of the cells on the measured impedance is mainly due to the cytoplasm and the membrane of the cells similarly to [FS98]. The cytoplasm compartment is assumed only conductive while the membranes compartment is modeled by a constant phase element (CPE) of parameters (C_m, α_m) in parallel with a resistance denoted by R_m following [Lvo12, Chapter 3]. Before the pulse, R_m is fixed at the value 2.34 MΩ. The impedance of our equivalent circuit with cells $Z_{\mathrm{C,th}}$ (before and after pulse) is defined by

$$\frac{1}{Z_{\mathrm{C,th}}(f,\theta)} = \frac{\sigma_b([\mathrm{KCl}]_b)\phi}{k} + \frac{1}{\dfrac{R_{cyt}}{(1-\phi)} + \dfrac{R_m}{(1+R_m C_m (2i\pi f)^{\alpha_m})}}, \tag{3.1}$$

where θ is a vector which concatenates the 6 parameters: $\theta = (\phi, \Delta\sigma_0, [\mathrm{KCl}]_b, R_{\mathrm{cyt}}, \alpha_m, C_m)$.

Before pulse, the parameters are estimated under constraints. The constraints and the estimated values are given in [29]. After pulse, the parameters are fixed at the estimated values before pulse except R_m and $[\mathrm{KCl}]_b$ which are fit by the minimization algorithm without any model.

Figure 3.2 shows the calibrated data $Z^{(c,12)}_{\mathrm{C,BP},\mathcal{T}}$ (dot points and top-left) fitted with the electrical circuit before pulse *i.e.* with R_m fixed at 2.34 MΩ (straight line) and the calibrated data $Z^{(c,12,t)}_{\mathrm{C,AP},\mathcal{T}}$ (dot points, top-right and bottom) fitted with the electrical circuit after pulse (straight line) for $t = 30, 90$ and 300 s.

As expected, the generated true impedances with cells before the pulse delivery $Z^{(c,v)}_{C,BP,\mathcal{T}}$ display a flat modulus for low frequencies. This is due to the shielding effect of the membrane at low frequency. These results validate simultaneously our calibration procedure and the electrical circuit combined with Kohlrausch's conductivity to model the buffer. The curves with $v = 30$ V are given in [29]. One can seen again that the impedances are accurately determined by the model. The errors on the phase are smaller than 2 degrees (for 12 V and 30 V) and the relative errors on the amplitudes are smaller that 1% for 12 V and for 30 V, which is very satisfactory for such a complex experimental setup.

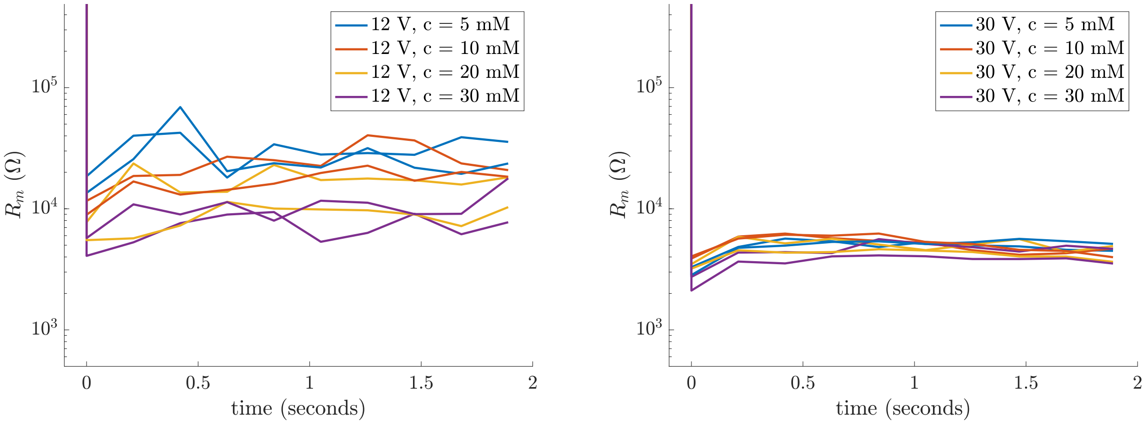

(a) Exp. pulse at 12V

(b) Exp. pulse at 30V

Figure 3.3 – Evolutions of the membrane resistance R_m within the first 2 seconds after the permeabilizing pulse (12V and 30V resp.).

The previous calibration enables us to follow the influence of electroporation on the changes in the parameters corresponding to the cell membrane of the equivalent electrical circuit proposed. Figure 3.3 (resp. Figure 3.4) presents the evolution of R_m (resp. [KCl] concentration) during 2 seconds (resp. 300 seconds) after electroporation. Let us emphasize that this postpulse calibration of R_m and $[\text{KCl}]_b$ is performed without any *a priori* on the evolution of these 2 parameters.

As for the membrane resistance, the dynamics show a very fast and strong decrease due to the pulse, followed by a small increase (see Figure 3.3) within the first milliseconds after the pulse. These initial dynamics on the membrane could be interpreted as the opening and closing of the pores of the membrane due to the pulse. It is interesting to note that the instantaneous drop in membrane resistance at 30 V is much higher than at 12 V (see Figure 3.3), which again is consistent with the classical view of electropermeabilization (the pulses with higher magnitude produce more defects than the pulses with lower magnitude). As for the evolution of the membrane resistance within 5 min (see [29] for the figure), the calibration shows that the membrane compartment does not recover its original resistance after 5 min to the value before the pulse, which is consistent with several experimental observations showing that electroporation takes several minutes [PKW+07, MNS+22]. However, the membrane resistance we estimate continues to decrease after several tens of seconds. We think that this unanticipated behaviour is due to ion exchange between the buffer and the cells. Indeed, the cells and the buffer exchange more ions than just the KCl ions, so it is more likely that $\sigma_{0,b}$ increases with time. In [29] we explore a way to answer this problem and conclude that time point measurements of buffer conductivity after the pulse would allow us to better track the long-term behaviour of the membrane after the pulse.

In [29], we show that the evolution of [KCl] concentrations can be described by the following function

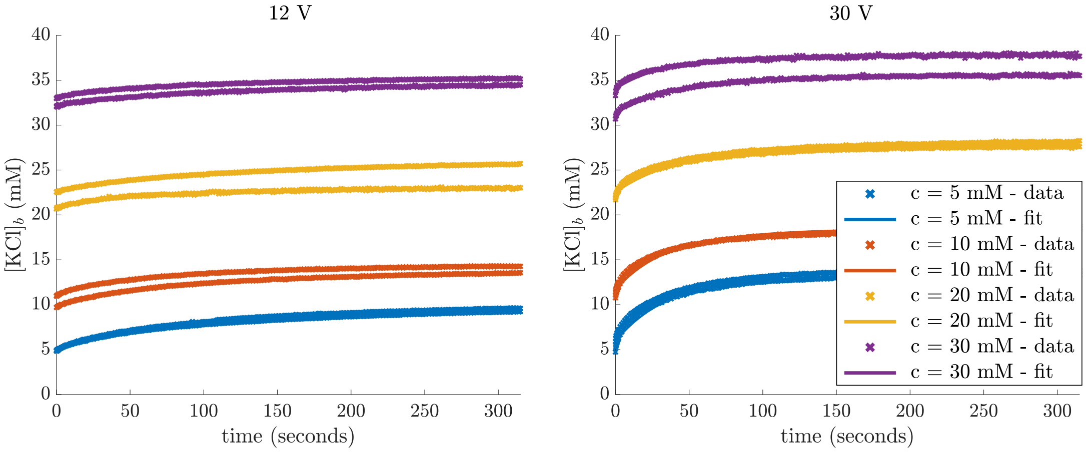

Figure 3.4 – $[\mathrm{KCl}]_b$ concentrations and fits obtained when fitting them with the function given in Equation (3.2).

$$[\mathrm{KCl}]_b^{\mathrm{fit}} = [\mathrm{KCl}]_b^{\mathrm{begin}} + ([\mathrm{KCl}]_b^{\mathrm{end}} - [\mathrm{KCl}]_b^{\mathrm{begin}})(1 - e^{-t/\tau_{[\mathrm{KCl}]_b}}). \tag{3.2}$$

The calibrations are plotted in Figure 3.4. The fits are very closed to the data, validating the model. From the values given in [29], one sees that for a given experiment, the release of [KCl] –that is $[\mathrm{KCl}]_b^{\mathrm{end}} - [\mathrm{KCl}]_b^{\mathrm{begin}}$– is higher after the pulse at 30 V than at 12 V, and the time constant of the release $\tau_{[\mathrm{KCl}]_b}$ is shorter at 30 V than at 12 V, meaning the dynamics of the release is faster at 30 V than at 12 V. Another interesting observation is the fact that the time constants $\tau_{[\mathrm{KCl}]_b}$ are similar between all the experiments for a given voltage, which is consistent with the fact that the permeabilisation depends on the magnitude of the pulse. We eventually note that for higher initial concentration in the buffer, the release is smaller due to a lower gradient between the cell and the buffer [KCl] concentrations.

Conclusion In summary, thanks to a robust setup calibration procedure, the data sets without and with cells were evaluated sequentially to appropriately calibrate the electrical circuit corresponding to the setup. Interestingly, we were able to distinguish between the release of [KCl] and the dynamics of the membrane resistance within the first seconds after the pulse. This work provides, for the first time, numerical quantification of membrane resealing after an electroporation pulse using bioimpedance measurements. Our calibration suggests that additional measurements of buffer conductance should be made to track membrane dynamics during the 5 min following the pulse. We emphasize that the electrical equivalent circuit approach is a very interesting step to decipher membrane resealing immediately after the pulse. However, a 3D simulation of the entire experimental setup, which is currently under investigation, could provide more insight. This could involve writing a model that includes an intracellular region corresponding to the cell layer, which means that the layer is considered as a very large cell. To do this, modeling electroporation at the cell scale and, in particular, membrane behavior is a necessary step. This topic will be explored in the next section. This means that we will focus on the local behavior of the membrane.

3.1.2 Membrane modeling

Even though the phenomenon of electroporation has been discovered in the late 1960s, the ways the membranes become permeable by the effect of an intense electric field is still not well understood. In the late 1990s, the teams of Chizmadzhev and Weaver [CCSZ95, WC96] proposed a description of the emergence of water pores in a sea of lipids, under very constraint geometries (the pores are cylindrical). Then Krassowska and Neu proposed a Smoluchovskii equation for the population of cylindrical pores $n(r,t)$ of radius $r > 0$ at the time t, and they derived an asymptotic analysis to link the transmembrane potential to the total density of pores $N(t) = \int_{\mathbb{R}^+} n(r,t)dr$, which satisfies an ordinary differential equation [NK99, DK98]. From this times, only slight modifications of the models have been proposed by Weaver [WSE$^+$12, SSGW14]. Kavian *et al.* proposed then a phenomenological version of the Krassowska and Debruin model, by limiting the number of parameter [KLPW14]. Leguèbe *et al.* proposed in [LSMP14] an extension by introducing the surface reaction-diffusion of oxidised lipids. This model – coupled with well-chosen boundary conditions for the electrodes used to measure, see Section 3.2.2 – could be used in a harmonic context to model the 3D configuration of the setup presented in the previous section. However, this model seems closer to the observations but it is phenomenological and lacks of any physical basis.

The aim of this section is to present a new model of membrane electroporation that combines the water content of the membrane (initially 0 for non porated membrane) and the transmembrane voltage. Interestingly, thanks to a well defined free-energy of the membrane, we somehow generalise the approach of Chizmadzhev and Weaver, getting rid of the geometrical cylindrical assumption. Our approach is physically relevant and we recover a surface diffusion equation of the lipid phase that can be seen as a justification of the model of Leguèbe *et al.*

Quick presentation of the model We model the state of the membrane by a function $\phi : \Gamma \to \mathbb{R}$ measuring the amount of lipid in the membrane Γ at any position x at time t. The state $\phi = 0$ represents the ideal pure lipid phase and $\phi = 1$ the ideal pure water phase. The free-energy of the membrane subjected to a transmembrane voltage $u^{(m)}$ is the functional energy so-called Gibbs energy given as [KP14]

$$\mathcal{E}(\phi, u^{(m)}) = \frac{\kappa}{2}\int_\Gamma |\nabla\phi|^2 + \int_\Gamma W_m(\phi) - \frac{1}{2}\int_\Gamma C_m(\phi)(u^{(m)})^2,$$

where the first term corresponds to the membrane diffusion, the second to the potential energy of the membrane and the third to the influence of the transmembrane voltage. More precisely, $\kappa > 0$ is linked with the interfacial tension [FMZB20] and W_m is the double-well potential energy that describes the stable states of the membrane. The term $|\nabla\phi|^2$ regularises ϕ and helps control the thickness of the water-lipid interface, as explained by Bray [Bra02]. The term $\frac{1}{2}C_m(\phi)(u^{(m)})^2$ is the electrical energy. The effect of the transmembrane voltage acting on the membrane is modeled as the energy associated to the change in specific capacitance of the membrane [AAC$^+$79]. In fact, Weaver and Chizmadzhev [WC96] consider a similar term taking into account the difference of dielectric coefficients for water and lipids. Roughly speaking, this term affects the potential energy to favor the phase $\phi = 1$ leading to the entry of water within the membrane (see Figure 3.5).

As the water volume fraction is not conserved (defects can be created and disappear from the membrane), we consider the non-conserved dynamics associated to this energy functional (also called model-A by Bray [Bra02]). The evolution of ϕ is determined by the L^2–gradient flow associated with the energy functional above. It corresponds to the Euler-Lagrange equation for the energy $\phi \mapsto \mathcal{E}(\phi, u^{(m)})$. In other words, for a given kinetics coefficient $\alpha > 0$ – also called phase field mobility – the order parameter ϕ

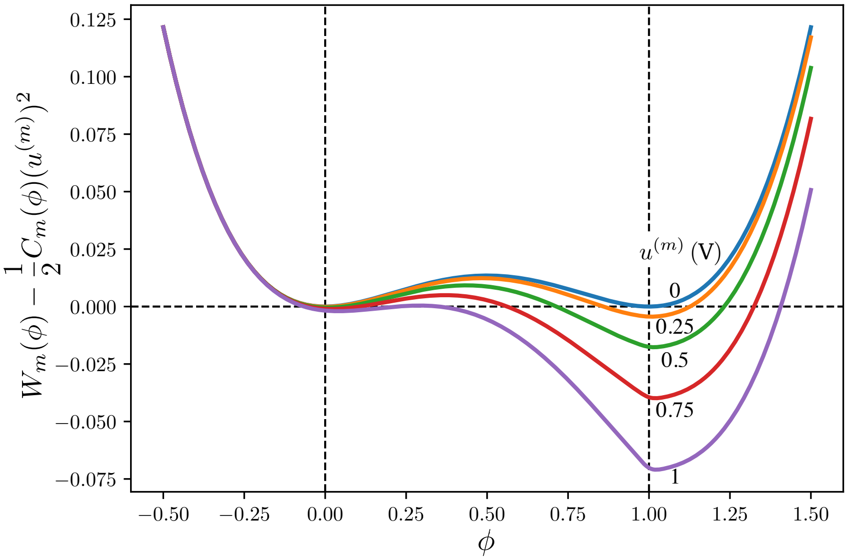

Figure 3.5 – Electrostatic term $W_m(\phi) - \frac{1}{2}C_m(\phi)(u^{(m)})^2$ versus ϕ when the transmembrane potential is assumed to be constant throughout the membrane. Each curve corresponds to a different value of $u^{(m)}$ between 0 and 1 V.

satisfies the following Allen-Cahn equation on the membrane surface Γ [AC79, Bra02, CH58]:

$$\partial_t\phi - D_0\Delta\phi = -\alpha\frac{\partial W_m}{\partial\phi}(\phi) + \frac{\alpha}{2}\frac{\partial C_m}{\partial\phi}(\phi)v^2, \quad \forall t > 0, \tag{3.3}$$

$$\phi(0,\cdot) = \phi^0(\cdot), \tag{3.4}$$

where $D_0 := \alpha\kappa$ is a diffusion coefficient in $\mathrm{m}^2.\mathrm{s}^{-1}$, and α is in $\mathrm{m}^2.\mathrm{J}^{-1}.\mathrm{s}^{-1}$.

Throughout the work, we consider for W_m the simple smooth double-well potential given by

$$W_m(\phi) := 16a_1\phi^2(1-\phi)^2 + 8a_2(\phi + \frac{1}{2})(\phi - 1)^2, \quad \forall\phi \in [0,1], \tag{3.5}$$

where $4a_1 > 3|a_2|$, so that W_m satisfies

$$W_m(1) = 0, \quad W_m'(1) = W_m'(0) = 0, \quad W_m''(0) > 0, \quad \text{and} \quad W_m''(1) > 0.$$

The above energy potential describes the fact that the pure lipid ($\phi = 0$) and pure water ($\phi = 1$) phases are the only two stable phases with an energy barrier roughly equal to $W_m(1/2)$ between them. In the above expression a_2 mainly controls the value of the first local minimum ($W(0) = 4a_2$) and a_1 the size of the local maximum (at $\phi_0 := 1/2 - 3a_2/8a_1$) which is the height of the energy barrier to pass from 0 to 1.

Remark 5. *Concerning the theoretical aspects, a well-posedness result for the model of the membrane under some known electric field influence has been established in [25]. Furthermore, there is an extensive literature studying the qualitative mathematical properties of* (3.3) *when* $u^{(m)} = 0$. *One can cite, for example [AC79, ESS92, AHM08].*

The equation on ϕ is coupled to the microscopic bidomain model already introduced in Chapter 1 (System (1.6)) in a cardiac context. In this work, Γ is a closed 2D-surface of $\mathbb{R}^3$ without boundary. We denote by Ω the bounded domain of $\mathbb{R}^3$ in which Γ is embedded, and $\Omega^{(e)}$ and $\Omega^{(e)}$ are the 2 connected components subsets of Ω separated by Γ. We denote as previously $u^{(i)}$ (resp. $u^{(e)}$) the intra-cellular (resp. extra-cellular) potential and $\sigma^{(i)}$) (resp. $\sigma^{(e)}$) its associated diffusion coefficient. The transmembrane potential $u^{(m)}$ is then as previously defined as the jump between $u^{(i)}$ and $u^{(e)}$ along the membrane Γ *i.e.* $u^{(m)} = [\![u^{(i)} - u^{(e)}]\!]_{|\Gamma}$. We will consider in this electroporation context the following bidomain model

$$\begin{cases} \vec{\nabla}_{\vec{x}} \cdot (\sigma^{(\alpha)} \vec{\nabla}_{\vec{x}}\, u^{(\alpha)}) = 0, & \text{in } \Omega^{(\alpha)} \\ \sigma^{(i)} \vec{\nabla}_{\vec{x}}\, u^{(i)} \cdot \underline{n}^{(i)} = \sigma^{(e)} \vec{\nabla}_{\vec{x}}\, u^{(e)} \cdot \underline{n}^{(i)}, & \text{on } \Gamma \\ -\sigma^{(i)} \vec{\nabla}_{\vec{x}}\, u^{(i)} \cdot \underline{n}^{(i)} = C_m(\phi) \partial_t u^{(m)} + S^{(m)}(\phi) u^{(m)}, & \text{on } \Gamma. \end{cases} \tag{3.6}$$

One can see that the differences with System (1.6) (when the mechanical deformations are neglected) concern the last equation which has been modified. Indeed the last equation in System (1.6) was

$$-\sigma^{(i)} \vec{\nabla}_{\vec{x}}\, u^{(i)} \cdot \underline{n}^{(i)} = C_m \partial_t u^{(m)} + I^{\text{ion}}(u^{(m)}, w),$$

meaning that the main differences are:

- The capacitance per unit area of the membrane C_m depends on ϕ (as one could have remarked in Equation (3.3)).

- Instead of the ionic term, we consider the conductance $S^{(m)}$ which measures the opposition to the flow of electric current. It models the electroporation of the cell meaning the opening of the pores. The ionic term is not considered as we do not consider cardiac cells in this context. However, a second term could be added to model the permeabilization of the membrane, see the conclusion paragraph of this subsection.

Furthermore, this system is then coupled to Dirichlet boundary condition on the electric potential

$$u^{(m)}(t, \cdot) = g(t, \cdot), \quad \partial\Omega,$$

where g corresponds to the applied voltage.

The analysis of the coupled model (3.6-3.3) has been done in [25]. It extends the results obtained in [KLPW14] to time-varying and space dependent capacitance.

The first step consists in eliminating the unknown electric potentials following an idea developed in [BCP09] for the bidomain equation at the macroscopic level or in [KLPW14] for an electroporation model at the microscopic level and already quickly introduced in Chapter 1 (see Equation 1.13). We show that there exist two regular operators Λ and G defined as a combination of Dirichlet-to-Neumman type of operators such that solutions of System (3.6) verify

$$C_m(\phi)\partial_t u^{(m)} + (S^{(m)}(\phi) + \Lambda) = Gg. \tag{3.7}$$

Spherical vs flat membranes Always in [25], we characterize the operator Λ in two important configurations: a spherical membrane $\mathbb{S}$ and a flat periodic membrane defined $(\mathbb{R}/(L\mathbb{Z}))^2$, see Figure 3.6 for the definitions and the notations. These two cases are of importance, because cells in suspension are mostly

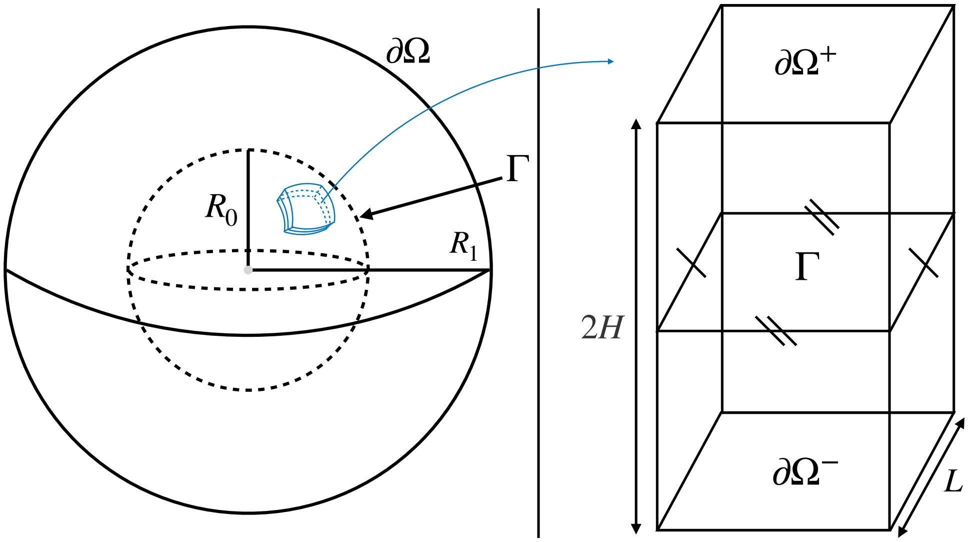

Figure 3.6 – Two situations of membrane. Left: Diagram of spherical cell model. The cell membrane Γ is the sphere of radius R_0 and the boundary condition at $\partial\Omega$ describes the effect of the electric field applied. Right: Bi-periodic square flat membrane of size L. The two surfaces $\partial\Omega^{\pm}$ parallel to Γ and equidistant from it, represent the electrodes. This very simplified geometry can be seen as a volume extraction close to the boundary Γ of the spherical case (see blue draw).

round, while molecular dynamic simulations deals mostly with flat membrane. It is thus important to compare these two settings, in particular to understand the main differences in terms of order of magnitude of the time constants. The operators in this two particular cases can be explicitly diagonalised in terms of the eigenfunctions of the Laplace-Beltrami operator on the sphere. The results are given in [25] and interestingly it allows to determine the charging times of these two cases. In order to consider the periodic flat membrane as a zoomed-in flat patch of the spherical cell model, it is thus necessary to match them accordingly. This means that to compare both settings, we need to consider the following condition

$$H = \frac{R_0}{2} \frac{\sigma^{(i)} + 2\sigma^{(e)}}{\sigma^{(i)} + \sigma^{(e)}}.$$

It is worth noting that this condition is far from being satisfied by the setup of the molecular dynamics simulations of membrane electroporation, for which the simulation boxes are a few nanometers thick, while cell radii are about several of micrometers. Therefore it is highly probably that the time constants of the molecular dynamic simulations are too small. It is clear that in the case of pulsed electric fields, this condition cannot be avoided by changing the duration or magnitude of pulses in each setting (spherical cell or flat membrane). In fact, as much as the charge time is affected by the geometry, so is the discharge time, therefore even between pulses different behaviors arise in both settings.

Aside from the height H, the other important geometric factor of the flat membrane is its length L. Its influence on the transmembrane potential is not so easy to quantify and compare to the spherical case. In [25], we show that small patches tend to flatten the transmembrane potential artificially even if we keep the same proportion of water in the membrane. This heuristic calculation suggests that large patches of flat membrane are needed so that flat torus can be seen as a zoom of the spherical setting.

Membrane conductance and capacitance models The membrane conductance S_m directly impacts on the amplitude of the transmembrane voltage $u^{(m)}$ whereas C_m directly affects the order parameter ϕ as it is directly responsible (along with the transmembrane potential) for pore formation, which is why we must also consider the membrane dynamics in this modeling. We consider for $S^{(m)}$ a sigmoid function which interpolates between the conductivity of the membrane σ_l (lipid conductivity) and the conductivity of a pore σ_w with $k_0 = 100$ the steepness of the transition and $\phi_{th} = 0.5$ the transition threshold. For C_m, we consider the modeling given in [Loo65] whose the parameter values are given in [25].

We emphasize that these choices will have little effect on the pore evolution once the membrane is discharged, so we can expect the same pore sealing behavior.

Numerical simulations We perform numerical simulations in the case of a flat toroidal membrane. To determine the values of the parameters of our coupled model, we either use the literature or compare our model to others or examine limiting cases, see [25] for the values.

An accurate splitting scheme combined with Fast Fourier Transforms for efficient computations of the model is presented in [25]. It is worth noting that the solving the problem in a geometry close to the cell geometry is still challenging. Indeed, a pore edge is somehow comparable in size to the width of the cell membrane $h \sim 10^{-9}$ m and the characteristic length of a cell membrane is comparable with the cell radius $R_0 \sim 10^{-5}$ m. Then to capture the evolution of pores we need a discretized membrane with a minimum amount of nodes of around $(\frac{10^{-5}}{10^{-9}})^2 = 10^8$. Additionally, calculating Dirichlet-to-Neumann operators is particularly slow even in the case where we know how to diagonalize it. Therefore such simulations require specific numerical strategies that will be addressed in a near future.

We simulate a flat biperiodic membrane of size $L = 200$ nm under the influence of a 12 ns square pulse of a uniform electric field of intensity $|E| = 3.2 \cdot 10^6$ V.m^{-1}. After the membrane discharges its transmembrane potential, we continue to simulate it for another 10 μs. We pick as the initial condition $\phi_\diamond : (x, y) \mapsto \mu(x, y)$, where $|\mu| < 1.5 \cdot 10^{-2}$ is a Gaussian random noise (which has been smoothed for numerical stability purposes).

During the initial charge time the membrane evolves more or less uniformly in space until about $t = 12$ ns. At this point the electric field is turned off, but the membrane remains charged. It then discharges like a capacitor, slowly, while the order parameter continues to evolve under the influence of the remaining transmembrane potential. At around $t = 27$ ns, the conductive effect of the membrane comes into play. At this point, the membrane is still charged, but now discharges mainly through the sites of high conductivity resulting from the affected order parameter ($\phi > 1/2$). These sites are better seen at the same time in the transmembrane potential distribution (bottom). However, because the membrane charge is low, the membrane discharges within nanoseconds after this phenomenon occurs. This sudden discharge of the transmembrane potential leads to the assumption that electroporation has occurred.

However, a definite membrane configuration does not occur until about 1 μs later. In this case, the membrane is almost completely discharged by $t = 33$ ns. From this point on, the transmembrane voltage no longer plays a significant role, and only the Allen-Cahn equation controls the membrane dynamics. Figure 3.7 shows the evolution of the transmembrane potential shortly after the initial electric pulse. The lifetime of the pores depends on their size. In our simulations, most pores disappeared before 10 μs. Of course, the evolution of these pores is consistent with the Allen-Cahn equation, since they minimize the mean curvature. Therefore, we see that the pores become rounder as they shrink.

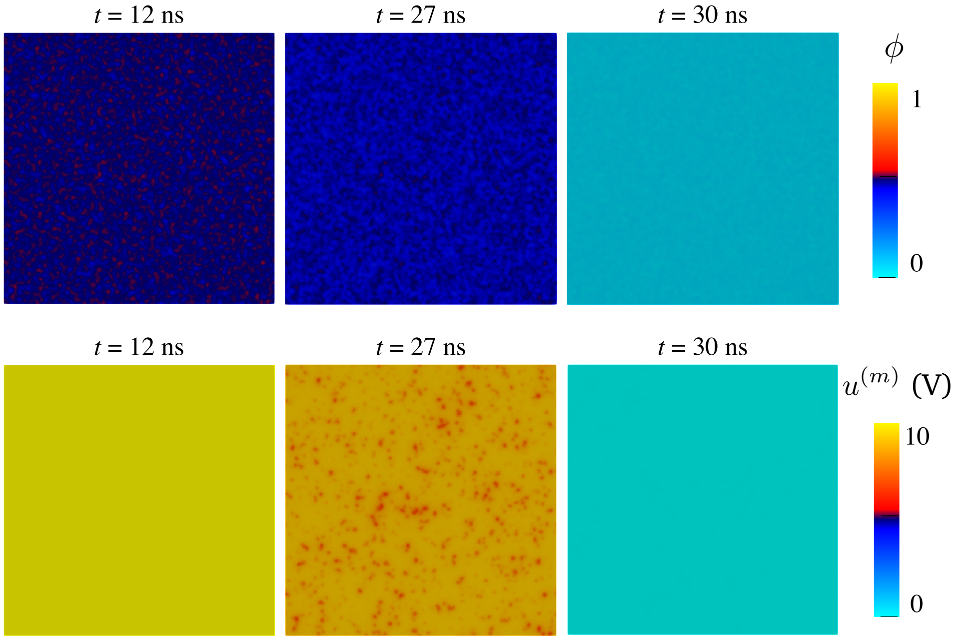

Figure 3.7 – The first row of simulations corresponds to the membrane order parameter ϕ while the second row gives the associated transmembrane potential $u^{(m)}$.

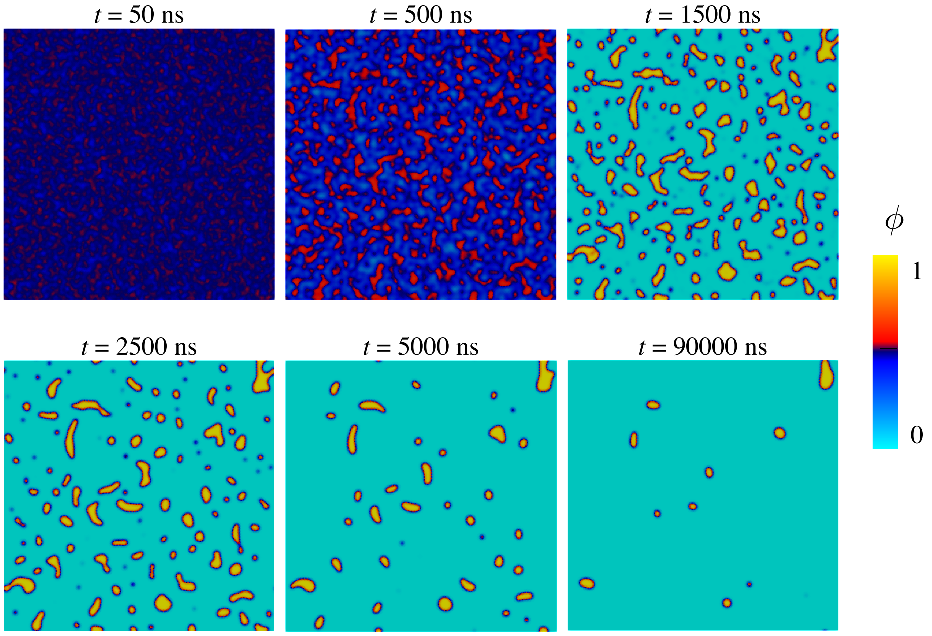

Figure 3.8 – The evolution of the membrane ϕ for 10 μs after the end of the pulse delivery.

Conclusion We present a new model of membrane electroporation that combines membrane water content and transmembrane voltage. Interestingly, thanks to a well-defined membrane free energy, we generalise the pioneering approach of Chizmadzhev, Weaver, and Krassowska by getting rid of the geometric cylindrical assumption on which most of the current electroporation models are based. Our approach is physically relevant and we recover a surface diffusion equation of the lipid phase proposed by Leguèbe et al. in an earlier phenomenological model. We also perform a fine analysis of the non-local operators involved in two simple configurations (a spherical membrane and a flat periodic membrane), which allows us to compare the time constants of the phenomenon in spherical and flat membranes. An accurate splitting scheme combined with Fast Fourier Transforms is developed for efficient computation of the model. Our numerical results allow us to establish a link between molecular dynamics simulations of membrane permeabilization and experimental observations on vesicles and cells.

From the modeling point of view, it is incomplete at it concerns only cell electroporation and not cell permeabilization. Indeed, it has been shown by L. M. Mir's group that the intense electric field generates an oxidation of the lipids, that could explain the long duration of the permeabilised state of the membrane. This means that the pores are closed but the membrane is still permeable. To integrate this phenomenon, a possible extension of our model is to consider two order parameters: ones which follows the (non conserved) Allen-Cahn equation for the water content and a second ones which follows Cahn-Hilliard equation on the lipid phases (oxidised or not).

Furthermore, the changes in the ionic and adenosine triphosphate (ATP) concentrations of the permeabilization modeling, and in the cellular volume need to be addressed if we would like to make this model compatible with electroporation of cardiac cells. More details will be given in my research project given in Chapter 4.

3.2 Tissue modeling

In parallel with the work – presented on the previous section – on membrane modeling, we examine modeling at the tissue scale. It is the subject of this new section. To obtain electroporation modeling at the tissue scale, one could consider homogenization of the microscopic electroporation bidomain model. The formal derivation of this model based on 2-scale convergence – see Section 1.2.2 of Chapter 1 – has not been done. This homogenization will allow to determine a model at the tissue scale compatible with the model at the cell scale. This point is on the list of my research project, see Chapter 4 for details.

However, other electroporation models are available in the literature. The objective of this section is to first present the classical models at the tissue scale which already exist and are used in the literature. We also introduce a macroscopic bidomain system inspired from our knowledge of the phenomenon but not validated through the homogenization of a microscopic model. More precisely, in [15], we compare them and we investigate their calibrations for electrostatic descriptions of a tissue from bioelectrical measurements on rabbit livers performed by Sel et al. [SCB$^+$05]. This work is presented in Section 3.2.1.

However, either the considered model, the choice of boundary conditions of the – very conductive and thin – passive electrodes is a difficult question because, unlike the active electrodes on which either the potential or the current is imposed – corresponding to Dirichlet or Neumann boundary conditions –for the inactive electrodes the value of the equipotential is an unknown of the PDE. This leads to a non-local constraint of the flux along the conductor interface, the so-called floating potential problem. We develop a strategy to address this problem presented in Section 3.2.2 and published in [18]. One could note that this problem appears in the bioimpedancemetry experiment presented in Section 3.1.1. Indeed, the setup includes six spiral micro-electrodes, see [29] whose two correspond to active electrodes to deliver the electroporating pulses and four to measure the voltage.

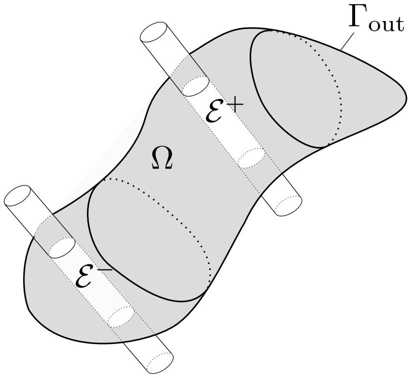

Figure 3.9 – The typical geometrical configuration consists of the tissue domain Ω in gray, deprived of the two needles $\mathcal{E}^{\pm}$, in white. The outer boundary Γ_{out} is represented in bold.

3.2.1 Comparison and calibration of different electroporation models

To compare the different models available in the literature, the following simple configuration is considered, see Figure 3.9. The domain $\tilde{\Omega}$ is a connected, open smooth subset of $\mathbb{R}^d$, $d \in \{2, 3\}$, and consists of two non intersecting subsets: Ω, which corresponds to the tissue under consideration (rabbit liver for instance in the experiment of Sel *et al.* [SCB$^+$05]) and the needles, represented by two parallel cylinders $\mathcal{E}^{\pm}$. The needles are set at the isopotential $\pm g$ respectively. The outer boundary is denoted by $\Gamma_{\text{out}} := \partial\Omega \setminus \mathcal{E}^{\pm}$.

3.2.1.1 Different electroporation models

The standard static model The most used model to describe tissue electroporation consists of the phenomenological electrostatic problem. The tissue is described as a conductive medium, whose conductivity tensor σ depends on the amplitude of the electric field $-\nabla u$. The model reads then

$$\begin{cases} -\nabla \cdot (\sigma(\|\nabla u\|)\nabla u) = 0, & \Omega, \\ \partial_n u|_{\Gamma_{\text{out}}} = 0, \quad u|_{\mathcal{E}^{\pm}} = g^{\pm}, & \end{cases} \tag{3.8}$$

The tissue conductivity consists of a 4 parameters sigmoid function. Typically

$$\forall \lambda \geq 0,\ \sigma(\lambda) = \sigma_0 + \frac{\sigma_1 - \sigma_0}{2}\left(1 + \operatorname{erf}(\mathrm{k}_{\mathrm{ep}}(\lambda - \mathrm{E}_{\mathrm{th}}))\right), \tag{3.9}$$

where σ_0 is the conductivity of the non electroporated tissue, σ_1 is the tissue conductivity of the fully porated tissue, E_{th} is the threshold amplitude for electroporation, and k_{ep} is the slope of the nonlinearity. Here, erf is the Gauss error function.

Remark 6. *It should be noted that this choice of σ is largely phenomenological, and as shown in [IVM10], the available experimental data does not seem sufficient to characterize the dependence of the conductivity on the electric field.*

The biphasic dynamical model In [VSM+18], Voyer et al. propose a biphasic dynamical model based on the description of an individual cell and surrounding matrix as an electric circuit. The ODEs at the cell level are formally generalized to PDEs at the tissue level. It describes the extra-cellular potential $u^{(e)}$ and the electric field inside cells $\mathbf{J}^{(i)}$. The parameters are the extra-cellular and intra-cellular electric conductivities, respectively $\sigma^{(e)}$ and $\sigma^{(i)}$. The conductivity of the cell membrane $\sigma^{(m)}$ depends on time in a way which mimics the effects of poration (appearance of holes on the membrane) and permeabilisation, (degradation of membrane molecules). Both phenomena increase the conductivity as discussed in the conclusion of the previous section in the context of microscopic scale. The resulting system reads

$$\left\{\begin{array}{ll} \nabla\cdot(\sigma^{(e)}\nabla u^{(e)}+\mathbf{J}^{(i)})=0, & \Omega,\\ \varepsilon_m\partial_t\mathbf{J}^{(i)}+(\sigma^{(m)}(t,\|\mathbf{E}^{(m)}\|)+\sigma^{(i)})\mathbf{J}^{(i)}=\sigma^{(i)}\sigma^{(m)}\nabla u^{(e)}, & \Omega,\\ \sigma^{(m)}(t,\|\mathbf{E}^{(m)}\|)=\sigma_0^{(m)}+\sigma_1^{(m)}X_1(t,\|\mathbf{E}^{(m)}\|)+\sigma_2^{(m)}X_2(t,\|\mathbf{E}^{(m)}\|), & \Omega,\\ \partial_n u^{(e)}|_{\Gamma_{\text{out}}}=0,\ u^{(e)}|_{\mathcal{E}^\pm}=g^\pm,\ \mathbf{J}^{(i)}|_{\Gamma_{\text{out}}}=0, & \end{array}\right. \tag{3.10}$$

where $\mathbf{E}^{(m)}=\nabla u^{(e)}-(\sigma^{(i)})^{-1}\mathbf{J}^{(i)}$. The functions X_1 and X_2 are the respective degrees of poration and degrees of permeabilisation. They satisfy

$$\dot{X}_1=\frac{\beta_1(\|\mathbf{E}^{(m)}\|)-X_1}{\tau_1}\text{ and }\dot{X}_2=\frac{\beta_2(X_1)-X_2}{\tau_2}, \tag{3.11}$$

where β_1 and β_2 are 2-parameters sigmoid functions of the form $\beta_l(x)=\frac{1}{2}\left(1+\operatorname{erf}(k_l\left(x-x_l^{\text{trans}}\right))\right)$, where k_l is the stiffness of the sigmoid and x_l^{trans} the transition threshold.

A simplified static version of this model allows to compare it with the standard model. Indeed, the static version of this model reads

$$\left\{\begin{array}{ll} \nabla\cdot(\sigma^{(e)}\nabla u^{(e)}+\mathbf{J}^{(i)})=0, & \Omega\\ (\sigma^{(m)}(\|\mathbf{E}^{(m)}\|)+\sigma^{(i)})\mathbf{J}^{(i)}=\sigma^{(i)}\sigma^{(m)}(\|\mathbf{E}^{(m)}\|)\nabla u^{(e)}, & \Omega\\ \partial_n u^{(e)}|_{\Gamma_{\text{out}}}=0,\quad u^{(e)}|_{\mathcal{E}^\pm}=g^\pm,\quad \mathbf{J}^{(i)}|_{\Gamma_{\text{out}}}=0, & \end{array}\right. \tag{3.12}$$

where $\sigma^{(m)}$ is a sigmoid function similar to (3.9). Written in $u^{(e)}$ and $\mathbf{E}^{(m)}$, the equations become

$$\left\{\begin{array}{ll} \nabla\cdot\Big((\sigma^{(e)}+\sigma^{(i)})\nabla u^{(e)}-\sigma^{(i)}\mathbf{E}^{(m)}\Big)=0, & \Omega,\\ (\sigma^{(m)}(\|\mathbf{E}^{(m)}\|)+\sigma^{(i)})\mathbf{E}^{(m)}=\sigma^{(i)}\nabla u^{(e)}, & \Omega,\\ \partial_n u^{(e)}|_{\Gamma_{\text{out}}}=0,\quad u^{(e)}|_{\mathcal{E}^\pm}=g^\pm,\quad \mathbf{E}^{(m)}|_{\Gamma_{\text{out}}}=0. & \end{array}\right. \tag{3.13}$$

System (3.13) makes it possible to define the equivalent tissue conductivity. Actually, the potential $u^{(e)}$ satisfies

$$\nabla\cdot\left(\left(\sigma^{(e)}+\frac{\sigma^{(i)}\sigma^{(m)}(\|\mathbf{E}^{(m)}\|)}{\sigma^{(i)}+\sigma^{(m)}(\|\mathbf{E}^{(m)}\|)}\right)\nabla u^{(e)}\right)=0.$$

The equivalent tissue conductivity can thus be defined as

$$\sigma_{\text{eq}}(\|\mathbf{E}^{(m)}\|)=\sigma^{(e)}+\frac{\sigma^{(i)}\sigma^{(m)}(\|\mathbf{E}^{(m)}\|)}{\sigma^{(i)}+\sigma^{(m)}(\|\mathbf{E}^{(m)}\|)}.$$

A simplified version of the problem consists in assuming that $\sigma^{(m)}$ depends on $\|\nabla u^{(e)}\|$ instead of $\|\mathbf{E}^{(m)}\|$.

Then the simplified problem reads

$$\left\{\begin{array}{l} \nabla \cdot \left(\left(\sigma^{(e)} + \frac{\sigma^{(i)}\sigma^{(m)}(\|\nabla u^{(e)}\|)}{\sigma^{(i)}+\sigma^{(m)}(\|\nabla u^{(e)}\|)} \right) \nabla u^{(e)} \right) = 0, \quad \Omega, \\ \partial_n u^{(e)}|_{\Gamma_{\text{out}}} = 0, \quad u^{(e)}|_{\mathcal{E}^\pm} = g^\pm, \end{array}\right. \tag{3.14}$$

which is similar to the standard model (3.8) since the function σ_{eq} is a sigmoid function

$$\forall \lambda \geq 0, \qquad \sigma_{eq}(\lambda) = \sigma^{(e)} + \frac{\sigma^{(i)}\sigma^{(m)}(\lambda)}{\sigma^{(i)} + \sigma^{(m)}(\lambda)}.$$

The static bidomain model As explained in Section 1.2.2 of Chapter 1, the bidomain model has been proven to be the homogenization limit of the cell scale electric potential. We consider the following static bidomain written it in terms of the extra-potential $u^{(e)}$ and the transmembrane potential $u^{(m)}$

$$\left\{\begin{array}{ll} \nabla \cdot \left((\sigma^{(e)} + \sigma^{(i)})\nabla u^{(e)} - \sigma^{(i)}\nabla u^{(m)} \right) = 0, & \Omega \\ A_m S^{(m)}(\|\nabla u^{(e)}\|) u^{(m)} - \nabla \cdot \left(\sigma^{(i)} \nabla u^{(m)} \right) + \nabla \cdot (\sigma^{(i)} \nabla u^{(e)}) = 0, & \Omega \\ \sigma^{(e)} \nabla u^{(e)} \cdot \vec{n}|_{\Gamma_{\text{out}}} = 0, \quad u^{(e)}|_{\mathcal{E}^\pm} = g^\pm, \qquad \sigma^{(i)} \nabla u^{(m)} \cdot \vec{n}|_{\partial\Omega} = \sigma^{(i)} \nabla u^{(e)} \cdot \vec{n}|_{\partial\Omega}, & \end{array}\right. \tag{3.15}$$

where as always A_m (m^{-1}) is the ratio of membrane area by unit volume and S_m (S.m^{-2}), the conductance of the cell membranes. To account for the electroporation phenomenon – corresponding to the increase of the membrane conductance – we assume that $S^{(m)}$ follows a sigmoid function of $-\nabla u^{(e)}$

$$S^{(m)}(\|\nabla u^{(e)}\|) = S_0^{(m)} + \frac{1}{2}(S_1^{(m)} - S_0^{(m)}) \left[1 + \text{erf}(\text{k}_{\text{ep}}(\|\nabla u^{(e)}\| - \text{E}_{\text{th}})) \right].$$

In cardiac electrophysiology (see Chapter 1), the nonlinearity usually depends on the homogenised transmembrane voltage $u^{(m)} = u^{(i)} - u^{(e)}$ through the ionic term I^{ion}. However, the nonlinearity in $u^{(m)} = u^{(i)} - u^{(e)}$ is inconsistent with the electroporation phenomenon. Actually, assuming that $g^- = -g^+$ is constant, the symmetry along the axis (Oy) implies that $u^{(e)}$, $u^{(i)}$ and the transmembrane voltage vanishes along (Oy), which is inconsistent with the fact that electroporation occurs between the needles. For this reason, a nonlinearity depending on $\|\nabla u^{(e)}\|$ is chosen, which is relevant with the nonlinearity of the static nonlinear model. This choice has not been validated and it is one main perspective that I will develop in my research project (see Chapter 4) but we emphasize that this model seems more physiological than the previous phenomenological models, see Remark 6.

Numerical simulations The numerical discretizations that have been used to solve the different models are presented in [15]. One can remark that the strong non-linearity of the systems require the use of iteration schemes as for example the modified fixed point proposed in [BBK+15]. In the article, we also develop other strategies allowing to reduce the computational times.

3.2.1.2 Comparison on an experimental setup

We compare the previous model on a realistic situation coming from the experimental setup of Sel *et al.*. It consists of an *ex-vivo* cubic piece of rabbit liver in which two needles are inserted (Figure 3.10-Left).

Square pulses of different amplitudes are applied on the needles and the corresponding intensities are recorded. The data set consists of the measurements of the electric intensity that flows through one

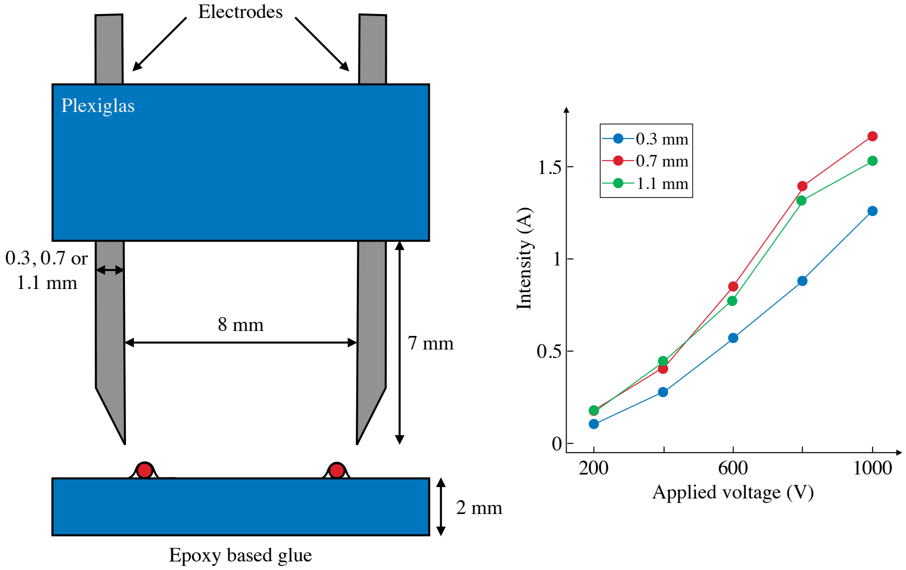

Figure 3.10 – Left: Experimental setup of Sel *et al.*. The piece of rabbit liver is located below the plexiglass. Right: Intensity measurements done at different voltages and with different size of electrodes.

needle, say $\mathcal{E}^+$ for instance. Taking advantage of the symmetries of the liver piece, the computational domain is restricted to a quadrant with homogeneous Neumann conditions at the right, top, and bottom borders, homogeneous Dirichlet conditions at the left border, and the non-homogeneous Dirichlet conditions at the needle. The expression of the numerical electric intensity depends on the model. Denoting by $\ell_{\mathcal{E}^+}$ the length of the electrode in the perpendicular plane to the 2D simulation plane, one has

$$\begin{aligned}
\mathrm{I}^1_{\mathcal{E}} &= \ell_{\mathcal{E}^+} \int_{\mathcal{E}^+} \sigma\left(\|\nabla u\|\right) \nabla u \cdot \vec{n}\, ds, && \text{where } u \text{ is the solution to (3.8)},\\
\mathrm{I}^2_{\mathcal{E}} &= \ell_{\mathcal{E}^+} \int_{\mathcal{E}^+} \sigma_{\mathrm{eq}}(\|\mathbf{E}^{(m)}\|)\nabla u^{(e)} \cdot \vec{n}\, ds, && \text{where } (u^{(e)}, \mathbf{E}^{(m)}) \text{ is the solution to (3.13), or to (3.10)}\\
\mathrm{I}^{2,s}_{\mathcal{E}} &= \ell_{\mathcal{E}^+} \int_{\mathcal{E}^+} \sigma_{\mathrm{eq}}(\|\nabla u^{(e)}\|)\nabla u^{(e)} \cdot \vec{n}\, ds, && \text{where } u^{(e)} \text{ is the solution to (3.14)},\\
\mathrm{I}^3_{\mathcal{E}} &= \ell_{\mathcal{E}^+} \int_{\mathcal{E}^+} \sigma^{(e)}\nabla u^{(e)} \cdot \vec{n}\, ds, && \text{where } (u^{(e)}, u^{(m)}) \text{ is the solution to (3.15)}.
\end{aligned}$$

The above definition of the electrical intensities of the models involve the gradient of the solution along the needle. This is numerically unstable since the electric field is the most intense nearby the electrodes. To smoothen this behavior, it is possible to introduce a specific function w such that the surface integral is replaced by a volume integral. More precisely, let w be defined by

$$-\Delta w = 0, \quad \text{in } \Omega, \tag{3.16a}$$

$$w|_{\mathcal{E}^\pm} = \pm 1, \quad \nabla w \cdot \vec{n}|_{\Gamma_{out}} = 0. \tag{3.16b}$$

Then, thanks to appropriate integration by parts one has

$$\begin{aligned}
\mathrm{I}^1_{\mathcal{E}} &= \frac{\ell_{\mathcal{E}^+}}{2}\int_\Omega \sigma\left(\|\nabla u\|\right)\nabla u\cdot\nabla w\,dx, && \text{where } u \text{ is the solution to (3.8)},\\
\mathrm{I}^2_{\mathcal{E}} &= \frac{\ell_{\mathcal{E}^+}}{2}\int_\Omega \sigma_{\mathrm{eq}}(\|\mathbf{E}^{(m)}\|)\nabla u^{(e)}\cdot\nabla w\,dx, && \text{where } (u^{(e)},\mathbf{E}^{(m)}) \text{ is the solution to (3.13)},\\
\mathrm{I}^{2,s}_{\mathcal{E}} &= \frac{\ell_{\mathcal{E}^+}}{2}\int_\Omega \sigma_{\mathrm{eq}}(\|\nabla u^{(e)}\|)\nabla u^{(e)}\cdot\nabla w\,dx, && \text{where } u^{(e)} \text{ is the solution to (3.14), or to (3.10)}\\
\mathrm{I}^3_{\mathcal{E}} &= \frac{\ell_{\mathcal{E}^+}}{2}\int_\Omega \left((\sigma^{(e)}+\sigma^{(i)})\nabla u^{(e)}-\sigma^{(i)}\nabla u^{(m)}\right)\cdot\nabla w\,dx, && \text{where } (u^{(e)},u^{(m)}) \text{ is the solution to (3.15)}.
\end{aligned}$$

Figure 3.11 shows the characteristic solutions of all models with an electrode diameter of 0.7 mm and a voltage of 800 V (see [15] for the values of the parameters). The results for the standard static model (3.8) (see top row), the dynamic biphasic model (3.10) at $t = 8$ ms (see middle row), and the bidomain model (3.15) (see bottom row) are shown. Although the unknowns of the two systems are not identical, we can make a comparison by comparing the potentials (see left column), the electric flux (see middle column), and the electroporated areas (see right column). For the potential (see left column), we could consider $u(\cdot)$, the solution of (3.8), $u^{(e)}(8\text{ ms},\cdot)$, the solution of (3.10), and $u^{(e)}(\cdot)$, the solution of (3.15). We can see that the potentials are very similar. Regarding the electric flux, we decide to compare $\|\nabla u(\cdot)\|$, $\mathbf{E}^{(m)}$ and $\|\nabla u^{(e)}(\cdot)\|$. The results are still comparable (see middle column). Finally, one could try to define the electroporated region. It can be considered as the region where $\sigma(\|\nabla u(\cdot)\|)$ (or $\sigma^{(m)}(\|\mathbf{E}^{(m)}(8\text{ ms},\cdot)\|)$) reaches a high value for the standard static (resp. dynamic biphasic) model. More precisely, one could define thresholds to select the irreversible or reversible electroporated domains. For the bidomain model, the situation is quite different, since the extracellular conductivity does not depend on the electric flux. We then consider the conductance. Of course, as mentioned earlier, this highlights the need for better comparison of these tissue models, for example by asymptotic analysis. This point will be discussed in my research project. Nevertheless, we can conclude that the solutions of the different models are realistic and can be qualitatively compared. All models seem to be able to represent the electroporation phenomena at the tissue scale.

We will now focus on an important question: Can we calibrate the models using the available data? For this purpose and for simplicity, we will focus on the standard static model. The parameters are then the parameters of the sigmoid function: E_{th}, σ_0, σ_1, and k_{ep}. The data given in [SCB+05] are intensity measurements for 5 voltages and 3 electrode sizes. To estimate the parameters, we use a stochastic algorithm based on the unscented transform, see [15] for details. We first validate the estimation strategy on synthetic data in a framework close to the real data. We reach the following conclusions:

- only E_{th}, σ_0, and σ_1 can be estimated from the data, since there is no sensitivity associated with k_{ep},
- the sensitivity of σ_0 is weaker and more iterations are needed (compared to E_{th} and σ_1),
- without noise, the results are slightly better when three electrodes are considered,
- with noise, the more the data noise is important, the more it is difficult to well estimate the parameters and it becomes crucial to consider measurements performed with different electrodes sizes.

As for the real data (see Figure 3.10-Right), the estimation of the parameters allows to perform simulations of the experiment and, in particular, to determine the electroporated area. Figure 3.12 illustrates the results using $\sigma(\|\nabla u\|)$ for all electrode sizes and for all voltages. These results are very encouraging as they show that we are able to estimate tissue conductivities that allow direct inference of reversible or irreversible electroporated regions based on intensity measures. This work can be considered as a first step in determining the treated zone of a patient's organ.

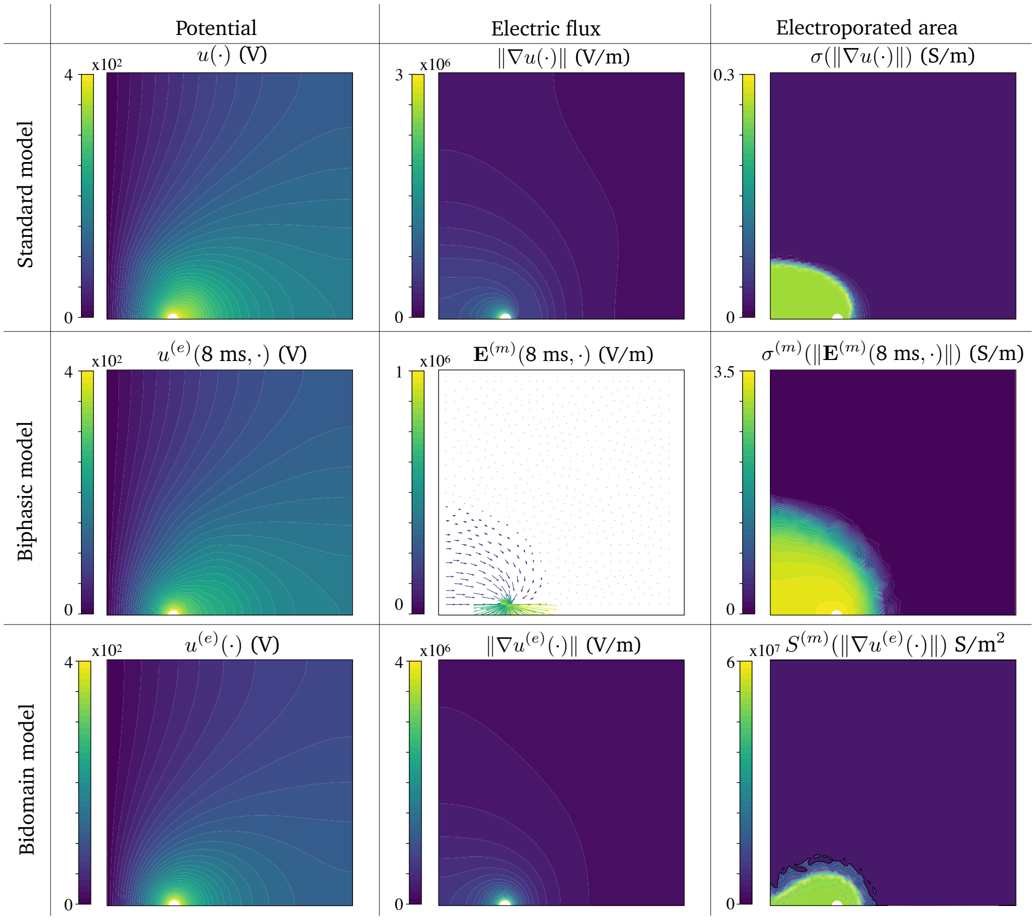

Figure 3.11 – Top: results for the standard static model (3.8). Middle: Results for the dynamic biphasic model (3.10) at 8 ms. Bottom: Results for the static bidomain model (3.15). Even though the unknowns of the systems are not the same, we can make a comparison by comparing the potentials (see left column), the electric flux (see middle column), and the electroporated areas (see right column).

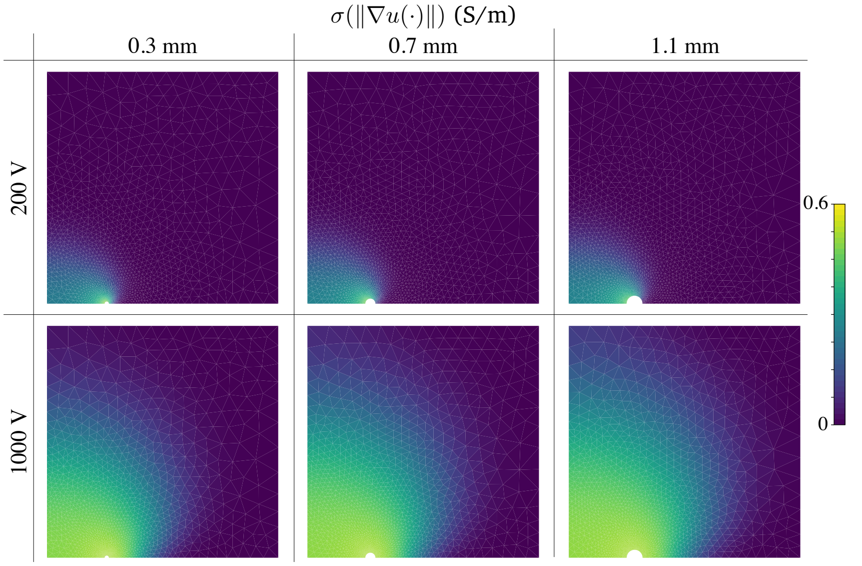

Figure 3.12 – $\sigma(\|\nabla u\|)$ in S/m for applied voltages 200 V and 1000 V and the three geometries for the parameters estimated on all geometries simultaneously.

However, before we move on to clinical applications, there are some mathematical challenges. In particular, multiple electrodes are required in the clinical context. In the context of tumor ablation, the authors in [SCN$^+$17] explain that three to six electrodes are used for inoperable hepatocellular carcinoma. They explain that this number of electrodes correlates with tumor size. In the context of cardiac ablation, multiple electrodes are included in a catheter, see, for example, the Faraware or Faraflex catheter developed by Farapulse Inc. [RDN$^+$21] Because IRE is a multibipolar ablative technology, the electrodes are used in pairs. This means that during a pulse, two electrodes are active and the others are passive. The choice of boundary conditions for these very conductive and thin passive electrodes is a difficult question. While Dirichlet (resp. Neumann) boundary conditions model the imposed potential (resp. the current), the value of the equipotential on the inactive electrodes is an unknown of the PDE. This leads to a nonlocal constraint on the flux along the conductor interface, the so-called floating potential problem. One might also note that this problem also applies to the 3D simulation of the entire experimental setup currently under investigation, which is presented in Section 3.1.1. The next section is devoted to the presentation of our work on the floating potential problem in the context of electroporation.

3.2.2 Floating potential

As explained earlier, when multiple needles are inserted, the influence of the inactive electrodes on the distribution of the electric field must be carefully considered in order to accurately determine the ablation region. The focus of this section, – which summarizes our article [18] – is to present an effective and rigorous way to compute the static electric field in the case of highly conductive thin inclusions.

Electroquasistatic theory states that the surface of a highly conductive conductor is an equipotential surface whose value is implicitly determined by the constraints of the problem. This is the so-called floating potential problem, which has been studied for several decades. In [ABOS14], Amann *et al.* have shown that the penalization method, which consists of imposing a high conductivity in the inclusion provides a less accurate electric potential than a well-designed numerical method for the floating potential problem. This result may seem strange, since the penalization is a kind of model of the real problem, while the floating potential is a perfect conductor approximation. Therefore, the question naturally arises as to how the floating potential approximates the real electric potential, whether there is a relationship between the size and the conductivity of the high conductive material that prevents the use of this approximation, and whether it is possible to increase the accuracy with an asymptotic analysis.

We first examine the observations of Amann *et al.* on a simplified case for which an explicit solution is available. We consider the case of a dielectric (low) conductive material Ω which is the annulus of radii $r_0 \in (0,1)$ and 1 and with conductivity equal to 1, surrounded by a high conductive sheet $\mathcal{O}_\varepsilon$ of thickness ε, and whose conductivity – after nondimensionalization – is of order $1/\varepsilon^\ell$, where $\ell = 1$ or 2 and ε is a small parameter. The electroquasistatic potential u_ε satisfies the following elliptic problem coupled with transmission conditions (TC) and boundary conditions (BC)

$$\left\{\begin{array}{rcll} \frac{1}{r}\partial_r(r\partial_r u_\varepsilon) + \frac{1}{r^2}\partial_\theta^2 u_\varepsilon & = & 0, & (\{r_0 < r < 1\} \cup \{1 < r < 1+\varepsilon\}) \times \mathbb{R}/(2\pi\mathbb{Z}), \\ u_{\varepsilon|r=1^-} - u_{\varepsilon|r=1^+} & = & 0, & \text{(TC)}, \\ \partial_r u_{\varepsilon|r=1^-} - \dfrac{1}{\varepsilon^\ell}\partial_r u_{\varepsilon|r=1^+} & = & 0, & \text{(TC)}, \\ \partial_r u_{\varepsilon|r=1+\varepsilon} & = & 0, & \text{(BC)}, \\ u_{\varepsilon|r=r_0} & = & 1 + e^{\mathrm{i}\theta}, & \text{(BC)}. \end{array}\right. \tag{3.17}$$

The corresponding floating potential (FP) problem consists in finding $(u,\alpha) \in H^1(\Omega) \times \mathbb{R}$ such that

$$\left\{\begin{array}{rcll} \frac{1}{r}\partial_r(r\partial_r u) + \frac{1}{r^2}\partial_\theta^2 u & = & 0, & \{r_0 < r < 1\} \times \mathbb{R}/(2\pi\mathbb{Z}), \\ u_{|r=1} & = & \alpha, & \text{(FP)}, \\ \int_0^{2\pi} \partial_r u(1,\theta)\, d\theta & = & 0, & \text{(FP)}, \\ u_{|r=r_0} & = & 1 + e^{\mathrm{i}\theta}, & \text{(BC)}. \end{array}\right. \tag{3.18}$$

The expression of the exact solution is given in [18]. This solution is then compared with the numerical resolution by standard second order finite difference scheme. This enables us to compare simultaneously how the solution of System (3.17) is approached by the solution of System (3.18), and how accurate is a standard second order numerical scheme for System (3.17). Numerical results are shown in Figure 3.13. Two main observations arise from these simplistic simulations.

First, the floating potential for $\ell = 1$ does not approach the solution of System (3.17), while for $\ell = 2$ it approximates with an accuracy of the order of $O(\varepsilon)$, which means that the floating potential cannot be used to approximate the electric potential when the ratio R_{length} of the thickness of the conductor divided by the characteristic length of the dielectric is of the same order of magnitude as the ratio R_{cond} of the conductivity of the dielectric divided by the conductivity of the high conductive sheet. Second, one can see that the numerical solution of System (3.17) is inaccurate when ε becomes too small compared to the mesh grid . Indeed, the condition number of the matrix for the discretization grows considerably as ε approaches zero. For small discretization steps, the instability increases and the numerical solution has lower accuracy, which provides an explanation for the statement of Amann *et al.* that the penalization method is less accurate than the floating potential.

As shown on this simplistic example, the direct resolution of the electroquasistatic problem in a domain with highly conductive inclusion leads to *ill-conditioned* matrix and floating potentials are preferred to avoid the computational cost. The numerical resolution of such floating potential problems has been studied for several decades. One can cite for instance the paper by Dular *et al.* [DHM$^+$97], where the authors proposed a finite element method, which consists in enriching the finite elements space with spe-

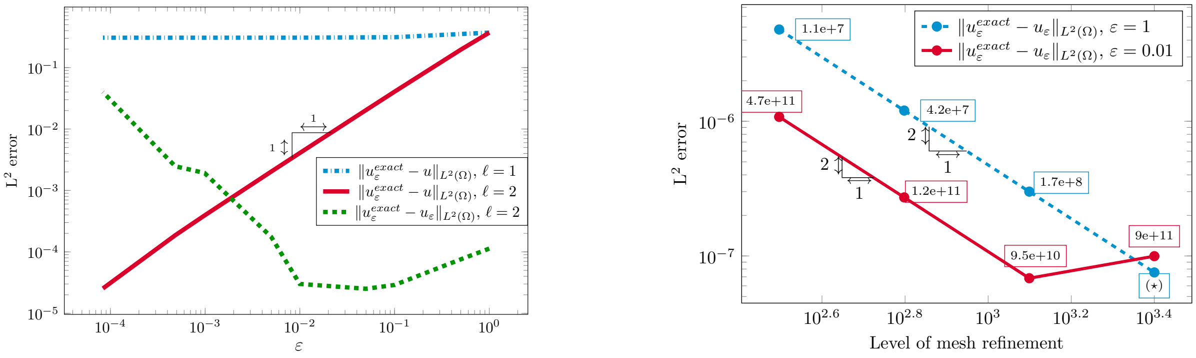

Figure 3.13 – Left: Comparison of the exact solution u_ε^{exact} to (3.17) with the floating potential problem for $\ell = 1$ (blue line) and 2 (red line), and comparison of the explicit and the numerical solutions (3.17) (green line) as ε tends to zero. Right: Numerical convergence with the steps $(d\theta, dr) \in \{(314, 200), (628, 400), (1256, 800), (2512, 1600)\}$ of the 2$^{\text{nd}}$ order scheme to solve System (3.17) for $\varepsilon = 1$ (blue line) and $\varepsilon = 0.01$ (red line).
$^{(\star)}$value not available due to computational cost.

cific functions defined on the nodes of the interfaces Γ_k. Amann *et al.* proposed in [ABOS14] a boundary element method to tackle the problem using single boundary layer integral formulation of the solution. Note that recently, a hybrid Galerkin method has been proposed by Sala *et al.* for a similar problem in the context of ocular hemodynamic, the electric potential being replaced by the Darcy pressure [SPGS18].

The aim of our work on floating potential is threefold. First, we give the proof of the well-posedness of the floating potential problem in the case of N multiple highly conductive inclusions. Second, we propose a new numerical strategy to tackle the floating potential problem. Unlike the previous works cited above, our numerical strategy does not require any new specific numerical method. More precisely, it consists in characterizing the solution to the floating potential problem as a linear combination of $N+1$ explicit Dirichlet problems thanks to the definition of well designed Steklov-Poincaré operators. Finally, we propose an asymptotic analysis of the electroquasistatic potential in the case of a highly conductive thin inclusion, in the asymptotic regime where the ratio of the conductivities R_{cond} is of order ε^2, while the ratio R_{length} is of order ε. In particular, we prove the convergence of the asymptotic approximation at any order as ε goes to 0. We quickly give the results in what follows.

3.2.2.1 Problem setting and analysis

Let us state precisely the problem. Let $\mathcal{O}$ be a domain of $\mathbb{R}^d$, $d = 2, 3$ and let $(\mathcal{O}_k)_{k=1}^N$ be N highly conductive inclusions embedded in $\mathcal{O}$. We denote by Γ_{out} the outer boundary of $\mathcal{O}$, and by Γ_k the boundary of $\mathcal{O}_k$ for $k = 1, \cdots N$. Define $\Omega = \mathcal{O} \setminus \cup \overline{\mathcal{O}_k}$. Let $\sigma \in L^\infty(\Omega)$ be the conductivity map of Ω which satisfies for a given constant $a > 0$: $a \leq \|\sigma\|_{L^\infty(\Omega)} \leq 1/a$. Given $(g_k)_{k=1}^N \in \mathbb{R}$ and $f \in H^{-1}(\Omega)$, the floating potential problem[1] consists in finding the $N+1$-uple $(u, \alpha_1, \cdot, \alpha_N) \in H^1(\Omega) \times \mathbb{R}^N$ such that

$$\left\{ \begin{array}{rcll} -\nabla \cdot (\sigma \nabla u) & = & f, & \text{in } \Omega, \\ u|_{\Gamma_{\text{out}}} & = & 0, & \text{(BC)}, \\ u|_{\Gamma_k} = \alpha_k, \quad \int_{\Gamma_k} \sigma \partial_n u \, ds & = & g_k, & \Gamma_k, \ \forall k = 1, \cdots N. \end{array} \right. \tag{3.19}$$

---

[1] Note that if the inclusion $\mathcal{O}_k$ is isolated, then g_k is nothing but 0.

Even though the well-posedness of System (3.19) has been addressed by Amann *et al.* in [ABOS14] for one inclusion, we present a variant proof for N inclusions that will lead to our simple numerical strategy. For $i = 1, \cdots, N$, we consider the following Steklov-Poincaré operators defined as

$$\begin{aligned} \Lambda^{(i)}_{\text{out}} : H^{-1}(\Omega) &\longrightarrow H^{-1/2}(\Gamma_i) \\ f &\longmapsto \sigma\partial_n v_{|\Gamma_i} \quad \text{s. t.} \quad \begin{cases} -\nabla\cdot(\sigma\nabla v) = f & \text{in } \Omega, \\ v_{|\Gamma_{\text{out}}} = 0, \quad v_{|\Gamma_\ell} = 0, & \text{for } \ell = 1, \cdots, N. \end{cases} \end{aligned}$$

For $k = 1, \cdots, N$, we define $\Lambda^{(i)}_k$ by

$$\begin{aligned} \Lambda^{(i)}_k : H^{1/2}(\Gamma_k) &\longrightarrow H^{-1/2}(\Gamma_i) \\ \gamma &\longmapsto \sigma\partial_n v_{|\Gamma_i} \quad \text{s. t.} \quad \begin{cases} -\nabla\cdot(\sigma\nabla v) = 0 \quad \text{in } \Omega, \\ v_{|\Gamma_i} = \gamma, \\ v_{|\Gamma_{\text{out}}} = 0, \qquad v_{|\Gamma_\ell} = 0, \quad \text{for } \ell \neq i. \end{cases} \end{aligned}$$

If it exists, the solution $(u, \alpha_1, \cdots, \alpha_N)$ to System (3.19) satisfies $\sigma\partial_n u_{|\Gamma_i} = \sum_{\ell=1}^N \alpha_\ell \Lambda^{(i)}_\ell(1) + \Lambda^{(i)}_{\text{out}}(f)$, for $i = 1, \cdots, N$ and the nonlocal constraints of System (3.19) read

$$g_i = \sum_{\ell=1}^N \alpha_\ell \int_{\Gamma_i} \Lambda^{(i)}_\ell(1)ds + \int_{\Gamma_i} \Lambda^{(i)}_{\text{out}}(f)ds, \qquad \text{for } i = 1, \cdots, N. \tag{3.20}$$

By defining $\mathcal{M} = (\mathcal{M}_{ij})_{i,j=1,\cdots,N}$ and $\mathcal{B} = (\mathcal{B}_i)_{i=1,\cdots,N}$, Equality (3.20) can be rewritten as

$$\mathcal{M}\begin{pmatrix} \alpha_1 \\ \vdots \\ \alpha_N \end{pmatrix} = \mathcal{B}, \text{ where } \mathcal{M}_{ij} = \int_{\Gamma_i} \Lambda^i_j(1)ds \text{ and } \mathcal{B}_i = g_i - \int_{\Gamma_i} \Lambda^i_{\text{out}}(f)ds. \tag{3.21}$$

The proof – given in [18] – of the well-posedness of System (3.19) is reduced to proving the invertibility of $\mathcal{M}$.

Proposition 7. *Let Ω be a domain of $\mathbb{R}^d$, $d = 2, 3$. Let us endow the space $(L^2(\Omega))^d$, $d = 2, 3$ with the scalar product $< \cdot, \cdot >_{(L^2(\Omega))^d}$ defined by*

$$< F, G >^\sigma_{(L^2(\Omega))^d} = \int_\Omega \sigma F \cdot G\, dx, \qquad \forall (F, G) \in (L^2(\Omega))^d.$$

The matrix $\mathcal{M}$ is a Gram matrix of the linearly independent vectors $\nabla v_1, \cdots, \nabla v_N$ of $(L^2(\Omega))^d$, where the functions $(v_\ell)_{\ell=1}^N$ are defined by

$$\begin{cases} -\nabla\cdot(\sigma\nabla v_\ell) = 0 \quad \textit{in } \Omega, \\ v_\ell|_{\Gamma_\ell} = 1, \\ v_\ell|_{\Gamma_{\text{out}}} = 0, \qquad v_\ell|_{\Gamma_k} = 0, \quad \textit{for } k \neq \ell. \end{cases} \tag{3.22}$$

Therefore $\mathcal{M}$ is invertible and there exists a unique N+1-uple $(u, \alpha_1, \cdots, \alpha_N) \in H^1(\Omega) \times \mathbb{R}^N$ solution of System (3.19).

3.2.2.2 Numerical strategy to solve the floating potential problem

Proposition 7 leads to a simple characterization of the solution of System (3.19), and thus a simple numerical strategy. We first compute v_ℓ solution to (3.22) for $\ell = 1, \cdots, N$ and v_{out}, solution to

$$\begin{cases} -\nabla \cdot (\sigma \nabla v_{\text{out}}) = f & \text{in } \Omega, \\ v_{\text{out}|_{\partial\Omega}} = 0. \end{cases} \tag{3.23}$$

Second, we compute $(\mathcal{M}_{ij})$ and $(\mathcal{B}_{ij})$ given by (3.21) or equivalently

$$\mathcal{M}_{ij} = \int_\Omega \sigma \nabla v_i \cdot \nabla v_j \, dx, \qquad \mathcal{B}_i = g_i - \int_\Omega \sigma \nabla v_{\text{out}} \cdot \nabla v_i \, dx,$$

and deduce $(\alpha_1, \cdots, \alpha_N)$ by solving the linear system (3.21). Finally, the solution u to the floating potential problem (3.19) is obtained by the following linear combination

$$u = v_{\text{out}} + \sum_{\ell=1}^{N} \alpha_\ell v_\ell,$$

meaning that to compute u, one just has to solve $N+1$ Dirichlet problems, which can be parallelized.

3.2.2.3 Asymptotic analysis

Always in [18], we have proposed an asymptotic analysis to approach accurately the solution to the electroquasistatic potential in a smooth domain with a highly conductive inclusion. We have shown that the so-called floating potential approaches the electroquasistatic potential with a first order accuracy, and we have given the expansion at any order. For the sake of simplicity, we have only considered the case where the relative thickness of the inclusion is of order ε and the ratio of the conductivities (the conductivity of the conductive inclusion divided by the conductivity of the domain) is of order $\frac{1}{\varepsilon^2}$.
Following the classical strategy:
(1) derive uniform estimates of the solution,
(2) make formal expansion (after defining local coordinates and Laplace operator),
(3) and prove the convergence,
we show that the so-called floating potential approaches the electroquasistatic potential.

3.2.3 Conclusion

In this section, we briefly present our work on modeling electroporation at the tissue level. We first give a comparison of the classical models available in the literature and compare them with a bidomain model that now needs to be justified mathematically. Second, we propose a mathematical strategy for dealing with inactive electrodes which is compatible with all these models. The work of this section is closely related to the work of the first section on cell modeling, while the last section, instead of modeling the electroporation phenomenon, focuses on the effects of electroporation on tumor cells.

3.3 Growth of tumor spheroids subjected to pulsed electric field

The aim of this section is to investigate the effects of irreversible and reversible electroporation on tumor growth. It is closely related to the work presented in Chapter 2. The aim of this work was to study the growth specificities of cancer cells in spheroids exposed to a pulsed electric field. Data were obtained by our collaborators Jelena Kolosnjaj, Muriel Golzio and Marie-Pierre Rols (IPBS, Toulouse University). Our strategy is based on an advection model (compatible with System 2.1 of Chapter 2) and well-fitted estimation strategies.

While irreversible electroporation is efficient in most cases, with a complete ablation rate of approximately 75% of treated tumor nodules after an irreversible electroporation procedure [CEH+13], it is known that in some patients ablation is unsuccessful and the event can lead to an accelerated tumor growth. To improve our understanding of the effects of pulsed electric fields on tumor response, we use multicellular tumor spheroids as *in vitro* micro-tumor model. Multicellular tumor spheroids are 3D structures composed of cancer cells that can accurately reproduce the behavior of small solid tumors in their avascular early stages. Multicellular spheroids are becoming an important tool in cancer research as they represent an intermediate stage between 2D monolayer cell models and *in vivo* solid tumors. Spheroids resemble solid microtumors in many ways, such as heterogeneous architecture, internal gradients of signaling factors, nutrients, and oxygenation. In addition, cells within multicellular spheroids interact with each other via cell-cell interactions, and their growth kinetics resemble those observed in tumors *in vivo*. These similarities offer great potential for studying the biological properties of tumors, so they are often used for screening drugs and determining therapeutic efficacy. Such models have already demonstrated their relevance for the study of electroporation phenomena [GWTR13, FGM+15]. The aim of this work was to characterize the regrowth of multicellular spheroids after pulse delivery as a function of pulse magnitude.

Thanks to mathematical models and a calibration strategy, we fit the model to the experimental data to evaluate the global behavior of the spheroid population. Two approaches were considered. The first is to study only the resumption of growth after exposure to the pulsed electric field using the Gompertz model (see Section 2.1.2.2 of Chapter 2). The second model is a partial differential equations as introduced in Section 2.1 of Chapter 2. Three populations of tumor cells are considered: the proliferative cells, the quiescent cells, and the cells whose functioning is altered by the effect of the electric pulse. This more complex approach requires additional parameters but allows us to represent the heterogeneity of the tumor cell response within the multicellular spheroids.

We begin with a presentation of the data in Section 3.3.1. In Section 3.3.2 we present a volume approach that shows encouraging preliminary results, and in Section 3.3.3 we present a 3D model that accounts for cell population heterogeneity. These first three sections correspond to the work published in [21]. Finally, in Section 3.3.4, we illustrate a population-based estimator for PDE systems that we developed ourselves (see [28]) on this system.

3.3.1 Biological experiments

Multicellular HCT-116-GFP spheroids were exposed to different electric field intensities – more specifically, 80 unipolar pulses of 100 μs and a frequency of 1 Hz at 0 V.cm^{-1} (referred to as EF0) or 500 V.cm^{-1} (referred to as EF500 group) or 1000 V.cm^{-1} (referred to as EF1000 group) or 2000 V.cm^{-1} (referred to as EF2000 group) – and their volumes were monitored by fluorescence and bright-field microscopy. The field magnitudes reported are the *nominal magnitudes*, i.e., the voltage between the electrodes divided by their distance. It should be noted that this is not the electric field seen by the cells. There are two control

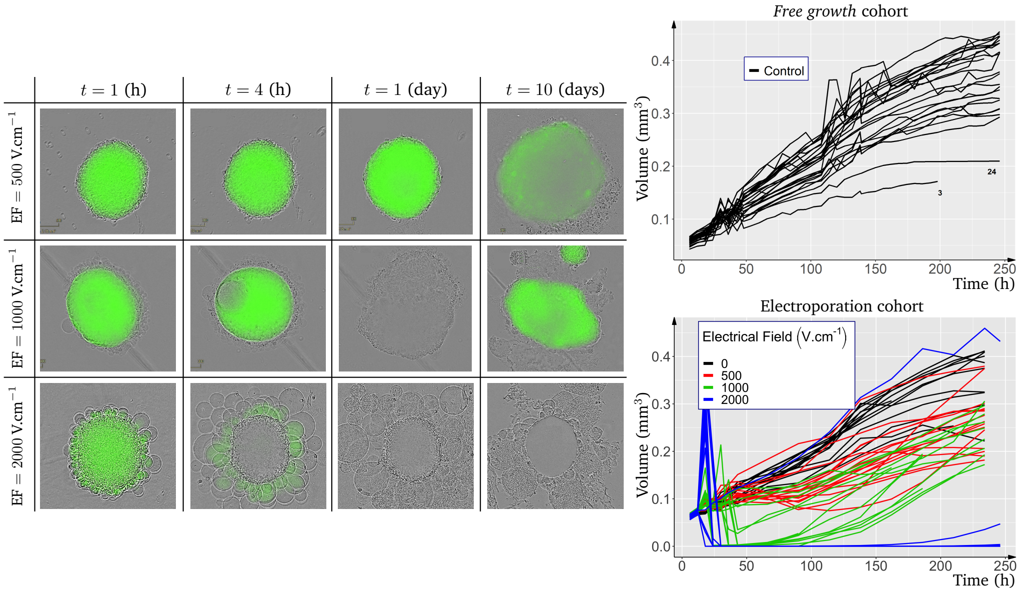

Figure 3.14 – Left: Micrographs of multicellular spheroids followed by fluorescence microscopy of treated spheroids, after the application of electric pulses (80 unipolar pulses of 100 μs and a frequency of 1 Hz). Right: Volume evolutions of multicellular spheroids. Top: Control experiment (24 cases). Bottom: Electroporation experiment (59 cases: 13 for EF0, 16 for EF500, 14 for EF1000 and 16 for EF2000)

groups: *free growth* or 0 V.cm^{-1}. In free growth condition, the spheroids are kept in growth medium. For 0 V.cm^{-1} condition, the spheroids are transferred to the low conduction buffer for 10 minutes, following which the spheroids are rinsed in phosphate saline buffer and re-transferred to growth medium. The experiments were designed and performed by Jelena Kolosnjaj, Muriel Golzio, and Marie-Pierre Rols of the IPBS Institute at the University of Toulouse and are described in detail in [21]. Very large volume values were measured because of the osmotic shock in the cells forming the spheroids after the electric shock. Figure 3.14-Left shows for a spheroid of each of the 3 categories: EF500, EF1000, and EF2000 tumor development. Figure 3.14-Right shows the extracted volume of spheroids: *free growth* at the top and electroporation group at the bottom. In total 83 multicellular spheroids were tracked over 250 hours.

In [21] we first eliminate outliers and explain why the EF1000 group should be divided into two groups: in group A (6 spheroids) there are the multicellular spheroids very damaged by electric shock, whose volume of green fluorescing cells reached almost 0 mm^3 after 48 hours, and in group B (5 spheroids) there are the spheroids whose dynamics are very similar to those observed in cohort EF500.

3.3.2 Modeling of volume evolution

Control groups We consider the Gompertz model already introduced in Chapter 2 for the volume evolution for the two control groups

$$V(t) = V_0 e^{\frac{a}{b}(1-e^{-bt})},$$

where – as already said – V_0 corresponds to the initial volume at time $t = 0$, b^{-1} corresponds to the characteristic time at which the tumor growth capacity decreases and a is a constant corresponding to

	EF500	EF1000-B	EF1000-A
t_{init}	90h	90h	43h
V_{last}	0.24 **(mean)** - 0.039 **(std)**	0.24 **(mean)** - 0.017 **(std)**	0.19 **(mean)** - 0.051 **(std)**
k	3.17 **(mean)** - 0 **(std)**	3.32 **(mean)** - 0 **(std)**	10.7 **(mean)** - 0 **(std)**
b	0.013 **(mean)** - 0.0021 **(std)**	0.0086 **(mean)** - 0.0047 **(std)**	0.011 **(mean)** - 0.0014 **(std)**
MSE	4.6×10^{-5}	1.7×10^{-5}	2.9×10^{-5}

Table 3.1 – Estimated parameters of reversed reduced Gompertz model after electrical shock. Left: EF500. Middle: EF1000B. Right: EF1000A.

the initial growth rate. As with the meningioma cohort, we estimate parameters using a mixed-effects approach. Full details are provided in [21]. The population estimation strategy for the Gompertz model is applied to the 22 multicellular spheroids of the *free growth* cohort and the 13 multicellular spheroids EF0 of the electroporation experiment to test whether the cohorts are similar. The aim is to confirm the assumption that the electrodes have no effect on growth. As a first result, we show that the estimated parameter values are very close, implying that the electrodes do not interfere with growth (see [21]). Moreover, as already stated in Section 2.3.3 of Chapter 2, there is a strong correlation between a and b, and in [VRF+20] even a reduced Gompertz model is introduced, which consists in estimating b as before and to use $k = \frac{a}{b}$ as a constant parameter in the population. As a second result, we show in [21] that this reduced Gompertz model is valid in this context. The estimated parameters are $k = 2.18$ (mean) - 0.0 (std) and $b = 0.010$ (mean) - 0.0017 (std).

Electroporation In this paragraph, we want to study the growth of multicellular spheroids after the electric shock in order to answer the following questions.

- After the electric shock, is there a resumption of growth?
- Is it still a Gompertz growth?
- What are the impacts on the parameters of the model?

First of all, for most of the spheroids which have been electroporated (excepted of spheroids for cohort EF2000), a resumption of the growth occurs, see Figure 3.14-Right. Letting t_{init}, the time of resumption and t_{last} the time of the last measurement, we rewrite the reduced Gompertz model in an inverted form

$$V(t) = V_{last} e^{k e^{-b t_{last}(1 - e^{b(t_{last} - t)})}}.$$

For the 3 cohorts EF500, EF1000-A and EF1000-B, we will estimate the parameters V_{last}, b and k for each fixed t_{last} using the population approach presented previously (in which V_0 plays the role of V_{last}). The parameter t_{last} will be estimated by considering the minimal value given reasonable errors.

Using the mean squared error (MSE) associated with each initial time considered for EF500, EF1000-B, and EF1000-A, and by checking the stability of the estimated parameters and the quality of the fits, we set the value to $t_{init} = 90$h (resp. 90h and 43h) for cohort EF500 (resp. EF1000-B and EF1000-A). The corresponding fits are shown in Figure 3.15 and the corresponding estimated parameters in Table 3.1. As a third result, we can note that the regrowth still follows a Gompertz law and that it also seems to be an accelerated regrowth. Namely, while the estimated mean values of b are comparable to the estimated value of the control cohorts ($b = 0.010$), the estimated values of k are larger than the estimated value of the control cohorts ($k = 2.18$).

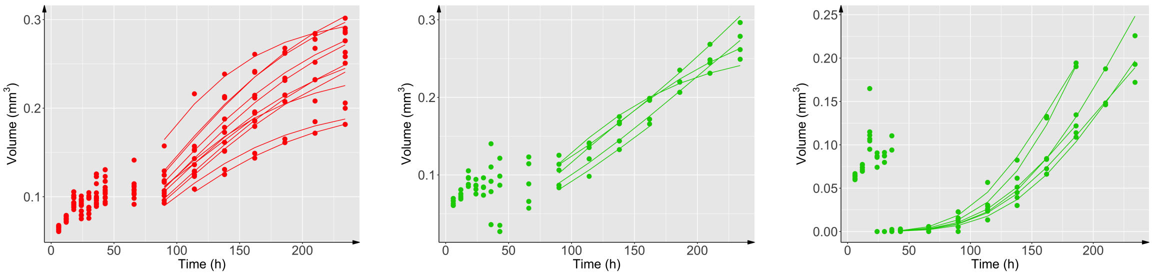

Figure 3.15 – Volume evolution after electrical shock. Left: fits using reduced Gompertz model for EF500 ($t_{init} = 90$h). Middle: fits using reduced Gompertz model for EF1000-B ($t_{init} = 90$h). Right: fits using reduced Gompertz model for EF1000-A ($t_{init} = 43$h).

Even if this volume approach shows encouraging preliminary results, this approach does not allow to properly quantify the impact of the electroporation and does not integrate the heterogeneity of the tumor, *i.e.* the fact that the tumor is composed of proliferative and quiescent cells. These two limitations motivate the introduction of a PDE system enabled to represent the tumor evolution upon submission to electrical shocks.

3.3.3 Modeling the 3D evolution of spheroid

Modeling In this section, we complexify the growth model to introduce a heterogeneity in the cell population. The model has been designed to describe the 3D evolution of the spheroids with two constraints: (1) to be compatible with the Gompertz model at the volume scale, (2) to depend on few parameters which are identifiable with the available data.

We consider an advanced mathematical model based on advection model which is compatible with System 2.1 of Chapter 2. We will consider 3 compartments of cells: the proliferative ones whose the density denoted by P, the quiescent ones whose the density denoted by Q and the cells with a functioning altered by the impact of the electrical shock whose the density denoted by F. By denoting the tumor spheroid domain at time t by $\Omega(t)$, the evolution of the density P is supposed to satisfy the following equation

$$\partial_t P + \nabla \cdot (\vec{v}P) = f(t, P, Q), \quad \Omega(t), \tag{3.24}$$

and the density of Q follows

$$\partial_t Q + \nabla \cdot (\vec{v}Q) = g(t, P, Q), \quad \Omega(t), \tag{3.25}$$

where $\vec{v}$ denotes the velocity field that describes the motion of tumor cells. The evolution of the density F is supposed to satisfy the following equation

$$\partial_t F + \nabla \cdot (\vec{v}F) = 0, \quad \Omega(t). \tag{3.26}$$

Using the saturation hypothesis $P + Q + F = 1$ in $\Omega(t)$, we have $\nabla \cdot \vec{v} = f(t, P, Q) + g(t, P, Q)$. This implies that the volume defined by

$$V(t) = \int_{\Omega(t)} dX$$

verifies

$$\begin{aligned}V'(t) &= \frac{d}{dt}\int_{\Omega(t)} dX = \int_{\partial\Omega(t)} (\vec{v}\cdot\vec{n})dX = \int_{\Omega(t)} \nabla\cdot\vec{v}\,dX \\ &= \int_{\Omega(t)} [f(t,P,Q)+g(t,P,Q)]dX.\end{aligned}$$

Our objective is to have the volume following a Gompertz law when there is no electroporation (then $P+Q=1, \Omega(t)$). One can prove – following the proof given in [17] – that a way to do so consists in imposing

$$f(t,P,Q)+g(t,P,Q) = \tau_G(t)(P(t,x)+Q(t,x)), \forall t, \tag{3.27}$$

where $\tau_G(t) = ae^{-bt}$ corresponds to the growth rate. The function g has to be defined in order to obtain realistic behavior. Assuming that proliferative cells become quiescent cells, we assume that $g(t,P,Q) = \tau_{PtoQ}P$. The function τ_{PtoQ} depending on (t,x) has to be chosen to describe the appearance of a high quiescent proportion of cells in the center of the spheroid. When electroporation pulses occur, three phenomenas are considered:

(1) a part of cells is destroyed,

(2) the functioning of a part of the cells is modified *i.e.* a part of proliferative and quiescent cells changes their functioning,

(3) the initial growth rate is modified.

Denoting by t_{as} the time just after the electrical shock, these three phenomenas can be mathematically modeled by:

(1) the death of proliferative and quiescent cells leads to $P(t_{as},x)=0$, for $x\in\omega_P\subset\Omega(t<t_{as})$ and $Q(t_{as},x)=0$, for $x\in\omega_Q\subset\Omega(t<t_{as})$ then $\Omega(t_{as})$ decreases,

(2) the functioning modification of proliferative and quiescent cells leads to $F(t_{as},x)=\lambda(P(t_{as},x)+Q(t_{as},x))$, for $x\in\Omega(t_{as})$,

(3) the value of the parameter is decomposed into two parts:

$$a = \begin{cases} a_{bs}, \forall t < t_{as}, \\ ma_{bs}, \forall t \geq t_{as}, \end{cases} \tag{3.28}$$

where m is a constant (always estimated superior to 1) which can be interpreted as a boost of the growth after the electrical shock.

Radial equation Inspiring from the work of [MFL+18], the spherical symmetry of spheroid can be used to rewrite the model in radial and relative coordinates. Interestingly, this implies that the velocity field $\vec{v}$ is entirely determined by its divergence, therefore no assumption on the rheology of the tumor spheroid is needed (contrary to System 2.2). For all $x\in\Omega(t)$, we denote the normalized radial coordinate ($r=0$ at the center of the spheroid, $r=1$ at the surface)

$$r(t,x) = \frac{\|x\|}{R(t)},$$

where R the radius of the spheroid. We define, for all (t, x):

$$\tilde{u}(t, r(t,x)) = u(t,x), \text{ for unknowns } P, Q, \tau_{PtoQ} \text{ and } \vec{v}.$$

We denote by $\tilde{v}$ the radial component of the velocity $\tilde{\vec{v}}$ and the invariance by rotation implies that $\tilde{\vec{v}} = \tilde{v}\vec{e}_r$. One can easily show that the volume V (resp. the radius R) follows

$$V'(t) = \tau_G(t) \int_{\Omega(t)} (P(t,x) + Q(t,x))dX.$$

We denote by I the following function of t and r

$$I(t,r) = \int_0^r (\tilde{P}(t,\underline{r}) + \tilde{Q}(t,\underline{r}))\underline{r}^2 d\underline{r}$$

Using radial coordinate (see the proof given in Appendix of [21]) and the fact that $V = \frac{4}{3\pi}R^3$, one can show that

$$\left\{ \begin{aligned} R'(t) &= R(t)\tau_G(t)I(t,1), \\ \partial_t \tilde{P}(t,r) + \tau_G(r^{-2}I(t,r) - rI(t,1))\partial_r \tilde{P}(t,r) &= \tau_G(1-\tilde{F})(1-\tilde{P}) - \tilde{\tau}_{PtoQ}\tilde{P}, \\ \partial_t \tilde{F}(t,r) + \tau_G(r^{-2}I(t,r) - rI(t,1))\partial_r \tilde{F}(t,r) &= -\tau_G(1-\tilde{F})\tilde{F}, \\ \tilde{Q} &= 1 - (\tilde{P} + \tilde{F}). \end{aligned} \right. \tag{3.29}$$

To close the system, the evolution of the rate $\tilde{\tau}_{PtoQ}$ has to be described. Seen as representing the lack of oxygen, one can consider the following logistic function

$$\tilde{\tau}_{PtoQ}(t,r) = \tilde{\tau}_{PtoQ}^{begin} - \frac{\tilde{\tau}_{PtoQ}^{begin} - \tilde{\tau}_{PtoQ}^{end}}{1 + e^{\frac{(R(t)(1-r)-d)}{s}}}.$$

The parameter d corresponds to the distance from the tumor front for which the oxygen is easily accessible. The parameter s corresponds to the slope of the function. The parameters $\tilde{\tau}_{PtoQ}^{begin}$ (resp. $\tilde{\tau}_{PtoQ}^{end}$) corresponds to the value of $\tilde{\tau}_{PtoQ}$ far from (resp. close to) the tumor boundary.

Parameters estimation Six parameters need to be estimated: V_0, k, b, p, m and λ using volume evolution. We always want to use a population estimation strategy. However, the software `Monolix` [Ant19] cannot be used here to estimate the parameters because our model is a PDE system. We consider two different strategies to make the estimation. First in [21], we consider a `Matlab` library called *nlmefitsa* in which the SAEM algorithm is implemented. We will give the details obtained with the strategy right after. Second, we propose a population-based estimation for PDE systems in [28] and illustrate it using the PDE system and the data given here. We will develop this work in Section 3.3.4.

Very large volume values were measured because of the osmotic shock in the cells forming the spheroids after the electric shock. Because our model does not account for this phenomenon, these values are not used to estimate the parameters. Different strategies are possible: either not consider them or fix them at the minimum volume. To avoid identifiability issues, b and k can be estimated with the control cohort, and their mean values are used to estimate the other parameters in the 4 cases: EF500, EF1000A, EF1000B, and EF2000. Table 3.2 (first rows) gives the results obtained in this context.

	Case	EF500 (12 spheroids)	EF1000-B (5 spheroids)
λ	Function *nlmefitsa*	0.22 (mean) - 0.092 (std)	0.37 (mean) - 0.012 (std)
	Algo [28]	0.37 (mean) - 0.035 (std)	0.36 (mean) - 0.045 (std)
p	Function *nlmefitsa*	0.89 (mean) - 0.014 (std)	0.82 (mean) - 0.086 (std)
	Algo [28]	0.90 (mean) - 0.0028 (std)	0.86 (mean) - 0.012 (std)
m	Function *nlmefitsa*	1.11 (mean) - 0.024 (std)	1.40 (mean) - 0.16 (std)
	Algo [28]	1.14 (mean) - 0.18 (std)	1.21 (mean) - 0.16 (std)

	Case	EF1000-A (6 spheroids)	EF-2000 (14 spheroids)
λ	Function *nlmefitsa*	0.77 (mean) - 0.10 (std)	0.97 (mean) - 0.065 (std)
	Algo [28]	0.69 (mean) - 0.04 (std)	0.92 (mean) - 0.0015 (std)
p	Function *nlmefitsa*	0.17 (mean) - 0.010 (std)	0.0016 (mean) - 9×10^{-5} (std)
	Algo [28]	0.11 (mean) - 0.015 (std)	0.00097 (mean) - 2.1×10^{-6} (std)
m	Function *nlmefitsa*	5.19 (mean) - 1.02 (std)	x
	Algo [28]	5.3 (mean) - 0.77 (std)	x

Table 3.2 – Mean (mean) and standard deviation (std) of estimated parameters using real data. The first rows give the results obtained with the NLME algorithm using the `Matlab` function *nlmefitsa* and the second rows the results obtained using the population-based estimation presented in Section 3.3.4.

Results The estimated parameters of cohort EF1000-B are very similar to the parameters of cohort EF500. The values of λ increase with the intensity of the pulse. Concerning the value of p, it is interesting to note that there is small decrease of the volume for EF500 and EF1000-B while for the group EF1000-A (resp. EF2000), a decreasing of 75% (resp. almost 100%) is observed. Concerning m, the value increases with the value of the electrical field. Note that the post-pulse data for EF2000 do not really allow us to estimate the m parameter, since the data for all spheroids are close to 0. Therefore, this parameter is not estimated. Figure 3.16 shows the spheroid evolutions with distribution of proliferative cells for the 4 cohorts (column 2 to column 5) compared to the control cohort (column 1).

Discussion The use of a PDE system makes it possible to determine the percentage of cells destroyed and the percentage of cells whose functioning was altered by the effect of electroporation for each value of the electrical field. It was seen that at an electrical field close to 1000 V.cm^{-1} (partially irreversible electroporation and partially reversible electroporation), the increase of the electrical field seemed to boost the resumption of spheroid growth. Our results provide good insight into the effects of electroporation on tumor growth. When irreversible electroporation is used in clinics to ablate tumors, the treatment may induce cell death by irreversible electroporation. This effect is observed in a specific area, namely the area where the electric field strength is highest – at the optimal location with respect to the electrodes. The effectiveness of fully irreversible electroporation was well observed in the spheroid group exposed to 2000 V.cm^{-1}. Nevertheless, next to the epicenter of the highest electric field, where the tumor is ablated, we have zones that underwent milder electric field strengths exposure, and we have the occurrence of partially irreversible electroporation. Within this *shadow* zone, not all cells are killed, and the surviving cells resume growth. This effect was clearly present in the multicellular spheroids exposed to 1000 V.cm^{-1}. Thus, this field amplitude produced two radically different behaviors: either death or growth boost. We hypothesize that this variable response rate is due to the inhomogeneity of the electric field. If the spheroid (or tumor) was not reached efficiently, we have a relapse. If the positioning of the spheroid

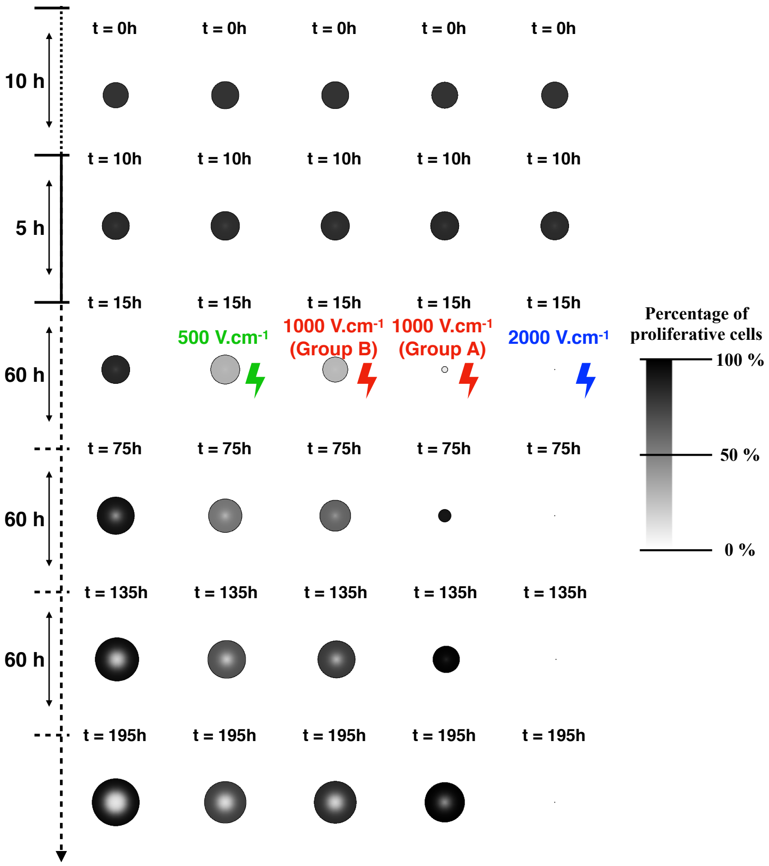

Figure 3.16 – Spheroid evolutions with distribution of proliferative cells. Black (resp. white) = 100 (resp. 0) % of proliferative cells. Column 1: free growth, column 2: EF500, column 3: EF1000B, column 4: EF1000A and column 5: EF2000.

(or tumor) is in the center of the electrodes, the treatment is efficient. This is a recurrent problem even in clinics, where physicians observe a different response rate – either efficient treatment of a patient with a decreased tumor or a tumor relapse [SNdJ+14]. The advantage of our model is that we can determine the trend of tumor growth shortly after electroporation. So, in practice, this model can be used to determine which tumors have been treated inefficiently and that the patient is on the path to relapse. This would alert the treating physician that the treatment was not efficient and that an additional electroporation cycle is needed to remove the tumor again. As for the growth boost, it is particularly intriguing and certainly requires further investigation from a biological, physical, and mathematical perspective.

3.3.4 Population-based estimation for PDE systems

The estimation of the parameters given in Table 3.2 (first rows) requires several hours for each of the cohorts even if the cohorts are small (< 15 spheroids) and the number of parameters is small (= 3) and it is a 1D PDE system. It is possible that the `Matlab` function used for estimation could be optimized, but it remains a challenge for a mixed-effects strategy to increase the size of the underlying dynamics – for example, when using PDE systems – with an acceptable complexity cost to the algorithm. To our knowledge, there is only one work that aims to develop a strategy for using population estimation strategies for PDE systems. In [GLV14], the PDE system is solved by interpolations of solutions precomputed on a *carefully constructed* mesh of the parameter domain.

In [28], we propose a formulation of a population-based estimator for PDE systems to address this challenge. The errors in the initial conditions are controlled by a Luenberger observer that corrects for the state, and the parameters are estimated using a population reduced-order Kalman-based filter restricted to the parametric space. This sophisticated method for solving this difficult problem is based on two important methodological strategies: (1) the population-based Kalman filter introduced in [23], (2) the joint state-parameter estimation introduced in [MCLT08]. More precisely, the population-based Kalman filter [23] captures all population information in a unified maximum likelihood estimation procedure assuming Gaussian disturbances. However even the proposed reduced version of this population-based Kalman filter – defined by combining clusters subpopulations with common observational backgrounds – results in the famous curse of dimensionality [Bel56] that makes it numerically intractable for partial differential equations (PDE). Assuming that the dimension of the parameters is smaller than the dimension of the system state, which is then responsible for the curse of dimensionality, one can restrict the population-based Kalman filter to parametric space and couple it with a Luenberger observer following the strategy presented in [MC11b]. This strategy assumes that a suitable Luenberger observer has been previously designed to control the trajectory.

The first section of [28] is devoted to the formalization of the estimation problem and the introduction of the population-based estimator and we refer to the paper for this part. The second section applies the complete strategy on spheroid electroporation. The problem, model, and data are the same as in Section 3.3.3. We first introduce and analyze a Luenberger observer, see Section 3.3.4.1 and we second perform numerical experiments on synthetic data to validate the approach, see Section 3.3.4.2. The choice of the 1D PDE model stems from the fact that the computational cost of solving the PDE system is still reasonable and allows to perform many replicates – 7500 simulations in total.

3.3.4.1 A Luenberger observer for System (3.29)

We design the following Luenberger-type observer

$$\begin{cases} \hat{R}'(t) & = \hat{R}(t)\tau_G(t)\hat{I}(t,1) - \gamma_{\text{obs}}(t)(\hat{R}-R), \\ \partial_t\hat{P}(t,r) + \tau_G(r^{-2}\hat{I}(t,r) - r\hat{I}(t,1))\partial_r\hat{P}(t,r) & = \tau_G(1-\hat{F})(1-\hat{P}) - \hat{\tau}_{PtoQ}\hat{P}, \\ \partial_t\hat{F}(t,r) + \tau_G(r^{-2}\hat{I}(t,r) - r\hat{I}(t,1))\partial_r\hat{F}(t,r) & = -\tau_G(1-\hat{F})\hat{F}, \\ \hat{Q} & = 1-(\hat{P}+\hat{F}). \end{cases} \tag{3.30}$$

with

$$\hat{I}(t,r) = \int_0^r (1-\hat{F})\underline{r}^2 d\underline{r}, \text{ and } \hat{\tau}_{PtoQ}(t,r) = \tilde{\tau}_{PtoQ}^{begin} - \frac{\tilde{\tau}_{PtoQ}^{begin} - \tilde{\tau}_{PtoQ}^{end}}{1+e^{\frac{(\hat{R}(t)(1-r)-d)}{s}}}.$$

The function γ_{obs} is the gain function. We assume that the function goes from $[0,T]$ to $]0,\infty[$ and is bounded *i.e.* there exists $\gamma_{\text{obs}}^{\min}, \gamma_{\text{obs}}^{\max} \in]0,\infty[$ such that $\gamma_{\text{obs}}^{\min} \leq \gamma_{\text{obs}}(t) \leq \gamma_{\text{obs}}^{\max}$, for all $t \in [0,T]$. Initial conditions are given by

$$\hat{R}(0) = \hat{R}_0, \quad \hat{P}(0,r) = \hat{P}_0 \in [0,1], \quad \hat{Q}(0,r) = 1-\hat{P}_0, \quad \hat{F}(0,r) = 0, \quad \forall r.$$

In this part, we only consider uncertainties reduced to the initial condition. The values of the parameters are fixed to the true values. We admit here that there exists unique solutions to System 3.29 and System 3.30 and these solutions are smooth (this can be proved by a Banach contraction mapping theorem). The proof of the following proposition is given in [28].

Proposition 8. *We have*

(1) $\forall t \geq 0$, $\forall r \in [0,1]$, $U(t,r) \in [0,1]$, *for* $U = \{\tilde{P}, \tilde{Q}, \tilde{F}, \hat{P}, \hat{Q}, \hat{F}\}$ *and* $(\tilde{P}+\tilde{Q})(t,r), (\hat{P}+\hat{Q})(t,r) \in [0,1]$,

(2) $\forall t \geq 0$, $\tilde{R}(t) \in \Big[\min\big(\tilde{R}(0), \tilde{R}(t_{as})\big)\ ,\ \tilde{R}(0)e^{\frac{m a_{bs}}{3b}}\Big]$.

In order to analyze the convergence of the observer we will study the estimation error defined by $\tilde{R} = R - \hat{R}$ and $\tilde{P} = P - \hat{P}$. One can prove the two following propositions (see [28] for the proofs and for numerical illustrations).

Proposition 9. *If* $\gamma_{obs}^{min} > \frac{m a_{bs}}{3}$, *the radius* $t \mapsto \tilde{R}(t)$ *converges exponentially to* 0 *when* t *goes to* $+\infty$.

Proposition 10. *If* $\gamma_{obs}^{min} > \frac{m a_{bs}}{3} + \mathcal{T}_O^{end}$ *and* $\tilde{P}(0,\cdot) \in H^s(]0,r[)$, *the norm* $t \mapsto \|\tilde{P}(t,\cdot)\|^2_{L^2(]0,1[)}$ *converges exponentially to* 0 *when* t *goes to* $+\infty$.

3.3.4.2 State and parameter estimation

We would like to test the ability of our algorithm to estimate parameters. First, a synthetic data benchmark is considered to validate our implementation. To do so, we run different simulation series with different numbers of spheroids denoted by N_S and with different measurement errors – *i.e.* with different values of the standard deviation of the additive Gaussian noise always denoted by σ_{err} – for 6 scenarios: strong priors with $\gamma_{\text{obs}} = 0$ (**str. pr.**), strong priors with $\gamma_{\text{obs}} > 0$ (**str. pr. - so**), weak priors with $\gamma_{\text{obs}} = 0$ (**w. pr.**), weak priors with $\gamma_{\text{obs}} > 0$ (**w. pr. - so**), weak priors and false initial conditions with $\gamma_{\text{obs}} = 0$ (**w. pr., f. IC**), weak priors and false initial conditions with $\gamma_{\text{obs}} > 0$ (**w. pr., f. IC - so**). To limit the energy consumption of this validation, we will focus on estimating only two parameters: b and a_{bs} considering the model in the free growth case, *i.e.* without electroporation. More precisely, instead of estimating a_{bs}, we will estimate $k = \frac{a_{bs}}{b}$ which is assumed to be fixed in the population when using the reduced Gompertz model introduced in [VRF⁺20]. To validate our algorithm, we consider several statistical validation criteria whose the definitions are given in [28]: the relative bias (rBIAS), the relative mean squared error (rMSE), the mean estimated standard deviation (STD), the empirical standard deviation of estimates, defined as the standard deviation of estimates at convergence (ESTD) and the coverage (COV). For information on how to generate data, please refer to [28]. We generate $N_R = 100$ simulation replicates for $N_S = 1, 5, 10, 20$ and $\sigma_{err} = 0, 0.04, 0.08$ for the 6 scenarios. We also generate $N_R = 100$ simulation replicates for $N_S = 40$ but only for the scenario **w. pr., f. IC - so**.

To illustrate how the algorithm works, Figure 3.17 shows the time evolution of the states and parameters of two spheroids belonging to a cohort of 10 spheroids and $\sigma_{err} = 0.08$. The generated data and the two selected spheroids are indicated (top, left). The second line corresponds to Spheroid 2 and the third line to Spheroid 6. In both cases, the first column corresponds to radius, the second to proliferative and quiescent densities, and the third to parameter b. The parameter k – estimated fixed in the population – is given in the upper right corner. The target states and target values of the parameters are shown in blue. The blue points correspond to the noisy observed data. The states and parameter values of the observer are shown in yellow. The dashed lines correspond to the 95% confidence interval when available (*i.e.* for

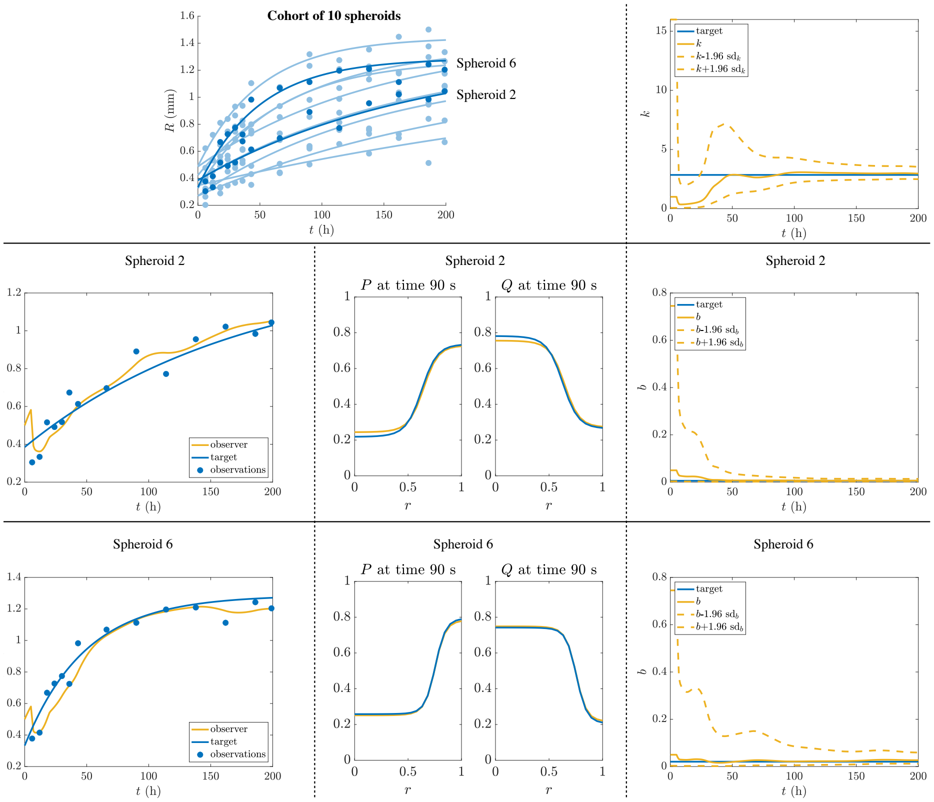

Figure 3.17 – Time evolution of states and parameters for two spheroids with $N_S = 10$ and $\sigma_{err} = 0.08$. The target states and target values of the parameters are shown in blue. The blue points in the graphs of the radius correspond to the noisy observed data. The states and parameter values with population estimation are shown in yellow. The dashed lines correspond to the 95% confidence interval. First line, left: generated data of a cohort of the 10 spheroids. The two selected spheroids are in dark blue. First line, right: evolution of parameter k (assumed fixed in the cohort). Second (resp. third) line: Spheroid 2 (resp. 6) with time evolution state of radius on the left, proliferative and quiescent cells at a time step in the middle and parameter b on the right.

the parameters only). One can see that the yellow lines converge to blue lines over time, showing the ability of our algorithm to estimate well.

Figure 3.18-Left shows the rMSE, the rBIAS, and the COV concatenated for both parameters b and k and the STD, the ESTD, and the BMIXED for parameter b against the number of spheroids considered N_S for a standard deviation error σ_{err} of 0.08 for the 6 scenarios. First, one can see that, as expected, the results are better when strong priors and true initial conditions are considered. Second, using the state observer in conjunction with the Kalman observer for the parameters leads to better results when weak priors are considered and especially when the initial conditions are false. Since Scenario **w. pr., f. IC - so** is the most interesting, we will focus on it. Figure 3.18-Right shows the rMSE, the rBIAS, and the COV concatenated for both parameters b and k and the STD, the ESTD and the BMIXED for parameter b against the considered errors. As expected, increasing the number of spheroids gives better results and increasing the errors worsens them, although it can be seen that they are still acceptable.

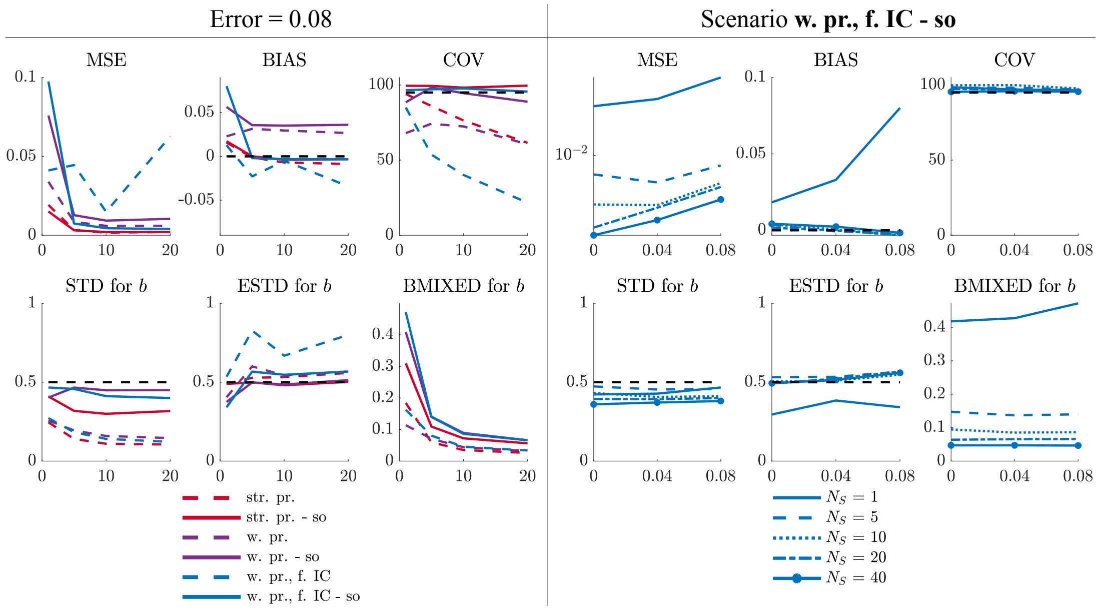

Figure 3.18 – Performances evaluated over 100 replicates for the 6 scenarios when $\sigma_{err} = 0.08$ (left) and for Scenario **w. pr., f. IC - so** (right). First lines: rMSE (log-scale), rBIAS and COV concatenated for both parameters b and k as a function of either the errors (left) or the number of spheroids (right) considered. Second line: STD, ESTD and BMIXED for parameter b (k is fixed in the population) as a function of either the errors (left) or the number of spheroids (right) considered.

Algo	Δ_x	$N_S = 1$	$N_S = 5$	$N_S = 10$	$N_S = 20$	$N_S = 40$
Algorithm [28]	0.05	0.03	0.3	1	4	12
Algorithm [28]	0.01	x	x	3.5	x	x
Algorithm [28]	0.001	x	x	60	x	x
Function *nlmefitsa*	0.05	x	80	x	x	x

Table 3.3 – Computation times given in **minutes** when estimating 2 parameters (b and k) in Scenario **w. pr., f. IC - so**. Comparison with the `Matlab` function *nlmefitsa* average of computation times for 10 replicates).

These estimates are supplemented by computational times obtained using a 2.3 GHz quad-core Intel Core i7 computer and an implementation in `MATLAB-2020-b`, see Table 3.3. This gives an order of magnitude numerical complexity of the algorithm, albeit with a not fully optimized implementation. In particular, we give the computation times when no parallelization of the code is performed, although it is very easy to parallelize the loop on sigma points. Our strategy must solve N_σ ($= N_S \times N_\theta + 1$ using simplex sigma-points) times a time step of the PDE system at each time step. Therefore – even if the estimation part was reduced to the parameters with the Kalman filter, which means, that the dimension of the covariance matrix goes to $N_S \times (N_\theta + N_{\Delta x}) = N_S \times (2 + 2 \times \frac{1}{\Delta_x} + 1) = 43N_S$ to $N_S N_\theta = 2N_S$ – the computation times are always strongly related to the size of $N_{\Delta x}$. To illustrate this, we also shrink the spatial step Δ_x for $N_S = 10$. We can see that the computation times for a non-optimized algorithm are still reasonable and this shows the possibility of applying it to 2D or 3D PDE systems.

Finally, for comparison, we use the `Matlab` function *nlmefitsa*, which is an implementation of the nonlinear mixed effects model (NLME) with the stochastic EM algorithm, but only for $N_S = 5$ because of the high computational cost. We report the mean of the computation times for 10 replicates. The rMSE – equal to 0.0067 (mean for only 10 replicates) – is very close to the rMSE – equal to 0.0074 (mean for 100 replicates) – obtained with our algorithm in exactly the same context.

Our approach shows to be successful on synthetic data. It is clear that using the state observer in conjunction with the Kalman observer for the parameters leads to better results when weak priors are considered and especially when the initial conditions are false. This implies that we recommend the use of a state observer especially when the confidence in the initial conditions is low. We are aware that building a state observer to handle errors in the initial conditions can be a very difficult step and is the main drawback of our strategy. We also perform estimation on real data – see second rows of Table 3.2 – and our results compare very well with the estimation procedures used in the literature as standard for estimating parameters of nonlinear mixed-effects models represented here through *nlmefistsa* function.

Having demonstrated the concept of our strategy and these performances in terms of accuracy, manageability and computation times, the main perspective of this work is to develop a code that can be easily used by the community, see more details in my research project given in Chapter 4.

Conclusion

This chapter presents my contributions to electroporation modeling, an innovative therapy. More specifically, I present the work done to develop mathematical approaches to track membrane dynamics, the work done to compare and improve tissue-scale electroporation models, and then how we are beginning to investigate the effects of irreversible and reversible electroporation on tumor growth. Although our work to date has enabled great progress in the understanding of electroporation phenomenon, much work remains to be done, and I will present my future work in this area in my research project given in the next chapter.

Chapter 4

Research project

In this very short chapter, some perspectives and future work are given. I plan, at least in the short and medium term, to continue working on mathematical models for biomedical problems.

4.1 Tumor growth modeling

I intend to continue work around tumor growth modeling, focusing on three main projects.

Free growth of solid tumors The first project is on free growth of solid tumors, which was studied as part of V. Montalibet's PhD (funded by the University of Bordeaux as part of the ANR project AI by UBx).

First, we will continue our work with our collaborators at the CHU of Bordeaux (J. Engelhardt and H. Loiseau, neurosurgeons) on meningiomas. The open clinical questions are: Can we segment the tumor fully automatically? Can we use the first medical image to determine clustering obtained with mathematical models? Can we perform 3D simulations within minutes? To answer at least the first two questions, we will use machine and deep learning strategies. We have recently gained this expertise in the MONC team by expanding our knowledge in these areas. To answer clinical questions, it is often essential to combine different mathematical branches.

Second, a new collaboration with IHU of Strasbourg (A. Venkatasamy, radiologist) has been started, dealing with acoustic neuroma, also called vestibular schwannoma. This is a noncancerous and usually slow-growing tumor that arises on the main nerve leading from the inner ear to the brain. The clinical questions are similar to meningiomas: Can we segment the tumor fully automatically? Can we model the volume dynamics? Can we classify schwannomas according to their aggressiveness? Can we predict the volume and shape of the tumor at a later time point with only two imaging examinations? This new project will test whether our strategies can be easily transferred to other contexts.

Dynamics of circulating tumor cells in the blood vessels As part of C. Etchegaray's collaboration with the Goetz Laboratory of Tumor Biomechanics at the University of Strasbourg, we are interested in the dynamics of circulating tumor cells (CTC) in blood vessels. This is a crucial phenomenon in the spread of metastases, which are responsible for about 90% of deaths in cancer patients. Indeed, some CTC manage to escape hydrodynamic forces and adhere to vessel walls before extravasating and further invading tissues and organs. Therefore, a deeper understanding of CTC dynamics will help to find new therapeutic targets against invasion in the future. Our goal is to better understand the competition between hydrodynamic forces and cell adhesion forces and their effects on CTC circulation. To this end, we aim to calibrate a mathematical model of cell dynamics using experimental data from *in vitro* (microfluidics) and *in vivo* (zebrafish embryos). This work will help provide insight into the biomechanical drivers of CTC invasion. It is funded by Inria through the post-doc of G. Ciavolella.

Effect of the drug propanolol on tumors Propranolol belongs to a group of drugs called beta-blockers. Although it is mainly used to treat heart problems, anxiety, and to prevent migraines, it is also used in oncology. More specifically, propranolol is currently the first-line treatment for severe infantile hemangiomas, the most common childhood tumor affecting 1-5% of newborns [SdlRB+09]. The molecular mechanism of action of propranolol and the cellular and molecular targets of the drug are still being explored [MOKC+21]. Recently I started a new collaboration with a biologist from the University of Bordeaux (F. Moisan). The goal is to use 3D spheroids to better understand the antitumor mechanism of action of this beta-blocker and to identify new predictive markers of response. This challenge is very important because this new therapeutic strategy could also be useful for the treatment of other vascular tumors, especially angiosarcomas, which are rare malignant tumors with poor prognosis.

4.2 Electroporation modeling

As far as electroporation modeling is concerned, three main directions will be investigated in the coming years. Most of this work will be done in a manner consistent with cardiac electroporation. One of the major treatments for cardiac arrhythmias is catheter ablation, in which small areas of cardiac tissue are destroyed to isolate or eliminate the cause of the rapid and irregular heartbeats. Most catheter ablation therapies are performed thermally through the application of radiofrequency electromagnetic field (RFA), and pulsed electric field ablation (PFA), which takes advantage of irreversible electroporation, is still in its infancy. Preclinical evaluations of PFA in atrial fibrillation [KKI+19a] and ventricular ablation in large animal studies [COJ+20b] show successful results with possible transmural lesions, sparing vulnerable adjacent structures. In terms of clinical performance, the recurrence of atrial fibrillation is on the order of 15% [RDN+21] with PFA and 30% with RFA [WN06]. Despite these promising results, there are still some difficulties in applying PFA in routine clinical practice because of the technical complexity of this novel approach. As in oncology, mathematical models and numerical strategies could be developed to improve the understanding of PFA and to develop numerical criteria for treatment assessment thanks to clinical data. This area of research offers me the opportunity to combine two of my main areas of application: cardiac electrophysiology and electroporation modeling.

Membrane modeling compatible with cardiac cells The cell-level modeling presented in Section 3.1.2 of Chapter 3 is not compatible with cardiac cells because changes in ion and adenosine triphosphate (ATP) concentrations and cell volume were not considered. Therefore, the PDE system needs to become considerably more complex to incorporate other aspects of the electroporation phenomenon and adapt it to cardiac cells. In particular, the increase in cell membrane permeability when short high-voltage pulses are applied probably leads to cardiac cell death by Ca2+ uptake. To quantify what happens in cardiac cells under PFA – apoptosis or necrosis – the model should describe the *in vitro* process of internalization of extracellular species. This new model will additionally incorporate the formation of conduction defects, ion and molecular efflux and influx, and cell swelling. Since electroneutrality can be temporarily broken near the membrane due to ion exchange, the electroosmosis model should be preferred. This means coming back to the Nernst-Planck equation corresponding to System 1.4 given in Chapter 1, and coupling it to the Stokes equation

$$-\eta \Delta_{\underline{x}} \underline{v}_s + \vec{\nabla}_{\vec{x}} P_s = q \sum_{k=1}^{N^{(\alpha)}} z_k c_k^{(\alpha)} \vec{\nabla}_{\vec{x}} u^{(\alpha)} \text{ with } \vec{\nabla}_{\vec{x}} \cdot \underline{v}_s = 0.$$

In this context, the velocity $\underline{v}_s$ does not correspond to the mechanical deformation, but to the velocity of the fluid. The viscosity is denoted by η. The transmission through the cell membrane has not yet been derived for this complete model, especially in the context of electroporation, but our goal is to couple it with the membrane equation of state ϕ and define a realistic electroporation current.

The goal is to include the currents of passive ion channels, Na/K-ATPase and calcium pumps, and Na/H channels, which are essential for the equilibrium of the cell. One may refer to the electrophysiological laws as in [Arm03, FH04, PSC+11]. In addition, specific nonlinearities must be introduced in the jump conditions to account for the various degrees of membrane permeabilization. We assume that we can derive such jump conditions thanks to the knowledge of electroporation acquired through classical electroporation modeling [KLPW14, LSMP14] and with a rigorous asymptotic analysis in the same vein as [PP13]. Our approach then generalizes the standard electroquasistatic models [LSMP14] by describing the ion and molecular fluxes and integrating the morphological properties of the cardiac cells through fitted geometries.

This work is funded by the ANR project MIRE4VTach, which I coordinate. A PhD student will be hired, and biological experiments to validate our modeling will be performed by our collaborators at IHU Lyric in Bordeaux (G. Caluori, cardiac arrhythmia researcher and P. Jaïs, cardiologist).

A mascroscopic bidomain model for electroporation As explained in Chapter 3, System 3.15 was not formally derived by a homogenization procedure. Our goal is to use 2-scale convergence to derive a dynamic bidomain equation for electroporation that is compatible with cardiac cells *i.e.* accounting for ionic current. Preliminary results show that an effective model whose unknown is the sum of the first terms of the asymptotic development of the potentials could be a solution to this difficult problem, which is due to the scale difference between ion and electroporation currents. Of course, this work is valid even in the absence of ionic current, which means that the model is also suitable for electroporation of other organs and should make it possible either to justify System (3.15) or to propose a mathematically justified alternative.

Once this model is available, we would like to perform numerical simulations for ventricular tachycardia. Ventricular tachycardia (VTach) – common in both men and women – generates disorder of rapid heartbeat due to abnormal electrical signals in the ventricles. We will study the effects of cardiac geometry (wall thickness and fibrosis) and fibers orientation using a few patients. Regarding the catheter, one of the biggest challenges is the distance between the tissue and the catheter. Using CT or MRI images, we will consider the most realistic configuration and add appropriate variability to see the impact on the ablated area. The signal data recorded during the ablation procedure by our clinical collaborators will be used to derive the electroporation protocol (*i.e.* find out which electrodes are used for each pulse), to validate the model, and to estimate its parameters such as the conductivities. This last part is a challenge in terms of data assimilation.

This work is funded by the Fédération Française de Cardiologie and Inria through the PhD thesis of S. Bihoreau. Access to real data from IHU Lyric will be provided in the context of the ANR project MIRE4VTach. Interestingly, we should obtain depolarization maps, and we could use the estimation strategy presented in Section 1.4.3 of Chapter 1 to complete them.

Bidomain model of a cardiac domain containing a region ablated by PFA In this third part, we aim to derive an electrophysiological model of a cardiac domain containing a region ablated by PFA. To this end, we aim to combine the bidomain model in the healthy parts of the heart with an adapted bidomain system in the electroporated region. Our main goal is to propose a numerical explanation for the higher rate of fibrillation recurrence after RFA compared with PFA. For PFA, the model results from an asymptotic analysis in which the small parameter is the thickness of the electroporated region and its low intracellular conductivity tensor. Preliminary results were obtained and published in the following conference proceeding [27].

4.3 Data assimilation aspects

I do not focus on this work in this manuscript, but an important part of my work is to develop efficient strategies for estimating the parameters of ODE or PDE systems. More specifically, together with P. Moireau (DR Inria) and M. Prague (CR Inria), we have developed a population-based Kalman filter in [23]. An extension to PDE systems using a coupling with a Luenberger observer to handle state errors was proposed in [28]. Important work has been done to validate the approach, and we have demonstrated its potential in two real-world and difficult examples: (1) to evaluate associations between governmental nonpharmaceutical interventions – such as lockdowns, curfews, or school closures – introduced to control the pandemic COVID -19 and transmission rates without prior knowledge of the dynamics of the transmission rates [22] (see Figure 2 in the introduction chapter for illustration) and (2) for very efficient estimation of the parameters of a 1D PDE system [28] (see Section 3.3.4.2 of Chapter 2). Since the proof of concept shows very interesting results, we would now like with my two collaborators to disseminate the method. This means that we need to develop a code and an associated interface that is easy to use, and very accurate documentation. We want to have code that is capable of solving ODE systems, and that is also compatible with any existing ODE or PDE solver. This is still under consideration, but a medium term solution is to seek funding to hire an engineer for this project.

My publications (peer-review journals and proceedings)

[1] D. Chapelle, A. Collin, and J.-F. Gerbeau. A surface-based electrophysiology model relying on asymptotic analysis and motivated by cardiac atria modeling. *M3AS*, 23(14):2749–2776, 2013. Link.

[2] A. Collin, J.-F. Gerbeau, M. Hocini, M. Haïssaguerre, and D. Chapelle. Surface-based electrophysiology modeling and assessment of physiological simulations in atria. In *International Conference on Functional Imaging and Modeling of the Heart*, volume 7945, pages 352–359, 2013. Link.

[3] D. Chapelle and A. Collin. Strong convergence results for the asymptotic behavior of the 3D-shell model. *Journal of Elasticity*, 115(2):173–192, 2014. Link.

[4] A. Collin, D. Chapelle, and P. Moireau. A Luenberger observer for reaction–diffusion models with front position data. *Journal of Computational Physics*, 300:288–307, 2015. Link. See Section 1.4.1 of Chapter 1 for details.

[5] A. Collin, D. Chapelle, and P. Moireau. Sequential state estimation for electrophysiology models with front level-set data using topological gradient derivations. In *International Conference on Functional Imaging and Modeling of the Heart*, pages 402–411. Springer, 2015. Link. See Section 1.4.2 of Chapter 1 for details.

[6] E. Schenone, A. Collin, and J.-F. Gerbeau. Numerical simulation of electrocardiograms for full cardiac cycles in healthy and pathological conditions. *International Journal for Numerical Methods in Biomedical Engineering*, 2015. Link.

[7] A. Collin, G. Sangalli, and T. Takacs. Analysis-suitable G1 multi-patch parametrizations for C1 isogeometric spaces. *Computer Aided Geometric Design*, 47:93–113, 2016. Link.

[8] A. Collin and S. Imperiale. Mathematical analysis and 2-scale convergence of a heterogeneous microscopic bidomain model. *Mathematical Models and Methods in Applied Sciences*, 28(05):979–1035, 2018. Link. See Section 1.2 of Chapter 1 for details.

[9] M. C. Rochoux, A. Collin, C. Zhang, A. Trouvé, D. Lucor, and P. Moireau. Front shape similarity measure for shape-oriented sensitivity analysis and data assimilation for eikonal equation. *ESAIM: Proceedings and Surveys*, 63:258–279, 2018. Link.

[10] N. Tarabelloni, E. Schenone, A. Collin, F. Ieva, A. M. Paganoni, and J.-F. Gerbeau. Statistical assessment and calibration of numerical ECG models. *JP Journal of Biostatistics*, 15(2):151–173, 2018. Link.

[11] A. Collin, S. Imperiale, P. Moireau, J.-F. Gerbeau, and D. Chapelle. Apprehending the effects of mechanical deformations in cardiac electrophysiology: A homogenization approach. *Mathematical Models and Methods in Applied Sciences*, 29(13):2377–2417, 2019. Link. See Sections 1.1 and 1.3 of Chapter 1 for details.

[12] A. Gérard, A. Collin, G. Bureau, P. Moireau, and Y. Coudière. Model assessment through data assimilation of realistic data in cardiac electrophysiology. In *International Conference on Functional Imaging and Modeling of the Heart*, pages 121–130. Springer, 2019. Link. See Section 1.4.3 of Chapter 1 for details.

[13] C. Zhang, A. Collin, P. Moireau, A. Trouvé, and M. C. Rochoux. Front shape similarity measure for data-driven simulations of wildland fire spread based on state estimation: Application to the rxcadre field-scale experiment. *Proceedings of the Combustion Institute*, 37(3):4201–4209, 2019. Link.

[14] C. Zhang, A. Collin, P. Moireau, A. Trouvé, and M. C. Rochoux. State-parameter estimation approach for data-driven wildland fire spread modeling: Application to the 2012 rxcadre s5 field-scale experiment. *Fire Safety Journal*, 105:286–299, 2019. Link.

[15] G. Jankowiak, C. Taing, C. Poignard, and A. Collin. Comparison and calibration of different electroporation models. Application to rabbit livers experiments. *ESAIM: Proceedings and Surveys*, 67:242–260, 2020. Link. See Section 3.2.1 of Chapter 3 for details.

[16] D. Voyer, S. Corridore, A. Collin, R. Scorretti, and C. Poignard. Numerical modeling of floating potentials in electrokinetic problems using an asymptotic method. *IEEE Transactions on Magnetics*, 56(4):1–4, 2020. Link.

[17] A. Collin, C. Copol, V. Pianet, T. Colin, J. Engelhardt, G. Kantor, H. Loiseau, O. Saut, and B. Taton. Spatial mechanistic modeling for prediction of the growth of asymptomatic meningiomas. *Computer Methods and Programs in Biomedicine*, 199:105829, 2021. Link. See Sections 2.1.2 and 2.2 of Chapter 2 for details.

[18] A. Collin, S. Corridore, and C. Poignard. Floating potential boundary condition in smooth domains in an electroporation context. In *Methods of Mathematical Oncology: Fusion of Mathematics and Biology, Osaka, Japan, October 26–28, 2020*, pages 91–106. Springer, 2021. Link. See Section 3.2.2 of Chapter 3 for details.

[19] A. Collin, V. Groza, L. Missenard, F. Chomy, T. Colin, J. Palussière, and O. Saut. A model-strengthened imaging biomarker for survival prediction in EGFR-mutated non-small-cell lung carcinoma patients treated with tyrosine kinase inhibitors. *Bulletin of Mathematical Biology*, 83(6):68, 2021. Link.

[20] A. Collin, T. Kritter, C. Poignard, and O. Saut. Joint state-parameter estimation for tumor growth model. *SIAM Journal on Applied Mathematics*, 81(2):355–377, 2021. Link. See Section 2.3 of Chapter 2 for details.

[21] A. Collin, H. Bruhier, J. Kolosnjaj, M. Golzio, M.-P. Rols, and C. Poignard. Spatial mechanistic modeling for prediction of 3D multicellular spheroids behavior upon exposure to high intensity pulsed electric fields. *AIMS Bioengineering*, 9(2):102–122, 2022. Link. See Section 3.3 of Chapter 3 for details.

[22] A. Collin, B. P. Hejblum, C. Vignals, L. Lehot, R. Thiébaut, P. Moireau, and M. Prague. Using population based Kalman estimator to model COVID-19 epidemic in France: estimating the effects of non-pharmaceutical interventions on the dynamics of epidemic. *International Journal of Biostatistics*, 2022. Link. See Figure 2 of the introduction chapter for the main result in terms of application.

[23] A. Collin, M. Prague, and P. Moireau. Estimation for dynamical systems using a population-based Kalman filter–Applications in computational biology. *MathematicS In Action*, 2022. Link.

[24] J. Engelhardt, V. Montalibet, H. Loiseau, O. Saut, and A. Collin. Evaluation of four tumour growth models to describe the natural history of meningiomas. *EBioMedicine*, 2023. Link. See Section 2.2 of Chapter 2 for details.

[25] P. Jaramillo-Aguayo, A. Collin, and C. Poignard. Phase-field model of bilipid membrane electroporation. *Journal of Mathematical Biology*, 87(1):18, 2023. Link. See Section 3.1.2 of Chapter 3 for details.

[26] P. Loubet, A. Vincent, A. Collin, C. Dejous, A. Ghiotto, and C. Jego. Life cycle assessment of ict in higher education: a comparison between desktop and single-board computers. *The International Journal of Life Cycle Assessment*, pages 1–19, 2023. Link.

[27] S. Nati Poltri, G. Caluori, P. Jaïs, A. Collin, and C. Poignard. Electrocardiology modeling after catheter ablations for atrial fibrillation. In *International Conference on Functional Imaging and Modeling of the Heart*. Springer, 2023. Link.

[28] A. Collin. Population-based estimation for PDE systems – Applications in spheroids electroporation. *ESAIM: Control, Optimisation and Calculus of Variations*, 2023 (in press). Link. See Section 3.3.4 of Chapter 3 for details.

[29] A. Collin, T. García-Sánchez, S. Corridore, L. M. Mir, and C. Poignard. Deciphering immediate post-pulse membrane resealing from 4–electrode impedance measurements by numerical modeling. *Bioelectricity*, 2023 (in press). Link. See Section 3.1.1 of Chapter 3 for details.

Bibliography

[AAC$^+$79] I. G. Abidor, V. B. Arakelyan, L. V. Chernomordik, Y. A. Chizmadzhev, V. F. Pastushenko, and M. P. Tarasevich. Electric breakdown of bilayer lipid membranes. *Journal of Electroanalytical Chemistry and Interfacial Electrochemistry*, 104:37–52, jan 1979.

[ABE16] S. Alonso, M. Bär, and B. Echebarria. Nonlinear physics of electrical wave propagation in the heart: a review. *Reports on Progress in Physics*, 79(9):096601, 2016.

[ABOS14] D. Amann, A. Blaszczyk, G. Of, and O. Steinbach. Simulation of floating potentials in industrial applications by boundary element methods. *Journal of Mathematics in Industry*, 4(1):13, 2014.

[AC79] S. M. Allen and J. W. Cahn. A microscopic theory for antiphase boundary motion and its application to antiphase domain coarsening. *Acta Metallurgica*, 27(6):1085–1095, jun 1979.

[ACFS00] L. Ambrosio, P. Colli Franzone, and G. Savaré. On the asymptotic behaviour of anisotropic energies arising in the cardiac biodomain model. *Interfaces and Free Boundaries*, 2(3):213–266, 2000.

[ADH95] G. Allaire, A. Damlamian, and U. Hornung. Two-scale convergence on periodic surfaces and applications. *In Proceedings of the International Conference on Mathematical Modelling of Flow through Porous Media*, 1995.

[AHM08] M. Alfaro, D. Hilhorst, and H. Matano. The singular limit of the Allen–Cahn equation and the FitzHugh–Nagumo system. *Journal of Differential Equations*, 245(2):505–565, jul 2008.

[AHZ$^+$13] I. Adeniran, J. C. Hancox, H. Zhang, et al. Effect of cardiac ventricular mechanical contraction on the characteristics of the ECG: A simulation study. *Journal of Biomedical Science and Engineering*, 6(12):47, 2013.

[All92] G. Allaire. Homogenization and two-scale convergence. *SIAM Journal of Mathematical Analysis*, 23(6):1482–1518, 1992.

[All12] G. Allaire. *Shape optimization by the homogenization method*, volume 146. Springer Science & Business Media, 2012.

[AM10] F. M. Andre and L. M. Mir. Nucleic acids electrotransfer in vivo: mechanisms and practical aspects. *Current gene therapy*, 10(4):267–280, 2010.

[Ant19] Antony, France: Lixoft SAS. Monolix version 2019R1, 2019.

[AP96] R. Aliev and A. Panfilov. A simple two-variable model of cardiac excitation. *Chaos, Solitons Fractals*, 3(7):293–301, 1996.

[Arm03] C. M. Armstrong. The Na/K pump, Cl ion, and osmotic stabilization of cells. *Proceedings of the National Academy of Sciences*, 100(10):6257–6262, 2003.

[BAB$^+$12] S. Benzekry, N. André, A. Benabdallah, J. Ciccolini, C. Faivre, F. Hubert, and D. Barbolosi. Modeling the impact of anticancer agents on metastatic spreading. *Mathematical Modelling of Natural Phenomena*, 7(1):306–336, 2012.

[BBB$^+$15] E. Baratchart, S. Benzekry, A. Bikfalvi, T. Colin, L. S. Cooley, R. Pineau, E. J. Ribot, O. Saut, and W. Souleyreau. Computational modelling of metastasis development in renal cell carcinoma. *PLoS computational biology*, 11(11):e1004626, 2015.

[BBK$^+$15] M. Breton, F. Buret, L. Krähenbühl, M. Leguèbe, L. M. Mir, R. Perrussel, C. Poignard, R. Scorretti, and D. Voyer. Non-linear steady-state electrical current modeling for the electropermeabilization of biological tissue. *IEEE Transactions on Magnetics*, 51(3):1–4, 2015.

[BBRRH$^+$19] F. Brugada-Bellsolà, P. T. Rodríguez, A. Rodríguez-Hernández, R. Garcia-Armengol, M. Tardáguila, A. Gonz'alez-Crespo, C. J. Domínguez, and J. M. Rimbau. Growth prediction in asymptomatic meningiomas: the utility of the aimss score. *Acta Neurochirurgica*, 161(11):2233–2240, nov 2019.

[BCF$^+$10] M. Boulakia, S. Cazeau, M.A. Fernández, J.-F. Gerbeau, and N. Zemzemi. Mathematical modeling of electrocardiograms: a numerical study. *Annals of Biomedical Engineering*, 38(3):1071–1097, 2010.

[BCG$^+$10] D. Bresch, T. Colin, E. Grenier, B. Ribba, and O. Saut. Computational modeling of solid tumor growth: the avascular stage. *SIAM Journal on Scientific Computing*, 32(4):2321–2344, 2010.

[BCP94] Y. Bourgault, Y. Coudière, and C. Pierre. A collocation-galerkin finite element model of cardiac action potential propagation. *IEEE Transactions on Biomedical Engineering*, 41(8):743–757, 1994.

[BCP09] Y. Bourgault, Y. Coudière, and C. Pierre. Existence and uniqueness of the solution for the bidomain model used in cardiac electrophysiology. *Nonlinear Analysis-Real World Applications*, 10(1):458–482, 2009.

[BDS93] J.-Z. Bao, C. C. Davis, and R. E. Schmukler. Impedance spectroscopy of human erythrocytes: system calibration, and nonlinear modeling. *IEEE Transactions on biomedical engineering*, 40(4):364–378, 1993.

[BDS$^+$12] M. Breton, L. Delemotte, A. Silve, L. M. Mir, and M. Tarek. Transport of siRNA through lipid membranes driven by nanosecond electric pulses: an experimental and computational study. *Journal of the American Chemical Society*, 134(34):13938–13941, 2012.

[BEB$^+$18] I. Baldi, J. Engelhardt, C. Bonnet, L. Bauchet, E. Berteaud, A. Grüber, and H. Loiseau. Epidemiology of meningiomas. *Neurochirurgie*, 64(1):5–14, 2018.

[Bel56] R. Bellman. Dynamic programming and Lagrange multipliers. *Proceedings of the National Academy of Sciences of the United States of America*, 42(10):767, 1956.

[Ben71] A. Bensoussan. *Filtrage optimal des systèmes linéaires*. Dunod, 1971.

[BGA+11] I. Baldi, A. Gruber, A. Alioum, E. Berteaud, P. Lebailly, A. Huchet, T. Tourdias, G. Kantor, JP. Maire, A. Vital, et al. Descriptive epidemiology of cns tumors in france: results from the gironde registry for the period 2000–2007. *Neuro-oncology*, 13(12):1370–1378, 2011.

[BHR04] M. Burger, B. Hackl, and W. Ring. Incorporating topological derivatives into level set methods. *Journal of Computational Physics*, 194(1):344–362, 2004.

[BLB+14] S. Benzekry, C. Lamont, A. Beheshti, A. Tracz, J. ML. Ebos, L. Hlatky, and P. Hahnfeldt. Classical mathematical models for description and prediction of experimental tumor growth. *PLoS computational biology*, 10(8):e1003800, 2014.

[BLP78] A. Bensoussan, J.-L. Lions, and G. Papanicolaou. *Asymptotic Analysis for Periodic Structures*. Elsevier, 1978.

[BOCF08] A. Bueno-Orovio, E. M. Cherry, and F. H. Fenton. Minimal model for human ventricular action potentials in tissue. *Journal of Theretical Biology*, 253:544–560, 2008.

[BP11] M. Bishop and G. Plank. Bidomain ecg simulations using an augmented monodomain model for the cardiac source. *Biomedical Engineering, IEEE Transactions on*, 58(8):2297–2307, 2011.

[Bra02] A. J. Bray. Theory of phase-ordering kinetics. *Advances in Physics*, 51(2):481–587, mar 2002.

[Bri93] M. Briane. Three models of non periodic fibrous materials obtained by homogenization. *RAIRO-Modélisation mathématique et analyse numérique*, 27(6):759–775, 1993.

[BRS+09] F. Billy, B. Ribba, O. Saut, H. Morre-Trouilhet, T. Colin, D. Bresch, J.-P. Boissel, E. Grenier, and J.-P. Flandrois. A pharmacologically based multiscale mathematical model of angiogenesis and its use in investigating the efficacy of a new cancer treatment strategy. *Journal of theoretical biology*, 260(4):545–562, 2009.

[BV97] J. B. Braunstein and N. A. Vick. Meningiomas: the decision not to operate. *Neurology*, 48(5):1459–1462, 1997.

[Cas34] A. E. Casey. The experimental alteration of malignancy with an homologous mammalian tumor material: I. results with intratesticular inoculation. *The American Journal of Cancer*, 21(4):760–775, 1934.

[CCJ+15] T. Colin, F. Cornelis, J. Jouganous, J. Palussière, and O. Saut. Patient-specific simulation of tumor growth, response to the treatment, and relapse of a lung metastasis: a clinical case. *Journal of Computational Surgery*, 2(1):1, 2015.

[CCSZ95] Y. A. Chizmadzhev, F. S. Cohen, A. Shcherbakov, and J. Zimmerberg. Membrane mechanics can account for fusion pore dilation in stages. *Biophysical Journal*, 69(6):2489–2500, dec 1995.

[CEH+13] R. Cannon, S. Ellis, D. Hayes, G. Narayanan, and R. CG. Martin. Safety and early efficacy of irreversible electroporation for hepatic tumors in proximity to vital structures. *Journal of surgical oncology*, 107(5):544–549, 2013.

[CFPS14] P. Colli Franzone, L.F. Pavarino, and S. Scacchi. *Mathematical Cardiac Electrophysiology*, volume XIV of *MS&A*. Springer, 2014.

[CFPS16] P. Colli Franzone, L.F. Pavarino, and S. Scacchi. Bioelectrical effects of mechanical feedbacks in a strongly coupled cardiac electro-mechanical model. *Mathematical Models and Methods in Applied Sciences*, 26(01):27–57, 2016.

[CFPS17] P. Colli Franzone, L. F. Pavarino, and S. Scacchi. Effects of mechanical feedback on the stability of cardiac scroll waves: A bidomain electro-mechanical simulation study. *Chaos: An Interdisciplinary Journal of Nonlinear Science*, 27(9):1–15, 2017.

[CFPS18] P. Colli Franzone, L F. Pavarino, and S. Scacchi. A numerical study of scalable cardiac electro-mechanical solvers on hpc architectures. *Frontiers in Physiology*, 9:1–16, 2018.

[CFPT05] P. Colli Franzone, L.F. Pavarino, and B. Taccardi. Simulating patterns of excitation, repolarization and action potential duration with cardiac Bidomain and Monodomain models. *Mathematical Biosciences*, 197(1):35–66, 2005.

[CFS02] P. Colli Franzone and G. Savaré. Degenerate evolution systems modeling the cardiac electric field at micro and macroscopic level. *Progress in Nonlinear Differential Equations and Their Applications*, 50:49–78, 2002.

[CH58] J. W. Cahn and J. E. Hilliard. Free energy of a nonuniform system. I. Interfacial free energy. *The Journal of Chemical Physics*, 28(2):258–267, feb 1958.

[CMLT09] D. Chapelle, P. Moireau, and P. Le Tallec. Robust filtering for joint state parameter estimation for distributed mechanical systems. *Discrete and Continuous Dynamical Systems-Series A*, 23(1-2):65–84, 2009.

[COJ$^+$20a] G Caluori, E. Odehnalova, T. Jadczyk, M. Pesl, I. Pavlova, L. Valikova, S. Holzinger, V. Novotna, V. Rotrekl, A. Hampl, et al. AC pulsed field ablation is feasible and safe in atrial and ventricular settings: a proof-of-concept chronic animal study. *Frontiers in bioengineering and biotechnology*, 8:552357, 2020.

[COJ$^+$20b] G. Caluori, E. Odehnalova, T. Jadczyk, M. Pesl, I. Pavlova, L. Valikova, S. Holzinger, V. Novotna, V. Rotrekl, A. Hampl, et al. AC pulsed field ablation is feasible and safe in atrial and ventricular settings: a proof-of-concept chronic animal study. *Frontiers in bioengineering and biotechnology*, 8:552357, 2020.

[Cou06] W. T. Couldwell. Asymptomatic meningiomas. *Journal of neurosurgery*, 105(4):536–537, 2006.

[CRN98] M. Courtemanche, R.J. Ramirez, and S. Nattel. Ionic mechanisms underlying human atrial action potential properties: insights from a mathematical model. *American Journal of Physiology*, (275):H301–H321, 1998.

[CV91] T.F. Chan and L.A. Vese. Active contours without edges. *IEEE Transactions on Image Processing*, 10(2):266–277, 1991.

[DHM$^+$97] P. Dular, F. Henrotte, B. Meys, A. Genon, and W. Legros. Une méthode naturelle de traitement des potentiels flottants associée a la méthode des élements finis. *Journal de Physique III*, 7(11):2201–2209, 1997.

[DK98] K. A. DeBruin and W. Krassowska. Electroporation and shock-induced transmembrane potential in a cardiac fiber during defibrillation strength shocks. *Annals of Biomedical Engineering*, 26(4):584–596, July 1998.

[DMR05] R. V. Davalos, L. M. Mir, and B. Rubinsky. Tissue ablation with irreversible electroporation. *Annals of biomedical engineering*, 33(2):223, 2005.

[Don21] E. Donada. La moindre efficacité du vaccin contre la transmission remet-elle en cause le principe du pass sanitaire ? *Libération*, 2021.

[ESS92] L. C. Evans, H. M. Soner, and P. E. Souganidis. Phase transitions and generalized motion by mean curvature. *Communications on Pure and Applied Mathematics*, 45(9):1097–1123, oct 1992.

[Eve09] G. Evensen. *Data Assimilation: The Ensemble Kalman Filter*. Springer, 2009.

[FGM$^+$15] S. K. Frandsen, L. Gibot, M. Madi, J. Gehl, and M.-P. Rols. Calcium electroporation: evidence for differential effects in normal and malignant cell lines, evaluated in a 3D spheroid model. *PLoS One*, 10(12):e0144028, 2015.

[FH04] J. A. Fraser and C. L.-H. Huang. A quantitative analysis of cell volume and resting potential determination and regulation in excitable cells. *The Journal of Physiology*, 559(2):459–478, 2004.

[Fit61] R. Fitzhugh. Impulses and physiological states in theoretical models of nerve membrane. *Biophysical Journal*, 1(6):445–466, 1961.

[FMZB20] D. Fraggedakis, M. Mirzadeh, T. Zhou, and M. Z. Bazant. Dielectric breakdown by electric-field induced phase separation. *Journal of The Electrochemical Society*, 167(11):113504, 2020.

[FPP$^+$16] M. Favino, S. Pozzi, S. Pezzuto, F.W. Prinzen, A. Auricchio, and R. Krause. Impact of mechanical deformation on pseudo-ECG: a simulation study. *EP Europace*, 18(4):77–84, 2016.

[FS98] E. C. Fear and M. A. Stuchly. Modeling assemblies of biological cells exposed to electric fields. *IEEE Transactions on Biomedical Engineering*, 45(10):1259–1271, 1998.

[Geh08] J. Gehl. Electroporation for drug and gene delivery in the clinic: doctors go electric. *Electroporation Protocols*, pages 351–359, 2008.

[Gér19] A. Gérard. *Modèles numériques personnalisés de la fibrillation auriculaire*. PhD thesis, Université de Bordeaux, 2019.

[GLV14] E. Grenier, V. Louvet, and P. Vigneaux. Parameter estimation in non-linear mixed effects models with SAEM algorithm: extension from ODE to PDE. *ESAIM: Mathematical Modelling and Numerical Analysis*, 48(5):1303–1329, 2014.

[Gom25] B. Gompertz. XXIV. On the nature of the function expressive of the law of human mortality, and on a new mode of determining the value of life contingencies. In a letter to Francis Baily, Esq. FRS &c. *Philosophical transactions of the Royal Society of London*, (115):513–583, 1825.

[GSAL+15] T. García-Sánchez, A. Azan, I. Leray, J. Rosell-Ferrer, R. Bragos, and L. M. Mir. Interpulse multifrequency electrical impedance measurements during electroporation of adherent differentiated myotubes. *Bioelectrochemistry*, 105:123–135, 2015.

[GWTR13] L. Gibot, L. Wasungu, J. Teissié, and M.-P. Rols. Antitumor drug delivery in multicellular spheroids by electropermeabilization. *Journal of controlled release*, 167(2):138–147, 2013.

[GXCI+19] A. Gupta, Z. Xu, O. Cohen-Inbar, M. H. Snyder, L. K. Hobbs, C. Li, Q.-T. Nguyen, and J. P. Sheehan. Treatment of asymptomatic meningioma with gamma knife radiosurgery: Long-term follow-up with volumetric assessment and clinical outcome. *Neurosurgery*, 2019.

[HA76] J. E. Hoke and R. A. Anthes. The initialization of numerical models by a dynamic-initialization technique. *Monthly Weather Review*, 104(12):1551–1556, 1976.

[HAS07] H. L. P. Harpold, E. C. Alvord, and K. R. Swanson. The Evolution of Mathematical Modeling of Glioma Proliferation and Invasion. *J Neuropathol Exp Neurol*, 66(1):1–9, January 2007.

[Hec21] C. Hecketsweiler. Covid-19 : face à la quatrième vague, les effets trop tardifs de l'accélération de la vaccination, selon l'Institut Pasteur. *Le Monde*, 2021.

[HH52] A.L. Hodgkin and A.F. Huxley. A quantitative description of membrane current and its application to conduction and excitation in nerve. *Journal of Physiology*, 117(4):500–544, 1952.

[HHI+09] T. Hashiba, N. Hashimoto, S. Izumoto, T. Suzuki, N. Kagawa, M. Maruno, A. Kato, and T. Yoshimine. Serial volumetric assessment of the natural history and growth pattern of incidentally discovered meningiomas. *Journal of neurosurgery*, 110(4):675–684, 2009.

[HKO07] L. He, C.Y. Kao, and S. Osher. Incorporating topological derivatives into shape derivatives based level set methods. *Journal of Computational Physics*, 225(1):891–909, 2007.

[HL09] M. Hintermüller and A. Laurain. Multiphase image segmentation and modulation recovery based on shape and topological sensitivity. *Journal of Mathematical Imaging and Vision*, 35(1):1–22, 2009.

[HM05] S. N. Healy and A. D. McCulloch. An ionic model of stretch-activated and stretch-modulated currents in rabbit ventricular myocytes. *Europace*, 7(s2):S128–S134, 2005.

[HP10] P. E. Hand and C. S. Peskin. Homogenization of an electrophysiological model for a strand of cardiac myocytes with gap-junctional and electric-field coupling. *Bulletin of Mathematical Biology*, 72:1408–1424, 2010.

[Hui98] G. Huiskamp. Simulation of depolarization in a membrane-equations-based model of the anisotropic ventricle. *Biomedical Engineering, IEEE Transactions on*, 45(7):847–855, 1998.

[IMM+19a] A. I. Islim, M. Mohan, R. DC. Moon, N. Srikandarajah, S. J. Mills, A. R. Brodbelt, and M. D. Jenkinson. Correction to: Incidental intracranial meningiomas: a systematic review and meta-analysis of prognostic factors and outcomes. *Journal of neuro-oncology*, 144(2):427–429, 2019.

[IMM+19b] A. I. Islim, M. Mohan, R. DC. Moon, N. Srikandarajah, S. J. Mills, A. R. Brodbelt, and M. D. Jenkinson. Incidental intracranial meningiomas: a systematic review and meta-analysis of prognostic factors and outcomes. *Journal of neuro-oncology*, 142(2):211–221, 2019.

[ITC$^+$13] P. B. Ishai, M. S. Talary, A. Caduff, E. Levy, and Y. Feldman. Electrode polarization in dielectric measurements: a review. *Measurement Science and Technology*, 24(10):102001, 2013.

[IVM10] A. Ivorra, J Villemejane, and L. M. Mir. Electrical modeling of the influence of medium conductivity on electroporation. *Physical chemistry chemical physics : PCCP*, 12:10055–64, 2010.

[JKK$^+$11] K.-W. Jo, C.-H. Kim, D.-S. Kong, H.-J. Seol, D.-H. Nam, K. Park, J.-H. Kim, and J.-I. Lee. Treatment modalities and outcomes for asymptomatic meningiomas. *Acta neurochirurgica*, 153(1):62–67, 2011.

[JOV$^+$11] D. R. Johnson, J. E. Olson, R. A. Vierkant, J. E. Hammack, A. H. Wang, A. R. Folsom, B. A. Virnig, and J. R. Cerhan. Risk factors for meningioma in postmenopausal women: results from the Iowa Women's Health Study. *Neuro-oncology*, 13(9):1011–1019, 2011.

[JU97] S.J. Julier and J.K. Uhlmann. A new extension of the Kalman filter to nonlinear systems. In *Proc. of AeroSense: The 11th Int. Symp. on Aerospace/Defence Sensing, Simulation and Controls*, 1997.

[JU04] S. J. Julier and J. K. Uhlmann. Unscented filtering and nonlinear estimation. *Proceedings of the IEEE*, 92(3):401–422, 2004.

[KB61] R. Kalman and R. Bucy. New results in linear filtering and prediction theory. *Trans. ASME J. Basic. Eng.*, 83:95—108, 1961.

[KCM$^+$10] E. Konukoglu, O. Clatz, B. H. Menze, B. Stieltjes, M.-A. Weber, E. Mandonnet, H. Delingette, and N. Ayache. Image guided personalization of reaction-diffusion type tumor growth models using modified anisotropic eikonal equations. *Medical Imaging, IEEE Transactions*, 29(1):77–95, 2010.

[Kee91] J. P. Keener. An eikonal-curvature equation for action potential propagation in myocardium. *Journal of Mathematical Biology*, 29:629–651, 1991.

[Kir10] B. J. Kirby. *Micro- and Nanoscale Fluid Mechanics: Transport in Microfluidic Devices*. Cambridge University Press, 2010.

[KKC$^+$18] K. H. Kim, S. J. Kang, J.-W. Choi, D.-S. Kong, H. J. Seol, D.-H. Nam, and J.-I. Lee. Clinical and radiological outcomes of proactive Gamma Knife surgery for asymptomatic meningiomas compared with the natural course without intervention. *Journal of neurosurgery*, 130(5):1740–1749, 2018.

[KKI$^+$19a] J. Koruth, K. Kuroki, J. Iwasawa, Y. Enomoto, R. Viswanathan, R. Brose, E. D. Buck, M. Speltz, S. R. Dukkipati, and V. Y. Reddy. Preclinical evaluation of pulsed field ablation: electrophysiological and histological assessment of thoracic vein isolation. *Circulation: Arrhythmia and Electrophysiology*, 12(12):e007781, 2019.

[KKI$^+$19b] J. Koruth, K. Kuroki, J. Iwasawa, Y. Enomoto, R. Viswanathan, R. Brose, ED. Buck, M. Speltz, SR. Dukkipati, and VY. Reddy. Preclinical evaluation of pulsed field ablation: electrophysiological and histological assessment of thoracic vein isolation. *Circulation: Arrhythmia and Electrophysiology*, 12(12):e007781, 2019.

[KL05] E. Kuhn and M. Lavielle. Maximum likelihood estimation in nonlinear mixed effects models. *Computational Statistics & Data Analysis*, 49(4):1020–1038, 2005.

[KLPW14] O. Kavian, M. Leguèbe, C. Poignard, and L. Weynans. “Classical” electropermeabilization modeling at the cell scale. *Journal of mathematical biology*, 68(1-2):235–265, 2014.

[KNP+04] W. Krampla, S. Newrkla, W. Pfisterer, S. Jungwirth, P. Fischer, T. Leitha, W. Hruby, and K. H. Tragl. Frequency and risk factors for meningioma in clinically healthy 75-year-old patients: Results of the transdanube ageing study (VITA). *Cancer: Interdisciplinary International Journal of the American Cancer Society*, 100(6):1208–1212, 2004.

[KNP08] R. H. Keldermann, M. P. Nash, and A. V. Panfilov. Modeling cardiac mechano-electrical feedback using reaction-diffusion-mechanics systems. *Physica D*, 238:1000–1007, 2008.

[KP14] D. Kondepudi and I. Prigogine. *Modern thermodynamics: from heat engines to dissipative structures*. John Wiley & Sons, 2014.

[Kri18] T. Kritter. *Utilisation de données cliniques pour la construction de modèles en oncologie*. PhD thesis, Bordeaux, 2018.

[KS04] J. Keener and J. Sneyd. *Mathematical Physiology*. Springer, 2004.

[KSW+07] D. Keller, G. Seemann, D. Weiss, D. Farina, J. Zehelein, and O. Dössel. Computer based modeling of the congenital long-QT 2 syndrome in the visible man torso: From genes to ECG. In *Engineering in Medicine and Biology Society, 2007. EMBS 2007. 29th Annual International Conference of the IEEE*, pages 1410–1413, 2007.

[Lai64] A. K. Laird. Dynamics of tumour growth. *British journal of cancer*, 18(3):490, 1964.

[Lai65] A. K. Laird. Dynamics of tumour growth: comparison of growth rates and extrapolation of growth curve to one cell. *British Journal of Cancer*, 19(2):278, 1965.

[Lav14] M. Lavielle. *Mixed effects models for the population approach: models, tasks, methods and tools*. CRC press, 2014.

[LBG+03] G.T. Lines, M.L. Buist, P. Grottum, A.J. Pullan, J. Sundnes, and A. Tveito. Mathematical models and numerical methods for the forward problem in cardiac electrophysiology. *Comput. Visual. Sci.*, 5(4):215–239, 2003.

[LDAW18] K. A. Layne, P. I. Dargan, J. RH. Archer, and D. M. Wood. Gadolinium deposition and the potential for toxicological sequelae–A literature review of issues surrounding gadolinium-based contrast agents. *British journal of clinical pharmacology*, 84(11):2522–2534, 2018.

[Lev44] K. Levenberg. A method for the solution of certain non-linear problems in least squares. *Quarterly of applied mathematics*, 2(2):164–168, 1944.

[LKP+17] E. J. Lee, J. H. Kim, E. S. Park, Y.-H. Kim, J. K. Lee, S. H. Hong, Y. H. Cho, and C. J. Kim. A novel weighted scoring system for estimating the risk of rapid growth in untreated intracranial meningiomas. *Journal of neurosurgery*, 127(5):971–980, 2017.

[LL08] S. Lakshmivarahan and J.M. Lewis. Nudging methods: A critical overview. In S.K. Park and L. Xu, editors, *Data Assimilation for Atmospheric, Oceanic, and Hydrologic Applications*, volume XVIII. Springer, 2008.

[Loo65] H. Looyenga. Dielectric constants of heterogeneous mixtures. *Physica*, 31(3):401–406, 1965.

[LPPK17] E. J. Lee, J. H. Park, E. S. Park, and J. H. Kim. "Wait-and-see" strategies for newly diagnosed intracranial meningiomas based on the risk of future observation failure. *World neurosurgery*, 107:604–611, nov 2017.

[LSMP14] M. Leguebe, A. Silve, L. M. Mir, and C. Poignard. Conducting and permeable states of cell membrane submitted to high voltage pulses: mathematical and numerical studies validated by the experiments. *Journal of theoretical biology*, 360:83–94, 2014.

[Lue63] D. G. Luenberger. *Determining the State of a Linear with Observers of Low Dynamic Order*. PhD thesis, Stanford University, 1963.

[Lue71] D. G. Luenberger. An introduction to observers. *IEEE Transactions on Automatic Control*, 16:596–602, 1971.

[Lvo12] V. F. Lvovich. *Impedance spectroscopy: applications to electrochemical and dielectric phenomena.* John Wiley & Sons, 2012.

[LW82] N. M. Laird and J. H. Ware. Random-effects models for longitudinal data. *Biometrics*, pages 963–974, 1982.

[Mar63] D. W. Marquardt. An algorithm for least-squares estimation of nonlinear parameters. *Journal of the society for Industrial and Applied Mathematics*, 11(2):431–441, 1963.

[MC11a] P. Moireau and D. Chapelle. Reduced-order unscented Kalman filtering with application to parameter identification in large-dimensional systems. *ESAIM: Control, Optimisation and Calculus of Variations*, 17(2):380–405, 2011.

[MC11b] P. Moireau and D. Chapelle. Reduced-order Unscented Kalman Filtering with application to parameter identification in large-dimensional systems. *ESAIM: Control, Optimisation and Calculus of Variations*, 17(2):380–405, 2011.

[MCLT08] P. Moireau, D. Chapelle, and P. Le Tallec. Joint state and parameter estimation for distributed mechanical systems. *Computer Methods in Applied Mechanics and Engineering*, 197:659–677, 2008.

[MCLT09] P. Moireau, D. Chapelle, and P. Le Tallec. Filtering for distributed mechanical systems using position measurements: Perspectives in medical imaging. *Inverse Problems*, 25(3):035010 (25pp), 2009.

[MCZ$^+$17] M. H. Mohammad, E. Chavredakis, R. Zakaria, A. Brodbelt, and M. D. Jenkinson. A national survey of the management of patients with incidental meningioma in the United Kingdom. *British journal of neurosurgery*, 31(4):459–463, 2017.

[MDFG12] V. Martin, A. Drochon, O. Fokapu, and J-F. Gerbeau. Magnetohemodynamics in the aorta and electrocardiograms. *Physics in Medicine and Biology*, 57:3177–3195, 2012.

[MFL$^+$18] T. Michel, J. Fehrenbach, V. Lobjois, J. Laurent, A. Gomes, T. Colin, and C. Poignard. Mathematical modeling of the proliferation gradient in multicellular tumor spheroids. *Journal of theoretical biology*, 458:133–147, 2018.

[Mir01] L. M. Mir. Therapeutic perspectives of in vivo cell electropermeabilization. *Bioelectrochemistry*, 53(1):1–10, 2001.

[MLR05] L. Miller, J. Leor, and B. Rubinsky. Cancer cells ablation with irreversible electroporation. *Technology in cancer research & treatment*, 4(6):699–705, 2005.

[MNS$^+$22] C. Merla, M. Nardoni, M. Scherman, S. Petralito, L. Caramazza, F. Apollonio, M. Liberti, P. Paolicelli, B. Attal-Tretout, and L. M. Mir. Changes in hydration of liposome membranes exposed to nanosecond electric pulses detected by wide-field Coherent anti-Stokes Raman microspectroscopy. *Bioelectrochemistry*, 147:108218, 2022.

[MOBP91] L. M. Mir, S. Orlowski, J. Belehradek, and C. Paoletti. Electrochemotherapy potentiation of antitumour effect of bleomycin by local electric pulses. *European Journal of Cancer and Clinical Oncology*, 27(1):68–72, 1991.

[MOKC$^+$21] F. Moisan, S. Oucherif, P. Kaulanjan-Checkmodine, S. Prey, B. Rousseau, M. Bonneu, S. Claverol, E. Gontier, S. Lacomme, L. Dousset, et al. Critical role of Aquaporin-1 and telocytes in infantile hemangioma response to propranolol beta blockade. *Proceedings of the national academy of sciences*, 118(7):e2018690118, 2021.

[Mor09] Y. Mori. From three-dimensional electrophysiology to the cable model: an asymptotic study. *arXiv preprint arXiv:0901.3914*, 2009.

[MP95] J. Malmivuo and R. Plonsey. *Bioelectromagnetism - Principles and Applications of Bioelectric and Biomagnetic Fields*. Oxford University Press, 1995.

[MS83] J. J. Moré and D. C. Sorensen. Computing a trust region step. *SIAM Journal on scientific and statistical computing*, 4(3):553–572, 1983.

[MS03] C. C. Mitchell and D. G. Schaeffer. A two-current model for the dynamics of cardiac membrane. *Bulletin Math. Bio.*, 65:767–793, 2003.

[MSB$^+$12] D. Miklavčič, G. Serša, E. Brecelj, J. Gehl, D. Soden, G. Bianchi, P. Ruggieri, C. R. Rossi, LG. Campana, and T. Jarm. Electrochemotherapy: technological advancements for efficient electroporation-based treatment of internal tumors. *Medical & biological engineering & computing*, 50(12):1213–1225, 2012.

[NAY62] J. S. Nagumo, S. Arimoto, and S. Yoshizawa. An active pulse transmission line stimulating nerve axon. *Proceedings of the IEEE*, 50:2061–2071, 1962.

[NFF$^+$98] A. Nygren, C. Fiset, L. Firek, J.W. Clark, D.S. Lindblad, R.B. Clark, and W.R. Giles. Mathematical model of an adult human atrial cell the role of K+ currents in repolarization. *Circulation Research*, 82(1):63–81, 1998.

[NFN$^+$05] S. Nakasu, T. Fukami, M. Nakajima, K. Watanabe, M. Ichikawa, and M. Matsuda. Growth pattern changes of meningiomas: long-term analysis. *Neurosurgery*, 56(5):946–955, 2005.

[Ngu89] G. Nguetseng. A general convergence result for a functional related to the theory of homogenization. *SIAM Journal on Mathematical Analysis*, 20(3):608 – 623, 1989.

[NK93] J. C. Neu and W. Krassowska. Homogenization of syncytial tissues. *Critical Reviews in Biomedical Engineering*, 21(2):137–199, 1993.

[NK99] J. C. Neu and W. Krassowska. Asymptotic model of electroporation. *Physical Review E*, 59(3):3471–3482, mar 1999.

[NNF$^+$11] S. Nakasu, Y. Nakasu, T. Fukami, J. Jito, and K. Nozaki. Growth curve analysis of asymptomatic and symptomatic meningiomas. *Journal of neuro-oncology*, 102(2):303–310, 2011.

[Nor88] L. Norton. A gompertzian model of human breast cancer growth. *Cancer research*, 48(24 Part 1):7067–7071, 1988.

[NP04] M. P. Nash and A. V. Panfilov. Electromechanical model of excitable tissue to study reentrant cardiac arrhythmias. *Progress in Biophysics and Molecular Biology*, 85(2-3):501–522, 2004.

[NRM$^+$03] M. Nakamura, F. Roser, J. Michel, C. Jacobs, and M. Samii. The natural history of incidental meningiomas. *Neurosurgery*, 53(1):62–71, 2003.

[OGF$^+$13] Q. T. Ostrom, H. Gittleman, P. Farah, A. Ondracek, Y. Chen, Y. Wolinsky, N. E. Stroup, C. Kruchko, and J. S. Barnholtz-Sloan. CBTRUS statistical report: Primary brain and central nervous system tumors diagnosed in the united states in 2006-2010. *Neuro-oncology*, 15(suppl_2):ii1–ii56, 2013.

[OKSL11] S. Oya, S.-H. Kim, B. Sade, and J. H. Lee. The natural history of intracranial meningiomas. *Journal of neurosurgery*, 114(5):1250–1256, 2011.

[OVVR11] T. O'Hara, L. Virág, A. Varró, and Y. Rudy. Simulation of the undiseased human cardiac ventricular action potential: Model formulation and experimental validation. *PLoS Comput Biol*, 7(5):e1002061, 2011.

[PDG03] M. Potse, B. Dubé, and R.M. Gulrajani. ECG simulations with realistic human membrane, heart, and torso models. In *Engineering in Medicine and Biology Society, 2003. Proceedings of the 25th Annual International Conference of the IEEE*, volume 1, pages 70–73, 2003.

[PDV09] M. Potse, B. Dubé, and A. Vinet. Cardiac anisotropy in boundary-element models for the electrocardiogram. *Medical & biological engineering & computing*, 47(7):719–729, 2009.

[PKN05] A. V. Panfilov, R. H. Keldermann, and M. P. Nash. Self-organized pacemakers in a coupled reaction-diffusion-mechanics system. *Physical review letters*, 95(25):258104, 2005.

[PKW$^+$07] A. G. Pakhomov, J. F. Kolb, J. A. White, R. P. Joshi, S. Xiao, and K. H. Schoenbach. Long-lasting plasma membrane permeabilization in mammalian cells by nanosecond pulsed electric field (nsPEF). *Bioelectromagnetics*, 28(8):655–663, 2007.

[PP13] R. Perrussel and C. Poignard. Asymptotic expansion of steady-state potential in a high contrast medium with a thin resistive layer. *Applied Mathematics and Computation*, 221:48–65, 2013.

[PSC$^+$11] C. Poignard, A. Silve, F. Campion, L. M. Mir, O. Saut, and L. Schwartz. Ion fluxes, transmembrane potential, and osmotic stabilization: a new dynamic electrophysiological model for eukaryotic cells. *European Biophysics Journal*, 40(3):235–246, 2011.

[PSCF05] M. Pennacchio, G. Savaré, and P. Colli Franzone. Multiscale modeling for the bioelectric activity of the heart. *SIAM Journal on Mathematical Analysis*, 37(4):1333–1370, 2005.

[Pta17] M. Ptashnyk. Multiscale modelling and analysis of signalling processes in tissues with non-periodic distribution of cells. *Vietnam Journal of Mathematics*, 45(1):295–316, 2017.

[QLRRB17] A. Quarteroni, T. Lassila, S. Rossi, and R. Ruiz-Baier. Integrated heart-coupling multiscale and multiphysics models for the simulation of the cardiac function. *Computer Methods in Applied Mechanics and Engineering*, 314:345–407, 2017. Special Issue on Biological Systems Dedicated to William S. Klug.

[RC11] G. Richardson and J. Chapman. Derivation of the bidomain equations for a beating heart with a general microstructure. *SIAM Journal on Applied Mathematics*, 71(3):657–675, 2011.

[RDN$^+$21] V. Y. Reddy, S. R. Dukkipati, P. Neuzil, A. Anic, J. Petru, M. Funasako, H. Cochet, K. Minami, T. Breskovic, I. Sikiric, et al. Pulsed field ablation of paroxysmal atrial fibrillation: 1-year outcomes of IMPULSE, PEFCAT, and PEFCAT II. *Clinical Electrophysiology*, 7(5):614–627, 2021.

[RHM$^+$14] B. Ribba, Nick H. Holford, P. Magni, I. Trocóniz, I. Gueorguieva, P. Girard, C. Sarr, M. Elishmereni, C. Kloft, and Lena E. Friberg. A review of mixed-effects models of tumor growth and effects of anticancer drug treatment used in population analysis. *CPT: pharmacometrics & systems pharmacology*, 3(5):1–10, 2014.

[Ric09] G. Richardson. A multiscale approach to modelling electrochemical processes occurring across the cell membrane with application to transmission of action potentials. *Mathematical Medicine and Biology*, 26(3):201–224, 2009.

[RKP$^+$12] B. Ribba, G. Kaloshi, M. Peyre, D. Ricard, V. Calvez, M. Tod, B. Čajavec-Bernard, A. Idbaih, D. Psimaras, L. Dainese, et al. A tumor growth inhibition model for low-grade glioma treated with chemotherapy or radiotherapy. *Clinical Cancer Research*, 18(18):5071–5080, 2012.

[Ros21] F. Rosier. COVID-19 : malgré cinq semaines de baisse continue en métropole, les épidémiologistes restent prudents. *Le Monde*, 2021.

[RRBP18] R. Romani, G. Ryan, C. Benner, and J. Pollock. Non-operative meningiomas: long-term follow-up of 136 patients. *Acta neurochirurgica*, 160(8):1547–1553, 2018.

[RSC$^+$06] B. Ribba, O. Saut, T. Colin, D. Bresch, E. Grenier, and J.-P. Boissel. A multiscale mathematical model of avascular tumor growth to investigate the therapeutic benefit of anti-invasive agents. *Journal of theoretical biology*, 243(4):532–541, 2006.

[Sac04] F.B. Sachse. *Computational Cardiology: Modeling of Anatomy, Electrophysiology and Mechanics*. Springer-Verlag, 2004.

[SAM00] K. R. Swanson, E. C. Alvord, and J. D. Murray. A quantitative model for differential motility of gliomas in grey and white matter. *Cell Prolif.*, 33(5):317–329, 2000.

[SB93] D. R. Stauffer and J.-W. Bao. Optimal determination of nudging coefficients using the adjoint equations. *Tellus A*, 45(5):358–369, 1993.

[SBMAJ03] K. R. Swanson, C. Bridge, J.D. Murray, and E. C. Alvord Jr. Virtual and real brain tumors: using mathematical modeling to quantify glioma growth and invasion. *Journal of the neurological sciences*, 216(1):1–10, 2003.

[SCB$^+$05] D. Sel, D. Cukjati, D. Batiuskaite, T. Slivnik, L. M. Mir, and D. Miklavcic. Sequential finite element model of tissue electropermeabilization. *IEEE Transactions on Biomedical Engineering*, 52(5):816–827, 2005.

[Sch66] H. P. Schwan. Alternating current electrode polarization. *Biophysik*, 3(2):181–201, 1966.

[SCN$^+$17] O. Sutter, J. Calvo, G. N'Kontchou, J.-C. Nault, R. Ourabia, P. Nahon, N. Ganne-Carrié, V. Bourcier, N. Zentar, F. Bouhafs, et al. Safety and efficacy of irreversible electroporation for the treatment of hepatocellular carcinoma not amenable to thermal ablation techniques: a retrospective single-center case series. *Radiology*, 284(3):877–886, 2017.

[SdlRB$^+$09] V. Sans, E. D. de la Roque, J. Berge, N. Grenier, F. Boralevi, J. Mazereeuw-Hautier, D. Lipsker, E. Dupuis, K. Ezzedine, P. Vergnes, et al. Propranolol for severe infantile hemangiomas: follow-up report. *Pediatrics*, 124(3):e423–e431, 2009.

[SF68] H. P. Schwan and C. D. Ferris. Four-electrode null techniques for impedance measurement with high resolution. *Review of scientific instruments*, 39(4):481–485, 1968.

[SLCFS14] O. Saut, J.-B. Lagaert, T. Colin, and H. M. Fathallah-Shaykh. A multilayer grow-or-go model for GBM: effects of invasive cells and anti-angiogenesis on growth. *Bulletin of mathematical biology*, 76(9):2306–2333, 2014.

[SNdJ$^+$14] H. J. Scheffer, K. Nielsen, M. C. de Jong, A. van Tilborg, J. M. Vieveen, A. Bouwman, S. Meijer, C. van Kuijk, P. van den Tol, and M. R. Meijerink. Irreversible electroporation for nonthermal tumor ablation in the clinical setting: a systematic review of safety and efficacy. *Journal of Vascular and Interventional Radiology*, 25(7):997–1011, 2014.

[SPGS18] L. Sala, C. Prud'homme, G. Guidoboni, and M. Szopos. Ocular mathematical virtual simulator: A hemodynamical and biomechanical study towards clinical applications. *Journal of Coupled Systems and Multiscale Dynamics*, 6(3), 2018.

[SRA$^+$10] M. E. Sughrue, M. J. Rutkowski, D. Aranda, I. J. Barani, M. W. McDermott, and A. T. Parsa. Treatment decision making based on the published natural history and growth rate of small meningiomas: a review and meta-analysis. *Journal of neurosurgery*, 113(5):1036–1042, 2010.

[SS90] D. R. Stauffer and N. L. Seaman. Use of four-dimensional data assimilation in a limited-area mesoscale model. Part I: Experiments with synoptic-scale data. *Monthly Weather Review*, 118(6):1250–1277, 1990.

[SSGW14] K. C. Smith, R. S. Son, T. R. Gowrishankar, and J. C. Weaver. Emergence of a large pore subpopulation during electroporating pulses. *Bioelectrochemistry*, 100:3–10, dec 2014.

[TDP$^+$04] M.-C. Trudel, B. Dubé, M. Potse, R.M. Gulrajani, and L.J. Leon. Simulation of QRST integral maps with a membrane-based computer heart model employing parallel processing. *IEEE Transactions on Biomedical Engineering*, 51(8):1319–1329, 2004.

[TGR05] J. Teissie, M. Golzio, and MP. Rols. Mechanisms of cell membrane electropermeabilization: a minireview of our present (lack of?) knowledge. *Biochimica et Biophysica Acta (BBA)-General Subjects*, 1724(3):270–280, 2005.

[TM05] R. Temam and A. Miranville. *Mathematical Modeling in Continuum Mechanics*. Cambridge University Press, second edition, 2005.

[tTNNP04] K. H. W. J. ten Tusscher, D. Noble, P.J. Noble, and A. V. Panfilov. A model for human ventricular tissue. *American Journal of Physiology-Heart and Circulatory Physiology*, 286(4):H1573–H1589, 2004.

[tTP06] K. H. W. J. ten Tusscher and A. V. Panfilov. Alternans and spiral breakup in a human ventricular tissue model. *American Journal of Physiology-Heart and Circulatory Physiology*, 291(3):H1088–H1100, 2006.

[Tun78] L. Tung. *A bi-domain model for describing ischemic myocardial d-c potentials.* PhD thesis, Massachusetts Institute of Technology. Dept. of Electrical Engineering and Computer Science., 1978.

[Ver97] G. Verbeke. Linear mixed models for longitudinal data. In *Linear mixed models in practice*, pages 63–153. Springer, 1997.

[VIT$^+$07] M. W. Vernooij, M. A. Ikram, H. L. Tanghe, A. JPE Vincent, A. Hofman, G. P. Krestin, W. J. Niessen, M. MB Breteler, and A. van der Lugt. Incidental findings on brain MRI in the general population. *New England Journal of Medicine*, 357(18):1821–1828, 2007.

[VLDP03] P.A. Vidard, F.-X. Le Dimet, and A. Piacentini. Determination of optimal nudging coefficients. *Tellus A*, 55(1):1–15, 2003.

[VRF$^+$20] C. Vaghi, A. Rodallec, R. Fanciullino, J. Ciccolini, JP. Mochel, M. Mastri, C. Poignard, JML. Ebos, and S. Benzekry. Population modeling of tumor growth curves and the reduced Gompertz model improve prediction of the age of experimental tumors. *PLoS computational biology*, 16(2):e1007178, 2020.

[VSM$^+$18] D. Voyer, A. Silve, L. M. Mir, R. Scorretti, and C. Poignard. Dynamical modeling of tissue electroporation. *Bioelectrochemistry*, 119:98–110, 2018.

[War75] F. Wartak. *Electrocardiogram interpretation*. Medical Education Systems, 1975.

[WC96] J. C. Weaver and Y. A. Chizmadzhev. Theory of electroporation: A review. *Bioelectrochemistry and Bioenergetics*, 41(2):135–160, dec 1996.

[WGRS12] S. T. Wall, J. M. Guccione, M. B. Ratcliffe, and J. S. Sundnes. Electromechanical feedback with reduced cellular connectivity alters electrical activity in an infarct injured left ventricle: a finite element model study. *American Journal of Physiology-Heart and Circulatory Physiology*, 302(1):H206–H214, 2012.

[WN06] F. H. M. Wittkampf and H. Nakagawa. RF catheter ablation: lessons on lesions. *Pacing and Clinical Electrophysiology*, 29(11):1285–1297, 2006.

[WOH$^+$95] D. Wei, O. Okazaki, K. Harumi, E. Harasawa, and H. Hosaka. Comparative simulation of excitation and body surface electrocardiogram with isotropic and anisotropic computer heart models. *Biomedical Engineering, IEEE Transactions on*, 42(4):343–357, 1995.

[WSE$^+$12] J. C. Weaver, K. C. Smith, A. T. Esser, R. S. Son, and T. R. Gowrishankar. A brief overview of electroporation pulse strength–duration space: A region where additional intracellular effects are expected. *Bioelectrochemistry*, 87:236–243, oct 2012.

[ZAD$^+$08] L. A. Zeidman, W. J. Ankenbrandt, H. Du, N. Paleologos, and N. A. Vick. Growth rate of non-operated meningiomas. *Journal of neurology*, 255(6):891–895, 2008.

[ZLJ+15] L. Zeng, P. Liang, J. Jiao, J. Chen, and T. Lei. Will an asymptomatic meningioma grow or not grow? A meta-analysis. *Journal of Neurological Surgery Part A: Central European Neurosurgery*, 76(05):341–347, 2015.

[ZNLD92] X. Zou, I.M. Navon, and F.-X. Le Dimet. An optimal nudging data assimilation scheme using parameter estimation. *Quarterly Journal of the Royal Meteorological Society*, 118(508):1163–1186, 1992.